FERMILAB-THESIS-2002-34

NORTHWESTERN UNIVERSITY

A Precise Measurement of the Weak Mixing Angle in Neutrino-Nucleon Scattering

A DISSERTATION

SUBMITTED TO THE GRADUATE SCHOOL

IN PARTIAL FULFILLMENT OF THE REQUIREMENTS

for the degree

DOCTOR OF PHILOSOPHY

Field of Physics

By

Geralyn P. Zeller

EVANSTON, ILLINOIS

June 2002

ABSTRACT

A Precise Measurement of the Weak Mixing Angle in Neutrino–Nucleon Scattering

Geralyn P. Zeller

This dissertation reports a precise determination of the weak mixing angle, $\sin^2\theta_W$, from measurement of the ratios of neutral current to charged current neutrino deep inelastic cross sections. High statistics samples of separately collected neutrino and antineutrino events, resulting from exposure to the Fermilab neutrino beam during the period from 1996 to 1997, allowed the reduction of systematic errors associated with charm production and other sources. The final value, ${\sin^2\theta_W}^{\nu N} \equiv 1 - M_W^2/M_Z^2 = 0.2277 \pm 0.0013\ (\text{stat}) \pm 0.0009\ (\text{syst})$, lies three standard deviations above the prediction from global electroweak fits. The measurement is currently the most precise determination of $\sin^2\theta_W$ in neutrino–nucleon scattering, surpassing its predecessors by a factor of two in precision, and is statistics–dominated. Within the standard model, this measurement of $\sin^2\theta_W$ indirectly determines the W boson mass, M_W, with a precision comparable to direct measurements from high energy e^+e^- and $p\overline{p}$ colliders. Relaxing the standard model assumptions, a model independent analysis recasts the same data into a measurement of effective left and right handed neutral current quark couplings.

PLAIN ENGLISH THESIS SUMMARY

— dedicated to my parents —

The NuTeV experiment at Fermilab studies the manner in which neutrinos interact with matter. The unique feature of the experiment is the observation of millions of neutrino interactions. This is, however, not an easy task as neutrinos only rarely interact with matter. Sufficient numbers of neutrino events could be collected only by bombarding a massive detector with energetic neutrinos produced using the highest energy accelerator in the world (the Fermilab Tevatron).

To see these interactions, the NuTeV collaboration built a 700 ton stack of over a hundred alternating slices of steel and particle detectors. Even with 700 tons of material, approximately only one in a billion neutrinos from the accelerator interacted in the detector. In such an interaction, the neutrino slams into an iron nucleus in the NuTeV detector and breaks it apart. After the collision, the neutrino might emerge intact or turn into a muon (the heavy cousin to the electron). The measurement presented in this thesis involved counting the number of times the neutrino survived versus the number of times it changed into a muon. From this ratio, NuTeV determined a value for the weak mixing angle ($\sin^2\theta_W$), a key parameter in particle physics which relates the W and Z boson masses. This parameter is very precisely predicted by the standard theory of elementary particles to be 0.2227. The NuTeV experiment instead found a rather surprising result, measuring $\sin^2\theta_W$ to be 0.2277 ± 0.0016! This might not seem like a very large difference (the first two digits match the theoretical prediction), but given the precision of the measurement, the probability that it is consistent with the theoretical expectation is only 1 in 400.

Currently there is no known explanation for the results. However, perhaps this isn't so out of the ordinary. Neutrinos have surprised researchers and theoreticians in the past; first with their very existence and later with the unexpected experimental evidence that they transform from one type into another. Neutrinos might once again be pointing us in a new direction and thereby serendipitously providing us with a greater understanding of the basic theory of particles and forces.

Dr. Geralyn P. Zeller

May 8, 2002

Dedicated in loving memory

to:

Rev. Maurice S. Zeller, S.T.D., C.Ss.R.

Contents

List of Figures

List of Tables

Chapter 1

Introduction

This introductory chapter describes the standard model of elementary particles, deep inelastic scattering kinematics, the quark parton model, and the cross sections for neutrino deep inelastic scattering. This review is the foundation for the remainder of this dissertation. The final section provides an overview of the organization and content of the chapters to follow.

1.1 Standard Model of Fundamental Particles

In the current world view, all matter can be constructed from fundamental particles which are not comprised of smaller entities and do not exhibit internal structure. The fundamental particles we know of come in two varieties: fermions and bosons. Figure 1.1 provides the high energy physics equivalent to the chemist's periodic table; it contains all currently known elementary particles. The easiest way to understand the structure is to arrange the particles according to their interactions.

The fermions comprise two subgroups: quarks and leptons. Quarks interact via the electromagnetic, weak, and strong forces. Leptons interact via the electromagnetic (for those that carry electric charge) and weak forces. Both quarks and leptons consist of three "generations" of doublets. The quarks include six varieties: up (u), down (d), charm (c), strange (s), top (t), and bottom (b). In the most simplistic view, protons and neutrons inhabiting the nucleus of an atom are each comprised of a combination of three quarks: uud in the case of the proton, ddu in the case of the neutron. Table 1.1 indicates the charge assignments for each of the constituent quarks. Note that the fractional quark charges sum to the observed charge of the composite particle.

Leptons include both charged particles (electrons ($e^{\pm}$), muons ($\mu^{\pm}$), and taus ($\tau^{\pm}$)), as well as three electrically neutral neutrinos (ν_e, ν_μ, and ν_τ).

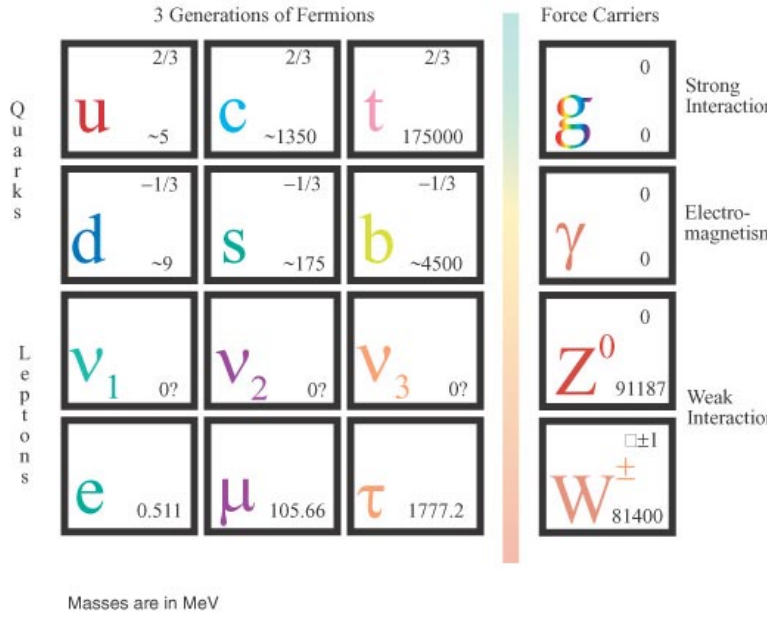

Figure 1.1: The standard model of fundamental particles. Each particle's electric charge is listed in the upper corner, their mass (in MeV) in the bottom corner.

At the right hand side of Figure 1.1 are the gauge bosons, named after the "gauge" theory that describes them. The bosons include the photon that carries the electromagnetic force, the $W^{\pm}$ and Z^0 bosons that carry the weak force, and the gluon that carries the strong force. What do we mean by force carriers? Recall the simple picture of two opposite charges repelling each other. Classical theory represents the attractive force acting between them as electric "field lines" (Figure 1.2). On the quantum level, this "field" representation reduces to the exchange of a single particle.

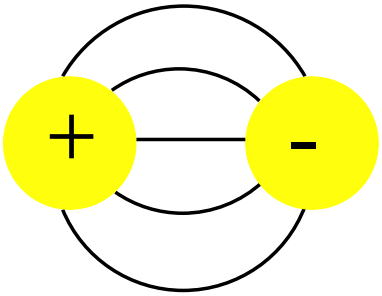

Figure 1.2: Classical picture of the electromagnetic force acting between two oppositely charged particles. The force is represented by electric field lines.

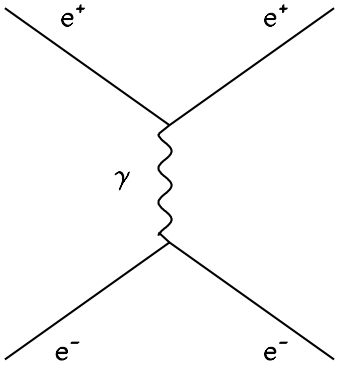

Figure 1.3: Quantum level picture of the electromagnetic force acting between two oppositely charged electrons. The force is mediated by the exchange of a photon. Time flow is from left to right.

Figure 1.3 shows the quantum level depiction, a Feynman diagram, in which the force between the two particles is assumed to be mediated by a force-carrying particle. In this case, the two electrons (e^- and e^+) attract each other because they exchange a photon, a quantum of light. The massless photon carries the electromagnetic force, transferring energy and momentum from one electron to the other. The quantum theory of the electromagnetic field is known as Quantum Electrodynamics

(or QED).

Neutrinos, on the other hand, have no charge and therefore cannot interact electromagnetically. The interactions of neutrinos require introduction of another force, the weak force, and another set of force carriers, the massive W and Z bosons. In fact, neutrinos can weakly interact in one of two ways. In the charged current (CC) case, the weak force is mediated by the exchange of a charged $W^{\pm}$ boson (Figure 1.4). In the neutral current (NC) case, the exchange particle is a Z^0 boson (Figure 1.5). The need for two different weak mechanisms arises from the need to describe two distinct final states.

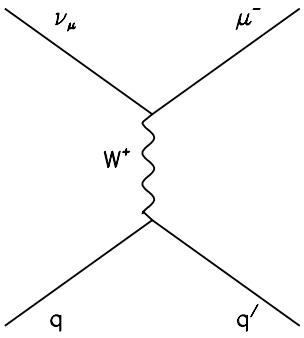

Figure 1.4: Quantum level picture of a neutrino interacting via the weak force through exchange of a W boson. This type of interaction is known as a charged current (CC) interaction because the mediator W boson is electrically charged.

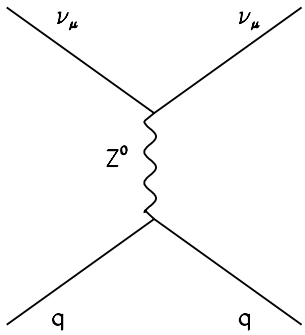

Figure 1.5: Quantum level picture of a neutrino interacting via the weak force through exchange of a Z boson. This type of interaction is known as a neutral current (NC) interaction because the mediator Z boson is electrically neutral.

Finally, gluons mediate the strong force between quarks (Figure 1.6). The quantum theory of the strong force is known as Quantum Chromodynamics (or QCD). According to QCD, each quark flavor may carry one of three possible strong charges, called "color". The quarks interact by exchanging spin–one, massless particles, called

gluons, which themselves carry colors. So unlike the other force–carriers, the gluons can directly interact with each other.

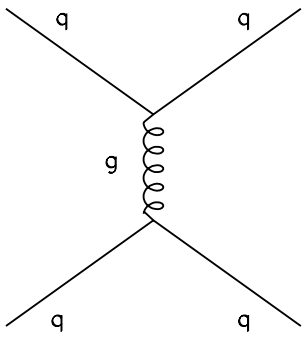

Figure 1.6: Quantum level picture of the strong force acting between quarks. The force is mediated by the exchange of a gluon.

The combination of QED, weak interactions, and QCD form the so–called "standard model" of particle interactions. Table 1.1 summarizes the four fundamental forces in nature and their corresponding field particles.

Force	Relative Coupling	Force Carrier
strong	> 1	gluon (g)
electromagnetic	$\sim 1/137$	photon (γ)
weak	$\sim 10^{-5}$	$W^{\pm}$, Z^0
gravitational	$\sim 10^{-42}$	graviton

Table 1.1: The four fundamental forces in nature arranged according to their relative couplings to particles in low energy interactions.

Because the work of this dissertation is a neutrino measurement, neutrino interactions require further discussion. Neutrinos can only interact weakly. It turns out that the weak force is very aptly named. Neutrinos rarely interact with each other or anything else. The mean free path length of 100 GeV neutrinos in steel is roughly

3×10^9 meters! As a result, detecting neutrino interactions requires both massive detectors and large numbers of neutrinos to be successful. In the standard model, the observed rarity of the weak interaction is not explained by a small coupling constant but rather by its short range. It follows from the Heisenberg uncertainty principle (ΔE Δt $\geq$ h), that the range (R) of an interaction inversely depends on the mass (M) of the exchanged virtual particle:

$$R = \frac{\hbar}{\mathrm{M\,c}} \tag{1.1}$$

So whereas the massless photon affords the electromagnetic force an infinite range, the weak force has a very short range because of the massiveness of the W and Z mediators.

1.2 Deep Inelastic Scattering

At NuTeV, neutrinos can inelastically scatter off nucleons in the iron target. This section introduces variables specific to deep inelastic scattering (DIS) processes. Figure 1.7 shows a generic deep inelastic scattering event which takes the form:

$$l\,(k) + p\,(p) \rightarrow l\,(k') + X\,(p') \tag{1.2}$$

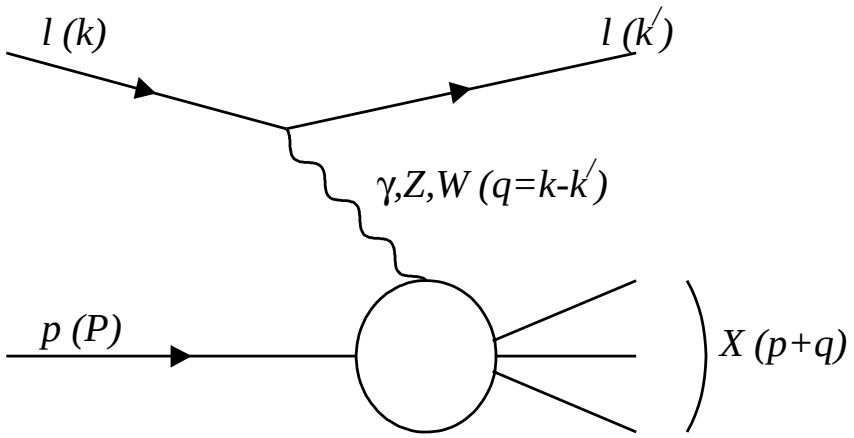

Figure 1.7: Schematic of a generic deep inelastic scattering event which consists of a lepton beam (e,μ,ν) incident on a nucleon target.

The incoming lepton can be an electron, muon, or neutrino; the exchanged vector boson can be a photon, $W^{\pm}$, or Z^0. The lepton scatters inelastically off the target nucleon, either a proton or neutron, producing a final state which includes the scattered lepton and the debris of the nucleon. Nucleon constituents, namely quarks and gluons, recombine very rapidly into hadrons and thus appear as a hadronic shower. Hadrons include any strongly–interacting composite particle, for example, protons, neutrons, pions, and kaons. Because pions are the lightest hadrons, they are emitted preferentially in such hadronic interactions. The X in Equation (1.2) indicates this

complex hadronic final state.

Consider the case of neutrino charged–current deep inelastic scattering. The four-momenta of the incoming neutrino (k), outgoing muon (k'), exchanged virtual W boson (q), target nucleon (p), and hadronic final state (p') in the lab frame are:

$$k = (E_\nu, 0, 0, E_\nu) \tag{1.3}$$

$$k' = (E_\mu, p_\mu \sin\theta_\mu \cos\phi_\mu, p_\mu \sin\theta_\mu \sin\phi_\mu, p_\mu \cos\theta_\mu) \tag{1.4}$$

$$p = (M, 0, 0, 0) \tag{1.5}$$

$$q = (\nu, \vec{q}) \tag{1.6}$$

$$p' = p + q = p + (k - k') \tag{1.7}$$

where M is the nucleon mass, E_ν is the incoming neutrino energy, p_μ is the momentum of the outgoing muon, θ_μ is the angle of the outgoing muon with respect to the incoming beam direction, and ν is the energy transfer to the nucleon. Several useful variables include:

- Q^2 = the momentum of the exchanged boson which defines the energy scale of the interaction; it is the "space–like" momentum transfer between the lepton and hadron:

$$Q^2 = -q^2 = -(k - k')^2 = m_\mu^2 + 2E_\nu(E_\mu - p_\mu \cos\theta_\mu) \tag{1.8}$$

- ν = the energy transferred from the lepton to the hadronic system:

$$\nu = \frac{p \cdot q}{M} = E_\nu - E_\mu = \mathrm{E_{had}} \tag{1.9}$$

- W^2 = the invariant mass of the hadronic system:

$$W^2 = (q+p)^2 \quad = \quad M^2 + 2M\nu - Q^2 \tag{1.10}$$

In addition, we define two dimensionless variables:

- y = inelasticity, the fraction of the total leptonic energy available in the target rest frame transferred to the hadronic system:

$$y = \frac{p \cdot q}{p \cdot k} = \frac{\mathrm{E_{had}}}{E_\nu} \tag{1.11}$$

  In terms of center-of-mass (CM) quantities (indicated by the *),

$$y \simeq 1 - \frac{\gamma\, E^*_\nu\, (1 + \cos\theta^*)}{2\gamma E^*_\nu} = 1 - \frac{1}{2}\,(1 + \cos\theta^*) \tag{1.12}$$

  where γ is the Lorentz boost factor relating the CM to the lab frame

- x = the Bjorken scaling variable, the fraction of the total nucleon momentum carried by the struck quark:

$$x = \frac{-q^2}{2p \cdot q} = \frac{Q^2}{2M\nu} = \frac{Q^2}{2ME_\nu y} \tag{1.13}$$

The NuTeV detector directly measures the energy (E_μ) and angle (θ_μ) of outgoing muons in CC neutrino interactions, and the energy of final state hadrons ($\mathrm{E_{had}}$). Given these parameters, the x and Q^2 of the CC event can be determined. However, x and Q^2 cannot be determined in the case of NC scattering because the energy of the outgoing neutrino is not known.

1.3 Neutrino-Nucleon Cross Sections

The inclusive cross sections for deep inelastic neutrino-nucleon scattering processes:

$$\nu_\mu(\overline{\nu}_\mu) + N \longrightarrow \mu^-(\mu^+) + X \tag{1.14}$$

$$\nu_\mu(\overline{\nu}_\mu) + N \longrightarrow \nu_\mu(\overline{\nu}_\mu) + X \tag{1.15}$$

are written in lowest order as the product of a leptonic tensor $L_{\mu\,\nu}$ and a hadronic tensor $W^{\mu\,\nu}$ which describe the leptonic and hadronic vertices, respectively [8]:

$$\frac{d^2\sigma^{\nu,\overline{\nu}}}{dx\,dy} = \frac{G_F^2\,y}{16\pi}\frac{1}{(1+Q^2/M_{W,Z}^2)^2}\,L_{\mu\,\nu}W^{\mu\,\nu} \tag{1.16}$$

Here, the vector boson mass is M_W for CC interactions and M_Z for NC interactions, G_F is the Fermi constant, and $y = \mathrm{E_{had}}/E$. The leptonic tensor is given by:

$$L_{\mu\,\nu} = 2\,\mathrm{Tr}[(\not{k}' + m)\gamma_\mu(1-\gamma_5)\not{k}\,\gamma_\nu] \tag{1.17}$$

with $m = m_\mu$ for the CC case and $m \simeq 0$ for the NC case. The most general form for the hadronic tensor is constructed in terms of scalar functions, W_i, which describe the structure of the nucleon [9]:

$$\begin{aligned} W^{\mu\,\nu} = \; & - \; g^{\mu\,\nu}\,W_1(x,Q^2) + \frac{p^\mu p^\nu}{M^2}\,W_2(x,Q^2) - i\epsilon^{\mu\,\nu\,\lambda\,\sigma}\frac{p_\lambda q_\sigma}{2M^2}\,W_3(x,Q^2) \\ & + \; \frac{q^\mu q^\nu}{M^2}\,W_4(x,Q^2) + (p^\mu q^\nu + p^\nu q^\mu)\,W_5(x,Q^2) \end{aligned} \tag{1.18}$$

In practice, the functions W_i are usually replaced by equivalent dimensionless structure functions, F_i, which, as seen in the next section, have a simple representation

in the quark parton model:

$$F_1(x,Q^2) = W_1(x,Q^2) \tag{1.19}$$

$$F_2(x,Q^2) = \frac{\nu}{M} W_2(x,Q^2) \tag{1.20}$$

$$F_3(x,Q^2) = \frac{\nu}{M} W_3(x,Q^2) \tag{1.21}$$

$$F_4(x,Q^2) = \frac{\nu}{M} W_4(x,Q^2) \tag{1.22}$$

$$F_5(x,Q^2) = W_5(x,Q^2) \tag{1.23}$$

Contraction of the leptonic and hadronic tensors yields the doubly–differential neutrino nucleon deep inelastic scattering cross section:

$$\frac{d^2\sigma^{\nu,\overline{\nu}}}{dx\,dy} = \frac{G_F^2 ME}{\pi\,(1+Q^2/M_{W,Z}^2)^2} \left[\begin{array}{c} (\frac{y^2}{2} + \frac{m^2 y}{4MEx})\,2xF_1(x,Q^2) \\ + \left(1 - y - \frac{Mxy}{2E} - \frac{m^2}{4E^2}\right)\,F_2(x,Q^2) \\ \pm \left(y\left(1-\frac{y}{2}\right) - \frac{m^2 y}{4MEx}\right)\,xF_3(x,Q^2) \\ + \left(\frac{m^2 xy}{2ME} + \frac{m^4}{4M^2E^2}\right)\,F_4(x,Q^2) \\ -\frac{m^2}{2MEx}\,xF_5(x,Q^2) \end{array} \right] \tag{1.24}$$

Neglecting the lepton mass terms, this expression reduces to:

$$\frac{d^2\sigma^{\nu,\overline{\nu}}}{dx\,dy} = \frac{G_F^2 ME}{\pi\,(1+Q^2/M_{W,Z}^2)^2} \left[\begin{array}{c} \frac{y^2}{2} 2xF_1(x,Q^2) + \left(1 - y - \frac{Mxy}{2E}\right)\,F_2(x,Q^2) \\ \pm y\left(1-\frac{y}{2}\right)\,xF_3(x,Q^2) \end{array} \right] \tag{1.25}$$

where the +(−) sign in the last term refers to the case of neutrino (antineutrino) scattering. The structure functions F_i(x,Q^2) in these expressions depend on the type of interaction and the target. Assuming a quark parton model description, the

structure functions can be expressed in terms of the quark composition of the target nucleons. This connection is presented in the next section.

1.4 The Parton Model of Hadrons

The parton model allows the description of neutrino–nucleon scattering processes in terms the scattering off nucleon constituents (Figure 1.8).

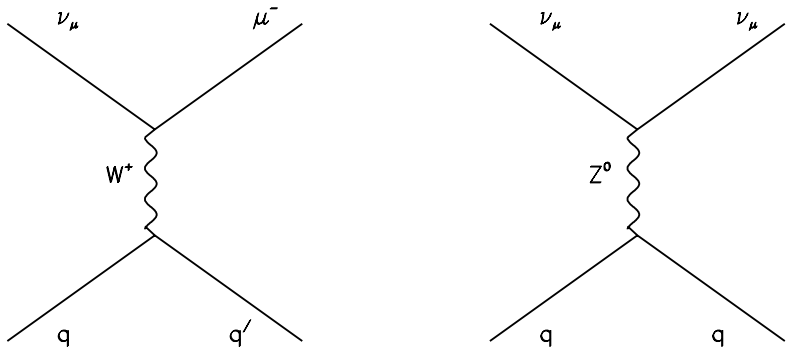

Figure 1.8: Feynman diagrams for CC and NC neutrino–quark scattering.

In the quark parton model, the nucleons consist of partons (quarks and gluons), which behave as pointlike particles. Roughly half of the nucleon's momentum is ascribed to gluons, which bind the quarks together but do not couple to the weak force. The remaining momentum is attributed to quarks, both valence and sea varieties. Valence quarks define the charge and spin of the nucleon. Protons, for instance, contain two u valence quarks and one d valence quark. Neutrons contain one u valence quarks and two d valence quark. The quarks interact primarily by exchanging gluons, which can themselves fluctuate into a quark–antiquark pair, which are generally called sea quarks.

In the infinite momentum frame in which the parton model is valid, the nucleon's momentum is assumed to be much larger than the transverse momentum associated with the strong interactions between the quarks. Hence, neutrino–nucleon scattering can be described in terms of elastic scattering off a single non–interacting parton. Because the partons are assumed to be essentially free, the nucleon structure functions F_i can then be written as the the sum of the probabilities of scattering from single partons. Our formalism is to consistently express leading order cross sections in terms of $2xF_1$ and xF_3, where:

$$\begin{aligned} 2xF_1(x,Q^2) &= 2\sum_{i=u,\,d,\,...} xq_i(x) + x\overline{q}_i(x) \\ xF_3(x,Q^2) &= 2\sum_{i=u,\,d,\,...} xq_i(x) - x\overline{q}_i(x) \end{aligned} \tag{1.26}$$

where the sum is over all parton species. The parton carries a fraction $x = Q^2/2M\nu$ of the nucleon's momentum, such that $q_i(x)$ is the probability of finding the parton with a given momentum fraction. Assuming free spin 1/2 partons, to lowest order in the quark parton model, $F_2(x,Q^2)$ is related to $F_1(x,Q^2)$ by the Callan–Gross relation [10]:

$$F_2(x,Q^2) = 2x\,F_1(x,Q^2) \tag{1.27}$$

Given the parton densities, calculation of the neutrino cross section is straightforward. With the above quark assignment replacements in Equation (1.25), and neglecting both target mass terms and the propagator factor, the charged current neutrino and antineutrino cross sections become:

$$\begin{aligned} \frac{d^2\sigma^{\nu}_{CC}}{dx\,dy} &= \frac{2G_F^2ME}{\pi}\left[xq(x) + (1-y)^2\,x\overline{q}(x)\right] \\ \frac{d^2\sigma^{\overline{\nu}}_{CC}}{dx\,dy} &= \frac{2G_F^2ME}{\pi}\left[x\overline{q}(x) + (1-y)^2\,xq(x)\right] \end{aligned} \tag{1.28}$$

The y dependence in the above cross section formulae follows from helicity arguments. The V–A, $\gamma_\mu(1-\gamma_5)$, nature of the weak charged current operator selects only left–handed particles and right–handed anti–particles. Both neutrinos and quarks are left–handed particles with spin aligned *opposite* to their direction of motion: they possess negative helicity. On the other hand, antineutrinos and antiquarks are right–handed, so their spin is aligned *with* their direction of motion and they have positive helicity. As a result, the spin–zero $\nu\, q$ and $\overline{\nu}\,\overline{q}$ charged current cross sections are isotropic (Figure 1.9), while the spin–one $\nu\,\overline{q}$ and $\overline{\nu}\, q$ cross sections exhibit a $(1-y)^2$ angular dependence (Figure 1.10).

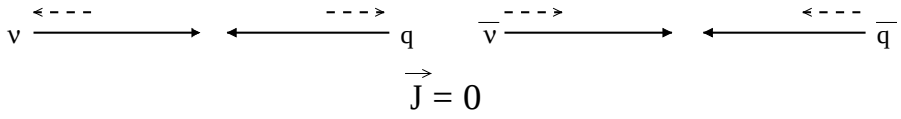

Figure 1.9: Allowed particle helicities for νq and $\overline{\nu}\,\overline{q}$ CC scattering. The total spin of the system is zero, hence there is no preferred scattering direction.

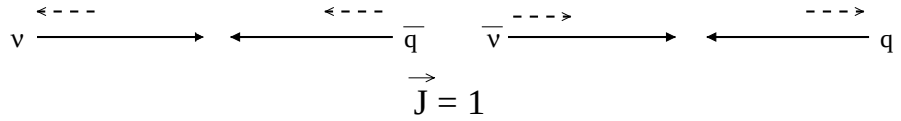

Figure 1.10: Allowed particle helicities for $\nu\overline{q}$ and $\overline{\nu}q$ CC scattering. The total spin of the system is one, therefore it follows from angular momentum conservation that backward scattering ($\cos\theta^* = 1, y = 1$) is forbidden.

Unlike the CC case, the NC contains both a V–A and a V+A component. The V+A, $\gamma_\mu(1+\gamma_5)$, portion selects right–handed particles and left–handed anti–particles; hence in analogy to Equation (1.28), we can write the neutral current neutrino and antineutrino cross sections as:

$$\frac{d^2\sigma^{\nu}_{NC}}{dx\,dy} = \frac{2G_F^2 ME\rho_0^2}{\pi}\left[\begin{array}{c} g_L^2[xq(x)+(1-y)^2\,x\overline{q}(x)]+ \\ g_R^2[x\overline{q}(x)+(1-y)^2\,xq(x)] \end{array}\right] \tag{1.29}$$

$$\frac{d^2\sigma^{\overline{\nu}}_{NC}}{dx\,dy} = \frac{2G_F^2 ME\rho_0^2}{\pi}\left[\begin{array}{c} g_L^2[x\overline{q}(x)+(1-y)^2\,xq(x)]+ \\ g_R^2[xq(x)+(1-y)^2\,x\overline{q}(x)] \end{array}\right] \tag{1.30}$$

where g_L^2 and g_R^2 are the left and right–handed components of the weak neutral current. Electroweak theory predicts the strength of the coupling of the Z boson to each species of quark to scale as $I_3 - Q_{em}\sin^2\theta_W$, where I_3 is the third component of the weak isospin and Q_{em} is the fractional quark charge. The couplings to the light quarks become:

$$u_L = \frac{1}{2} - \frac{2}{3}\sin^2\theta_W \tag{1.31}$$

$$u_R = -\frac{2}{3}\sin^2\theta_W \tag{1.32}$$

$$d_L = -\frac{1}{2} + \frac{1}{3}\sin^2\theta_W \tag{1.33}$$

$$d_R = \frac{1}{3}\sin^2\theta_W. \tag{1.34}$$

The isoscalar couplings, g_L^2 and g_R^2, are defined as the sum of the squares of the quark couplings:

$$g_L^2 = u_L^2 + d_L^2 = \frac{1}{2} - \sin^2\theta_W + \frac{5}{9}\sin^4\theta_W \tag{1.35}$$

$$g_R^2 = u_R^2 + d_R^2 = \frac{5}{9}\sin^4\theta_W \tag{1.36}$$

Similarly, isovector couplings are defined as $\delta_L^2 = u_L^2 - d_L^2$ and $\delta_R^2 = u_R^2 - d_R^2$. Making the above substitutions,

$$\begin{aligned}
\frac{d^2\sigma^{\nu}_{NC}}{dx\,dy} &= \rho_0^2\left[\left(\frac{1}{2}-\sin^2\theta_W+\frac{5}{9}\sin^4\theta_W\right)\cdot\frac{d^2\sigma^{\nu}_{CC}}{dx\,dy}+\frac{5}{9}\sin^4\theta_W\cdot\frac{d^2\sigma^{\overline{\nu}}_{CC}}{dx\,dy}\right]\\
\frac{d^2\sigma^{\overline{\nu}}_{NC}}{dx\,dy} &= \rho_0^2\left[\left(\frac{1}{2}-\sin^2\theta_W+\frac{5}{9}\sin^4\theta_W\right)\cdot\frac{d^2\sigma^{\overline{\nu}}_{CC}}{dx\,dy}+\frac{5}{9}\sin^4\theta_W\cdot\frac{d^2\sigma^{\nu}_{CC}}{dx\,dy}\right]
\end{aligned}$$

Thus far we have been speaking in only very general terms. To obtain the structure functions for scattering off protons and neutrons, and in particular, specific quark flavors, first note that in CC interactions, neutrinos can only scatter off $d, s, \overline{u}$ and $\overline{c}$ quarks while antineutrinos can only scatter off $\overline{d}, \overline{s}, u$ and c quarks (Appendix D). As a result, the structure functions for CC neutrino–proton scattering are:

$$\begin{aligned}
F_2^{\nu\,p}(CC) &= 2x\,[\,d_v+\overline{d}+s+\overline{u}+\overline{c}\,]\\
xF_3^{\nu\,p}(CC) &= 2x\,[\,d_v+\overline{d}+s-\overline{u}-\overline{c}\,]
\end{aligned}\tag{1.37}$$

and for CC antineutrino–proton scattering:

$$\begin{aligned}
F_2^{\overline{\nu}\,p}(CC) &= 2x\,[\,u_v+\overline{u}+c+\overline{d}+\overline{s}\,]\\
xF_3^{\overline{\nu}\,p}(CC) &= 2x\,[\,u_v+\overline{u}+c-\overline{d}-\overline{s}\,]
\end{aligned}\tag{1.38}$$

Assuming isospin symmetry in the neutron scattering case, meaning exchange of u and d the above expressions, the structure functions for CC neutrino–neutron scattering become:

$$\begin{aligned}
F_2^{\nu\,n}(CC) &= 2x\,[\,u_v+\overline{u}+s+\overline{d}+\overline{c}\,]\\
xF_3^{\nu\,n}(CC) &= 2x\,[\,u_v+\overline{u}+s-\overline{d}-\overline{c}\,]
\end{aligned}\tag{1.39}$$

and similarly for CC antineutrino–neutron scattering:

$$\begin{aligned} F_2^{\overline{\nu}\,n}(CC) &= 2x\,[\,d_v + \overline{d} + c + \overline{u} + \overline{s}\,] \\ xF_3^{\overline{\nu}\,n}(CC) &= 2x\,[\,d_v + \overline{d} + c - \overline{u} - \overline{s}\,] \end{aligned} \tag{1.40}$$

As already mentioned, NC interactions involve scattering off both left and right handed particles, and therefore the NC structure functions contain additional coupling factors (Equation 1.34):

$$\begin{aligned} F_2^{\nu\,p}(NC) &= 2x\,[\,(u_L^2 + u_R^2)(u_v + 2\,\overline{u} + c + \overline{c}) + (d_L^2 + d_R^2)(d_v + 2\,\overline{d} + s + \overline{s})\,] \\ xF_3^{\nu\,p}(NC) &= 2x\,[\,(u_L^2 - u_R^2)(u_v + c - \overline{c}) + (d_L^2 - d_R^2)(d_v + s - \overline{s})\,] \end{aligned} \tag{1.41}$$

$$\begin{aligned} F_2^{\nu\,n}(NC) &= 2x\,[\,(u_L^2 + u_R^2)(d_v + 2\,\overline{d} + c + \overline{c}) + (d_L^2 + d_R^2)(u_v + 2\,\overline{u} + s + \overline{s})\,] \\ xF_3^{\nu\,n}(NC) &= 2x\,[\,(u_L^2 - u_R^2)(d_v + c - \overline{c}) + (d_L^2 - d_R^2)(u_v + s - \overline{s})\,] \end{aligned} \tag{1.42}$$

In the NC case, the neutrino and antineutrino expressions are identical, so $F_2^{\overline{\nu}}(NC) = F_2^{\nu}(NC)$ and $xF_3^{\overline{\nu}}(NC) = xF_3^{\nu}(NC)$.

1.5 Organization of the Thesis

The remainder of this thesis is divided into nine chapters:

- **Chapter 2** provides a brief introduction to the theory of electroweak interactions and a description of the quantities pertinent to the present analysis.
- **Chapter 3** describes the experimental apparatus, tracing the data collection path from the production of the neutrino beam, to the detection of neutrino interactions in the NuTeV detector, and finally to the readout of events.
- **Chapter 4** discusses handling of the data, including the reconstruction of neutrino events, the selection criteria, the analysis procedure, the subtraction of background events, and corrections to the final data sample.
- **Chapter 5** provides a complete description of the Monte Carlo simulation, which includes a neutrino cross section model, a neutrino flux simulation, and a detector response model.
- **Chapter 6** includes comparisons of event variable distributions in the data and Monte Carlo as well as checks of the stability of the data/Monte Carlo agreement.
- **Chapter 7** presents an evaluation of the statistical and systematic errors contributing to the overall $\sin^2\theta_W$ uncertainty.
- **Chapter 8** presents results of the electroweak fits and comparisons of those results to the rest of the world.
- **Chapter 9** offers some conclusions on the significance of the results.

Chapter 2

Electroweak Interactions

> *"Pure logical thinking cannot yield us any knowledge of the empirical world. All knowledge of reality starts from experience and ends on it."*
> — Einstein (1933)

In the late 1960's, Sheldon Glashow, Abdus Salam, and Steven Weinberg [1] independently formulated a gauge theory that unified the weak and electromagnetic interactions*. A consequence of this theory was that it predicted the existence of heavy intermediate bosons and neutral weak currents. The first weak neutral current (NC) interaction was soon discovered in the summer of 1973 at CERN's large liquid bubble chamber, Gargamelle [2]. There, they observed the first muon neutrino interaction without a charged muon in the final state:

$$\nu_\mu + e^- \rightarrow \nu_\mu + e^-$$

$$\overline{\nu}_\mu + e^- \rightarrow \overline{\nu}_\mu + e^-$$

* It is interesting to note that Glashow, Weinberg, and Salam were awarded the Nobel Prize for the unification of the weak and electromagnetic interactions exactly 100 years after Maxwell's formulation of a unified theory of electricity and magnetism. Perhaps this means we have to wait until 2079 for a grand unified theory of the weak, electromagnetic, and strong interactions?

This exciting result was later confirmed at Fermilab [3]. Following the discovery of the neutral currents, a host of experiments proceeded to measure their strength and structure. In the late 1970's, parity violating weak NC effects were first observed in the scattering of polarized electrons off deuteron [4] and in heavy atoms [5]. At the same time, early measurements of $\sin^2\theta_W$ [6] successfully pinpointed the W and Z boson mass predictions to the 80–95 GeV mass range, far beyond the energy reach of any existing accelerator at the time. Several years later, the long awaited discovery of the W and Z particles was announced by the UA1 and UA2 collaborations at CERN.

Since then, the experimental accuracy of electroweak measurements has steadily improved. Experiments in the 1980's and early 90's, of 1–5% precision, probed the standard model at the level of radiative corrections, and hence set the first useful limits on the top quark mass (Figure 2.1).

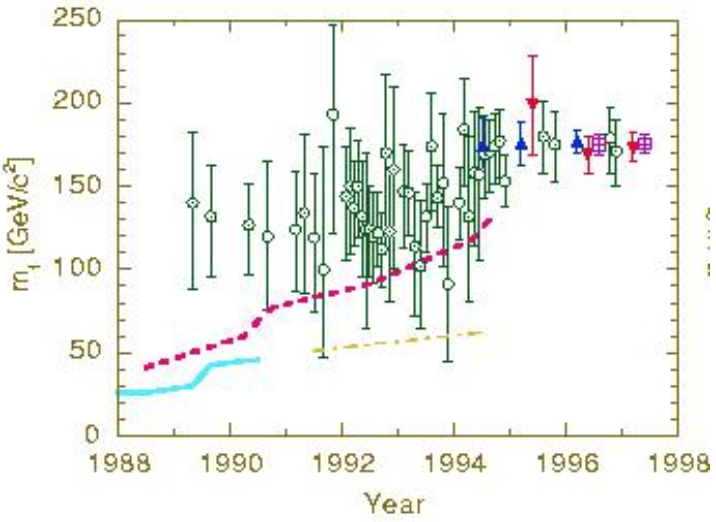

Figure 2.1: Indirect determinations of $M_{\rm top}$ (open circles) as a function of time. Also shown are the 95% confidence level lower bounds from direct searches in e^+e^- (solid line) and $p\overline{p}$ (dashed line) collisions, as well as from the W width in $p\overline{p} \rightarrow$ (W or Z) + anything (dot dash line). Direct measurements of $M_{\rm top}$ from CDF (triangles) and DØ (inverted triangles) are also indicated. Plot courtesy of C. Quigg [7].

During this time, precision studies of W and Z properties, asymmetries in e^+e^- scattering, neutrino scattering, and parity violating effects in atoms continued. Today, such experiments test the quantum structure of the electroweak standard model at the few 10^{-3} level. Present precision experiments aim to extract indirect information on the Higgs boson mass, $M_{\rm Higgs}$, and search for indications of new phenomena (e.g., supersymmetry, extra Z bosons, leptoquarks, non–standard Higgs, etc.) at or beyond the electroweak scale. Neutral currents have represented one of the most important predictions of the standard model. Their discovery sparked an impressive litany of experimental tests spanning more than three decades, and verified the standard model with a variety of probes over a wide kinematic range. The measurement presented in this thesis continues in this tradition.

2.1 $\sin^2\theta_W$, R^ν, and $R^{\overline{\nu}}$

Neglecting fermion masses, mixing, and $M_{\rm Higgs}$, electroweak observables can be expressed in terms of three free parameters which are known with high precision[†]:

$$\begin{aligned} G_F &= \text{Fermi constant} = 1.16637 \pm 0.00001 \times 10^{-5}\,(\text{GeV})^{-2} \\ \alpha &= \text{electromagnetic coupling constant} = \frac{\mathrm{e}^2}{4\pi} = 1/137.0359895\,(61) \\ M_Z &= \text{Z boson mass} = 91.1876 \pm 0.0021 \end{aligned}$$

Knowing G_F, α, and M_Z, one can predict all electroweak observables including the weak mixing angle, $\sin^2\theta_W$, and the W boson mass, M_W, at tree level. When loop corrections are included, terms that depend quadratically in $M_{\rm top}$ and logarithmically in $M_{\rm Higgs}$ modify the predicted values of $\sin^2\theta_W$ and M_W. The size of the corrections depends on the choice of renormalization scheme. For instance, NuTeV employs the Sirlin on–shell renormalization scheme [13], where to all orders $\sin^2\theta_W$ is expressed in terms of the physical boson masses:

$$\sin^2\theta_W^{\rm on-shell} = 1 - \frac{{M_W}^2}{{M_Z}^2} \tag{2.1}$$

This definition is chosen because it is comparatively free of theoretical uncertainties due to $M_{\rm top}$ and $M_{\rm Higgs}$. In the on–shell scheme, the leading contributions to the renormalization factors almost perfectly cancel [14]:

[†] G_F is known to 10 ppm from the muon lifetime [11], α is known to 45 ppb (200 ppm at M_Z) from the Quantum Hall effect [12], and M_Z is known to 23 ppm from precise measurements at LEP [12].

$$\delta\kappa = \frac{3G_F}{8\sqrt{2}\pi^2}\cot^2\theta_W {M_{\rm top}}^2 + \mathcal{O}\left(\ln\frac{{M_{\rm Higgs}}^2}{{M_W}^2}\right) + ... \quad (2.2)$$

$$\delta\rho = \frac{3G_F}{8\sqrt{2}\pi^2}{M_{\rm top}}^2 + \mathcal{O}\left(\ln\frac{{M_{\rm Higgs}}^2}{{M_W}^2}\right) + ... \quad (2.3)$$

This scheme was chosen at a time when the top mass was not well known and such cancellation was important. Today, the effects are small because $M_{\rm top}$ is well–known and the dependence in $M_{\rm Higgs}$ is logarithmic. Another choice is the modified minimal subtraction ($\overline{MS}$) scheme definition, where:

$$\sin^2\theta_W{}^{\overline{MS}} = 1 - \frac{{M_W}^2(\mu)}{{M_Z}^2(\mu)} \quad (2.4)$$

In this case, $M_W(\mu)$, $M_Z(\mu)$ are the renormalized masses at an arbitrary scale, μ, where μ is typically set equal to M_Z for electroweak processes. Finally, on–resonance measurements at LEP and SLD report a leptonic effective weak mixing angle. In this case, $\sin\theta_{\rm eff}^{\rm lept}$ is defined in terms of the ratio of effective vector and axial–vector couplings constants of the leptons ($l = e, \mu, \tau$) to the Z:

$$\sin\theta_{\rm eff}^{\rm lept} = \frac{1}{4}\left(1 - \frac{g_V^l}{g_A^l}\right) \quad (2.5)$$

These three definitions of $\sin^2\theta_W$ depend on the renormalization prescription, and hence numerically differ from one another as a result of radiative corrections. The relation between them depends on both $M_{\rm top}$ and $M_{\rm Higgs}$, and has been explicitly calculated in many theoretical papers [15].

In the present analysis, electroweak observables are extracted from the ratios of neutral to charged current neutrino and antineutrino cross sections. Measurement

of such ratios avoids complications related to the measurement of absolute cross sections, in addition to reducing sensitivity to the neutrino spectrum and systematic uncertainties common to both NC and CC interactions (e.g., parton distribution functions). In standard electroweak theory, the ratio of neutral current to charged current total cross sections directly relates to $\sin^2\theta_W$. Assuming only isospin symmetry, the Llewellyn Smith formula relates these ratios to $\sin^2\theta_W$ for neutrino scattering on isoscalar targets composed of light quarks [16]. To lowest order in both QCD and electroweak theory:

$$\begin{aligned} R^{\nu} \equiv \frac{\sigma(\nu_\mu N \to \nu_\mu X)}{\sigma(\nu_\mu N \to \mu^- X)} &= \frac{\sigma^{\nu}_{NC}}{\sigma^{\nu}_{CC}} \\ &= g_L^2 + r\, g_R^2 \\ &= \frac{1}{2} - \sin^2\theta_W + \frac{5}{9}\,(1+r)\,\sin^4\theta_W \end{aligned} \tag{2.6}$$

$$\begin{aligned} R^{\overline{\nu}} \equiv \frac{\sigma(\overline{\nu}_\mu N \to \overline{\nu}_\mu X)}{\sigma(\overline{\nu}_\mu N \to \mu^+ X)} &= \frac{\sigma^{\overline{\nu}}_{NC}}{\sigma^{\overline{\nu}}_{CC}} \\ &= g_L^2 + \frac{1}{r}\, g_R^2 \\ &= \frac{1}{2} - \sin^2\theta_W + \frac{5}{9}\left(1 + \frac{1}{r}\right)\,\sin^4\theta_W, \end{aligned} \tag{2.7}$$

where $r = \sigma(\overline{\nu}_\mu N \to \mu^+ X)\ /\ \sigma(\nu_\mu N \to \mu^- X) = \sigma^{\overline{\nu}}_{CC}\ /\ \sigma^{\nu}_{CC}$ is the ratio of neutrino and antineutrino CC cross sections and the coupling factors, g_L^2, g_R^2, are given in Equation (1.36). When integrated over all y, $r \simeq 0.5$. For a typical detector without full hadronic energy acceptance, r reduces to roughly 0.3–0.4. Figure 2.2 illustrates the dependence of R^{ν} and $R^{\overline{\nu}}$ on $\sin^2\theta_W$. Assuming a value for r of 1/2, R^{ν} is about three times more sensitive to shifts in $\sin^2\theta_W$ than $R^{\overline{\nu}}$. However, assuming a value for r more close to the experimental value, $r \simeq 1/3$, R^{ν} is thirty times more sensitive

to $\sin^2\theta_W$ than $R^{\overline{\nu}}$.

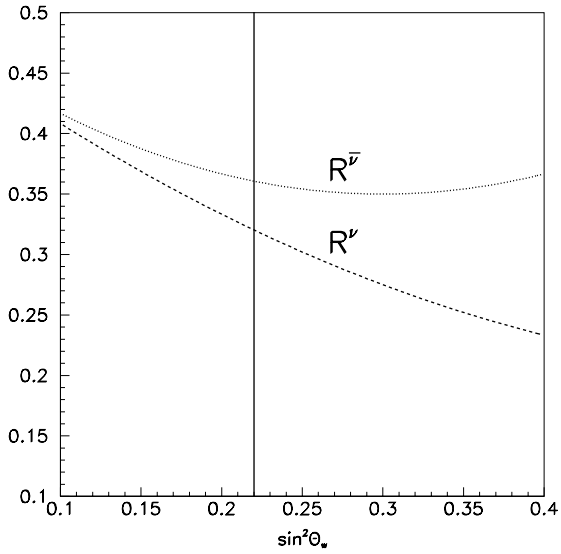

Figure 2.2: Dependence of R^{ν} and $R^{\overline{\nu}}$ on $\sin^2\theta_W$ assuming $r = 1/3$. Over the region of interest, R^{ν} has a larger slope than $R^{\overline{\nu}}$ and as a result, roughly 30 times more sensitivity to $\sin^2\theta_W$.

The above relations are, of course, exact only for the case of tree level scattering off an isoscalar target composed of light quarks. Necessary adjustments to this naive model include corrections for the non–isoscalar target, quark mixing, radiative effects, higher–twist processes, the longitudinal structure function (R_L), the W and Z propagators, and the heavy quark content of the nucleon (charm and strange). The last effect in the list contributes most to the uncertainty in the measurement of $\sin^2\theta_W$ from R^{ν}. Unfortunately, previous determinations of $\sin^2\theta_W$ measured in this way suffered from large theoretical uncertainties associated with heavy quark production thresholds, which mainly affect the CC denominator. These uncertainties, resulting from imprecise knowledge of the charm quark mass, dominated the CCFR measurement [17] and ultimately limited the precision of neutrino measurements of

electroweak parameters. For example, combining the five most precise neutrino–nucleon measurements yielded a value of $\sin^2\theta_W = 0.2277 \pm 0.0036$, [18] thereby implying an equivalent W mass error of 190 MeV.

The Paschos–Wolfenstein combination [19] provides an alternative method for determining $\sin^2\theta_W$ that is much less dependent on the details of charm production and other sources of model uncertainty:

$$\begin{aligned} R^- \equiv \frac{\sigma(\nu_\mu N \to \nu_\mu X) - \sigma(\overline{\nu}_\mu N \to \overline{\nu}_\mu X)}{\sigma(\nu_\mu N \to \mu^- X) - \sigma(\overline{\nu}_\mu N \to \mu^+ X)} &= \frac{R^\nu - rR^{\overline{\nu}}}{1-r} \\ &= g_L^2 - g_R^2 \\ &= \frac{1}{2} - \sin^2\theta_W \end{aligned} \tag{2.8}$$

Under the assumption that the neutrino–quark and antineutrino–antiquark cross sections are equal, use of the Paschos–Wolfenstein relation removes the effects of sea quark scattering which dominates the low x cross section. As a result, R^- is much less sensitive to heavy quark processes provided these contributions are the same for neutrinos and antineutrinos. Figure 2.3 illustrates the charm production cancellation. In this case, the only remaining charm–producing contributors are d_v quarks, which are not only Cabibbo suppressed but also at higher fractional momentum, x, where the mass suppression is less of an effect.

Inspired by the Paschos–Wolfenstein technique, the measurement presented here extracts electroweak parameters from neutrino and antineutrino deep inelastic scattering reactions. NuTeV, however, does not measure cross section ratios, such as those appearing in the above expressions (R^ν, $R^{\overline{\nu}}$, R^-) because of the inability to measure NC interactions down to zero recoil energy and because of the presence

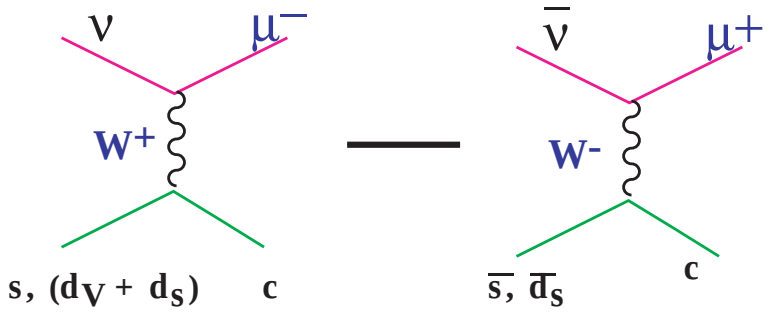

Figure 2.3: ν and $\overline{\nu}$ charm production diagrams illustrating the cancellation of sea effects in the Paschos–Wolfenstein relation.

of experimental cuts, backgrounds, and detector acceptance. NuTeV instead measures experimental ratios of short to long events, $R^{\nu}_{\rm exp}$ and $R^{\overline{\nu}}_{\rm exp}$. A detailed Monte Carlo simulation of the experiment then predicts these ratios and their dependence on electroweak parameters (Chapter 5). In the end, the NuTeV measurement has comparable precision to other experimental tests. In addition, NuTeV is complementary because neutrino scattering is a different physical process (and hence is sensitive to different new physics), it provides a precise measurement of NC neutrino couplings (the only other precise measurement is from the LEP I invisible line width), a measurement of processes at moderate space–like momentum transfers (as opposed to large time–like transfers probed at collider experiments), as well as a precise determination of the parameters of the model itself ($\sin^2\theta_W$, M_W, ρ_0, g_L^2, and g_R^2).

Chapter 3

The Apparatus

The three sections in this chapter describe the particle beam, detector, and triggering system used to collect neutrino data. The particle beam originates as high energy protons provided by the Fermilab Tevatron. The protons collide with a downstream target resulting in a cascade of particles that includes neutrinos. The neutrinos can be observed in the NuTeV detector which is triggered to record their interactions.

3.1 The Neutrino Beam

3.1.1 The Fermilab Tevatron

The NuTeV experiment operates in the Neutrino Center beamline at the Fermi National Accelerator Laboratory (Fermilab) in Batavia, Illinois. Fermilab is home to the Tevatron, the world's highest–energy particle accelerator and source of energetic protons needed to produce an intense neutrino beam. The Fermilab Tevatron accelerates protons through a series of stages that includes a Cockcroft–Walton accelerator, a linac, a booster, a main ring, and finally the superconducting Tevatron ring. This chain is illustrated at the top of Figure 3.1.

The protons originate as a negative hydrogen ion (H^-) beam, collected from a

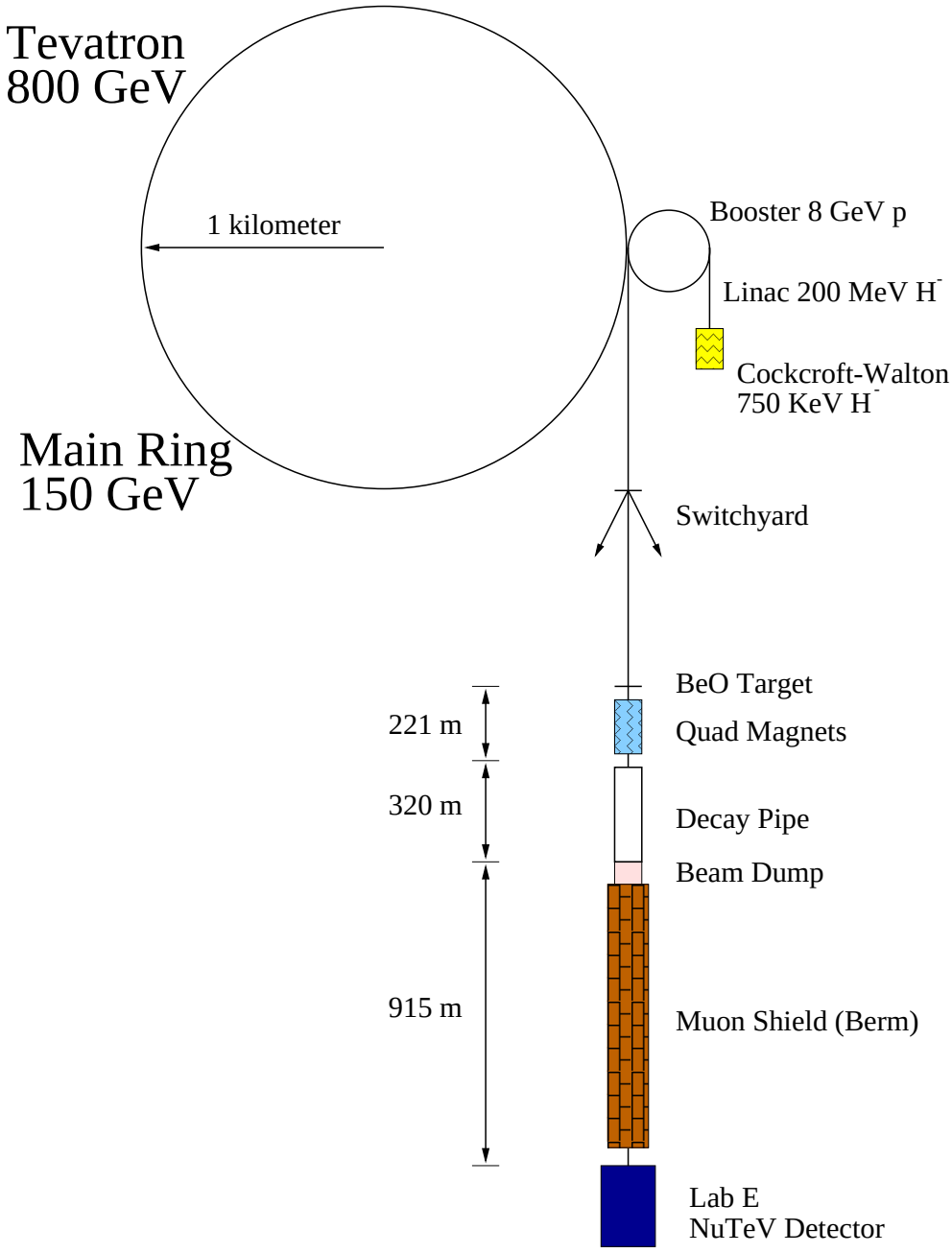

Figure 3.1: Schematic of the Fermilab Neutrino Center beamline.

dense plasma of hydrogen gas. The H^- ions are first electrostatically accelerated up to 750 keV by a five–stage Cockcroft–Walton generator before passing into a 79 m long two–stage linear accelerator (linac). The first stage of the drift-tube linac accelerates the ions up to 116 MeV through a series of radio frequency (RF) cavities, each of which resonates at 201 MHz. The second, more efficient stage, operates at 805 MHz and accelerates the beam to 400 MeV. The pulsed beam of 400 MeV H^- ions is then injected into the booster at a rate of 15 Hz. During injection, the ions pass through a carbon foil, which strips the ions of their free electrons, leaving bare protons. The process is known as charge–exchange injection.

The booster, a 140 m diameter synchrotron, constrains the protons to a closed orbit via a series of combined function dipole/quadrupole bending magnets, at the same time that RF accelerating fields increase the protons' energies to 8 GeV. The entire booster acceleration process takes about 0.033 seconds. The entire beam, extracted in one turn, is sent into the 2 km diameter Main Ring. The Main Ring is a 400 GeV proton synchrotron consisting of water–cooled dipole and quadrupole magnets. Once accelerated to 150 GeV, the protons are finally injected into the Tevatron, a superconducting synchrotron which shares the same tunnel enclosure as the main ring. Unlike the Main Ring, all of the Tevatron magnets are superconducting and must be cooled by liquid helium to a temperature of 4.6 K. After the protons are accelerated up to their maximum energy of 800 GeV, they are extracted from the Tevatron and sent to a switchyard which directs the beam to the various fixed target experimental areas: Meson, Proton or Neutrino*. Protons directed down the Neutrino line enter NuTeV's Sign–Selected Quadrupole Train.

* For more information on the operation of the Fermilab Tevatron, the interested reader should consult review articles written by Helen Edwards [20] and Joey Thompson [21].

3.1.2 The SSQT

The Sign Selected Quadrupole Train (SSQT) [22] was designed to reduce the largest systematics plaguing earlier neutrino–based determinations of $\sin^2\theta_W$ [17]. For CCFR, the two largest uncertainties in the determination of $\sin^2\theta_W$ resulted from the production of heavy charm quarks and the unknown rate at which neutral kaons were produced at the proton target. To eliminate these errors, the SSQT provides both separate ν_μ and $\overline{\nu}_\mu$ beams, and through a series of vertical bends, eliminates neutral kaon decays as the most significant source of ν_e uncertainty.

The SSQT is the source of neutrinos for the NuTeV experiment. Arriving at an upward 7.8 mrad angle, the intense beam of 800 GeV protons from the Tevatron first strikes a low–Z target located 1450 m upstream of the NuTeV detector. Specifically, the target is a twelve inch long[†], one inch diameter beryllium oxide (BeO) rod, segmented to resist thermal beam shock. The neutrino beam arises from the decay of mesons, primarily π, $K \rightarrow \mu + \nu$, among the multitude of secondary particles produced at the primary target. A series of strong dipole magnets downstream of the target selects mesons of one charge, for example π^+ and K^+, and directs them at a 6 mrad incline towards the NuTeV detector. Mesons of the opposite ("wrong") sign are bent away while non–interacting protons are stopped in beam dumps. Neutral particles pass through the magnet chain undeflected, thereby missing the NuTeV detector. Continuing their journey, right–sign pions and kaons decay in–flight in an evacuated 440 m decay region. Most of the unwanted non–neutrino decay products, including muons, "range out" in a 900 m earth and steel berm immediately following

[†] λ_I for BeO is 30.99 cm, hence the target is roughly one interaction length. The density of the target is 2.7 g/cm^3.

the decay region. Because of the large distance and thick shielding detector only neutrinos reach the Lab E detector.

The charge selection of the SSQT results in a beam that is almost purely neutrino or antineutrino. Antineutrinos contaminate 0.03% of the neutrino beam events, and neutrinos 0.4% of the antineutrino beam events. Separate neutrino and antineutrino mode running reduces the single largest systematic uncertainty in the determination of $\sin^2\theta_W$: the uncertainty resulting from the production of heavy charm quarks.

Furthermore, the beam is mostly muon neutrino in flavor. This is important because electron neutrinos are a large background to the analysis. The second largest uncertainty in the CCFR $\sin^2\theta_W$ measurement resulted from the unknown rate at which neutral kaons were produced at the proton target. Due to the series of vertical bends in the SSQT, this source is almost completely eliminated, leaving only a small component of electron neutrinos from $K^{\pm} \rightarrow \pi^0 e^{\pm} \nu_e(\overline{\nu}_e)$ decays. These produce 1.7% of the observed interactions in neutrino mode and 1.6% in antineutrino mode.

Figure 3.2 shows the expected event rates for neutrinos and antineutrinos in the NuTeV detector, normalized to 10^6 protons on target (POT), as a function of neutrino energy. The bulk of the neutrinos result from π and K decay in flight:

$$\pi^{\pm} \longrightarrow \mu^{\pm}\,\nu_{\mu}\,(\overline{\nu}_{\mu}) \qquad (\mathrm{BR} = 100\%) \tag{3.1}$$

$$K^{\pm} \longrightarrow \mu^{\pm}\,\nu_{\mu}\,(\overline{\nu}_{\mu}) \qquad (\mathrm{BR} = 63.5\%) \tag{3.2}$$

For these dominant two–body decay modes, the maximum neutrino energy from each species is:

$$E_\nu = \frac{E_{\pi,K}\left(1 - \frac{m_\mu}{m_{\pi,K}}\right)^2}{1 + (\gamma\,\theta_\nu)^2} \tag{3.3}$$

where $\gamma = E_{\pi,K}/m_{\pi,K}$, and θ_ν is the angle of the neutrino relative to the parent particle direction. At $\theta_\nu = 0$, neutrinos from pion decays have an energy $E_\nu \leq 0.47 \cdot E_\pi$, and neutrinos from kaon decays have an energy $E_\nu \leq 0.95 \cdot E_K$. Consequently, the neutrino energy spectrum exhibits two distinct peaks, with neutrinos from pion decays concentrated at lower energies and neutrinos from kaon decays populating higher energies (Figure 3.2). Further discussion of the Monte Carlo simulation of the incoming neutrino beam can be found in Chapter 5.

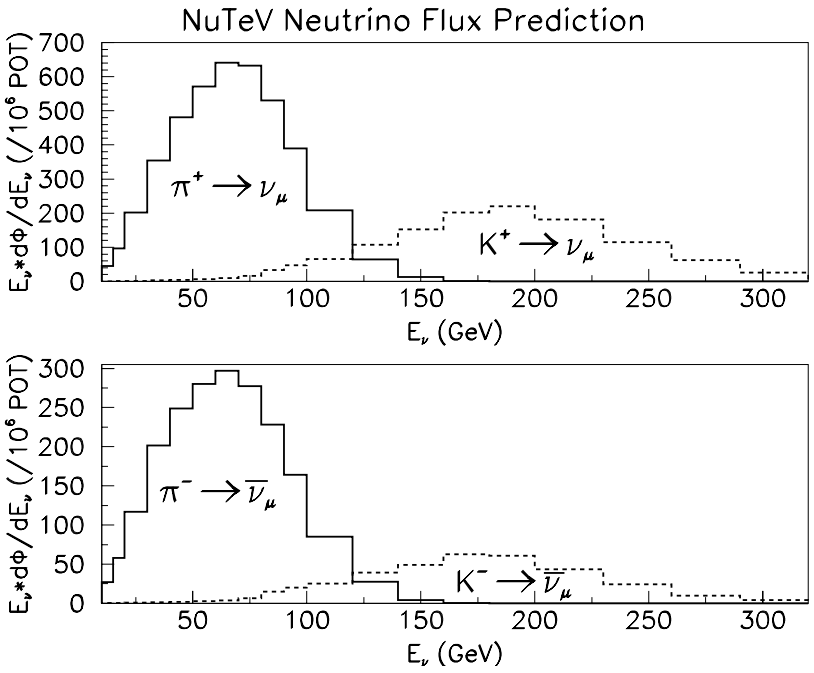

Figure 3.2: Contributions to the expected neutrino spectrum in the NuTeV detector for running in both neutrino (top) and antineutrino (bottom) modes.

3.1.3 Event Timing

In fixed target mode, the Tevatron operates on a 60.1 sec cycle. The neutrino beamline, as described in the previous section, provides two types of beam to the experimental area: the neutrinos are delivered in five "fast" 5 msec pulses[‡], and the calibration beam arrives in a "slow" 18 sec uniform spill. Figure 3.3 shows the accelerator time structure for each of these two components.

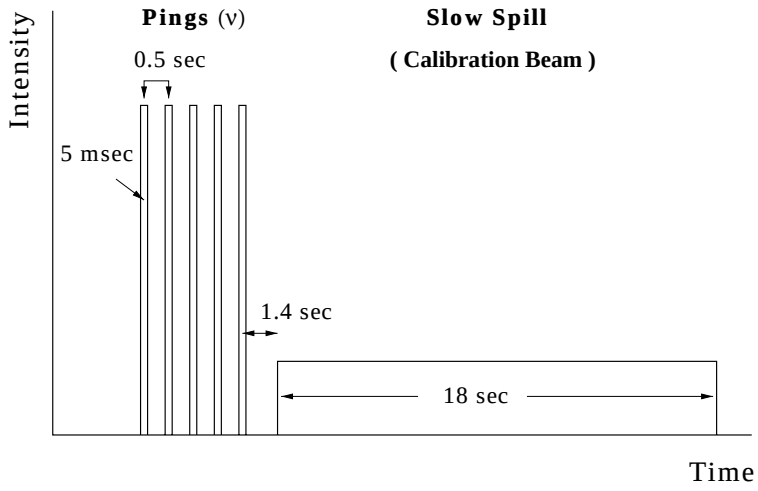

Figure 3.3: The accelerator time structure consists of two components: fast spill (neutrino beam) and slow (calibration beam) spill.

As a result of this structure, events arrive at the detector in several "gates" or "spills":

- **Fast Gate** (gates 1–5): The fast spill consists of 5 short, intense pulses or "pings", each roughly 1–2 $\times$ 10^{12} POT and lasting 5 msec. The pings are separated by 0.5 sec. This is the neutrino gate.

[‡] These fast resonant extractions are known as "pings".

- **Slow Gate** (gate 6): The slow spill has a duration of 18 sec. It begins 1.4 sec after the last fast spill ping, allowing for continuous calibration of the detector concurrent with neutrino data taking. Gate 6 is the calibration beam (or testbeam) gate. The calibration data are discussed in more detail in the next section and at the end of Chapter 3.

- **Cosmic Ray Gate** (gate 7): Cosmic ray data are collected for 5 seconds during each accelerator cycle in a separate "beam–off" gate during which the detector is not receiving beam from the accelerator. The importance of the data collected in this gate is discussed in Chapter 4.

3.1.4 The Calibration Beam

The NuTeV detector was exposed to a wide energy range (4.8 to 190 GeV) of hadrons, muons, and electrons delivered independently of the neutrino beam (Figure 3.4). This separate beamline allowed continuous calibration of the NuTeV detector in tandem with neutrino data–taking.

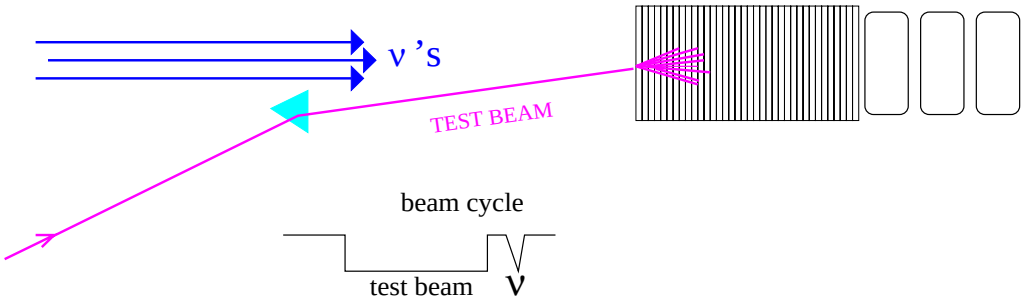

Figure 3.4: Schematic of the NuTeV calibration beamline, a long low mass spectrometer. Calibration beam was incident upon the NuTeV calorimeter at a 43 mrad angle. The momentum of testbeam particles ranged from 4.8 GeV to 190 GeV.

The calibration beam both sets the energy scale of the detector and maps the response of the detector to the products of neutrino interactions in the target. Further discussion on the energy calibration can be found in Section 3.3.4, while details on the modeling of the detector response can be found in Chapter 3. The collection of large volumes of testbeam data throughout the course of the run was crucial to the reduction of many systematic errors associated with the $\sin^2\theta_W$ analysis. For further details on the testbeam itself and calibration of the NuTeV detector, the reader is referred to Reference [23].

3.2 The NuTeV Detector

Neutrinos interact in the NuTeV detector [23], located 1450 m downstream of the proton target. The tiny neutrino cross section (σ/E $\sim 10^{-38}$ cm^2/GeV) requires not only a lot of incoming neutrinos but also a very massive neutrino detector in order to collect large neutrino data samples. The NuTeV detector weighs over 1000 tons; despite this, only a few interactions are observed for every billion neutrinos that pass through it.

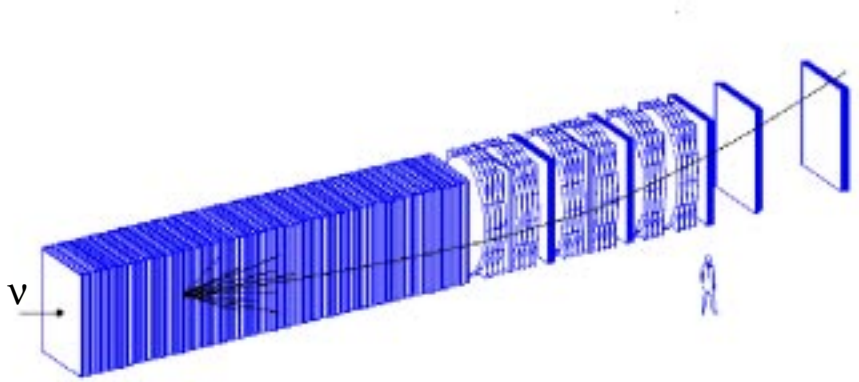

Figure 3.5: The NuTeV (Lab E) detector.

Specifically, the detector consists of two parts: a 18 m long, 690 ton steel–scintillator target, followed by an instrumented 10 m long, 400 ton iron toroid spectrometer (Figure 3.5). The target calorimeter[§] is composed of 168 steel plates interspersed with active elements that include liquid scintillation counters (spaced every 2 plates or 10.35 cm steel) and drift chambers (spaced every 4 plates or 20.7 cm steel). The geometry of one calorimeter unit is shown in Figure 3.6. The basic model is that

[§] The word "calorimeter" stems from the Greek word for heat. The idea is to absorb all of the energy of a particle in a detecting medium and hence maintain a record of its developing energy.

the particle showers develop in the (high Z) steel, and are sampled in the active (low Z) material. Table 3.1 summarizes the calorimeter's composition in terms of each component's length, radiation length, and interaction length[◇]:

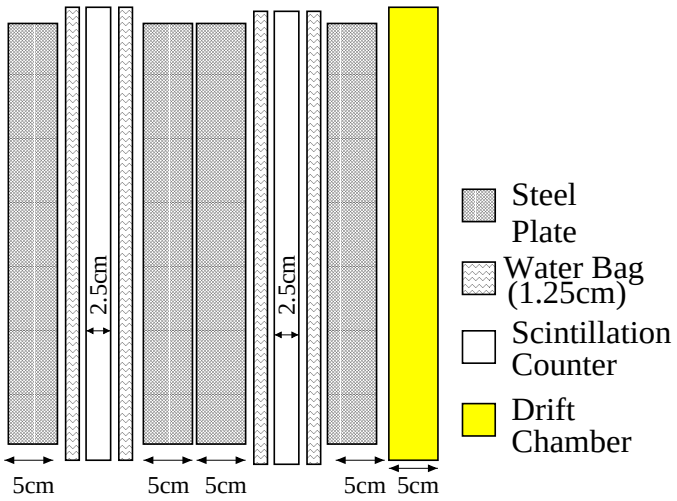

Figure 3.6: Side view of a single NuTeV detector target/calorimeter module. This unit is repeated 42 times throughout the total length of the calorimeter. Note: the scintillation counter on the right (left) hand side is an even (odd) numbered counter.

Component	Length (cm)	Radiation Length (X_0)	Interaction Length (λ_I)
4 steel plates	20.7	11.75	1.24
2 counters	13.0	0.51	0.16
1 drift chamber	3.7	0.17	0.03
Total	37.4	12.43	1.43

Table 3.1: Composition of a NuTeV target/calorimeter unit in terms of each component's length, radiation length, and interaction length. Source: Reference [23].

◇ Note: a minimum ionizing particle (or "mip") will lose approximately 0.2 GeV in the iron, compared to 0.004 GeV in a single scintillation counter.

A toroid spectrometer follows the target stack. A schematic is shown in Figure 3.7. In the case of CC neutrino interactions, the curvature of the final state muon's trajectory in the toroidal magnetic field determines the sign of the muon's charge as well as its momentum. For this analysis, the toroid is used only for the muon neutrino flux measurement in CC events, since the laboratory energy of the incident neutrinos, E_ν, can be determined from the sum of the muon energy and the hadron shower energy: $E_\nu = E_{had} + E_\mu$.

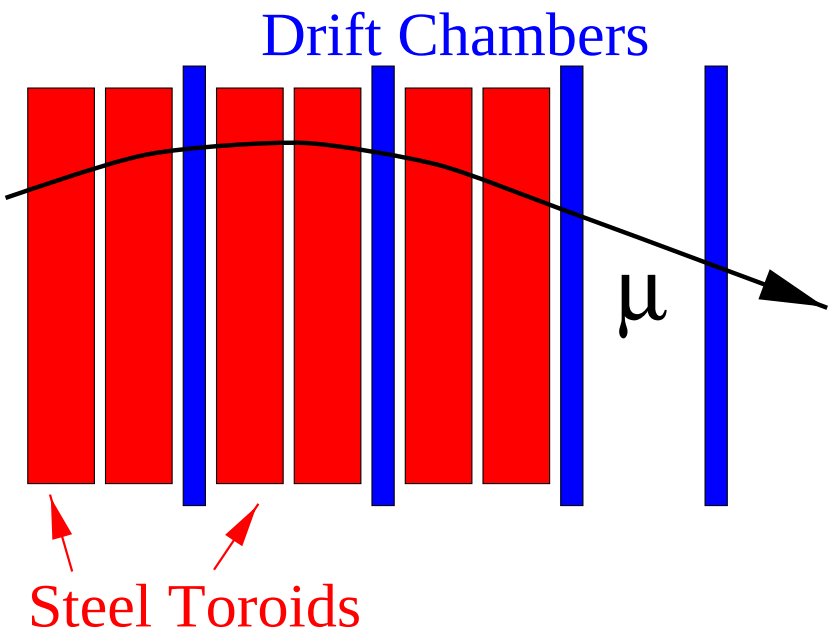

Figure 3.7: Side view of a NuTeV detector toroid module. The magnetic field bends right–sign muons inward.

The instrumentation of the detector provides the information necessary for performing the $\sin^2\theta_W$ analysis. The role of each detector element specific to this analysis is listed below:

- Target/Calorimeter:

  - 168 Fe plates (3 m × 3 m × 5.1 cm)

    – serve as the target for the incoming neutrinos

  - 84 liquid scintillation counters (3 m × 3 m × 2.5 cm):

    – provide triggering information

    – determine visible energy deposition

    – locate neutrino interaction point

    – measure event length

  - 42 drift chambers (3 m × 3 m × 5 cm):

    – determine localized transverse event vertex

- Toroidal Spectrometer (15 kG field, p_T = 2.4 GeV/c):

  – measures muon charge and momentum (for ν_μ flux measurement)

The remainder of this chapter describes each of the active detector elements in greater detail. Most of the detector components are the same as those used in the earlier CCFR experiment, with the exception of new liquid scintillator oil and new photomultiplier tubes.

3.2.1 Muon Spectrometer

While the toroidal spectrometer is not used directly in determining the kinematic quantities necessary for this analysis, it is used to tune the ν_μ and $\overline{\nu}_\mu$ fluxes. Hence, some discussion of its internal composition is warranted.

The spectrometer is comprised of three toroidal magnets. A cross section view of a toroid magnet is shown in Figure 3.8. Each magnet consists of eight 3.6 m diameter steel washers with a 24 cm diameter inner hole. Current in four copper coils magnetizes the steel in the washers, thereby producing a 15 kG field confined to the volume of the toroids.

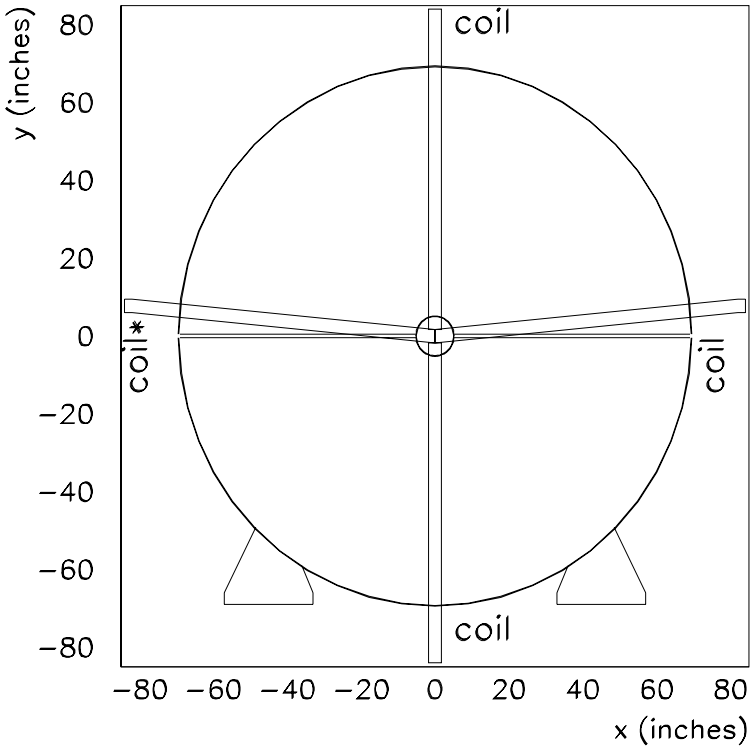

Figure 3.8: Cross section view of a NuTeV toroid magnet.

In the beginning of the run, one of the coils on the western side of the second toroid shorted to ground and had to be disconnected. Figure 3.9 shows the change in the predicted magnetic field in the second toroidal magnet as a result of the missing coil. Notice that the greatest effect is on the western side (–x in the ANSYS field simulation coordinate system) in the location of the disabled coil.

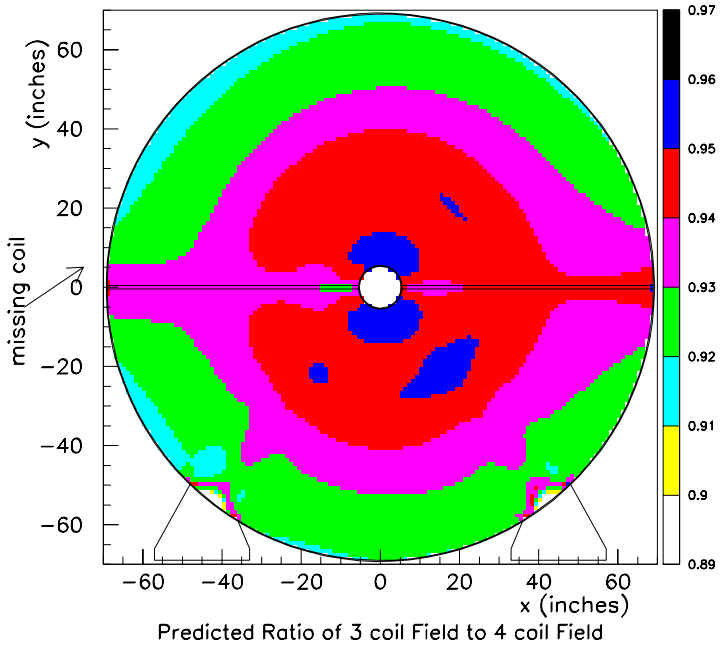

Figure 3.9: Effect of the disconnected coil on the ANSYS magnetic field simulation in the second toroid.

Combined, the three toroids provide on average a 2.4 GeV/c transverse momentum kick to muons traversing the spectrometer. The polarity of the current in the coils, and hence the sense of the magnetic field, is set such that during neutrino (antineutrino) mode running, negatively (positively) charged muons are bent towards the center of the spectrometer (Figure 3.7). Hit information from single wire drift chambers in the gaps downstream of each toroid allows the muon tracks to be reconstructed and the momentum of the particle determined. Two sets of three chambers located 2.4 m and 6.2 m downstream of the last chamber in the toroid comprise the "blue cart"; these provide an additional lever arm in the measurement of high momentum muon tracks. The NuTeV drift chamber configuration (Figure 3.10) differs

slightly from CCFR since five chambers were removed from the toroid system and moved upstream of the Lab E detector to form the Lab F decay channel [25]. The following section describes the functioning of the NuTeV drift chambers in greater detail.

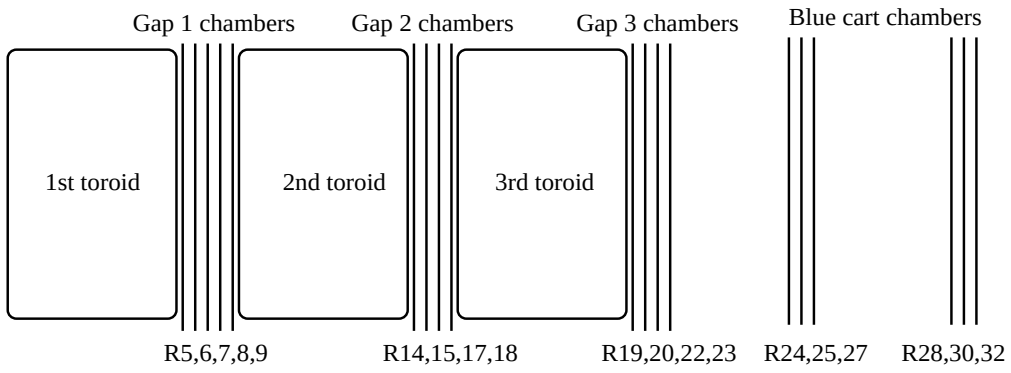

Figure 3.10: Arrangement of drift chamber stations in the NuTeV toroidal spectrometer. The numbers listed at the bottom indicate the labelling convention for each of the individual toroid drift chambers.

3.2.2 Drift Chambers

Drift chambers are a common instrument used in many high energy physics experiments. Such chambers typically consist of a gas volume strung with a series of anode wires. The gas is ionized by the passage of a charged particle. The subsequent ionization drifts in the electric field created by the anode wire, such that the collection and amplification of charge on the anode creates a detectable signal.

In the NuTeV experiment, there are a total of 42 three–wire drift chambers distributed throughout the calorimeter and 19 single–wire chambers placed within and behind the toroid. The chambers are constructed from 10 ft $\times$ 10 ft Hexcel–covered aluminum walls. A given chamber consists of two orthogonally oriented

planes, an X–view and a Y–view, each divided into 24 parallel cells 5 inches wide. Figure 3.11 shows a cut-away view of a drift chamber cell. The upper and lower surfaces of each cell are covered with copper–clad G10 panels, which are milled to form a set of 19 cathode strips per cell. Strip voltage is supplied by I–beams at the edge of each cell which are held at –4500 V. This voltage is distributed decrementally to each strip via a resistor card acting as a voltage divider; this maintains a uniform electric field across the drift space.

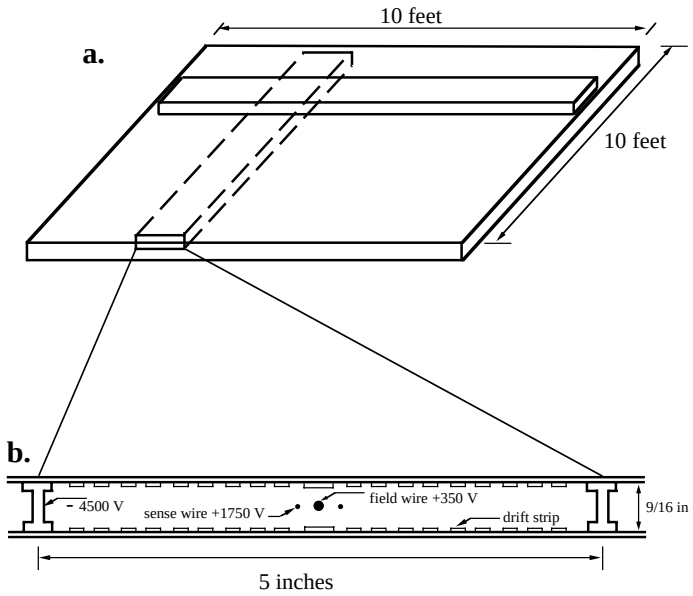

Figure 3.11: (a) Top view and (b) cross section of a three–wire drift chamber.

The chambers are filled with an equal mixture of argon and ethane gas. Charged particles can be detected in the drift chambers because particles ionize the gas along their flight path. The electrons drift towards the anode wire. The drift velocity, v_D, of the free electrons averages 52.4 μm/ns, so it takes an electron roughly 1.2 μs to cross half a drift chamber cell. The 50/50 mix of argon–ethane is a common choice

because the electron drift velocity in this mixture is essentially independent of the electric field, as long as the field is large. Hence, given a constant drift velocity, the drift time measurement becomes a linear measure of the distance traveled to the anode wire (Equation 3.4).

The high electric field near the wire ($E \sim 1/r$) results in a cascading amplification, as electrons are accelerated and cause further ionization. The multiplied electron ionization is collected by anode (sense) wires running the length of the cell. The two chamber models use slightly different wire configurations. Three–wire chambers in the calorimeter are strung with two +1750 V sense wires separated by 156 mils. The purpose of the two wires is to resolve the ambiguity of which side of the cell the charged particle traversed. Between the two sense wires is a field shaping wire held at +350 V, which acts as an accelerating potential between the two sense wires. Support of the three–wire cell assemblies is accomplished by several short lengths of monofilament nylon. The wires are melted into the monofilament segments, which act much like rungs on a ladder. The entire assembly is then strung[△] into the chamber and tensioned. Table 3.2 provides the sense and field wire specifications for the NuTeV drift chambers.

Wire type	Composition	Wire diameter	Operating voltage
field wire	silver–coated Cu-Be alloy	127 +/- 51 μm	+ 350 V
sense wire	gold–plated tungsten	30 μm	+ 1750 V

Table 3.2: Specifications for the wires used in NuTeV drift chamber cell construction and operation. Only three–wire chambers contain field wires.

[△]This delicate process was accomplished using a computer controlled wire-laying machine, for which I held much fondness in the very early stages of my graduate student career.

For the single–wire chambers populating the toroid, only a single +1900 V sense wire runs along the center of each cell. The optimal voltage for these sense wires is slightly different because there is no field–shaping wire. Throughout the run, the voltages for each drift chamber were monitored continuously to ensure their stability.

The anode signal from each sense wire is processed by a pre–amplification card mounted directly to each pair of drift chamber cells. Each card is capable of reading out two wires. For three–wire chambers, the pre–amps are staggered such that the wires in a given cell are not read out by a single pre–amp. The pre–amps produce an ECL logic pulse that is then fed into the time digitizing (TDC) system. Hence, the recorded delay between the time of the passage of the charged particle (T_0) and the time associated with the arrival of the drift electron pulse (T), allows the x or y position of the charged particle track to be determined:

$$x = x_0 + v_D \cdot (T - T_0)$$
$$y = y_0 + v_D \cdot (T - T_0) \tag{3.4}$$

where x_0 and y_0 denote the sense wire locations. In this analysis, the drift chambers are used only in the determination of the transverse coordinates of the neutrino interaction vertex, as described in Section 4.1.

3.2.3 Scintillation Counters

A scintillator plus photomultuplier tube (PMT) system is used to measure the energy deposited by charged particles in the calorimeter. There are 84 liquid scintillation counters in the NuTeV detector, numbered from 84 to 1, starting at the upstream end of the calorimeter. Each of the counters is a 3 m $\times$ 3 m $\times$ 2.5 cm lucite box viewed by PMTs mounted at each of the counter corners. To provide additional

structural support, 3 mm thick vertical lucite ribs, spaced approximately 2.5–5 cm apart, run the length of each counter. Since the ribs do not scintillate, the counters are staggered so that the ribs for consecutive counters do not align to create dead regions. A schematic of a NuTeV scintillation counter is shown in Figure 3.12.

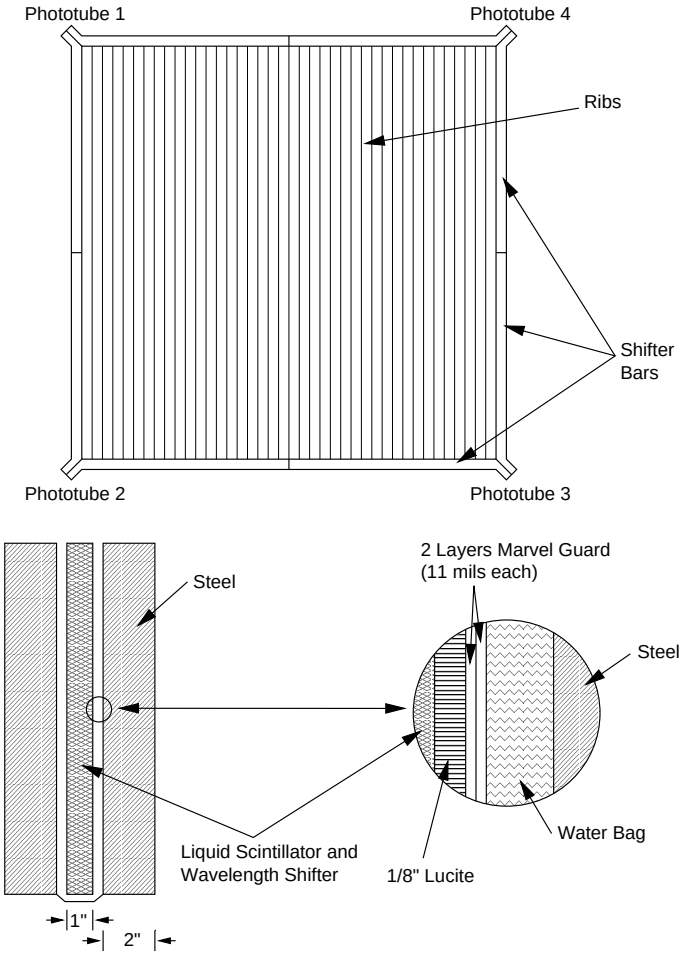

Figure 3.12: Front and side views of a NuTeV scintillation counter.

The counters are filled with roughly 65 gallons of Bicron 517L liquid scintillator oil. To balance the pressure of the liquid inside, each counter is flanked by two plastic water–filled bags (one on each side). When a charged particle passes through

the oil, it firsts excites a primary fluor which then de–excites and emits photons as ultraviolet light. This light is quickly absorbed by a secondary fluor which emits in the visible. The emitted blue light has a longer attenuation length in the oil and hence dominates the light output. Eight half–inch thick wavelength–shifter (WLS) bars surround the counter. These bars are doped with a third fluor which shifts the blue light to a longer wavelength, better suiting the response of the phototubes. This green light is then piped via total internal reflection to phototubes mounted on each of the four corners of the counter. To collect the light response, NuTeV uses 10–stage Hamamatsu R2154 phototubes with green–extended photocathodes. The photocathode, maintained at ∼1400 volts, has a 20% probability of converting the photon into a photoelectron by means of the photoelectric effect. A series of dynodes multiply the single photoelectron by a factor on the order of 10^6. Figure 3.13 shows the typical response of a counter to a muon passing through its volume as a function of position in the counter. The signal for a muon traversing the center of a counter is roughly 30 photoelectrons. For muons traveling closer to the edge of the counter (i.e., closer to the phototubes where light collection is more efficient) the response is higher.

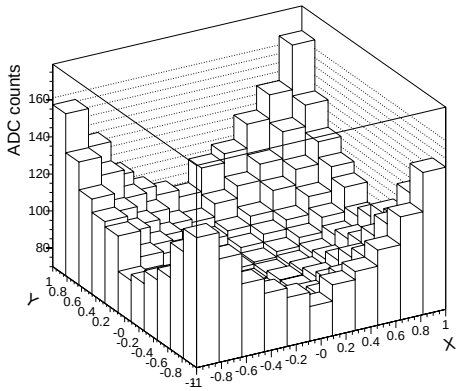

Figure 3.13: Average response of a NuTeV scintillation counter to the passage of a muon as a function of position in the counter.

3.3 Event Triggering and Readout

3.3.1 Phototube Pulse Heights

Analog–to–digital converters (ADCs) integrate the signal from the phototubes and turn that value into an ADC "count". The relation between ADC counts and GeV is determined from testbeam data (Section 3.1.4), but a rough estimate for muons is that one minimum ionizing particle (or mip) is approximately 0.2 GeV. The phototube signals from every target counter are stored in several ADC channels, each of which has a different dynamic range:

- **LOW**: A low channel corresponds to the response from an individual phototube; hence, there are four lows for each target counter. A muon passing through the center of a counter will typically produce 2 ADC counts in the lows.

- **COMBINATION LOW**: A combination low channel corresponds to the combined signal from all four of the phototubes from a given counter. Typically a muon passing through a counter will yield 8 ADC counts in this channel.

- **HIGH**: A high channel is the sum of the four low signals amplified by a factor 10, i.e., it is 10 $\times$ the combination low. A typical muon will generate 80 ADC counts in this channel.

- **SUPERLOW**: A superlow channel is the sum of eight phototube signals (lows) which come from eight different counters, each separated by ten counters. The signal is attenuated by a factor of 6 or 12 depending on the fan–in used. A typical muon signal in this channel is 0.2 ADC counts.

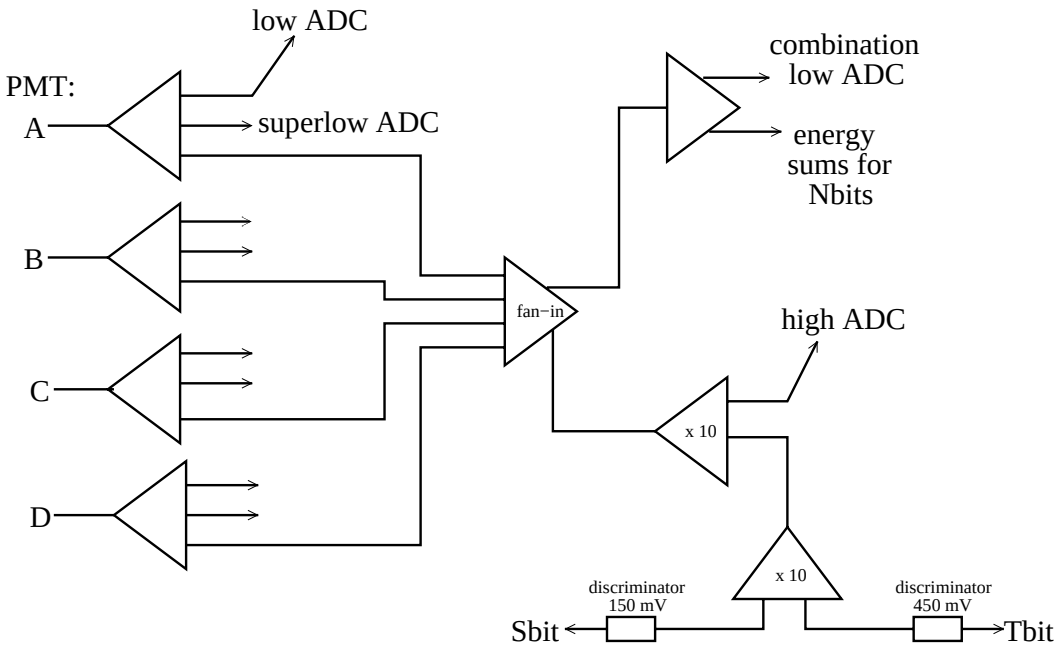

Figure 3.14: Readout configuration for a single scintillation counter.

The readout for a single counter is shown in Figure 3.14. The LOWs are used to measure hadron showers, which typically saturate the HIGHs. In the event that one of the four LOW channels is saturated (i.e., a lot of energy is deposited in a single counter or the neutrino interacts close to one of the phototubes), the attenuated SUPERLOW channel is used. The HIGHs are used to measure muons, since their signal is usually too small to be measured by the LOWs. COMBINATION LOWs are primarily used to form event triggers (Section 3.3.2).

The signals are also repeated by a fan–out. The fan–out channel is discriminated (tested for a minimum energy level) and its timing recorded in the TDCs. The discriminated logical signals or "bits" are constructed as follows:

- **Sbit** (single particle indicator): The linear sum of the signals from four phototubes in a target counter (i.e., a combination low) is amplified by 100 and put through a discriminator with a threshold of 150mV ($\sim$ 1/4 mip). Sbits are designed to identify at least one single muon passing through a counter.

- **Tbit** (more than one particle indicator): The linear sum of the signals from four phototubes in a target counter (i.e., a combination low) is amplified by 100 and put through a discriminator with a threshold of 450mV. Tbits are designed to distinguish between showers and single muons; a Tbit usually doesn't fire in the presence of a single charged particle.

- **Nbit** (shower indicator): The linear sum of the phototube signals from every combination of eight consecutive counters is put through a discriminator with a threshold of 55mV (5 GeV) with no amplification. Each counter in the middle of the detector contributes to eight Nbits.

- **NCbit** (shower indicator): A logical unit that looks at the energy and Tbits for each set of 4 consecutive target counters. The Tbits set the timing for the NCbits. The NCbit requires two of the four Tbits to fire, in addition to the Nbit which measures the energy of that set of four counters and the four immediately upstream (see Figure 3.15). NCbits identify energy deposition plus a small longitudinal development.

3.3.2 Event Triggers

Twelve separate triggers were used during the NuTeV run. Each one is designed to identify a particular event signature in the detector. Table 3.3 shows the number of

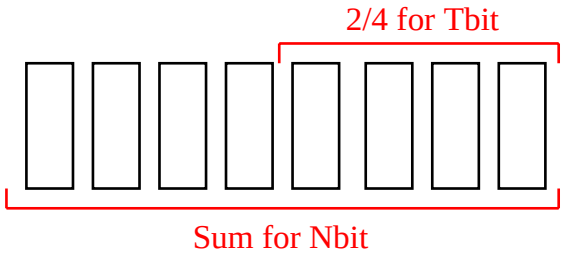

Figure 3.15: Schematic of the NCbit requirement for a set of eight consecutive scintillation counters.

events that were recorded for each trigger in both neutrino and antineutrino mode running.

Trigger	Description	Neutrino Mode	Antineutrino Mode
1	Charged Current	2,612,830	908,161
2	Neutral Current	5,445,024	2,804,981
3	Penetrating Muon	4,306,217	3,065,412
6	Straight Thru Muon	1,712,591	735,222
9	Neutral Heavy Lepton	1,334,675	1,616,637
10	In–Spill Pedestal	189,855	183,794
11	Toroid Pedestal	785,040	153,461

Table 3.3: Number of recorded neutrino gate events for each of the NuTeV triggers. The neutrino gate is described in Section 3.1.3. Note that an event can satisfy more than one trigger.

The following list details each of the NuTeV event triggers.

- **Trigger 1** (Charged Current): This trigger is designed to look for charged current events, specifically events originating in the calorimeter with a toroid–analyzed muon. It requires hits in the last calorimeter cart and in the toroid gap(s). Specifically, one of two event topologies must be satisfied: there must

be (a) either hits in at least two of the the last four counters (counters 1–4) and hits in both toroid gaps; or (b) hits in at least two of the the last four counters (counters 1–4), hits in at least two additional counters slightly upstream (counters 9–12), and hits in only the first toroid gap. The dimuon events which are used for the strange sea measurement and the single muon events used in the flux extraction are both selected by trigger 1.

- **Trigger 2** (Neutral Current): This trigger identifies showers with small penetration. It is the trigger that selects events for the present analysis. The trigger is an "OR" of the NCbits, and demands there be at least 5 GeV of energy in eight consecutive scintillation counters. No muon requirement is made. This trigger is described in further detail in the following section.

- **Trigger 3** (Penetrating Muon): This trigger is designed to find short charged current events in which the muon either ranges out or exits the calorimeter. It requires sixteen possibly non–consecutive counters in the calorimeter to fire with no additional minimum energy requirement. This is the trigger that is used to test trigger 2 efficiency.

- **Trigger 4** (Redundant Charged Current): This trigger is used to measure trigger 1 efficiency. It has slightly stricter geometric requirements than trigger one and uses different hardware (except for the veto). Instead of using hits in counters 1–4 and 9–12, trigger 4 uses counters 5–8 and 13–16, in addition to the toroid gap requirements from either trigger 3 or 6 in place of those for trigger 1.

- **Trigger 5** (Calibration Beam): Use of this trigger is reserved for testbeam

running when either a hadron, muon, or electron beam is incident on the calorimeter. It requires a coincidence between the two testbeam scintillation counters but makes no requirement on the energy deposited in the calorimeter. During the course of running, NuTeV collected roughly 17 million calibration beam triggers.

- **Trigger 6** (Straight Through Muon): This trigger selects muons produced upstream in the berm that traverse the entire detector. It requires a hit in each target cart and hits throughout the toroid which stay within one quadrant. The requirement that the hits remain confined within a toroid quadrant selects higher energy (stiff) muon tracks. Specifically, counters 81 or 82 must fire, as well as at least one counter from each set of four counters from each of the six target carts, plus at least two out of each set of four toroid counters within the same quadrant. Stiff track trigger 6 events are used for calibration, counter X–rays (Section 5.3.6), and drift chamber alignment.

- **Trigger 8** (Cosmic Ray): This trigger requires at least 40 semi–consecutive counters of penetration and hits in the first toroid gap. It is used to select off–spill cosmic ray muons.

- **Trigger 9** (NHL): This trigger is used for the neutral heavy lepton (NHL) analyses. It identifies events which have the characteristics of an NHL via a muon or electron/hadron signature in the front of the calorimeter.

- **Trigger 10** (In–Spill Pedestal): This trigger randomly fires during the spill so it is not correlated with beam activity.

- **Trigger 11** (Toroid Pedestal): The toroid shower trigger is correlated with beam activity. However, it was found to occasionally fire due to neutrino activity in the calorimeter (e.g., charged current events in which the muon catastrophically loses energy in the toroid), and not just from interactions in the toroid. It is designed to study the effect of an active toroid on the target electronics and to correctly calculate beam pile–up.

- **Trigger 12** (Pedestal): This trigger samples electronic levels outside of spill in order to establish a zero level on our electronics. The trigger is prescaled such that typically ten trigger 12 events are collected by the DAQ right after the beginning of each accelerator cycle.

The first four triggers also include a veto requirement. The veto can be thought of as an "anti–trigger". Since the veto system is enlisted to detect incident charged particles that may signal a false event, triggers 1–4 require that the veto not fire. For a very small portion of the run, the veto was provided by a coincidence of upstream and downstream counter planes in the "picture frame" veto wall positioned directly in front of the Lab E detector combined with the signal from the two most–upstream counters in the calorimeter (counters 83 and 84). In September of 1996, the veto was switched to being provided by the Lab F veto wall [25]. This array of nineteen scintillation counters, mounted far upstream of the calorimeter and decay channel, was shielded by the berm and hence yielded smaller deadtime.

3.3.3 Trigger 2 Efficiency

The trigger used for the $\sin^2\theta_W$ analysis (trigger 2) selects events with small showers in the calorimeter. The trigger scans regions consisting of four consecutive scintil-

lation counters, requiring two out of the four consecutive counters to contain more than one charged particle ($\geq$ 0.15 GeV/counter), and the total energy deposit in the four counters in addition to the four immediately upstream be larger than 5 GeV. Hence, the trigger 2 requirement is any NCbit (Figure 3.15). The efficiency of this trigger is determined using an independent muon trigger (trigger 3), which is sensitive to small single particle deposits of energy ($\geq$ 0.05 GeV/counter) over the entire calorimeter. Except for the veto, the hardware for trigger 2 and 3 are separate, so the two do not overlap.

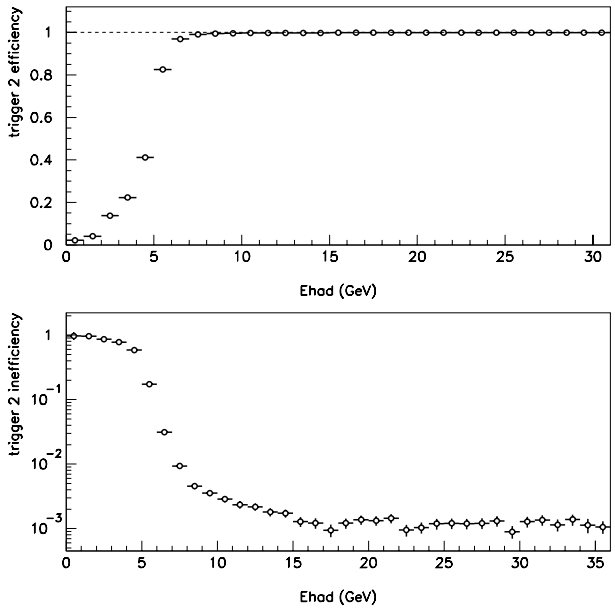

Figure 3.16: The top plot shows the measured efficiency of the $\sin^2\theta_W$ analysis trigger as a function of hadronic energy. The bottom plot displays the inefficiency of the trigger as a function of energy.

Figure 3.16 shows the measured efficiency of the $\sin^2\theta_W$ analysis trigger as a function of hadronic energy. The bottom plot of Figure 3.16 shows the trigger

inefficiency as a function of energy. The trigger is 99% efficient at 7.5 GeV. Most importantly, above the analysis cut, $E_{had} \geq 20$ GeV, the trigger is 100% for all events used in the analysis.

3.3.4 Calibration of the Readout Electronics

As described in Section 3.2.3, the energy in a scintillation counter registers as an electronic signal, the ADC pulse height. Calibration information converts this signal into an equivalent energy measure in GeV. Specifically, the energy deposited by a charged particle in the i^{th} single scintillation counter is derived from the pulse height PH(i) registered in either the LOW or HIGH ADC channel modified by a number of correction factors:

$$E_{cntr}(i) = \frac{C_\pi \cdot h\,(i) \cdot G(i,t) \cdot PH(i)}{Map\,(i, Vx, Vy, t)} \tag{3.5}$$

The pulse height, PH(i), is taken from the LOW channel as long as the signal is in what is considered to be a "safe" linear region, i.e., greater than 35 ADC counts in the LOWs, or else the HIGH is used. The SUPERLOWs are used if the LOW channel saturates with more than 1900 ADC counts[⋈]. Next, the pulse heights are pedestal subtracted using a measure of the baseline activity in quiet regions of the detector during neutrino data taking.

The counter gain factor, G(i,t), converts the pulse height response in ADC counts into mips. Muons produced in upstream neutrino interactions in the berm track the counter gains as a function of time. The average value is roughly 80 ADC counts in the HIGHs for most counters (Figure 3.13).

[⋈]The pulse height assignment and the use of the SUPERLOWs are improvements adopted after release of the preliminary $\sin^2\theta_W$ result [26].

The hadron energy calibration constant, C_π, converts the pulse height mip response into GeV and is known to 0.43%. The value for C_π of 0.212 GeV/mip is established from hadron testbeam data ranging in energy from 10 to 190 GeV, such that the mean energy response in the detector for 75 GeV hadrons matches the reconstructed mean momentum determined from the testbeam. Figure 3.17 shows the energy dependence of the calorimeter hadron energy response. The NuTeV non–linearity between 10 and 190 GeV is about 3%. Such a non–linearity is characteristic of non–compensating calorimeters which have slightly different response to hadronic and electromagnetic showers. The energy response is not necessarily linear because hadron showers contain both a hadronic and an electromagnetic component. On average, hadronic cascades produce 2/3 charged pions and 1/3 neutral pions because there is a nearly equal probability of producing π^+, π^-, and π^0. The neutral pions decay, with a mean lifetime of 10^{-16} sec, into two photons each of which initiate an electromagnetic cascade with a characteristic length much shorter than that of the hadronic transport. Therefore, if h is the calorimeter calibration constant for a "pure" hadronic shower and e for electromagnetic showers, then the calibration constant for the "real" hadronic shower is in fact given by the combination:

$$C_\pi = e \cdot f_{\pi^0}(E) + h \cdot [1 - f_{\pi^0}(E)] \tag{3.6}$$

where $f_{\pi^0}(E)$ is the fraction of π^0's produced in the shower. Fitting the hadron energy response shown in Figure 3.17 one arrives at a value, $e/h = 1.079 \pm 0.011$, assuming Groom's parameterization, $f_{\pi^0}(E) = 1 - \left(\frac{\mathrm{E_{had}}}{0.96\ \mathrm{GeV}}\right)^{-0.184}$ [27].

In addition, the pulse heights are corrected by a relative hadron gain factor, h(i), which accounts for non–uniformities in the detector geometry, for example, varying water bag or steel thicknesses.

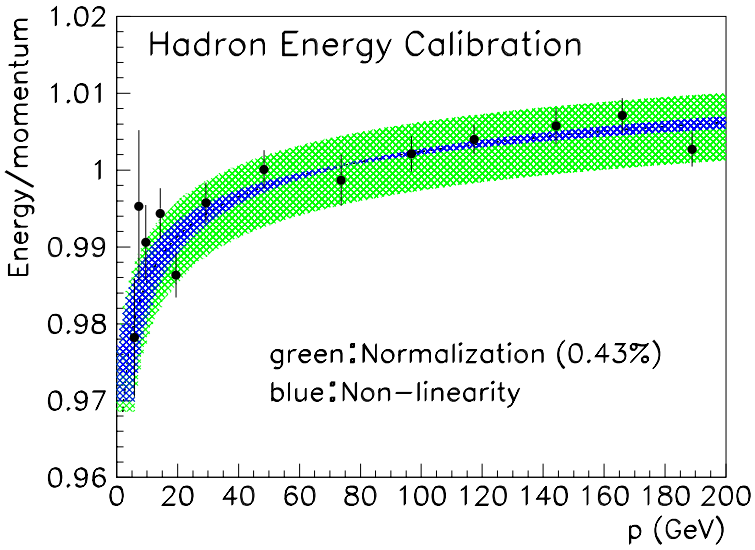

Figure 3.17: Hadron energy response as a function of testbeam momentum for testbeam hadron data ranging in energy from 4.8 to 190 GeV. The larger band reflects the overall 0.43% uncertainty in the hadron energy scale. The narrow inner curve is the result of a fit to Groom's parameterization [27] with $e/h = 1.079 \pm 0.011$, where e is the detector response to electrons and h is the response to hadrons.

Finally, because the response of the scintillation counters varies with position as a result of the geometry of the light collection (Figure 3.13), the pulse heights need correction from a muon map correction factor, Map(i,Vx,Vy,t). This factor is determined from neutrino–induced muons which are used to map the response of each counter as a function of position and time. It is simply the ratio of the counter response at position (x,y) to that at the center (0,0) of the counter. Map values typically range from 0.5 out to about 3 in the corners of the counter. Figure 3.18 displays map correction functions for several NuTeV counters. For each counter, the value for the map correction is chosen at the transverse event vertex (Vx,Vy) and is further required to be "reasonable", namely $0.1 \leq$ Map(i,Vx,Vy,t) ≤ 5.0 else no map correction is applied.

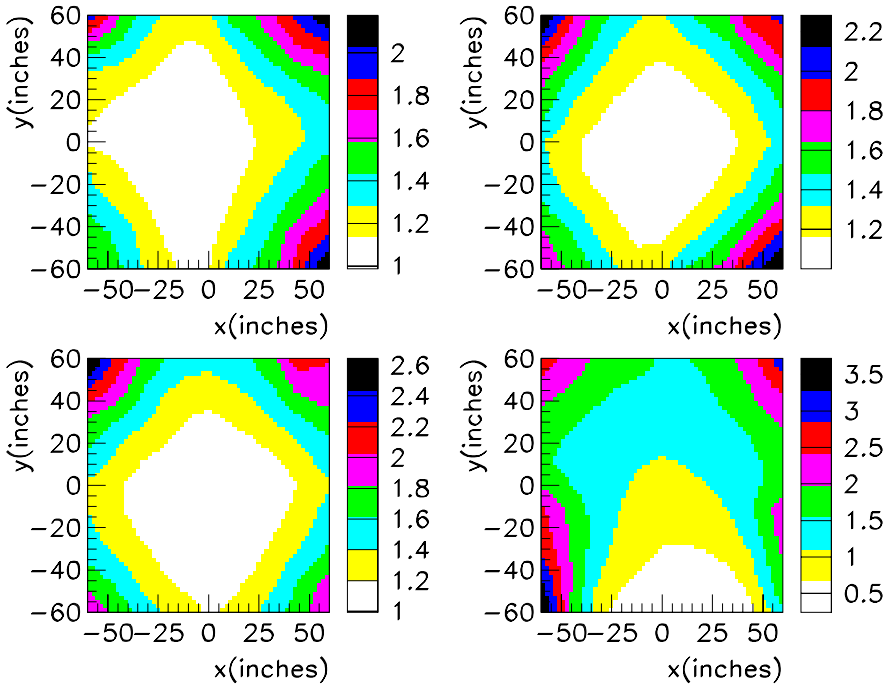

Figure 3.18: Muon map contours. These functions are used to correct for the position dependence of the counter pulse heights. The first three counters (counters 80, 70, and 60) were randomly selected; the last counter is an example of a counter with an oil leak (counter 35) exhibiting skewed optical properties.

Since the calorimeter is an energy measuring device, one of its most important characteristics is its energy resolution. Because the hadronic energy distribution of the event sample is a steeply falling function, the finite energy resolution of the calorimeter creates a smearing across energy bins. The calibration beam provides a measure of this resolution. The distribution of energy measured in the detector for a given hadron beam energy can be parametrized by a Poisson–like distribution [23]. The Poisson widths determine the energy resolution as a function of energy; for hadrons,

$$\frac{\sigma}{E} = \frac{0.86 \pm 0.01}{\sqrt{E}} + 0.022 \pm 0.001, \tag{3.7}$$

where the stochastic $1/\sqrt{E}$ term is due to fluctuations in sampling the number of particles in the shower, and the constant term reflects calibration uncertainties. For electromagnetic showers, the resolution is determined from testbeam electrons:

$$\frac{\sigma}{E} = \frac{0.499 \pm 0.008}{\sqrt{E}} + 0.042 \pm 0.002. \tag{3.8}$$

The various calibration constants used in the $\sin^2\theta_W$ analysis are summarized in Tables 3.4 and 3.5. Further discussion of their analogous use in the Monte Carlo simulation appears in Chapter 5.

Particle Type	Calibration Constant (GeV/mip)	Resolution σ(E)/E
hadrons	$C_\pi = 0.212$	$0.86/\sqrt{E} \oplus 0.022$
electrons	$C_e = 0.195$	$0.50/\sqrt{E} \oplus 0.042$
muons	$C_\mu = 0.158$	0.11 (toroid)

Table 3.4: NuTeV calibration constants used in this analysis; from Reference [23].

hadron energy scale uncertainty	0.43%
electron/hadron response (e/h)	1.08 ± 0.011
hadron non–linearity (5.9 to 190 GeV)	$3.0 \pm 0.5\%$

Table 3.5: NuTeV calibration measurements used in this analysis; from Reference [23].

Chapter 4

Data Analysis

This chapter describes the preparation of the data sample for the $\sin^2\theta_W$ analysis. The five sections describe the algorithms that compute event parameters, the event selection criteria, the procedure to classify events into NC and CC categories, the subtraction of background events from the data, and the corrections for inefficiencies in the vertex finding algorithms.

4.1 Event Reconstruction

This section introduces the event variables used in the $\sin^2\theta_W$ analysis. Five experimental quantities are reconstructed for each event: the longitudinal vertex position, the transverse vertex position, the hadronic shower energy, the event endpoint, and the event length. Because this determination of $\sin^2\theta_W$ is based on the measurement of the ratio of neutral current to charged current events, both types of events must be treated as identically as possible to avoid bias. This requirement drives all choices of how the event variables are reconstructed.

- **Longitudinal Vertex Position** (PLACE):

  Ideally, the measured variable, PLACE, identifies the first scintillation counter

immediately downstream of the neutrino interaction. This analysis uses the NNPLACE definition, as developed by Alexandru Romosan [28]. As such, PLACE is defined to be the most upstream of the first two consecutive counters, each with in–time Sbits and more than n mips of deposited energy, where:

$$n \;=\; \max(-1.0679 + 0.9660\,\sqrt{\mathrm{E_{had20}}},\, 3). \tag{4.1}$$

This value for n minimized the RMS of the difference between reconstructed and generated PLACE for NC events studied in GEANT [28]. Figure 4.1 shows the results of this study. In particular, n is parameterized as a function of $\mathrm{E_{had20}}$, the sum of the energy in the first 20 counters downstream of PLACE (see Equation 4.2), and is at least 3 mips. Romosan found this energy–dependent definition to be a much better indicator, than say a fixed mip definition, of the true interaction location for NC neutrino events. Note that in using this recursive algorithm, PLACE is determined circularly; PLACE is obtained from a PLACE–dependent energy sum; that energy sum is then recalculated at PLACE, and so on, such that PLACE = PLACE($\mathrm{E_{had20}}$(PLACE($\mathrm{E_{had20}}$))).

A dimuon–based study of the accuracy of the PLACE algorithm in determining the true location of neutrino interactions is discussed in Section 5.3.5.

- **Transverse Vertex Position** (Vx, Vy):

  Hits in the calorimeter drift chambers determine the transverse location of the neutrino interaction. For each drift chamber, the average hit position is determined by iteratively calculating the average hit centroid while simultaneously discarding chamber hits lying more than 20 inches from the calculated

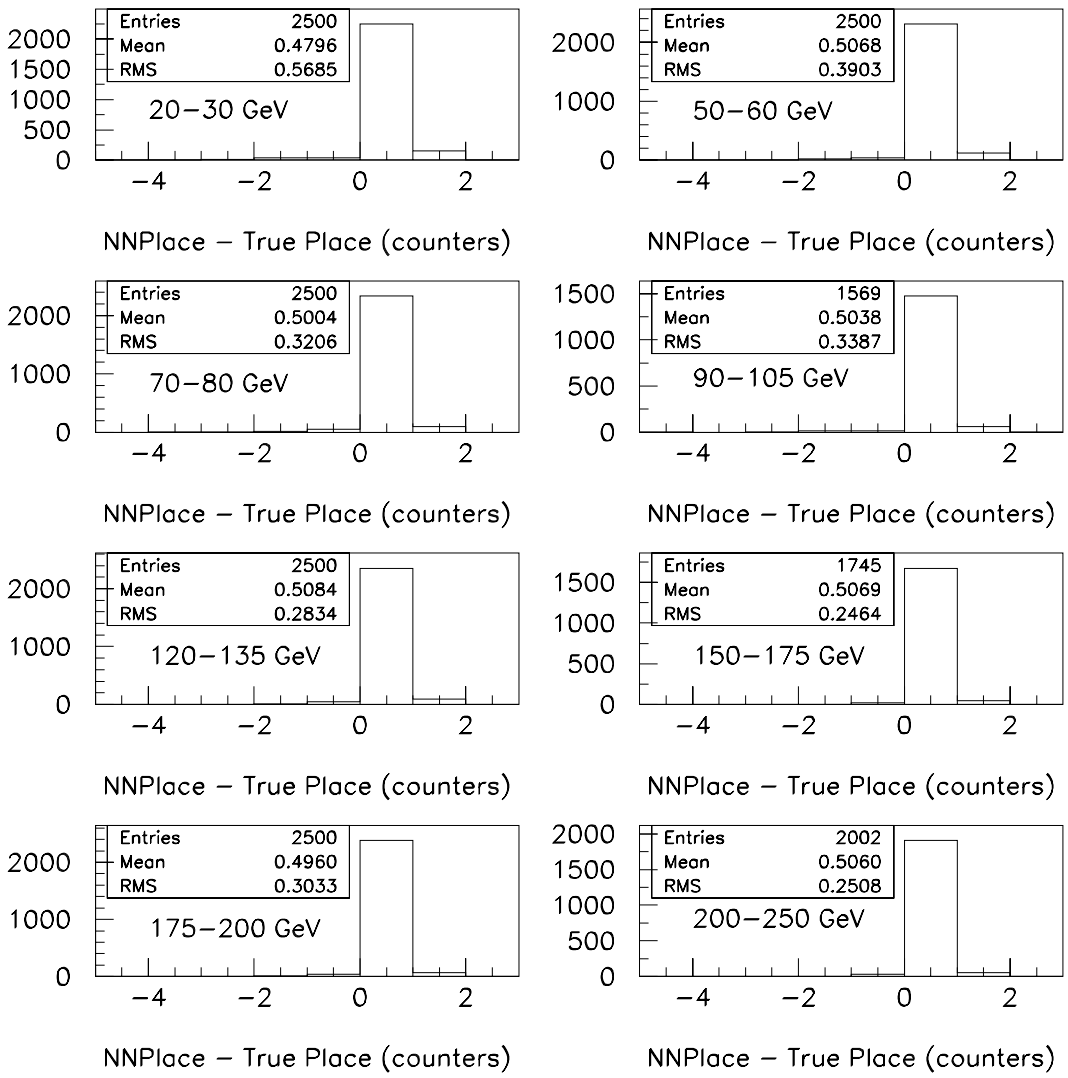

Figure 4.1: Difference between reconstructed PLACE, as determined from the NNPLACE algorithm, and true PLACE for GEANT NC neutrino interactions in E_{had20} bins.

centroid. The transverse vertex position is then obtained for each plane (x,y) from the mean of the hit centroids in the first chamber upstream of PLACE and the two nearest chambers downstream of PLACE. The hits are weighted by the sum of the energies in the two counters adjacent to each chamber. The choice of the number of chambers to sum includes an inherent trade-off: decreasing the number of chambers in the sum increases the inefficiency of the algorithm, but also reduces bias between short and long events (Figure 4.2). Because the latter is more important, we choose to sum the hits in only three chambers.

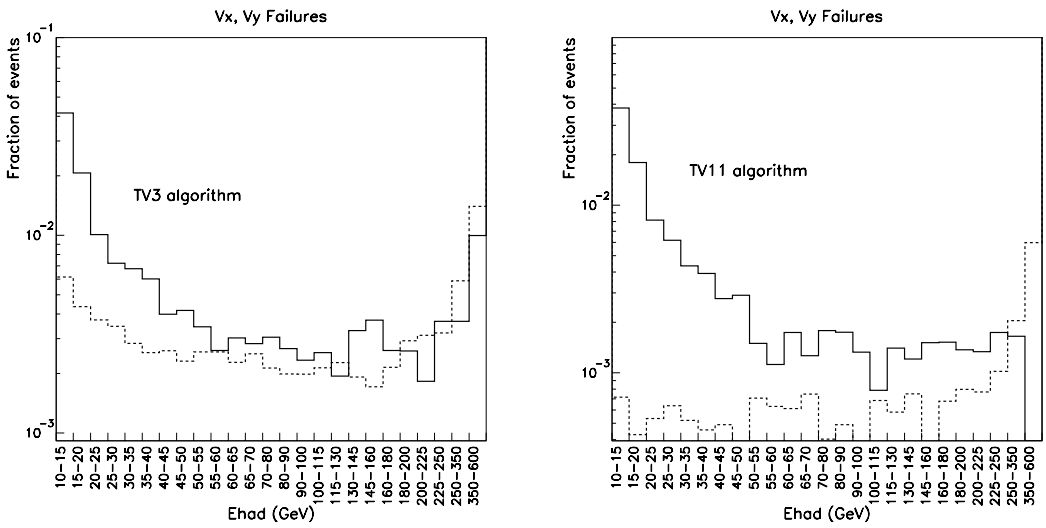

Figure 4.2: Comparison of the number of transverse vertex failures using a 3–chamber (top) versus an 11–chamber summation (bottom) for both short (solid) and long (dotted) events. The 3–chamber sum exhibits less of a short/long efficiency difference, while the 11–chamber sum is selectively more efficient for long events due to the added hits from the muon track.

- **Hadronic Shower Energy** ($E_{had} = E_{hadvar}$):

  The hadronic shower energy is calculated by summing the energy registered in the calorimeter scintillation counters. The conventional procedure selects the

energy deposited in a fixed number of counters, namely 20 counters* downstream of PLACE+1:

$$E_{had20} = \sum_{i=PLACE+1}^{PLACE-19} E_{cntr}(i) \quad (4.2)$$

where Section 3.3.4 describes the determination of the energy in a single scintillation counter, $E_{cntr}(i)$. The above energy definition contains almost all of the shower energy, because the probability that a hadron will penetrate beyond 20 counters is small; however, for testbeam hadrons this energy definition does not necessarily yield the most accurate shower energy estimate. For example, if a shower does not extend out to 20 counters, the sum will include additional pulse heights from pedestal noise or muons. It is therefore important to sum an energy–dependent number of counters. For this analysis, the energy definition is tuned to optimize containment. The process is iterative. To determine the appropriate summation length, testbeam hadrons ranging in energy from 10 to 200 GeV determine the length containing 99% of the hadronic energy using the E_{had20} energy definition:

$$L'_{var} = \text{int}\left[4.4827 + 1.41042 \cdot \ln\left(E_{had20}\right)\right] \quad (4.3)$$

This dependence is chosen because the longitudinal energy deposition depends logarithmically on energy. Based on this length, a new energy sum and resultant length are then calculated:

$$E_{hadvar}{}' = \sum_{i=PLACE+1}^{PLACE-L'_{var}+1} E_{cntr}(i) \quad (4.4)$$

* Twenty scintillation counters is roughly 2.1 m of steel; 14 nuclear interaction lengths (λ_I)

$$L_{var} = int\left[4.4827 + 1.41042 \cdot \ln\left(E_{hadvar}{}'\right)\right] \quad (4.5)$$

L_{var} is the length that contains 99% of the total shower energy, thereby yielding a variable length energy definition, E_{hadvar}, which yields 99% energy containment when compared to testbeam hadrons:

$$E_{hadvar} = \sum_{i=PLACE+1}^{PLACE-L_{var}+1} E_{cntr}(i) \quad (4.6)$$

This is the energy definition used for both CC and NC events.

- **Event End** (EXIT):

  The EXIT algorithm searches the scintillation counters starting at PLACE, and moving downstream until it finds three consecutive counters each either without in–time Sbits or less than 0.3 mip energy deposition. The event end is defined to be the last counter with deposition upstream of the gap of three; therefore, EXIT is the last counter consistent with at least single muon energy deposition.

- **Event Length (L)**

  The length of the neutrino event is simply defined to be the number of scintillation counters spanned by the neutrino event. It is the distance between the registered interaction location and the event end:

$$Length = L = PLACE - EXIT + 1 \quad (4.7)$$

Figure 4.3 summarizes the determination of the event length and the ingredients that enter into its definition.

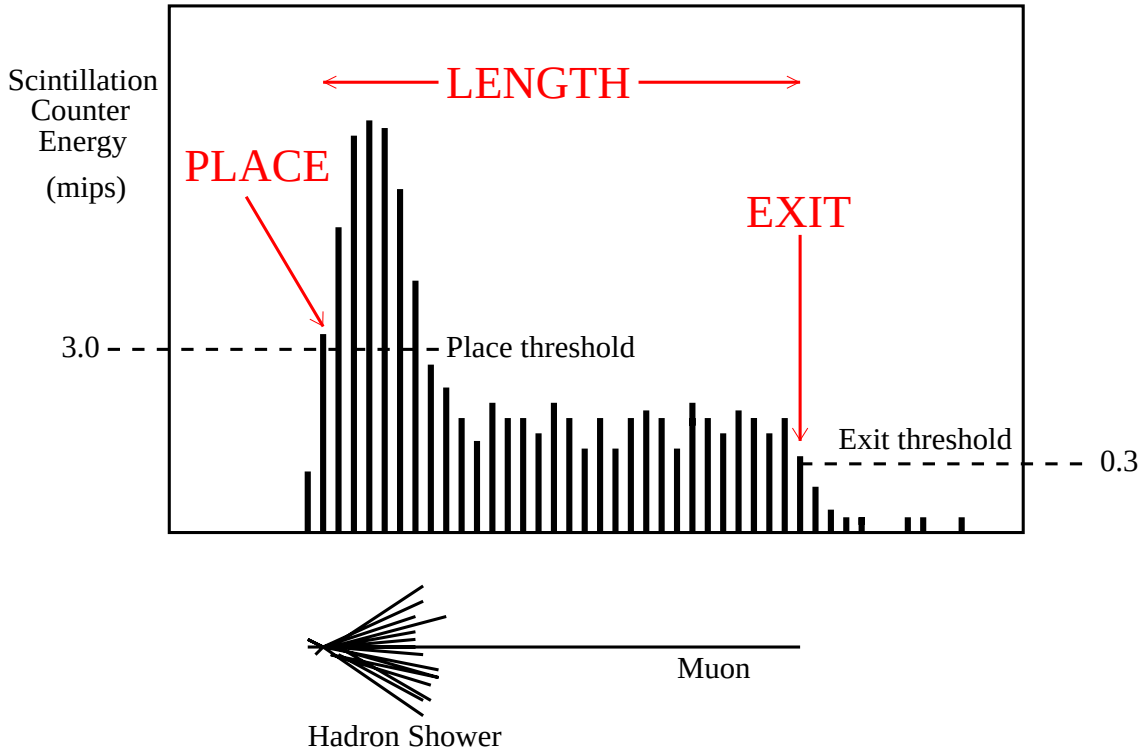

Figure 4.3: Illustration of the event length determination for a CC neutrino interaction. The length of an event in the data is determined solely from the calorimeter scintillation counters.

4.2 Event Selection

During the 1996–1997 fixed target run at Fermilab, NuTeV received a total integrated proton intensity of 3.22×10^{18} (Appendix C). Combined with an overall data-taking efficiency of ∼89%, NuTeV logged–to–tape events representing 1.27×10^{18} protons on target in neutrino mode and 1.58×10^{18} in antineutrino mode. The experiment could acquire up to 32 events/ping as determined by the trigger logic; having 5 pings implied the collection of a total of ∼160 events/spill. In the end, NuTeV accumulated approximately 300 Gb of useful neutrino data. From this, the following cuts select events of interest for the $\sin^2\theta_W$ analysis:

- **Bad Runs**: Careful examination of the run logs and overall data quality resulted in the removal of several runs (or portions of runs) because of known problems with the detector, beam quality, or data processing.

- **Data Gate**: Events from gates other than the neutrino gate (gates 1–5) or cosmic ray gate (gate 7) are discarded. Events collected during the cosmic ray gate are analyzed in the same manner as neutrino events and then subtracted as background (Section 4.4.1).

- **Analysis Trigger**: Events must satisfy the trigger 2 requirement. See Section 3.3.2 for the specifics of this trigger.

- **Event Time**: The event time measured from the scintillation counters must agree to within 72 ns of the time predicted by the trigger. This ensures that the offline event time from the Sbits for the identified interaction agrees with the online trigger time. Figure 4.4 shows the timing resolution for both short

and long events.

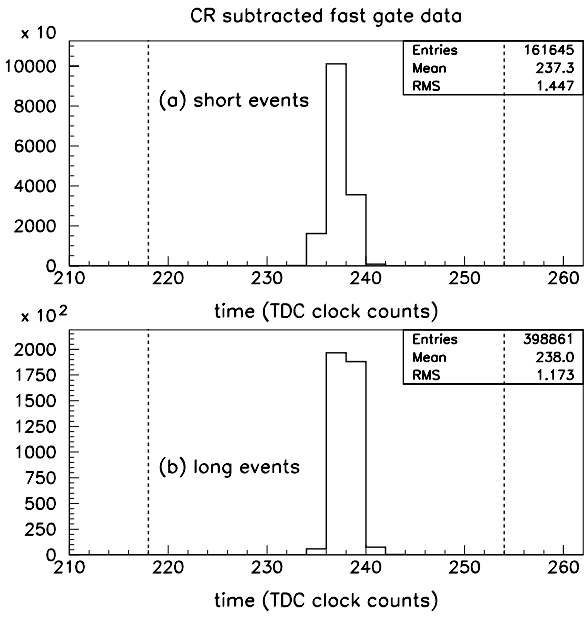

Figure 4.4: Event time distribution for (a) short and (b) long events. Each TDC clock count is 4ns. The analysis cut requires a trigger time in the range from 218 to 254 clock counts.

- **Interaction Location**: ($\mathrm{P_{cut}} \leq \mathrm{PLACE} \leq 80$)

  The longitudinal interaction vertex must lie within roughly 2m of the upstream and downstream ends of the calorimeter. The upstream limit ensures that the event is neutrino induced; the downstream limit allows adequate discrimation between short and long events. As was the case for the length cut, the downstream PLACE cut varies as a function of energy:

$$\begin{aligned} P_{\mathrm{cut}} &= 17, \qquad \mathrm{E_{had}} \leq 60\ \mathrm{GeV} \\ P_{\mathrm{cut}} &= 18, \qquad 60 < \mathrm{E_{had}} \leq 100\ \mathrm{GeV} \\ P_{\mathrm{cut}} &= 21, \qquad \mathrm{E_{had}} > 100\ \mathrm{GeV} \end{aligned} \tag{4.8}$$

- **Transverse Vertex Position**: ($|\mathrm{Vx}| \leq 40$ inches, $|\mathrm{Vy}| \leq 45$ inches)

  In the transverse place, the location of the neutrino interaction is restricted to a 40 inch box surrounding the center of the detector that includes an additional five inch section at the top and bottom. Figure 4.5 illustrates the chosen fiducial volume. This requirement ensures hadron shower and muon containment in the detector, and reduces the electron neutrino contamination because the kinematics of kaon decay are such that ν_e's preferentially populate the outer edges of the detector.

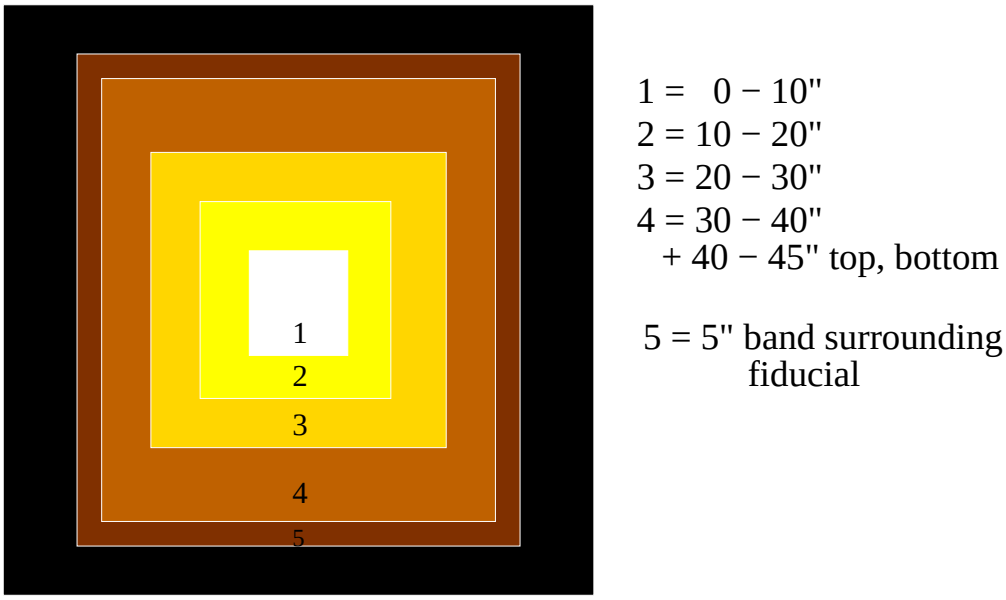

Figure 4.5: Frame box or "square" bins in the the $\sin^2\theta_W$ analysis. Bins 1–4 represent the chosen fiducial volume. Bin four is the only fiducial bin that is not square; it includes an added 40–45 inch section at the top and bottom of the detector. Bin five is a 5 inch band around the fiducial which is used only to check that the analysis results are stable outside the cut.

- **Energy Requirement**: ($20 \leq E_{had} \leq 180$ GeV)

  Events are required to deposit at least 20 GeV of visible hadronic energy in the calorimeter, but not more than 180 GeV. The lower bound ensures complete efficiency of the analysis trigger (Section 3.3.3), ensures vertex finding efficiency (Section 4.5), and reduces cosmic ray contamination (Section 4.4.1). The upper bound removes extremely high energy events that have large beam backgrounds.

During the fast gate, a total of 5.44×10^6 trigger 2 events were collected in neutrino mode and 2.80×10^6 in antineutrino mode. Roughly 0.06% of these events are removed by the bad run and event time requirements. Table 4.1 shows the number of events passing each of the remaining analysis cuts. After all cuts, the surviving data sample consists of 1.62×10^6 neutrino and 0.35×10^6 antineutrino events.

Analysis Cut	Neutrino Events	Antineutrino Events
Fast Gate, Trig 2, Event Time, Bad Run	5,442,030	2,803,305
$P_{cut} \leq$ PLACE ≤ 80	4,151,383	2,024,910
$\|Vx\| \leq 40$ in, $\|Vy\| \leq 45$ in	2,734,312	1,205,891
$E_{had} \geq 20$ GeV	1,720,283	363,149
$E_{had} \leq 180$ GeV	1,624,919	355,777

Table 4.1: Number of events sequentially passing each of the $\sin^2\theta_W$ analysis cuts.

4.3 Analysis Procedure

NuTeV detects neutrinos via their NC and CC interactions in our detector. Figures 4.6 and 4.7 show candidate NC and CC events. In each event display, the neutrino beam is incident from the left.

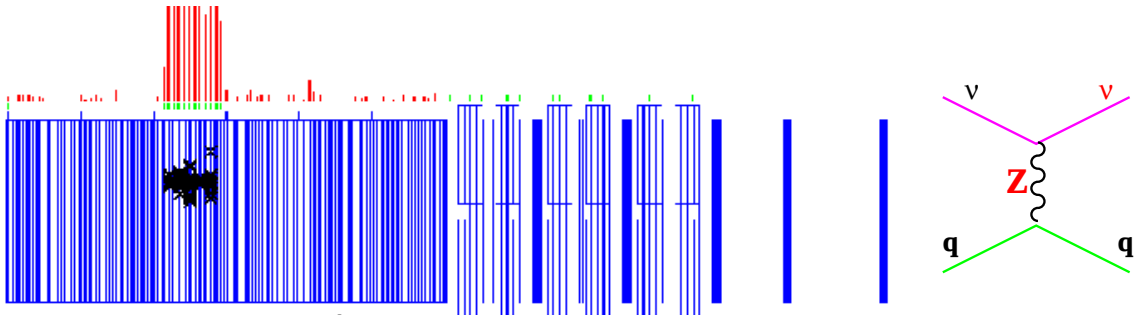

Figure 4.6: A typical NC event in the NuTeV detector.

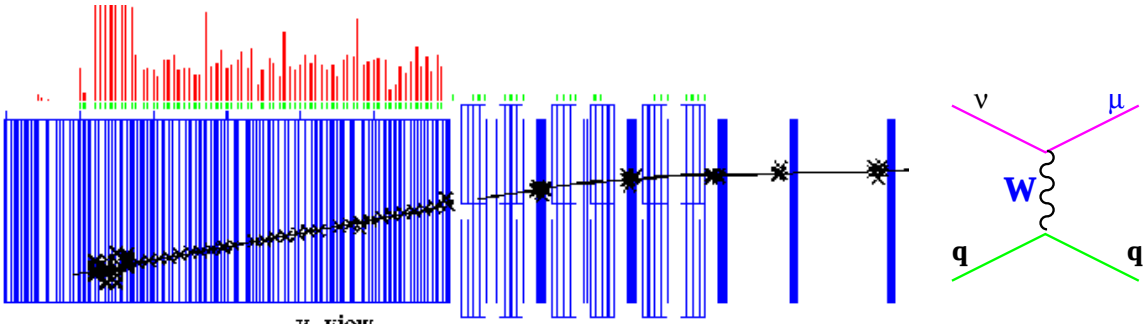

Figure 4.7: A typical CC event in the NuTeV detector.

Both CC and NC neutrino interactions initiate a cascade of hadrons that registers in the scintillation counters and drift chambers. In both cases, the hadronic shower appears as a cluster of energy at the location of the neutrino interaction. CC events distinguish themselves from NC events by the presence of a final state muon. The muon typically penetrates well beyond the hadronic shower and deposits energy in a large number of consecutive scintillation counters characteristic of a minimum

ionizing particle. The muon track is clearly visible in Figure 4.7. For NC events, the final state neutrino cannot be seen so that only the hadronic shower registers in the detector. These different event topologies enable the statistical separation of NC and CC interactions based solely on event length, i.e., longitudinal energy deposition. Events with a long length are identified as CC candidates; those with a short length are identified as NC candidates. Hence, the experimental quantity that is measured in both neutrino and antineutrino modes is the ratio:

$$R_{\rm exp} = \frac{\#\ \text{short events}}{\#\ \text{long events}} = \frac{\#\ \mathrm{L} \leq \mathrm{L_{cut}}}{\#\ \mathrm{L} > \mathrm{L_{cut}}} = \frac{\#\ \text{NC candidates}}{\#\ \text{CC candidates}} \tag{4.9}$$

The separation length increases with energy:

$$L_{\rm cut} = 16, \quad \mathrm{E_{had}} \leq 60\ \mathrm{GeV} \tag{4.10}$$

$$L_{\rm cut} = 17, \quad 60 < \mathrm{E_{had}} \leq 100\ \mathrm{GeV} \tag{4.11}$$

$$L_{\rm cut} = 18, \quad \mathrm{E_{had}} > 100\ \mathrm{GeV} \tag{4.12}$$

and is based on the location where the NC and CC contributions are roughly equal as determined from Monte Carlo ($L_{\rm cut} = 14, 15, 18$). The decision to cut more conservatively on length ($L_{\rm cut} = 14, 15, 18 \rightarrow 16, 17, 18$) resulted in the reduction of the systematic uncertainties associated with the event length determination: length systematics dropped by 10% while the statistical error increased by only 0.6%.

The energy dependent length cut minimizes the number of short CC background events in the NC sample (see below). Because we have chosen a simple length–based selection, both the numerator and denominator of our measured ratios contain backgrounds:

$$R_{\rm exp} = \frac{\#\ \text{short events}}{\#\ \text{long events}} = \frac{\#\ \text{true}\ \nu_\mu\ \text{NC events}\ +\ \text{backgrounds}}{\#\ \text{true}\ \nu_\mu\ \text{CC events} +\ \text{backgrounds}} \tag{4.13}$$

The backgrounds to the short ν_μ NC sample include short ν_μ CC events, short ν_e CC events, and cosmic rays. Short ν_μ CCs are high y events that evolve either as wide angle muons that exit out the side of the detector or low energy muons that range-out in the calorimeter. Charged current ν_e events always manifest as short events because the final state electron immediately showers inside the hadronic shower. Because of their usually vertical angle, cosmic ray events tend to extend over a short longitudinal distance in the detector, hence they primarily fall into the short length NC class rather than the long length CC class.

The long sample is predominantly ν_μ CC neutrino interactions, but also includes small contaminations of showering beam muons and ν_μ NC events in which the hadron shower fluctuates longer than the length cut. Table 4.2 lists the size of the background contributions to the short and long event samples for both neutrino and antineutrino interactions.

Short Backgrounds:	Fraction of Short ν Events	Fraction of Short $\overline{\nu}$ Events
Short ν_μ CC events	17.2%	6.6%
Short ν_e CC events	5.1%	6.0%
Cosmic rays	0.9%	4.7%
Long Backgrounds:	Fraction of Long ν Events	Fraction of Long $\overline{\nu}$ Events
Long ν_μ NC punch-through	0.7%	0.7%
Showering beam muons	0.2%	0.3%

Table 4.2: Percentage of background events in the short and long event samples.

In most cases, the backgrounds in the neutrino and antineutrino data samples have comparable size. However, in the antineutrino sample, a smaller background of short CC events and a larger background of cosmic rays directly result from the $(1-y)^2$ dependence of the antineutrino cross section. There is also a slightly larger

background of beam muons in the antineutrino data due to the leakage of testbeam muons during fast-spill that occurred only during antineutrino running[†].

4.4 Background Subtraction

Two backgrounds are directly removed from the data sample. Cosmic ray events are subtracted from the short event sample. Beam muon events are identified and removed from the long event sample. The following two sections describe these background subtractions in greater detail.

4.4.1 Cosmic Ray Subtraction

A significant background to the $\sin^2\theta_W$ analysis sample, especially at low hadronic energies, are cosmic ray events. Cosmic rays are soft showering particles that enter the detector nearly vertically and therefore leave short tracks in the calorimeter. Figure 4.8 shows a typical cosmic ray event in the NuTeV detector. Approximately 94% of cosmic ray events qualify as short events.

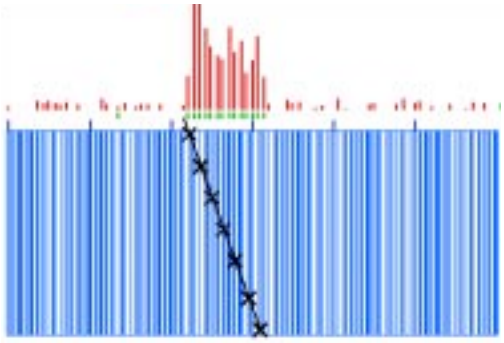

Figure 4.8: A sample cosmic ray event passing $\sin^2\theta_W$ analysis cuts.

[†] From an analysis of decay channel events, testbeam muon leakage was identified during runs 5961–5966 and runs 6154, 6159–6167. All of the events appeared during the fast gate and none fired the upstream veto.

These events are not identified during the neutrino gate, but during a separate beam–off gate during each accelerator cycle. Cosmic rays are then subtracted from the data sample, weighted by the relative ratio of neutrino to beam–off livetimes. For the specific set of runs used in this analysis, this ratio is 0.404 for ν running and 0.405 for $\overline{\nu}$ running. After all cuts, approximately 0.9% (4.7%) of short events in the ν ($\overline{\nu}$) data correspond to cosmic ray events. Figure 4.9 shows the cosmic ray fraction as a function of E_{had}. Extremely high energy cosmic ray events typically result from real cosmic air showers that illuminate most of the detector.

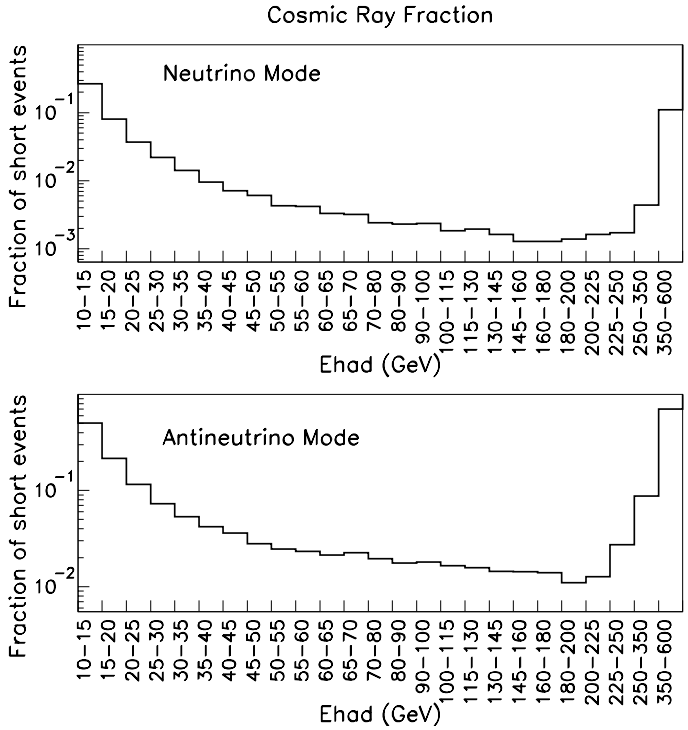

Figure 4.9: Fraction of short events that are cosmic rays for both ν (top) and $\overline{\nu}$ (bottom) events as a function of E_{had}.

4.4.2 Beam Muon Subtraction

Showering beam muons also influence the analysis. Muons produced upstream in CC neutrino interactions in the berm ($\nu N \rightarrow \mu X$) can evade the upstream veto and shower in the calorimeter. Such events can fake real neutrino interactions by potentially signaling a false event vertex. Figure 4.10 shows a so–called deep muon event in which PLACE was identified at the start of the catastrophic energy loss. Identification of these events is important because approximately 98% of deep muon events classify as long events.

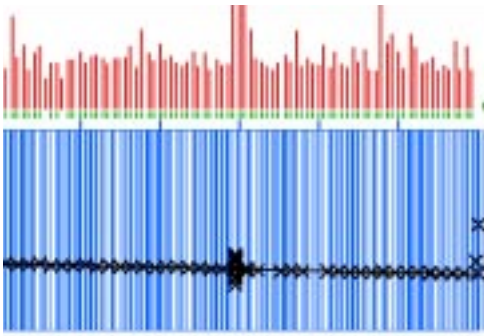

Figure 4.10: A sample beam muon background event passing $\sin^2\theta_W$ analysis cuts.

Beam muons are identified by searching upstream of the interaction vertex for an "upstream exit". The upstream exit is located in the same way as the downstream EXIT except the calorimeter is searched in the other direction (Section 4.1). If the distance between this upstream exit and PLACE is greater than the larger of eight counters or the shower length, L_{var}, then the event is a beam muon candidate. In locating prospective beam muon events, an additional requirement ensures adequate room to search upstream of the registered interaction vertex; hence, beam muon events are identified only in the region $23 \leq$ PLACE ≤ 60. The events are then scaled to the full longitudinal fiducial volume and subtracted from the data in each

length and square bin (Figure 4.5) of the analysis. After all cuts, approximately 0.2% (0.3%) of long events in the neutrino (antineutrino) data are identified as beam muons. Figure 4.11 shows the fraction of beam muon background as a function of shower energy.

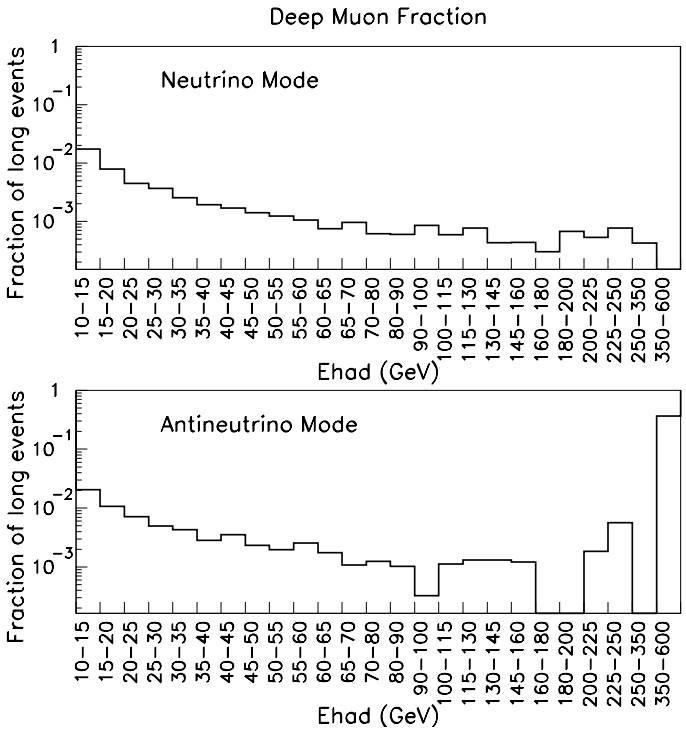

Figure 4.11: Fraction of long events that are deep muon events for both neutrino (top) and antineutrino (bottom) events as a function of E_{had}.

4.5 Data Corrections

Inefficiencies exist in both the longitudinal and transverse vertex finding algorithms. Adding in the measured number of events in which the algorithms failed accounts for events missing from the data that would naturally be included in the Monte Carlo simulation. The following two sections describe these efficiency corrections.

4.5.1 PLACE Efficiency

The data are corrected to account for inefficiencies in the longitudinal vertex finding algorithm. Figure 4.12 shows the efficiency of the PLACE algorithm as a function of hadronic energy. For neutrino events satisfying the $\sin^2\theta_W$ analysis transverse vertex cuts, the PLACE algorithm efficiency is 96% at 10 GeV, 99.5% at 15 GeV, and 99.9% at 20 GeV. Hence, this is predominantly an effect at very low energies.

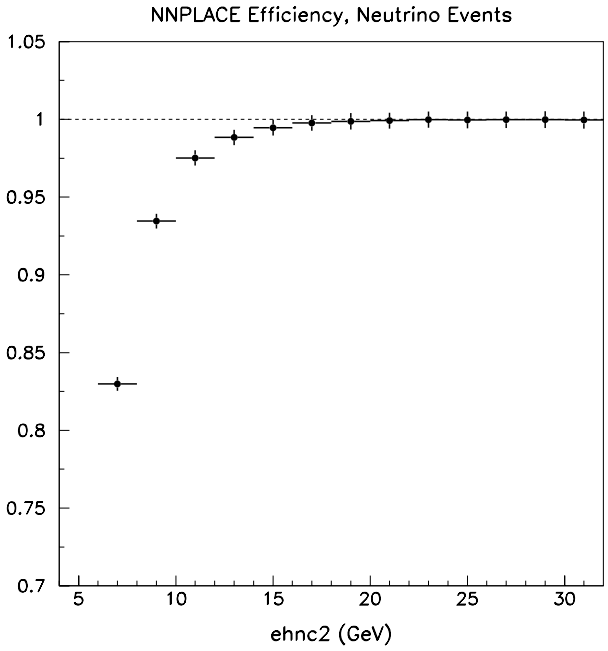

Figure 4.12: Efficiency of the longitudinal vertex finding algorithm as a function of hadron energy (variable `ehnc2`).

Sbit quantities are used to retrieve information regarding the location and length of events that fail the PLACE algorithm. These events are then added back into the sample in each length and square fiducial bin (Figure 4.5). The efficiency correction amounts to 0.006% (0.042%) of short events in neutrino (antineutrino) running. Figure 4.13 shows the size of the correction as a function of shower energy.

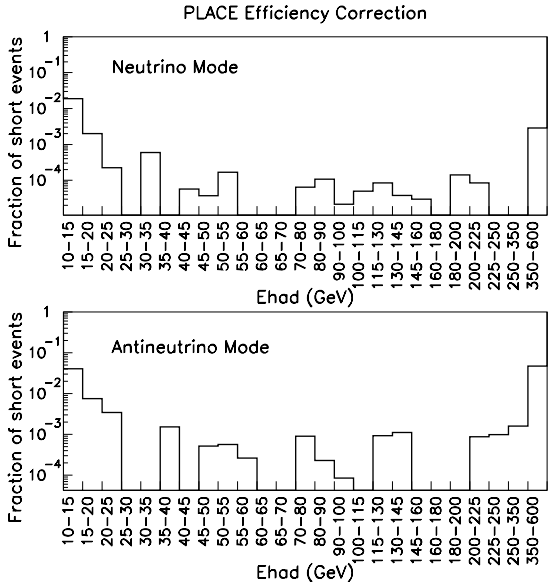

Figure 4.13: PLACE efficiency correction for short events as a function of E_{had}.

4.5.2 Transverse Vertex Efficiency

Similarly, the data are also corrected for failures in the transverse vertex finding algorithm. Such failures occur mainly in very low energy events. Figure 4.14, however, shows an example of a high energy transverse vertex failure. In this event, hit information is missing from the first three drift chambers downstream of the interaction and hence the transverse vertex could not be identified.

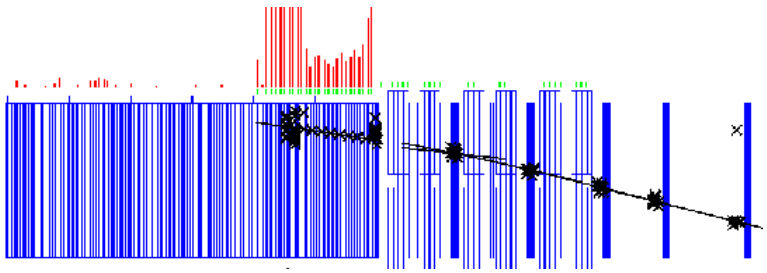

Figure 4.14: An event with no transverse event vertex. Note there is signal in the scintillation counters but no corresponding hits in the first three drift chambers.

Such events are retrieved using a PMT-based vertex algorithm and added back into the sample in length and square bins (Figure 4.5). The transverse vertex efficiency correction amounts to a 0.44% (0.26%) addition to the number of short (long) events in neutrino mode and 0.58% (0.37%) of short (long) events in antineutrino mode. Figure 4.15 displays the size of the transverse vertex efficiency correction as a function of energy.

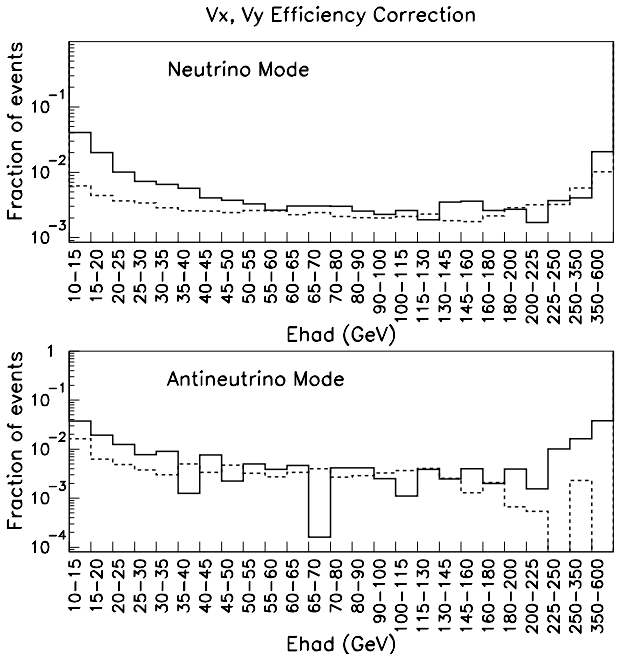

Figure 4.15: Transverse vertex efficiency correction for both short (solid) and long (dotted) events in as a function of E_{had}.

4.6 The Final Data Sample

Table 4.3 tallies the number of events that are either subtracted or added to the short and long event samples in the data for each of the corrections described in this chapter. The corrections are applied to the data in the order presented in the table.

Data Correction	ν Short	ν Long	$\overline{\nu}$ Short	$\overline{\nu}$ Long
Initial # of data events	459079	1165840	105605	250172
CR subtraction	-4238	-242	-4995	-311
deep muon subtraction	-62	-2005	-16	-846
PLACE efficiency correction	+29	+44	+42	-39
Vx, Vy efficiency correction	+2030	+3004	+586	+935

Table 4.3: Adjustments to the number of short and long events in the data.

After all subtractions and corrections, the final neutrino data sample includes 456,838 short events and 1,166,441 long events. The final antineutrino data sample consists of 101,222 short events and 249,911 long events. From the measured number of short and long events, the experimental ratios in each mode are:

$$R^{\nu}_{\rm exp} = 0.3916 \pm 0.0007\,({\rm stat}) \tag{4.14}$$

$$R^{\overline{\nu}}_{\rm exp} = 0.4050 \pm 0.0016\,({\rm stat}) \tag{4.15}$$

Note that the **measured** ratios are referred to as $R^{\nu,\overline{\nu}}_{\rm exp}$. The connection between the experimentally measured ratios of short to long events, $R^{\nu}_{\rm exp}$ and $R^{\overline{\nu}}_{\rm exp}$, and the **theoretical** predictions for the ratio of NC to CC events, R^{ν} and $\mathrm{R}^{\overline{\nu}}$, is obtained by building a detailed Monte Carlo simulation of the experiment. Using this relation as determined from the Monte Carlo, electroweak parameters, such as $\sin^2\theta_W$, can then be extracted from $R^{\nu}_{\rm exp}$ and $R^{\overline{\nu}}_{\rm exp}$. The following chapter describes the components of the Monte Carlo simulation used in the analysis.

Chapter 5

The Monte Carlo Simulation

A standard model value of $\sin^2\theta_W$ can be directly extracted from the measured short/long ratios, $R^{\nu}_{\rm exp}$ and $R^{\overline{\nu}}_{\rm exp}$, using a detailed Monte Carlo simulation of the experiment. The Monte Carlo is designed to fully simulate neutrino interactions in the NuTeV detector. It generates samples of neutrino and antineutrino events with event length, vertex, and energy distributions which match those in the data sample as closely as possible. To accomplish this, the Monte Carlo model includes three main components:

- the neutrino cross section (p. 85)
- the incoming neutrino fluxes: ν_μ, $\overline{\nu}_\mu$, ν_e, and $\overline{\nu}_e$ (p. 158)
- a detailed description of the NuTeV detector response (p. 174)

Monte Carlo events are treated in exactly the same way as the data and are subject to the same cuts as the data. However, the Monte Carlo does not attempt to simulate background events, such as cosmic rays or beam muons, which are removed from the data sample (Section 4.4), nor does it simulate inefficiencies in the vertex finding algorithms which are instead corrected for in the data (Section 4.5).

5.1 Cross Section Model

An enhanced leading order (LO) cross section model generates neutrino and antineutrino interactions, both NC and CC. The following sections describe the various components of the cross section model. Unless otherwise indicated, all of the formulae presented here are neutrino–proton cross sections. By invoking isospin symmetry, the neutrino–neutron cross sections result from simple exchange of the u and d quark assignments. The propagator factors (Section 5.1.9) do not appear in these cross section expressions; however, the forms are properly normalized (Appendix E). The total quark momentum densities, $xq(x)$, appearing in many of the expressions denote the sum of the valence and sea densities: $xq(x) = xq_v(x) + x\overline{q}(x)$.

Deep Inelastic Scattering at Tree Level

The standard neutrino cross section varies via three structure functions: xF_1, F_2, and xF_3. As such, the basic tree (Born)–level cross section, as derived in Chapter 1, is given by:

$$\frac{d^2\sigma^{\nu,\overline{\nu}}}{dx\,dy} = \frac{G_F^2 ME}{\pi} \left[\begin{array}{c} \frac{y^2}{2} 2xF_1(x,Q^2) + \left(1 - y - \frac{Mxy}{2E}\right) F_2(x,Q^2) \\ \pm y\left(1 - \frac{y}{2}\right) xF_3(x,Q^2) \end{array} \right] \tag{5.1}$$

where the + (–) sign in the last term refers to the neutrino (antineutrino) scattering cross section and G_F is the Fermi constant. The multiplicative propagator factor, $1/(1 + Q^2/M_{W,Z}^2)^2$, has been neglected in the above expression for simplicity. The dimensionless variables, Bjorken x and inelasticity y, are defined in Chapter 1. Figures 5.1 and 5.2 display the event kinematics for Monte Carlo events passing analysis cuts. The mean Q^2 is 25.6 GeV^2 for ν events and 15.4 GeV^2 for $\overline{\nu}$ events.

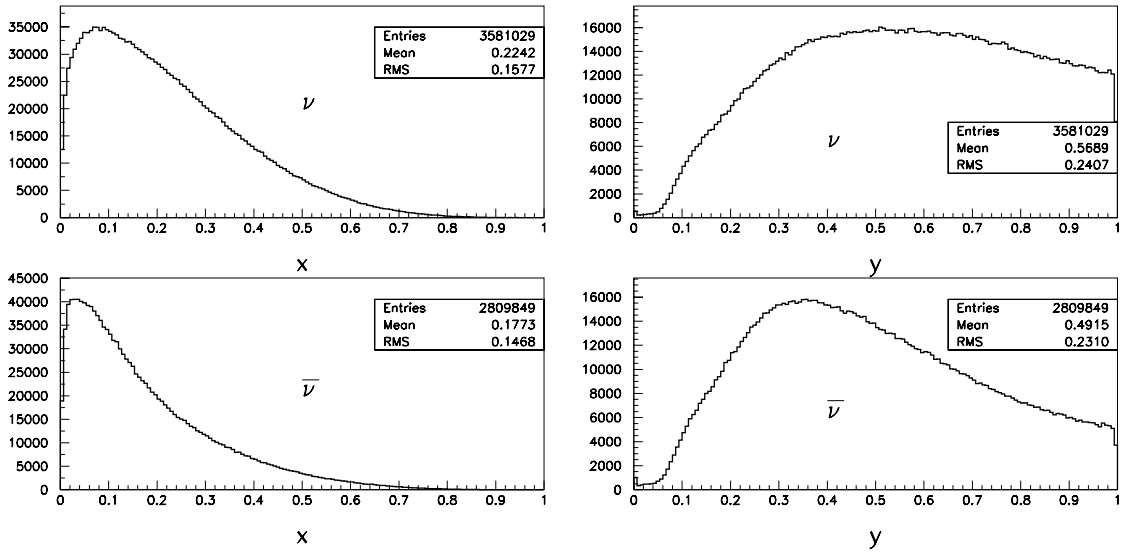

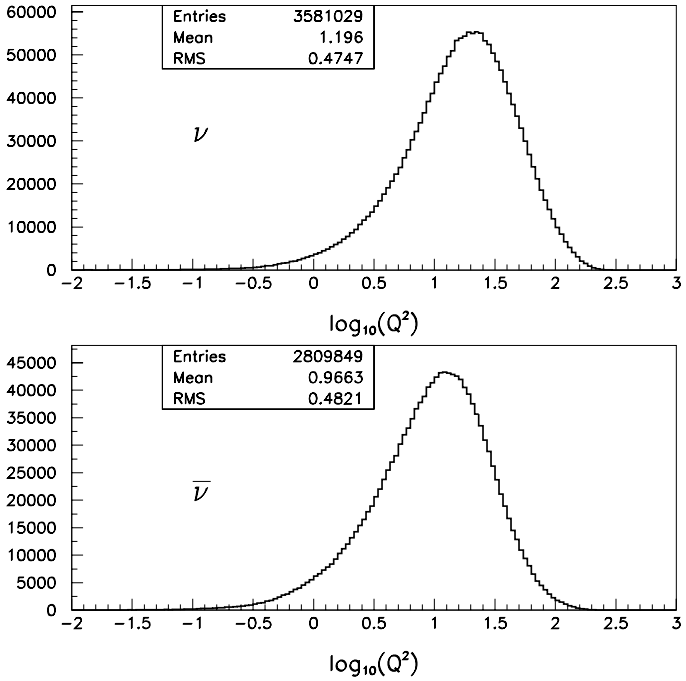

Table 5.1: Distributions of x, y, and Q^2 for a representative sample of the final Monte Carlo containing 3.6×10^6 ν and 2.8×10^6 $\overline{\nu}$ events.

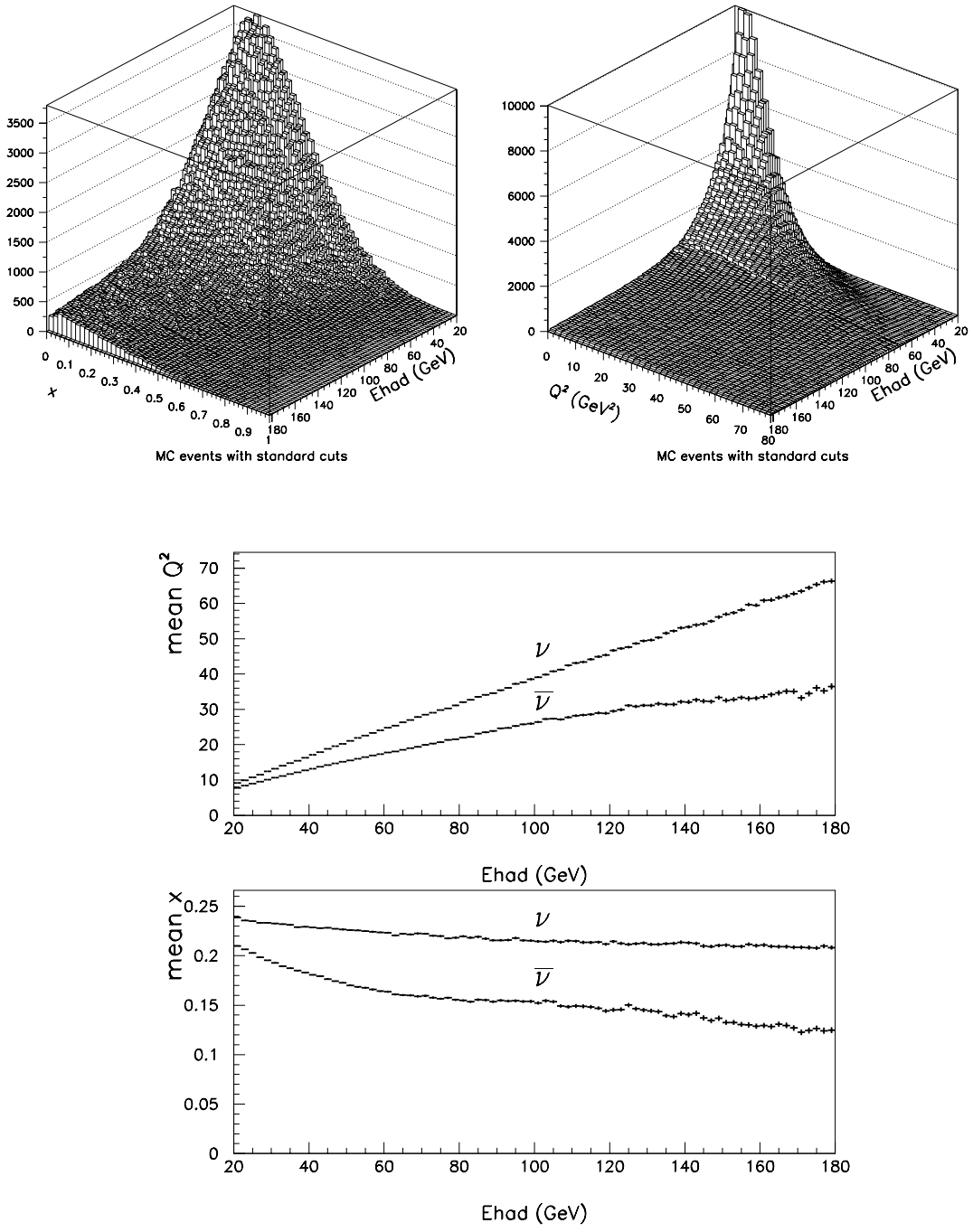

Table 5.2: The x (top left) and Q^2 (top right) distributions as a function of E_{had} for a representative sample of MC neutrino events. The bottom plot displays $< x >$ and $< Q^2 >$ as a function of E_{had} for both ν and $\overline{\nu}$ MC events passing cuts.

Assuming the Callan–Gross relation, scattering off only u and d quarks, and replacing F_2 and xF_3 with Equations (1.25), (1.37), and (1.38), the base quark parton model cross sections for CC scattering become:

$$\frac{d^2\sigma^{\nu p}_{CC}}{dx\,dy} = \frac{2\,G_F^2 ME}{\pi}\left[|V_{ud}|^2\,xd(x) + (1-y^2)\left(|V_{us}|^2 + |V_{ud}|^2\right)x\overline{u}(x)\right] \quad (5.2)$$

$$\frac{d^2\sigma^{\overline{\nu} p}_{CC}}{dx\,dy} = \frac{2\,G_F^2 ME}{\pi}\left[|V_{ud}|^2\,x\overline{d}(x) + (1-y^2)\left(|V_{us}|^2 + |V_{ud}|^2\right)xu(x)\right] \quad (5.3)$$

In the these expressions, target mass terms have been neglected, M $\rightarrow$ 0, and $|V_{ij}|^2$ are the Cabibbo-Kobayashi-Maskawa (CKM) matrix elements [29] denoting the strength of the charged current coupling to each quark species. The unitary CKM matrix describes three generation quark mixing. The two generation sub–matrix:

$$\begin{pmatrix} d' \\ s' \end{pmatrix} = \begin{pmatrix} V_{ud} & V_{us} \\ V_{cd} & V_{cs} \end{pmatrix} \begin{pmatrix} d \\ s \end{pmatrix} \quad (5.4)$$

transforms the weak eigenstates (primed states) into mixtures of the mass eigenstates (unprimed states). These matrix elements can be parametrized in terms of a single mixing angle, the Cabibbo angle, θ_C, such that:

$$\begin{pmatrix} V_{ud} & V_{us} \\ V_{cd} & V_{cs} \end{pmatrix} = \begin{pmatrix} \cos\theta_C & \sin\theta_C \\ -\sin\theta_C & \cos\theta_C \end{pmatrix} = \begin{pmatrix} 0.9754 & 0.2205 \\ -0.2205 & 0.9754 \end{pmatrix} \quad (5.5)$$

The exact values for the quark mixing used in the $\sin^2\theta_W$ analysis appear on the right hand side of Equation (5.5). These factors govern the strength of the flavor-changing transitions and multiply the parton densities in all of the CC scattering

expressions.

Unlike the CC case, the base NC cross section is complicated by the fact that neutrinos can scatter off both left and right handed particles (Chapter 1); therefore, the NC cross sections include additional coupling factors, q_L^2 and q_R^2:

$$\frac{d^2\sigma_{NC}^{\nu p}}{dx\,dy} = \frac{2\,G_F^2 ME}{\pi}\left[\begin{array}{l}\left[u_L^2+u_R^2(1-y^2)\right]\,xu(x)+\left[u_L^2\,(1-y^2)+u_R^2\right]\,x\overline{u}(x)+\\ \left[d_L^2+d_R^2(1-y^2)\right]\,xd(x)+\left[d_L^2\,(1-y^2)+d_R^2\right]\,x\overline{d}(x)\end{array}\right]$$

$$\frac{d^2\sigma_{NC}^{\overline{\nu}p}}{dx\,dy} = \frac{2\,G_F^2 ME}{\pi}\left[\begin{array}{l}\left[u_L^2+u_R^2(1-y^2)\right]\,x\overline{u}(x)+\left[u_L^2\,(1-y^2)+u_R^2\right]\,xu(x)+\\ \left[d_L^2+d_R^2(1-y^2)\right]\,x\overline{d}(x)+\left[d_L^2\,(1-y^2)+d_R^2\right]\,xd(x)\end{array}\right]$$

$$u_L^2 = \frac{1}{4}-\frac{2}{3}\sin^2\theta_W+\frac{4}{9}\sin^4\theta_W \tag{5.6}$$

$$u_R^2 = \frac{4}{9}\sin^4\theta_W \tag{5.7}$$

$$d_L^2 = \frac{1}{4}-\frac{1}{3}\sin^2\theta_W+\frac{1}{9}\sin^4\theta_W \tag{5.8}$$

$$d_R^2 = \frac{1}{9}\sin^4\theta_W \tag{5.9}$$

Note the cross section expressions for both NC and CC scattering assume $xu(x) \equiv xu_v(x)+x\overline{u}(x)$ and $xd(x) \equiv xd_v(x)+x\overline{d}(x)$.

The preceding introductory equations describe the simplest case of scattering off an isoscalar target composed of light quarks at tree level. The cross section model used in the $\sin^2\theta_W$ analysis is instead a full Monte Carlo simulation which includes radiative effects, non-quark-parton model contributions including the longitudinal structure function and higher twist effects, heavy quark effects, quasi–elastic and electron scattering, the W and Z propagators, the non-isoscalar iron target, and non-zero lepton mass terms. The remaining sections in this chapter describe these components in detail.

5.1.1 Radiative Corrections

The tree level cross sections are significantly modified by radiative effects. Radiative corrections, as computed within the framework of the quark parton model, are supplied by code provided by D. Yu. Bardin [30] and V6.34 of ZFITTER [31]. The radiative corrections consist of higher order purely electromagnetic (QED) and weak contributions.

QED Radiative Corrections

The 1–loop QED corrections correspond to the emission of real or virtual photons by a fermion. Such corrections are finite and calculable. They are applied as an x, y, and E dependent factor, which multiplies the Born level (0–loop) cross section:

$$\frac{d^2\sigma}{dx\,dy} = \left[\left(\frac{d^2\sigma}{dx\,dy}\right)_{1-\text{loop}} / \left(\frac{d^2\sigma}{dx\,dy}\right)_{\text{Born}}\right]_{\text{Bardin}} \cdot \left(\frac{d^2\sigma}{dx\,dy}\right)_{\text{Born}} \tag{5.10}$$

In practice, the QED corrections come from Bardin [30] and are interpolated from a table to minimize Monte Carlo run time. Such corrections include the radiation of real and virtual photons from the charged lepton and quark legs in addition to W–γ box diagrams. Figure 5.3 shows examples of several contributing diagrams. The largest contribution comes from electromagnetic photon radiation from the final state lepton in CC interactions, as displayed in Figure 5.3a, which has no NC counterpart. The experimental effect is an increase in the measured hadron energy for CC events due to the added electromagnetic shower. Note that the effect of this process is larger for ν_e events due to the fact that the electron is lighter than the muon (Figure 5.2). Smaller contributions include vertex and box diagrams (Figures 5.3b-c) and quark

leg radiation (Figure 5.3d), which produce no extra particles in the final state but do modify the overall scale of the total cross sections. Figure 5.1 displays the net size of these corrections to both the muon neutrino and antineutrino Born level CC cross sections; they can be as large as 20% in some kinematic regions. In contrast, the QED corrections for NC processes, as shown in Figure 5.3, are much smaller. Note that the QED corrections to neutrino and antineutrino scattering for $y \neq 0$ are not the same because of the differing $\nu, \overline{\nu}$ helicities.

Several minor* modifications were made to the original Bardin code [30] in the process of preparing the final Monte Carlo predicted cross sections. The adjustments include incorporation of heavy charm†, $m_c \neq 0$, and a change in the choice of initial state quark mass from the CCFR convention [17], $m_i = \mathrm{Q_{min}} = 1$ GeV, to Bardin's recommendation, $m_i = x \cdot m_N$, where m_N is the nucleon mass. Figure 5.4 shows the effect of these changes on the Bardin–predicted QED radiative corrections.

The application of QED corrections results in a large -0.0074 (-0.0109) decrease in the predicted values for R^{ν}_{exp} ($R^{\overline{\nu}}_{\mathrm{exp}}$), resulting in a -0.00795 correction to $\sin^2\theta_W$. The magnitude is due to the dominant effect of increased energy deposit for CC events, and hence an increase in the number of CC events passing the minimum $\mathrm{E_{had}}$ requirement.

* The net effect on $\sin^2\theta_W$ is less than 0.0001.
† The radiative contribution from charm will be suppressed because of its large mass.

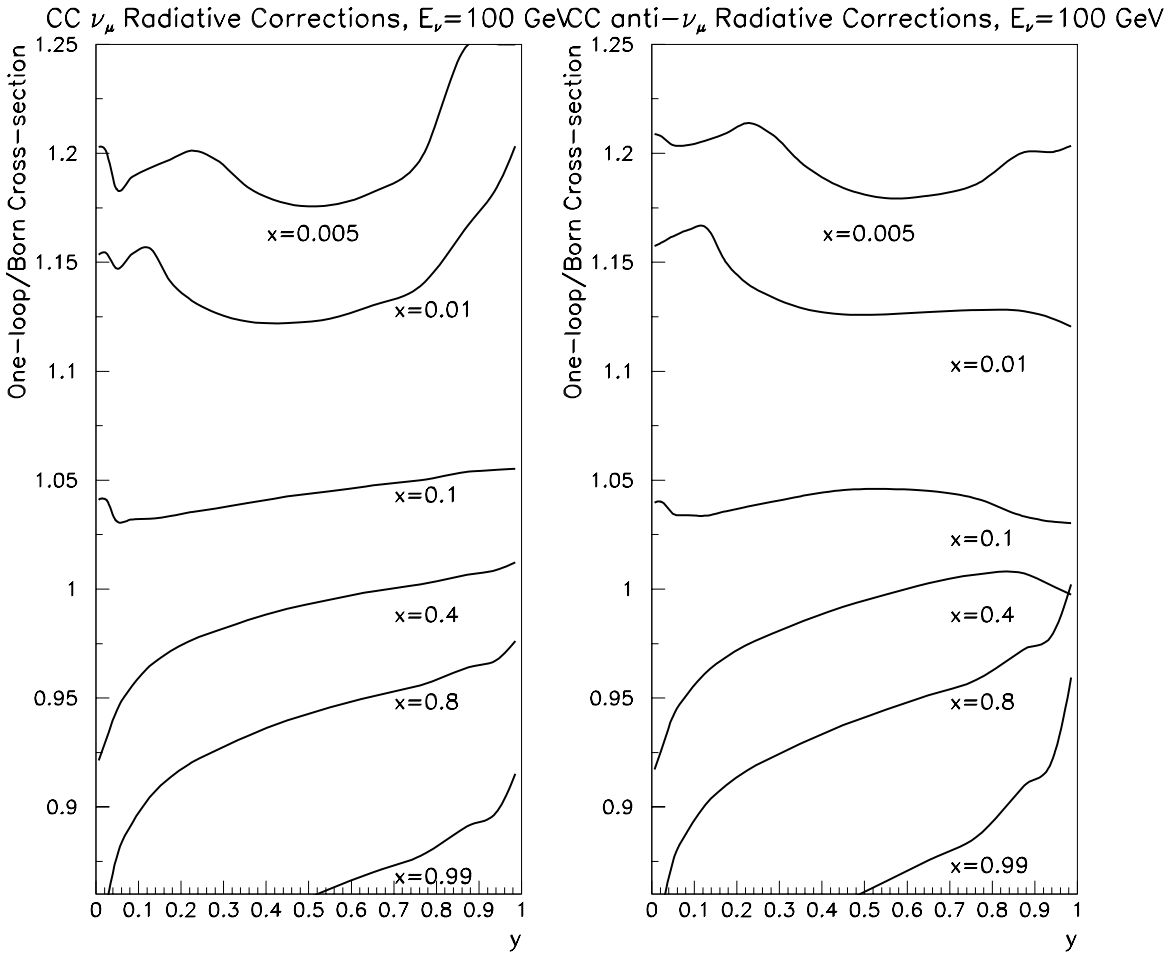

Figure 5.1: Total size of the QED radiative corrections for 100 GeV ν_μ (left) and $\overline{\nu}_\mu$ (right) CC scattering as a function of y.

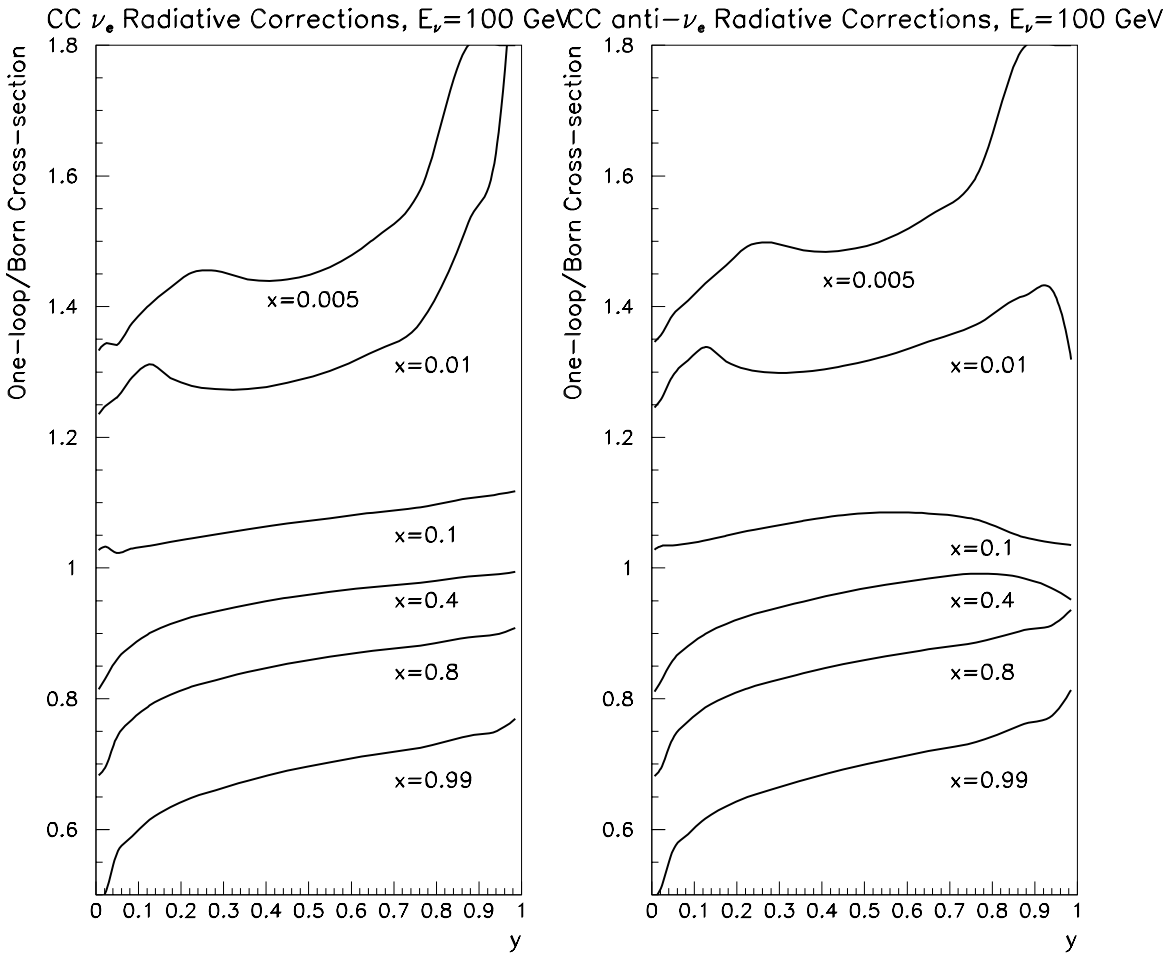

Figure 5.2: Total size of the QED radiative corrections for 100 GeV ν_e (left) and $\overline{\nu}_e$ (right) CC scattering as a function of y. Note the scale is enlarged relative to Figure 5.1.

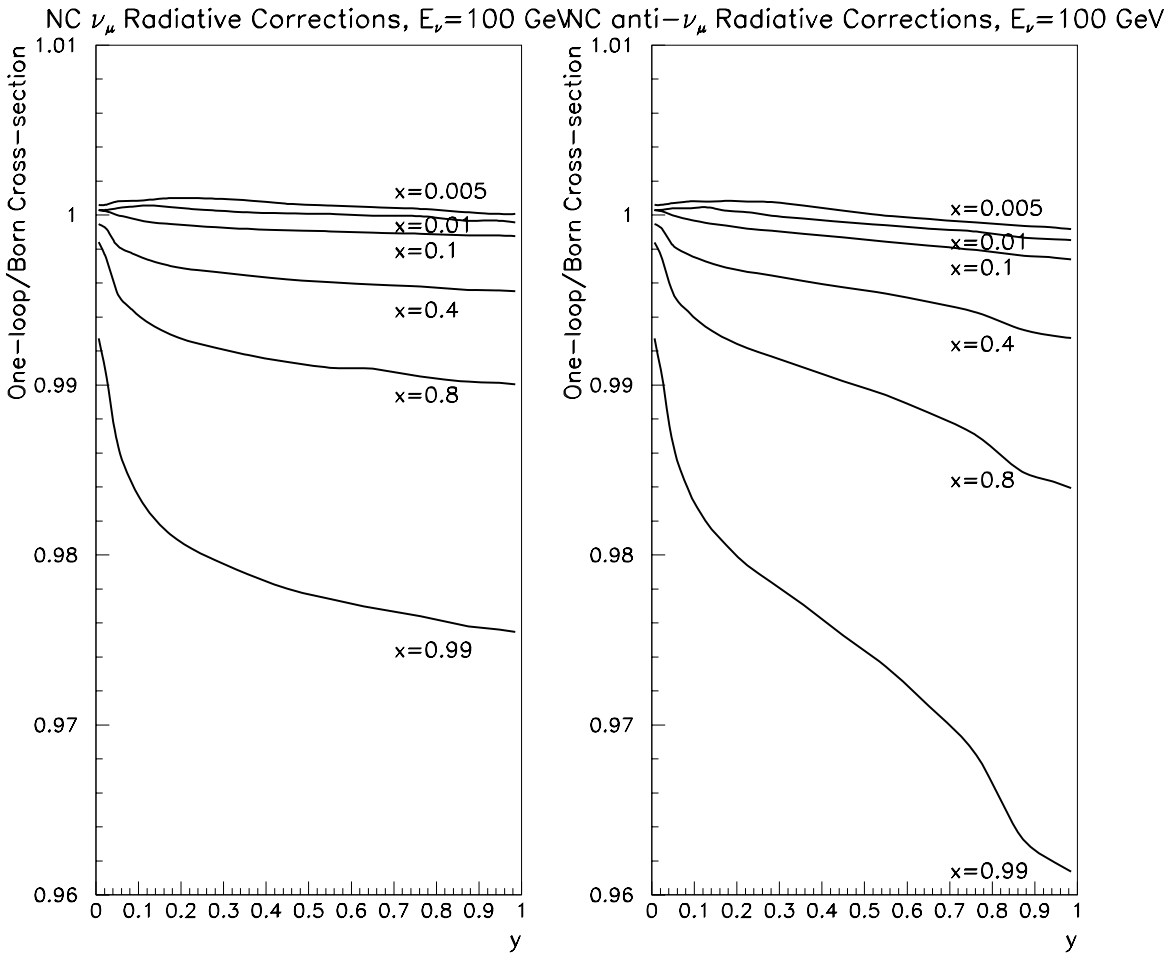

Figure 5.3: Total size of the QED radiative corrections for 100 GeV ν_μ (left) and $\overline{\nu}_\mu$ (right) NC scattering as a function of y. Note the scale is reduced relative to Figure 5.1.

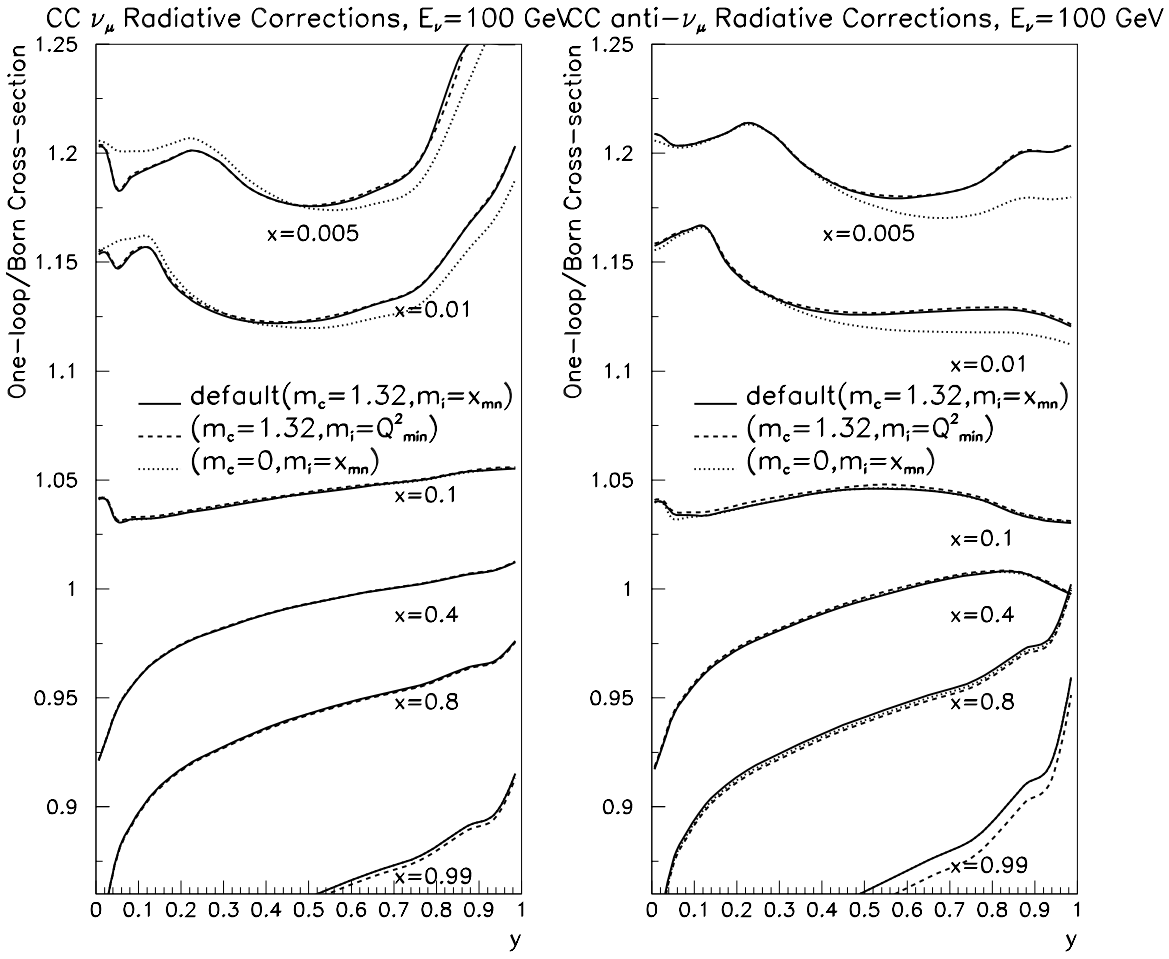

Figure 5.4: The effect of improvements on the Bardin QED radiative corrections. Shown are the corrections for 100 GeV ν_μ (left) and $\overline{\nu}_\mu$ (right) CC scattering as a function of y. The solid curves are the default corrections (m_c = 1.32 GeV, $m_i = x \cdot m_N$), the dashed curves are the corrections with the old convention $m_i = Q_{min}$ = 1 GeV, and the dotted curves are the corrections before the implementation of heavy charm (m_c = 0 GeV).

(a)

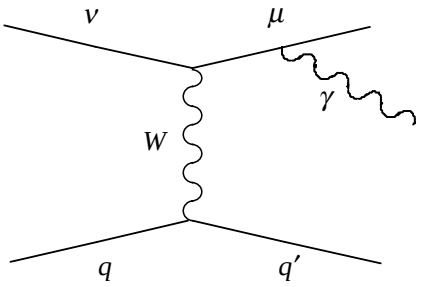

(b)

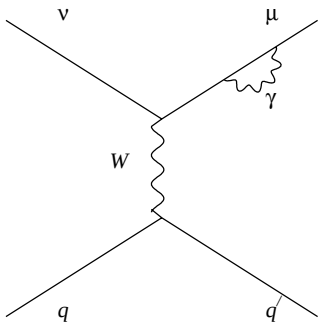

(c)

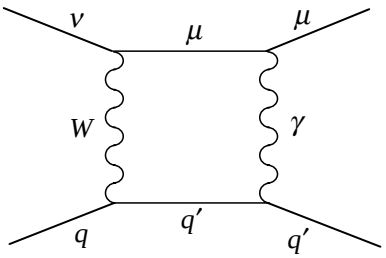

(d)

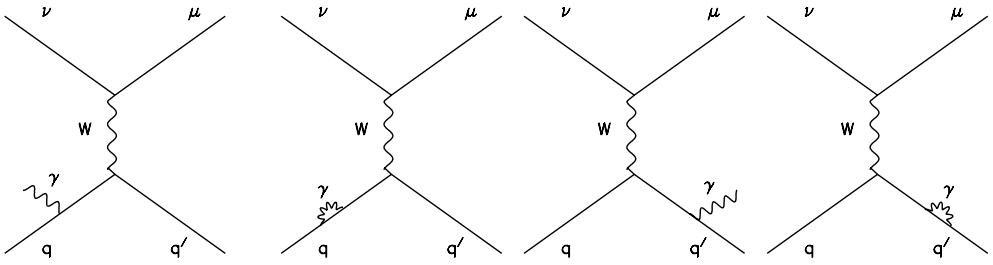

Table 5.3: Examples of CC QED radiative correction diagrams. The NC diagrams only include the initial and final state quark radiation processes depicted in (d).

Weak Radiative Corrections

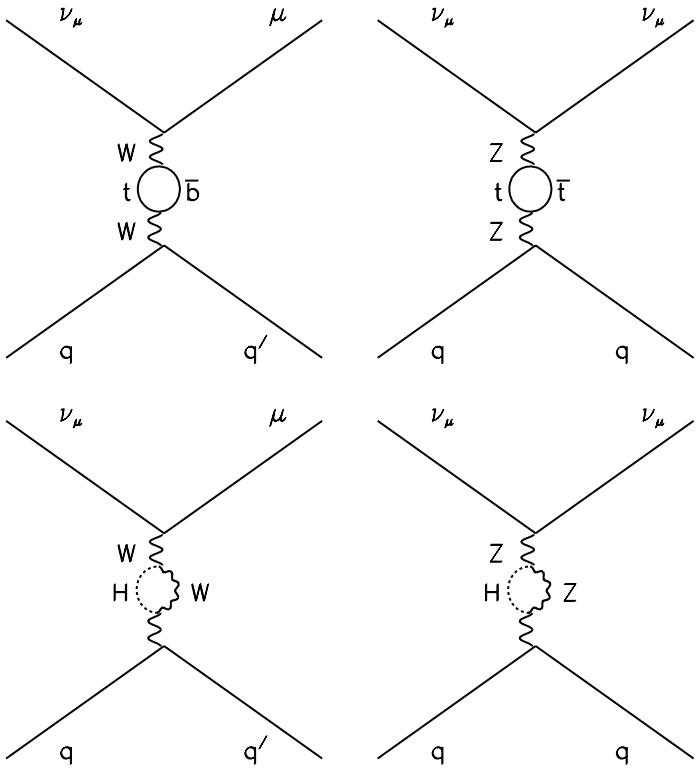

Table 5.4: WEAK radiative corrections that depend on $M_{\rm top}$ and $M_{\rm Higgs}$.

The weak corrections, such as the self-energy diagrams depicted in Figure 5.4, modify the electroweak propagators. The loop corrections are absorbed into effective Q^2 dependent parameters, $\rho_{u,d}(\mathrm{Q}^2)$ and $\kappa_{u,d}(Q^2)$, which modify the neutrino–quark couplings:

$$u_L^{\rm eff} = \rho_u\left(Q^2\right)\left(\frac{1}{2} - \frac{2}{3}\,\kappa_u\left(Q^2\right)\sin^2\theta_W\right) \tag{5.11}$$

$$u_R^{\rm eff} = \rho_u\left(Q^2\right)\left(-\frac{2}{3}\,\kappa_u\left(Q^2\right)\sin^2\theta_W\right) \tag{5.12}$$

$$d_L^{\rm eff} = \rho_d\left(Q^2\right)\left(-\frac{1}{2} + \frac{1}{3}\,\kappa_d\left(Q^2\right)\sin^2\theta_W\right) \tag{5.13}$$

$$d_R^{\rm eff} = \rho_d\left(Q^2\right)\left(\frac{1}{3}\,\kappa_d\left(Q^2\right)\sin^2\theta_W\right) \tag{5.14}$$

The modifications are due to the process dependent substitutions:

$$G_F \rightarrow \rho\,(Q^2) \cdot G_F \tag{5.15}$$

$$\sin^2\theta_W \rightarrow \kappa\,(Q^2) \cdot \sin^2\theta_W \tag{5.16}$$

involving corrective factors, $\rho(\mathrm{Q}^2)$ and $\kappa(\mathrm{Q}^2)$, multiplying the overall scattering amplitude and $\sin^2\theta_W$, respectively. Because the couplings are functions of q^2 (Figure 5.5), the weak corrections are computed and applied on an event by event basis. Note that the ρ and κ factors are calculated using an upgraded electroweak package[‡], ZFITTER v6.34 [31]. Their net effect is to increase R^{ν}_{exp} by +0.00052 and $R^{\overline{\nu}}_{\mathrm{exp}}$ +0.00576, for a net -0.00159 shift in $\sin^2\theta_W$.

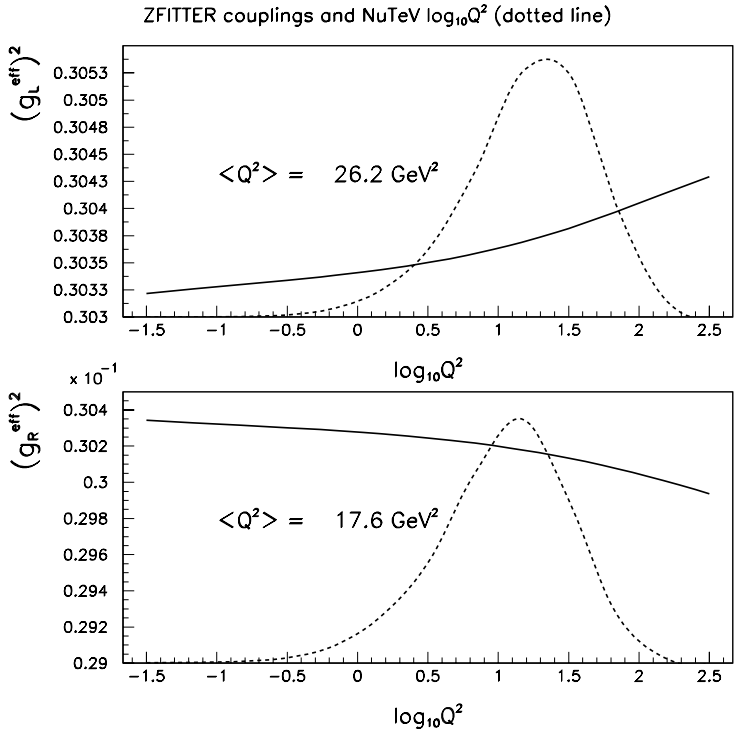

Figure 5.5: Q^2 dependence of $(g^{\mathrm{eff}}_{L,R})^2 = (u^{\mathrm{eff}}_{L,R})^2 + (d^{\mathrm{eff}}_{L,R})^2$ from ZFITTER. The top (bottom) dotted curve displays the Q^2 distributions for ν ($\overline{\nu}$) events in the analysis.

‡ The effect of upgrading from the 1986 Bardin [30] calculation of weak corrections to current ZFITTER [31] is actually quite small: -6×10^{-6}, -0.00016, +0.00005 in R^{ν}_{exp}, $R^{\overline{\nu}}_{\mathrm{exp}}$, $\sin^2\theta_W$.

Both ρ and κ depend on the mass of the top quark, $M_{\rm top}$, and the Higgs boson, $M_{\rm Higgs}$, through diagrams such as those depicted in Figure 5.4. This introduces a $M_{\rm top}$ and $M_{\rm Higgs}$ dependence to the result. The dependence is quadratic in $M_{\rm top}$ and logarithmic in $M_{\rm Higgs}$:

$$\begin{aligned} \delta \sin^2\theta_W^{\rm on-shell} = & - 0.00022 \cdot \left(\frac{{M_{\rm top}}^2 - (175\ {\rm GeV})^2}{(50\ {\rm GeV})^2} \right) \\ & + 0.00032 \cdot \ln\left(\frac{M_{\rm Higgs}}{150\ {\rm GeV}} \right) \end{aligned} \tag{5.17}$$

Because the calculations use the on–shell renormalization scheme (Equation 2.1), the dependence on $M_{\rm top}$ and $M_{\rm Higgs}$ is weak[§]. The shift in $\sin^2\theta_W^{\rm on-shell}$ for $\pm$ 5 GeV variation in $M_{\rm top}$ is $\pm$ 0.00015. Varying $M_{\rm Higgs}$ over its potential mass range from 50 GeV up to 1 TeV results in less than a 0.0010 shift in the measured $\sin^2\theta_W^{\rm on-shell}$. Figure 5.6 shows the standard model prediction for $\sin^2\theta_W^{\rm on-shell}$ plotted as a function of $M_{\rm top}$ and $M_{\rm Higgs}$.

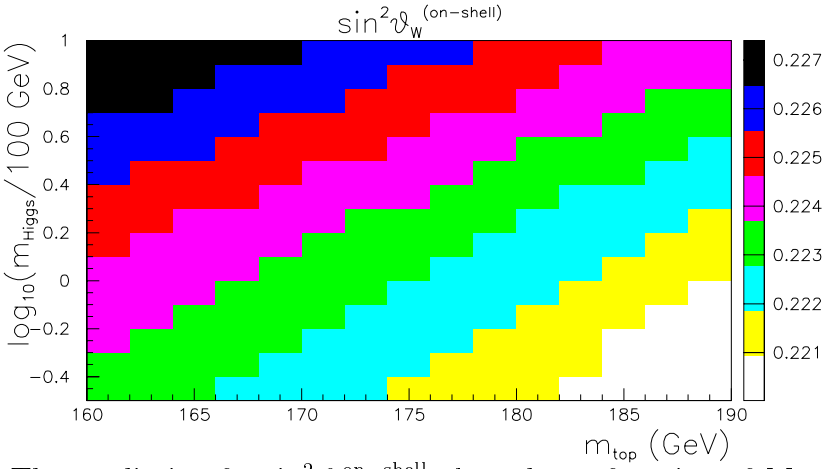

Figure 5.6: The prediction for $\sin^2\theta_W^{\rm on-shell}$ plotted as a function of $M_{\rm top}$ and $M_{\rm Higgs}$.

[§] The $M_{\rm top}$, $M_{\rm Higgs}$ dependence of the final result is actually less than what was reported for the preliminary analysis [26]. This is because the final analysis used less $\overline{\nu}$ data; when parametrized in terms of on-shell $\sin^2\theta_W$, $R^{\overline{\nu}}$ has a much larger dependence on $M_{\rm top}$ and $M_{\rm Higgs}$ than R^{ν}.

5.1.2 Parton Distribution Functions

The cross section model incorporates leading order parton distribution functions (PDFs) which are tightly constrained by charged current data measured using the same target and cross section model as NuTeV. Using the prescription formulated by Buras and Gaemers [33], we fit the measured CCFR differential cross section data [34] and extract the individual quark momentum densities. Unlike CC interactions, NC interactions discriminate between quark flavors, hence, a parameterization of the individual quark flavors is essential: $u(x,Q^2)$, $d(x,Q^2)$, $s(x,Q^2)$, and $c(x,Q^2)$. In this model (known as BGPAR), the quark distributions include five contributions:

- Valence: The valence distributions are characterized by the general form $x^E(1-x)^{E'}$. The model assumes a softer $d_v(x)$ distribution: $d_v \simeq (1-x)\,u_v$.

- Sea: The fit initially assumes that the total number of anti-up and anti-down quarks in the proton is the same, $\overline{u}(x) = \overline{d}(x)$. Modifications to this assumption are discussed at the end of this section.

- Strange Sea: The strange sea is constrained by CCFR/NuTeV dimuon data (Section 5.1.2). The parameterization allows the strange sea to have a different shape from the non-strange sea, but the strange and anti-strange seas have the same momentum distributions, $s(x) = \overline{s}(x)$.

- Charm Sea: In practice the charm sea, $c(x)$, is neglected; however, a charm sea component as indicated from EMC $F_2^{c\overline{c}}$ data is added (Section 5.1.6).

- Gluons: This LO cross section model neglects gluon content, $g(x) = 0$. Gluons enter only indirectly as missing quarks: $\int xq(x) + x\overline{q}(x)dx \neq 1$.

Exploiting the following symmetries further reduces the number of free parameters in the differential cross section fit:

- Isospin: $u^p(x) = d^n(x) \equiv u(x), \quad \overline{u}^p(x) = \overline{d}^n(x) \equiv \overline{u}(x)$
  $d^p(x) = u^n(x) \equiv d(x), \quad \overline{d}^p(x) = \overline{u}^n(x) \equiv \overline{d}(x)$
  $s^p(x) = s^n(x) \equiv s(x), \quad \overline{s}^p(x) = \overline{s}^n(x) \equiv \overline{s}(x)$
  $c^p(x) = c^n(x) \equiv c(x), \quad \overline{c}^p(x) = \overline{c}^n(x) \equiv \overline{c}(x)$
- Light Quark Sea: $\overline{u}(x) = \overline{d}(x)$
- Strange Sea: $s(x) = \overline{s}(x)$
- Charm Sea: $c(x) = \overline{c}(x)$

The BGPAR model describes the behavior of these parton densities as a function of x and their evolution in Q^2 as follows:

$$
\begin{aligned}
x\,u_v(x,Q^2) &= u_v^{\mathrm{tot}} \cdot \left[x^{E_1}(1-x)^{E_2} + AV_2\,x^{E_3}(1-x)^{E_4} + AV_3\,x^{E_5}(1-x)^{E_6}\right] \\
x\,d_v(x,Q^2) &= d_v^{\mathrm{tot}} \cdot x\,u_v(x,Q^2) \cdot (1-x) \\
x\,\overline{u}(x,Q^2) = x\,\overline{d}(x,Q^2) &= \frac{1}{2\,(\kappa+2)}\,xS(x,Q^2) \\
&= \frac{1}{2\,(\kappa+2)}\,\left[AS(1-x)^{ES} + AS_2(1-x)^{ES_2}\right] \\
x\,s(x,Q^2) = x\,\overline{s}(x,Q^2) &= \frac{\kappa}{2\,(\kappa+2)}\,xSS(x,Q^2) \\
&= \frac{\kappa}{2\,(\kappa+2)}\,\frac{AS}{ES+1}(ES+\alpha+1)(1-x)^{ES+\alpha}
\end{aligned}
$$

The remaining sections describe the above components in greater detail.

Valence Quark Distributions

$$\begin{aligned} x\,u_v(x,Q^2) &= u_v^{\rm tot}\cdot\left[x^{E_1}(1-x)^{E_2}+AV_2\,x^{E_3}(1-x)^{E_4}+AV_3\,x^{E_5}(1-x)^{E_6}\right] \\ x\,d_v(x,Q^2) &= d_v^{\rm tot}\cdot x\,u_v(x,Q^2)\cdot(1-x) \end{aligned} \tag{5.18}$$

As can be seen from the above expressions, the BGPAR model assumes $d_v \simeq u_v(1-x)$. Furthermore, because the valence distributions do not vanish as rapidly in x as the sea distributions, they are more sensitive to higher moments and require the inclusion of additional $x^E(1-x)^{E'}$ terms. A variant of the Gross–Llewellyn–Smith (GLS) sum rule [35] determines the normalization of the valence densities:

$$\int_0^1 x\,F_3(x)\,\frac{dx}{x} = \int_0^1 (x\,u_v(x,Q^2)+x\,d_v(x,Q^2))\,\frac{dx}{x} = 3\left(1-\frac{\alpha_s(Q^2)}{\pi}\right) \tag{5.19}$$

such that:

$$u_v^{\rm tot} = \frac{2}{3}\cdot\frac{3\,(1-A_1/T-A_2/T^2)}{\beta(E_1,E_2+1)+AV_2\,\beta(E_3,E_4+1)+AV_3\,\beta(E_5,E_6+1)} \tag{5.20}$$

$$d_v^{\rm tot} = \frac{1}{3}\cdot\frac{3\,(1-A_1/T-A_2/T^2)}{\beta(E_1,E_2+2)+AV_2\,\beta(E_3,E_4+2)+AV_3\,\beta(E_5,E_6+2)} \tag{5.21}$$

The relative normalization between u_v and d_v results from the fact that the proton contains two up valence quarks and one down valence quark:

$$\int_0^1 x\,u_v(x,Q^2)\,\frac{dx}{x} = 2\int_0^1 x\,d_v(x,Q^2)\,\frac{dx}{x} = 2\,(1-A_1/T-A_2/T^2) \tag{5.22}$$

Hence, in analogy to Equation 5.19, the total number of valence quarks is:

$$\int_0^1 (x\,u_v(x,Q^2)+x\,d_v(x,Q^2))\,\frac{dx}{x} = 3\,(1-A_1/T-A_2/T^2) \implies \text{baryon number}$$

In addition, the following charge constraint is also satisfied:

$$\frac{2}{3}\int_0^1 x\,u_v(x,Q^2)\,\frac{dx}{x} - \frac{1}{3}\int_0^1 x\,d_v(x,Q^2)\,\frac{dx}{x} = (1 - A_1/T - A_2/T^2) \implies \text{charge}$$

Here, A_1, A_2, AV_2, and AV_3 are fit parameters. Also recall that Euler's β function in these expressions is simply:

$$\beta(m,n) = \frac{\Gamma(m)\Gamma(n)}{\Gamma(m+n)} = \frac{(m-1)!\,(n-1)!}{(m+n-1)!} = \int_0^1 x^{m-1}(1-x)^{n-1}\,dx \qquad (5.23)$$

such that, for example, $\beta(E_1, E_2+2) = \beta(E_1, E_2+1)\cdot(1+E_2)/(1+E_1+E_2)$. The Q^2 dependence of the valence distributions is much simpler than that for the sea and is contained in the analytic expressions:

$$\begin{aligned} E_1 &= E_{10} + E_{11}\cdot s \\ E_2 &= E_{20} + E_{21}\cdot s \\ E_3 &= E_{30} + E_{11}\cdot s \\ E_4 &= E_{40} + E_{21}\cdot s \\ E_5 &= E_{50} + E_{11}\cdot s \\ E_6 &= E_{60} + E_{21}\cdot s \end{aligned} \qquad (5.24)$$

where

$$s = \ln\left[\frac{\ln(Q^2/A_0^2)}{\ln(Q_0^2/A_0^2)}\right] \qquad (5.25)$$

Note that $s = 0$ at the starting momentum Q_0^2. As can be seen from the above expressions, E_3 and E_5 vary with Q^2 in the same way as E_1, while E_4 and E_6 vary with Q^2 in the same way as E_2. The strength of the scaling violations, A_0, the initial values, E_{i0}, and slopes, E_{i1}, are determined from the fit.

Light Sea Quark Distributions

$$x\,\overline{u}(x,Q^2) = x\,\overline{d}(x,Q^2) = \frac{1}{2\,(\kappa+2)}\,xS(x,Q^2) \tag{5.26}$$
$$= \frac{1}{2\,(\kappa+2)}\,\left[AS(1-x)^{ES} + AS_2(1-x)^{ES_2}\right]$$

Because the sea distributions decrease rapidly with x, they can be determined from their first two moments, SQ_2 and SQ_3, where in general:

$$SQ_n = \int_0^1 x^{n-2}\,xS(x,Q^2)\,dx \tag{5.27}$$

In the context of a 4–flavor SU(3) gauge theory, SQ_2 and SQ_3 are represented by the functions:

$$SQ_2 = \frac{3}{4}D_{22} + \frac{1}{4}D_{12} \tag{5.28}$$
$$SQ_3 = \frac{3}{4}D_{23} + \frac{1}{4}D_{13} \tag{5.29}$$

where:

$$D_{12} = S_2\,e^{-0.427\cdot s} \tag{5.30}$$
$$D_{13} = S_3\,e^{-0.667\cdot s} \tag{5.31}$$
$$D_{22} = \left[(1-0.429)\,(S_2+V_{82}) - 0.429\cdot G_2\right]e^{-0.747\cdot s} \tag{5.32}$$
$$+\left[0.429\,(S_2+V_{82}) + 0.429\cdot G_2\right] - V_{82}\,e^{-0.427\cdot s} \tag{5.33}$$
$$D_{23} = \left[(1-0.925)\,(S_3+V_{83}) - 0.288\cdot G_3\right]e^{-1.386\cdot s} \tag{5.34}$$
$$+\left[0.925\,(S_3+V_{83}) + 0.288\cdot G_3\right]e^{-0.609\cdot s} - V_{83}\,e^{-0.667\cdot s} \tag{5.35}$$

The numerical values in these expressions are fully specified by leading order QCD (Table 1 in the original Buras-Gaemers paper [33]). The sea normalization constants, V_{82} and V_{83}, come from the valence distribution moments evaluated at the initial momentum, Q_0^2:

$$
\begin{aligned}
V_{82} &= u_v^{\rm tot}\cdot[\beta(E_1+1,E_2+1)+AV_2\,\beta(E_3+1,E_4+1)+AV_3\,\beta(E_5+1,E_6+1)]+ \\
&\quad d_v^{\rm tot}\cdot[\beta(E_1+1,E_2+2)+AV_2\,\beta(E_3+1,E_4+2)+AV_3\,\beta(E_5+1,E_6+2)] \\
V_{83} &= u_v^{\rm tot}\cdot[\beta(E_1+2,E_2+1)+AV_2\,\beta(E_3+2,E_4+1)+AV_3\,\beta(E_5+2,E_6+1)]+ \\
&\quad d_v^{\rm tot}\cdot[\beta(E_1+2,E_2+2)+AV_2\,\beta(E_3+2,E_4+2)+AV_3\,\beta(E_5+2,E_6+2)]
\end{aligned}
$$

The parton distributions evolve from a starting value of $\mathrm{Q}_0^2 = 12.6$ GeV^2, which was the mean Q^2 of the previous Fermilab neutrino experiments E616/E701. The evolution is coupled to that of the gluon via the third moment of the gluon density, G_3, which is a parameter in the fit. The second gluon moment, $G_2 = \int x\,g(x,Q^2)\,dx$, constrains the momentum sum rule:

$$
G_2 + \int_0^1 \frac{1+R_L(x,Q^2)}{1+4M^2x^2/Q^2}\,\left[x\,u_v(x,Q^2)+x\,d_v(x,Q^2)+xS(x,Q^2)\right]\,dx = 1 \quad (5.36)
$$

The remaining parameters, AS_2 and ES_2, vary linearly with $\ln(\mathrm{Q}^2)$:

$$
AS_2 = AS_{20} + AS_{21}\ln(Q^2) \quad (5.37)
$$

$$
ES_2 = ES_{20} + ES_{21}\ln(Q^2) \quad (5.38)
$$

while ES and AS are chosen to give second and third moments which match SQ_2 and SQ_3:

$$
ES = \left(\frac{SQ_2 - AS_2/(ES_2+1)}{SQ_3 - AS_2/(ES_2+1)(ES_2+2)}\right) - 2 \quad (5.39)
$$

$$
AS = (ES+1)\left(\frac{SQ_2 - AS_2}{ES_2+1}\right) \quad (5.40)
$$

In practice, AS_{20}, AS_{21}, ES_{20}, ES_{21}, S_2, S_3, and G_3 are the sea parameters that are allowed to vary in the fit.

Strange Sea Distributions

A leading order analysis of events with two oppositely charged muons in the final state ($\nu N \to \mu^+\mu^- X$ and $\overline{\nu} N \to \mu^+\mu^- X$) provides a reliable measurement of the strange sea distribution [48]. Figure 5.7 shows a typical "dimuon" event.

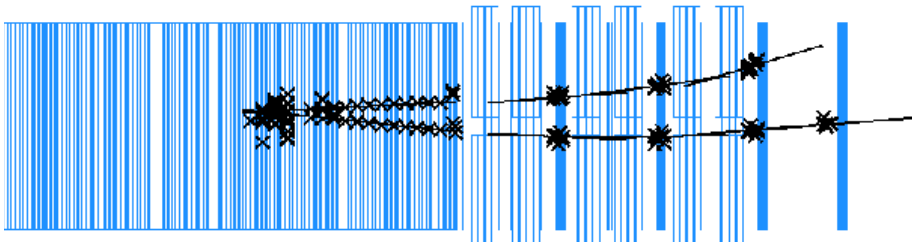

Figure 5.7: An opposite–sign dimuon event in the NuTeV detector.

The underlying leading order process is a neutrino (antineutrino) charged current scatter off an s or d ($\overline{s}$ or $\overline{d}$) quark in the nucleon, which results in the production of charm. The subsequent semileptonic decay of the charm quark produces the oppositely charged muon. The process is described using the slow rescaling formalism as outlined in Section 5.1.4. Because scattering off d quarks is suppressed by a factor $|V_{cd}|^2 = 0.05$ relative to s quark scattering, where $|V_{cs}|^2 = 0.95$, the strange quark contribution dominates despite the fact that its content is roughly ten times smaller. Hence, dimuon events provide a unique probe of the strange content of the nucleon. The fit to the CCFR dimuon data [48] uses the form:

$$\begin{aligned} x\,s(x) = x\,\overline{s}(x) &= \frac{\kappa}{2\,(\kappa+2)}\,xSS(x,Q^2) \\ &= \frac{\kappa}{2\,(\kappa+2)}\,\frac{AS}{ES+1}(ES+\alpha+1)(1-x)^{ES+\alpha} \\ &\propto \kappa\,\frac{x\,\overline{u}(x)+x\,\overline{d}(x)}{2}\,(1-x)^{\alpha} \end{aligned} \tag{5.41}$$

where α describes the shape of the strange quark distributions and ES determines the shape of the non-strange sea. The normalization of the strange sea is given by κ, the ratio of the strange to non-strange seas:

$$\kappa = \frac{S + \overline{S}}{\overline{U} + \overline{D}} = \frac{2\,S}{\overline{U} + \overline{D}} \tag{5.42}$$

where $S \equiv \int x\,s(x)\,dx$, $\overline{S} \equiv \int x\,\overline{s}(x)\,dx$, $D \equiv \int x\,d(x)\,dx$, etc. The parameters obtained from the fit, α and κ, are explicitly given in Table 5.6 in Section 5.1.4. Although this parameterization differs slightly from Reference [42], both yield similar strange sea distributions. A comparison of the leading order CCFR and NuTeV strange sea distributions is shown in Figure 5.8.

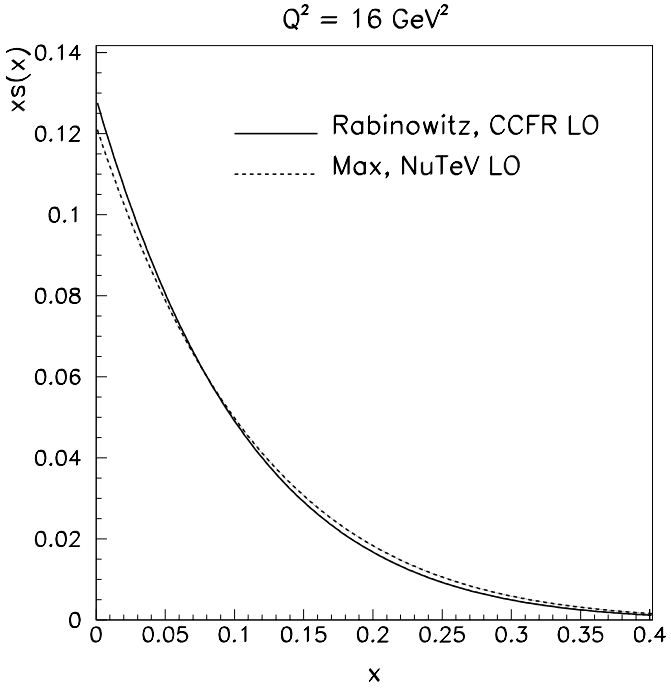

Figure 5.8: A comparison of the LO strange sea distributions obtained from CCFR (solid) [48] and NuTeV (dotted) [42] fits to dimuon data with $s(x) = \overline{s}(x)$. Plotted are the x weighted $s(x)$ distributions at $\mathrm{Q}^2 = 16$ GeV^2.

The PDF Fit

A fit to the CCFR ν and $\overline{\nu}$ CC differential cross section data in the region $x < 0.7$, $30 < \mathrm{E}_\nu < 360$ GeV determines the parameters describing the parton momentum densities [34]. In fitting the data, the PDFs include an external constraint on the ratio of the antineutrino to neutrino total cross sections, $\sigma^{\overline{\nu}}/\sigma^{\nu} = 0.499 \pm 0.007$ [36], which effectively fixes the relative momentum fractions carried by the valence and sea quarks. The parameters describing the strange sea, κ and α, take their values from the CCFR dimuon fit (Section 5.1.2). The BGPAR model has a total of 20 free parameters[◇] and provides a good fit to the data (see also Section 5.1.14). The χ^2/dof for the fit is 2676/2750, which equates to a probability of 84.1%. The parameters obtained from the fit are listed in Table 5.5.

Figure 5.9 shows the resultant contributions of the various parton distributions as a function of x, evolved to the experimental mean momentum transfer, $\mathrm{Q}^2 = 20$ GeV^2. The modifications which give $\overline{u}(x) \neq \overline{d}(x)$ and $c(x) \neq 0$, as shown in the plot, are discussed later in this Chapter. At this Q^2, roughly 33% of the proton's momentum is carried by valence quarks, 6% by u and d sea quarks, 1.3% by s quarks, and 0.5% by c quarks.

[◇] In previous analyses, 9 parameter BGPAR fits had been employed. The upgrade to 20 parameters achieves better agreement with the data, especially at low x.

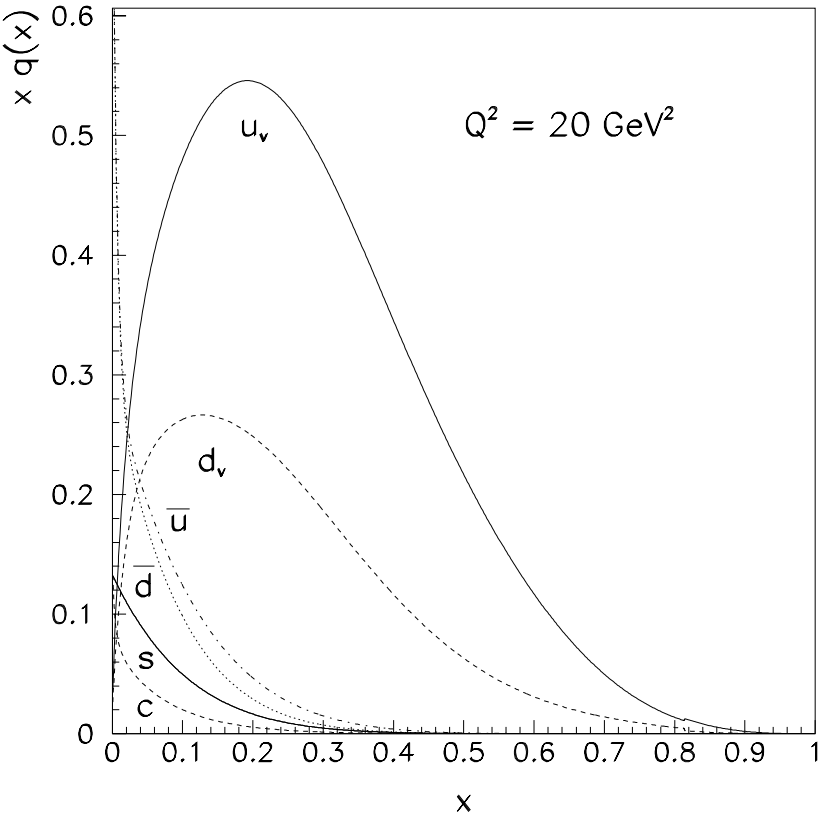

Figure 5.9: Parameterization of the BGPAR model parton distribution functions, $x\,q(x)$, plotted as a function of x at $\mathrm{Q}^2 = 20$ GeV^2. The area underneath each curve represents the total momentum fraction carried by each constituent.

BGPAR parameter	Description	Fit Value
A_0	strength of scaling violations (Λ)	0.67029
A_1	overall valence normalization	0.50286
A_2	overall valence normalization	-0.42750
AV_2	2nd valence constant term	98.0710
AV_3	3rd valence constant term	10.9900
E_{10}	1st valence term x exponent at Q_0^2	0.60666
E_{11}	valence x exponents slope in Q^2	0.031154
E_{20}	1st valence term (1–x) exponent at Q_0^2	2.8607
E_{21}	valence x exponents slope in Q^2	1.5194
E_{30}	2nd valence term x exponent at Q_0^2	3.8535
E_{40}	2nd valence term (1–x) exponent at Q_0^2	10.907
E_{50}	3rd valence term x exponent at Q_0^2	1.9651
E_{60}	3rd valence term (1–x) exponent at Q_0^2	30.711
S_2	total sea 2nd moment in x at Q_0^2	0.14379
S_3	total sea 3rd moment in x at Q_0^2	0.013643
G_3	gluon 3rd moment (factors into Q^2 dep of sea)	0.046198
AS_{20}	2nd sea term constant at Q_0^2	0.48783
AS_{21}	2nd sea term constant slope in Q^2	0.22661
ES_{20}	2nd sea term (1–x) exponent at Q_0^2	65.118
ES_{21}	2nd sea term (1–x) exponent slope in Q^2	2.6398
κ	strange sea level	0.373
α	strange sea shape	2.50
m_c	effective charm mass parameter (GeV)	1.32

Table 5.5: BGPAR parameters used in the $\sin^2\theta_W$ analysis from the best fit to the final CCFR charged current differential cross section data [34]. The first 20 parameters are varied as fit parameters, the last three are held fixed. These parameters are from the `bgpar-jhk-ukcomb2-fixed` pdf set and are used to specify the valence and sea densities in the Monte Carlo cross section model.

The d/u Correction

The simple BGPAR model operates under the assumption that $\overline{d}(x) = \overline{u}(x)$. External constraints from both NMC muon scattering [37] and E866 Drell-Yan data [38, 40] modify the BGPAR u, d fit distributions to reproduce the suggested inherent u, d asymmetry. These small adjustments are made under the assumption that $d^p = u^n$ and $u^p = d^n$ for both quark and antiquark distributions.

Since the NMC data has no sensitivity to separate out d_v/u_v from $\overline{d}/\overline{u}$, the constraint on the sea ratio is based on a fit to E866 data [38]. In order to reproduce the large flavor asymmetry in the proton sea as suggested by the E866 data, the BGPAR u and d sea distributions are each modified by the factor:

$$\mathrm{f}\left(\overline{\mathrm{d}}/\overline{\mathrm{u}}\right) = \frac{1}{\max\left(1.0 - \mathrm{x}\left(2.7 - 0.14\ln(\mathrm{Q}^2) - 1.9\,\mathrm{x}\right), 0.1\right)} \tag{5.43}$$

Under the constraint that the total sea is conserved, $\overline{u}' + \overline{d}' = \overline{u} + \overline{d}$, the light sea distributions now become:

$$\begin{aligned} \overline{u}' &= \overline{u} \cdot \left(\frac{\overline{u} + \overline{d}}{\overline{u} + \overline{d} \cdot \mathrm{f}\left(\overline{\mathrm{d}}/\overline{\mathrm{u}}\right)} \right) \\ \overline{d}' &= \overline{d} \cdot \left(\frac{\overline{u} + \overline{d}}{\overline{u} + \overline{d} \cdot \mathrm{f}\left(\overline{\mathrm{d}}/\overline{\mathrm{u}}\right)} \right) \cdot \mathrm{f}\left(\overline{\mathrm{d}}/\overline{\mathrm{u}}\right) \end{aligned}$$

This parameterization was originally based on a fit to preliminary E866 data [38], but is also consistent with their most recently published results [40]. The level of agreement can be seen from Figure 5.10. Note there is only a very weak constraint on the sea ratios at high x. NMC $\mathrm{F}_2^d/\mathrm{F}_2^p$ data provides a correction to the BGPAR prediction for the valence ratio [63]:

$$d_v'/u_v' = d_v/u_v + \delta\left(d/u\right). \tag{5.44}$$

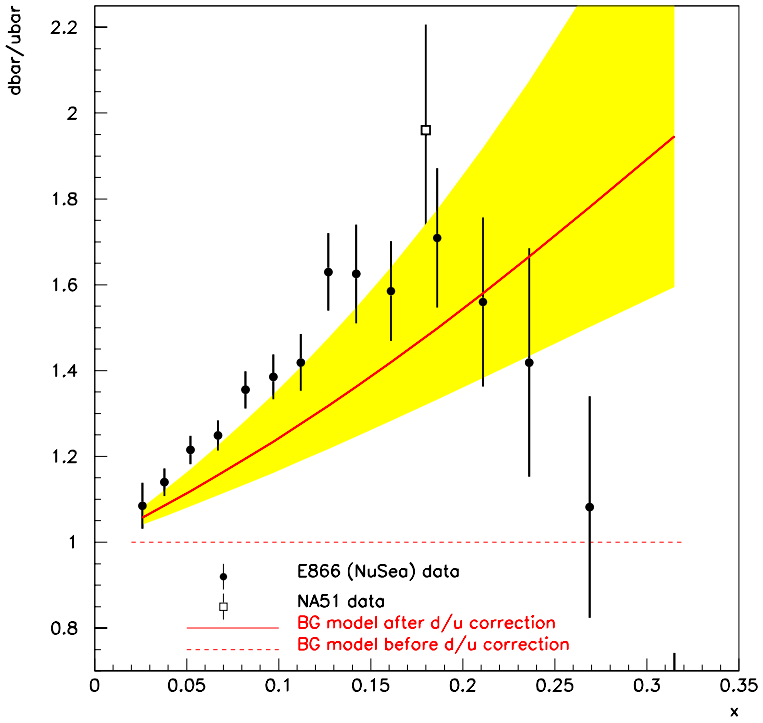

Figure 5.10: Comparison of the BGPAR ratio $\overline{d}/\overline{u}$ to the most recent E866 data [40]. The NA51 data point [39] is also shown. The values are plotted as a function of x for a fixed Q^2 value of 54 GeV^2. The yellow band indicates our assigned 40% uncertainty on the d/u sea correction.

Under the assumption that the total valence is conserved, $d'_v + u'_v = d_v + u_v$, the modifications to the valence distributions can be written as:

$$u'_v = \frac{u_v}{1 + \delta\,(d/u) \cdot u_v/(u_v + d_v)} \tag{5.45}$$

$$d'_v = \frac{d_v + u_v \cdot \delta\,(d/u)}{1 + \delta\,(d/u) \cdot u_v/(u_v + d_v)} \tag{5.46}$$

The constraint on d_v/u_v arises from measurement of the ratio:

$$\frac{F_2^n}{F_2^p} = \frac{1/9\,[4\,(d_v + 2(\overline{d} + c)) + u_v + 2(\overline{u} + s)]}{1/9\,[4\,(u_v + 2(\overline{u} + c)) + d_v + 2(\overline{d} + s)]} \tag{5.47}$$

which is extracted from the precise NMC F_2^D/F_2^p data after correcting for nuclear effects [41]. Because F_2^n/F_2^p is approximately constant for $Q^2 > 1$ GeV^2, the NMC measurement is used to modify the x dependence of our BGPAR valence distributions (Figure 5.11). In particular, after fitting the difference between the NMC data and the BGPAR model prediction (Table 5.5), we find [63]:

$$\delta\,(d/u) = 0.12079 - 1.3303\,x + 4.9829\,x^2 - 8.4465\,x^3 + 5.7324\,x^4 \qquad (5.48)$$

Figure 5.12 shows the level of agreement between the NMC nuclear-corrected F_2^D/F_2^p data and the BGPAR prediction for F_2^n/F_2^p after both the d_v/u_v and $\overline{d}/\overline{u}$ corrections. The effect of the external d/u constraints to both the valence and sea BGPAR distributions is small; inducing +0.00023, +0.00022, +0.00028 shifts in $R^{\nu}_{\rm exp}$, $R^{\overline{\nu}}_{\rm exp}$, and $\sin^2\theta_W$, respectively.

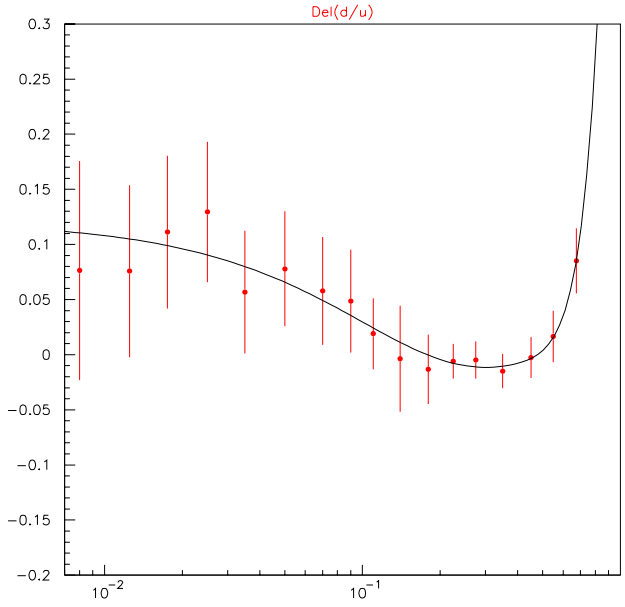

Figure 5.11: The d_v/u_v correction to the BGPAR parton densities as a function of x based on a parameterization of the difference between F_2^d/F_2^p from NMC [37] and the BGPAR model prediction. The functional form is provided in Equation 5.48. Plot courtesy of U.K. Yang [63].

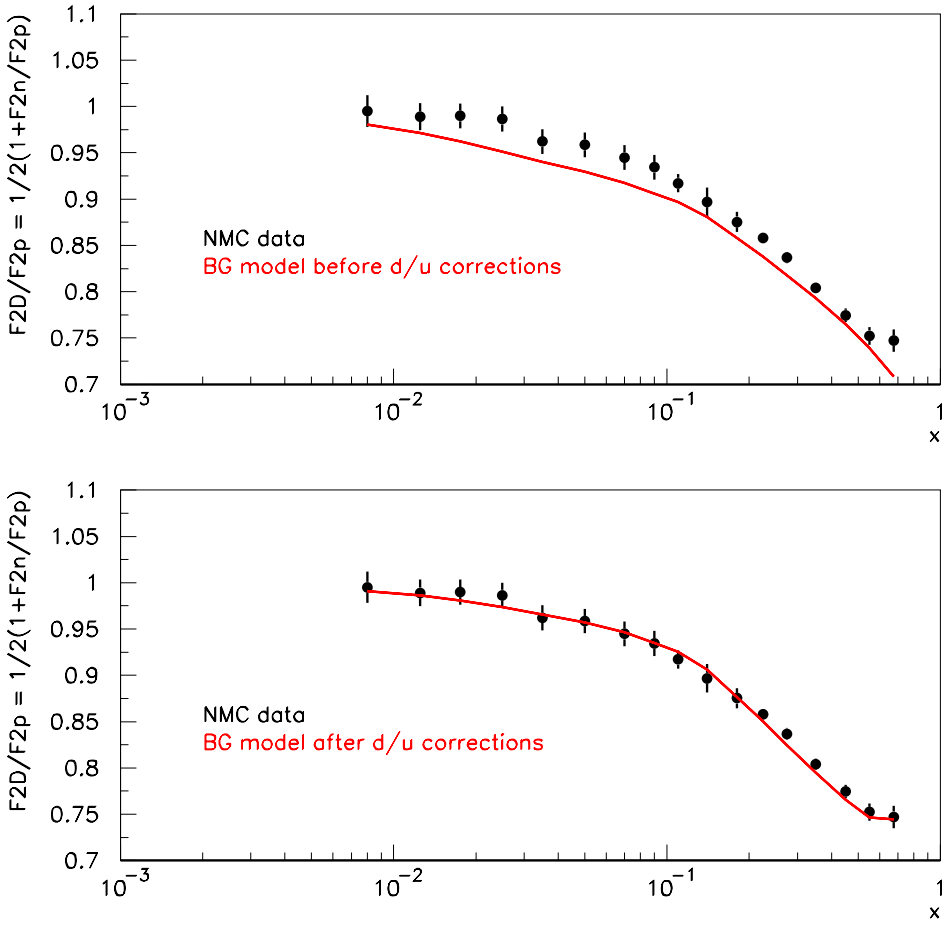

Figure 5.12: Comparison of BGPAR F_2^n/F_2^p model prediction to NMC data [37, 41] both before (top) and after (bottom) the d/u corrections have been applied to the sea and valence.

Low Q^2 Extrapolation

In the BGPAR model, the parton densities are not well–constrained at very low Q^2. In fact, the PDFs below $Q^2 = 1$ GeV^2 were traditionally assigned their values at $Q^2 = 1$ GeV^2. As a result of this unnatural flattening of the PDFs at low Q^2 (Figure 5.13), the resultant cross section predictions were grossly overestimated in this region (Figure 5.14).

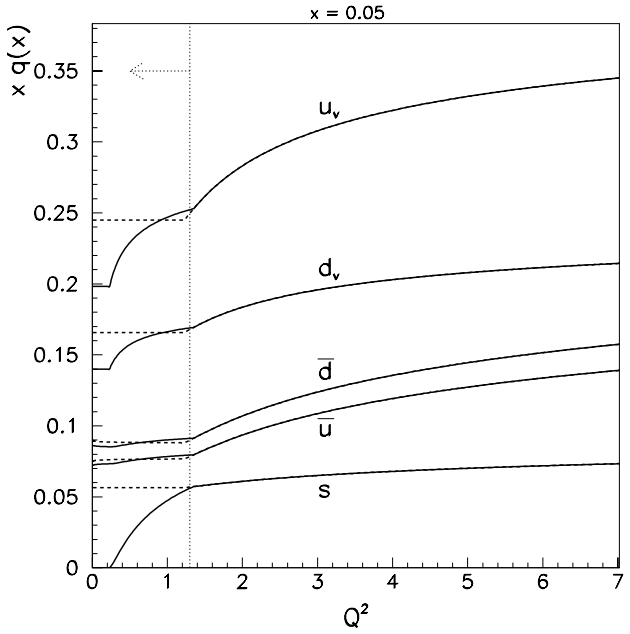

Figure 5.13: Parameterization of the BGPAR PDF extrapolation at low Q^2. The PDFs are plotted as a function of Q^2 for a fixed value of $x = 0.05$. The **dotted** curve shows the original flat extrapolation, the **solid** curve displays the new parameterization using the GRV PDF shape below $Q^2 = 1.35$ GeV^2. The second kink in the curves at very low Q^2 is a result of the GRV cutoff at $Q^2 = 0.23$ GeV^2.

To improve the behavior of the BGPAR PDFs at very low Q^2, the functional form for the PDF Q^2 evolution at low Q^2, as inspired by GRV94LO PDFs, is used to extrapolate the BGPAR parameterization down to Q^2=0.23 GeV^2 [63]. The normalization

of the GRV PDFs is fixed to the BGPAR PDFs at $Q^2 = 1.35$ GeV^2. While only 1.7% (3.7%) of the neutrino (antineutrino) data in this analysis lies below $Q^2 = 1$ GeV^2, the dominant effect is the resultant change in the extremely low x radiative corrections. Figure 5.15 shows the effect on the QED radiative corrections, and Figure 5.14 shows the improvement in the low x differential cross section agreement after incorporating the GRV-inspired PDF evolution for $Q^2 < 1.35$ GeV^2.

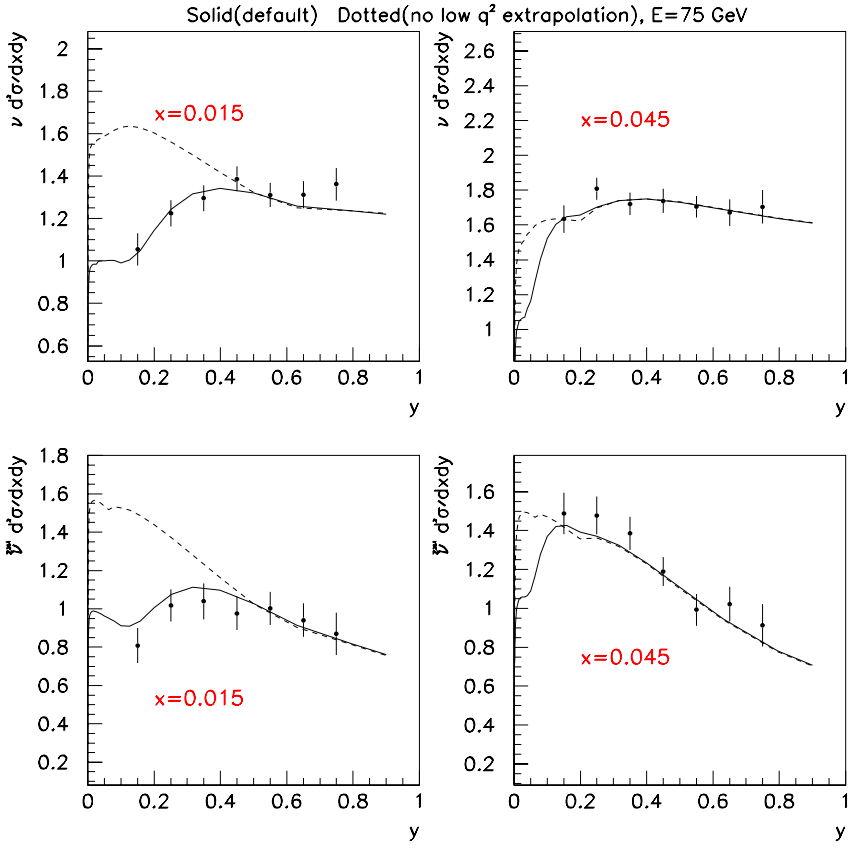

Figure 5.14: Improvement in the low x differential cross section model prediction after incorporating the GRV-based low Q^2 extension to the BGPAR PDFs. The plot displays CCFR neutrino (top) and antineutrino (bottom) cross section data at $E_\nu = 75$ GeV. The dotted curve is the model prediction *before* the low Q^2 extrapolation, the solid curve is the result *after* adopting the low Q^2 extrapolation.

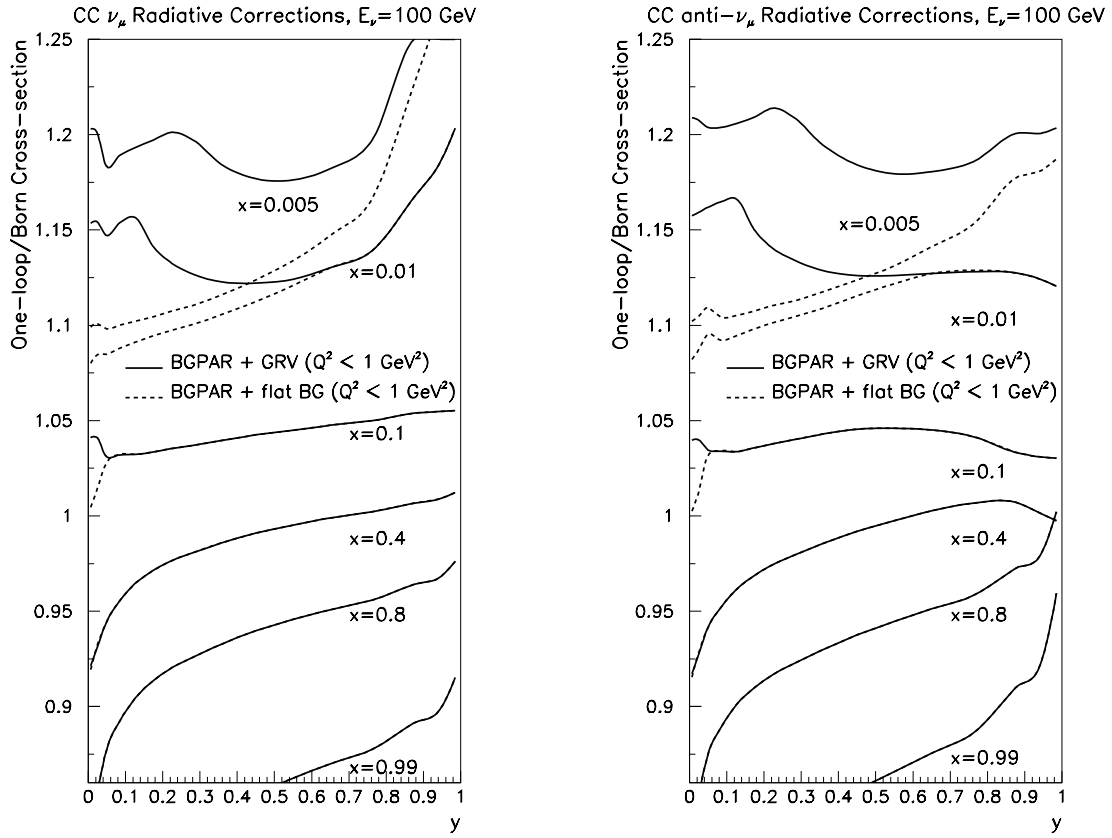

Figure 5.15: The effect of the low Q^2 pdf extrapolation on the QED radiative corrections for both neutrino (left) and antineutrino (right) CC scattering processes.

Again, because the analysis includes few events below Q^2 of 1.0 GeV^2, the effect of better low Q^2 modeling via the GRV shape extrapolation results in small shifts in the predictions for $R^{\nu}_{\rm exp}$, $R^{\overline{\nu}}_{\rm exp}$, and $\sin^2\theta_W$ of -0.00020, -0.00012, and -0.00027, respectively.

5.1.3 Longitudinal Structure Function

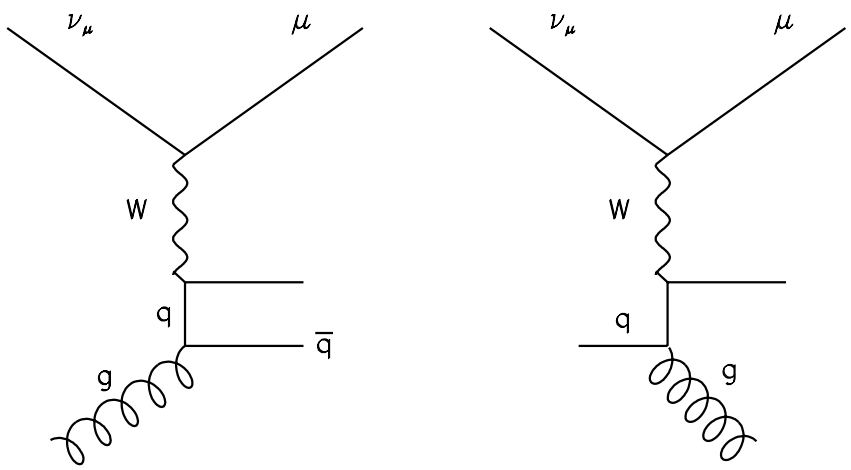

Figure 5.16: Higher order pair production (left) and gluon emission (right) diagrams illustrating how quarks can acquire transverse momentum.

In the simplest form of the parton model, the Callan–Gross relation [10] predicts $F_2(x,Q^2) = 2xF_1(x,Q^2)$ as a consequence of the pointlike spin 1/2 nature of quarks. This equality holds only if the boson initiating the scattering process is completely transverse. A quark with transverse momentum, however, can absorb a longitudinally polarized boson. The struck quark can acquire a transverse momentum component through higher order QCD processes such as those shown in Figure 5.16. Violation of the Callan-Gross relation, as predicted by QCD, is included in the Monte Carlo simulation by introducing the ratio, R_L, such that:

$$F_2(x,Q^2) = \frac{1+R_L(x,Q^2)}{1+4M^2x^2/Q^2}\,2xF_1(x,Q^2) \tag{5.49}$$

R_L is the ratio of the cross sections for absorption of longitudinally to transversely polarized bosons. It is expressed in terms of the ratio of longitudinal and transverse structure functions:

$$R_L(x,Q^2) = \frac{\sigma_L}{\sigma_T} = \frac{F_L}{2xF_1} = \frac{F_2}{2xF_1}\left(1+\frac{4M^2x^2}{Q^2}\right) \tag{5.50}$$

where F_L is the longitudinal structure function. R_L is the same for both neutrino and antineutrino scattering and is parametrized using an empirical fit to SLAC deep inelastic electron scattering data [45]:

$$\begin{aligned} R_L^{\mu,e}(x,Q^2) &= R_{\mathrm{Whitlow}}(x,Q^2) = \\ &= \frac{0.0635}{\ln(Q^2/0.04)}\,\Theta(x,Q^2) + \frac{0.5747}{Q^2} - \frac{0.3534}{Q^4+0.09} \end{aligned} \tag{5.51}$$

$$\Theta(x,Q^2) = 1 + 12\left(\frac{Q^2}{1+Q^2}\right)\left(\frac{0.125^2}{0.125^2+x^2}\right) \tag{5.52}$$

where R_{Whitlow} is assumed to be positive definite and valid down to $\mathrm{Q}^2 = 0.3$ GeV^2. Because of slow rescaling (next section), R_L contains two contributions in the case of neutrino scattering: a non–charm–producing part (Equation 5.49) and a charm–producing part (Equation 5.55). As a direct result, R_L in neutrino scattering is larger than what is expected from muon and electron scattering at low x and Q^2. Figure 5.18 displays R_L predictions for both neutrino and charged lepton scattering as compared to the world's available lepton scattering data.

Because such longitudinal cross section terms constitute a non-quark-parton-model contribution, radiative corrections are not applied to this portion of the cross section[△]. The effect of including a longitudinal cross section component is estimated

[△]Since longitudinal terms constitute roughly 3% (7%) of the total neutrino (antineutrino) cross section, the effect of *not* radiatively correcting these contributions is small: +0.00053, +0.00138, and +0.00018 in R^{ν}_{exp}, $R^{\overline{\nu}}_{\mathrm{exp}}$, and $\sin^2\theta_W$, respectively.

by setting R_L to zero in the Monte Carlo and comparing to the default prediction with $R_L = R_{\rm Whitlow}$ (Figure 5.17). The effect is large -0.0034 and -0.0105 shifts in $R^{\nu}_{\rm exp}$ and $R^{\overline{\nu}}_{\rm exp}$ that partially cancel, for a resultant -0.0015 shift in $\sin^2\theta_W$. The shifts, however, are an overestimate because the resultant $R_L = 0$ cross section no longer fits the CCFR differential cross section data.

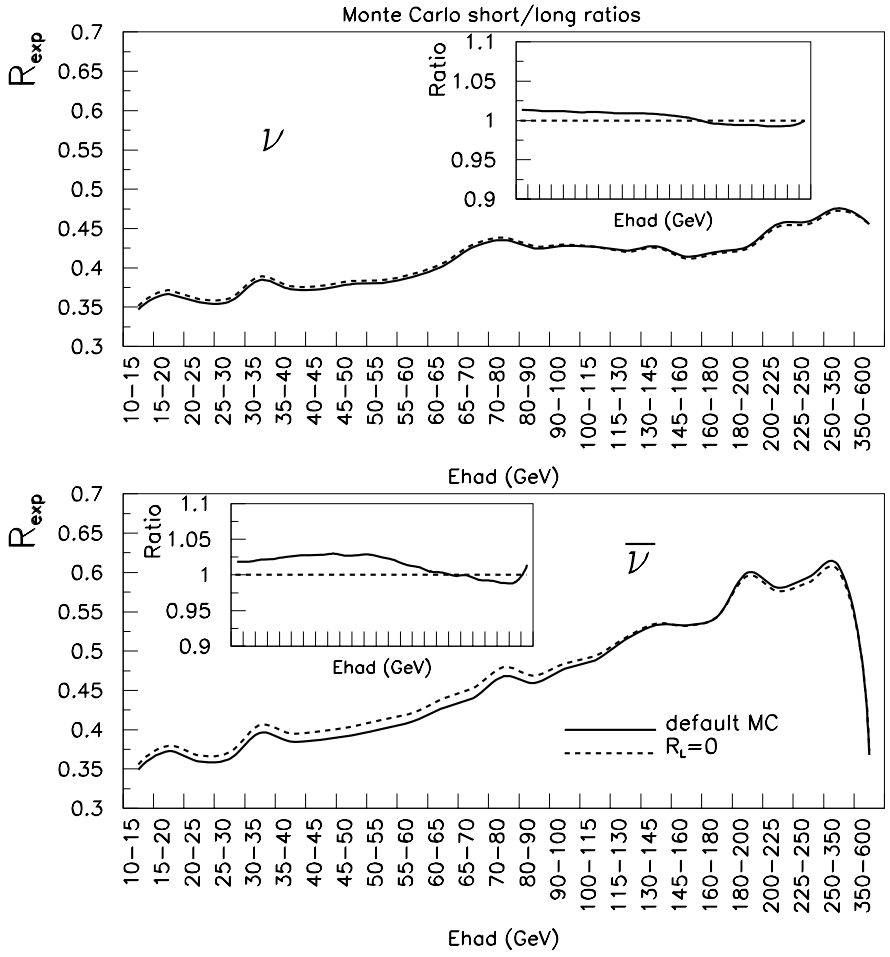

Figure 5.17: The effect of non–zero R_L on the Monte Carlo predictions for $R^{\nu}_{\rm exp}$ and $R^{\overline{\nu}}_{\rm exp}$. The inlays display the ratio of the MC prediction assuming Callan–Gross to the default prediction, $R^{\rm MC}_{\rm exp}(R_L = 0)/R^{\rm MC}_{\rm exp}(R_L = R_{\rm Whitlow})$.

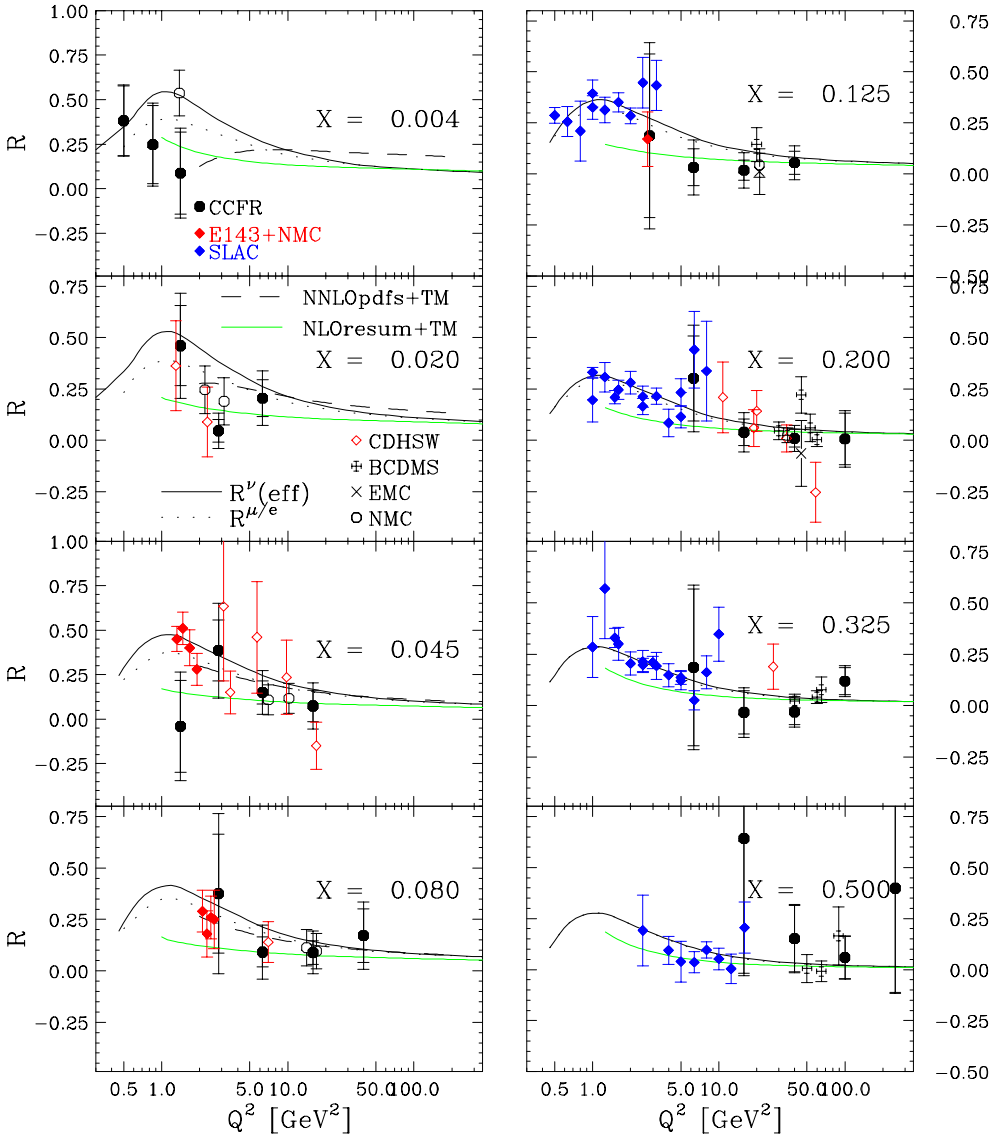

Figure 5.18: Comparison of R_L to lepton scattering data. The solid line is R_L for neutrino scattering (with $m_c = 1.3$ GeV) and is labelled R^{ν}(eff). Shown as the dotted line is R_L for charged lepton scattering, R_{Whitlow}, which is labelled $R^{\mu/e}$. Note that R^{ν} is larger than $R^{\mu/e}$ in the region of low x and low Q^2 because it contains an additional heavy quark component from the slow rescaling formalism. Plot courtesy of U.K. Yang [63].

5.1.4 Charm Production

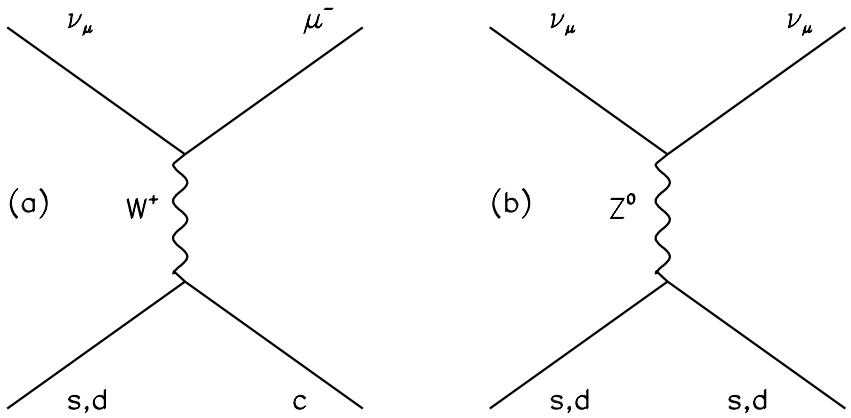

Figure 5.19: Leading order diagrams for neutrino scattering off of s or d quarks. The CC interaction (left) results in the production of a heavy final state charm quark. NC reactions (right) do not change the flavor of the struck quark.

Approximately 10% of the total CC cross section results from events in which a charm quark is produced. Such processes involve a hard scatter off an s or d quark in the nucleon (Figure 5.19). Because the standard model forbids NC flavor–changing interactions, there is no analogous reaction in the neutral current sector[⋈]. As a kinematic consequence of the heavy final state charm quark, the CC cross section is suppressed relative to the NC channel. This threshold suppression is modeled with a LO slow rescaling formalism [46, 47], whereby the normal scaling variable, x, no longer represents the momentum fraction carried by the struck quark; instead, the momentum fraction of the initial state parton, ξ, depends on the mass of the charm quark:

$$x \longrightarrow \xi = x \cdot \left(1 + \frac{{m_c}^2}{Q^2}\right) \tag{5.53}$$

[⋈]At LO, CC charm production is given by the direct process $\nu + s, d \rightarrow c$. The NC process $\nu + c \rightarrow \nu + c$ is discussed in Section 5.1.6.

This expression is derived as follows. Figure 5.20 shows the 4–vector assignments for a general CC neutrino-nucleon scattering event with a light initial state quark and a heavy final state quark.

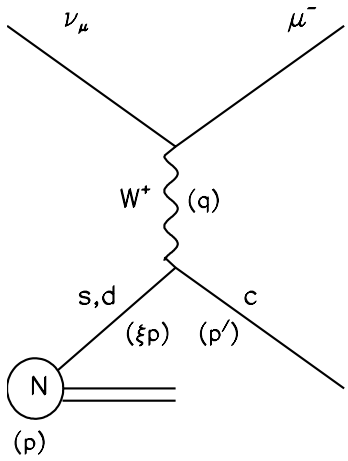

Figure 5.20: Momentum vector assignments for CC charm production.

By momentum conservation it follows that:

$$\begin{aligned}
(q+\xi p)^2 = p'^2 &= {\rm m_c}^2 \\
q^2 + 2\xi p\cdot q + \xi^2 M^2 &= {\rm m_c}^2 \\
\xi &\simeq \frac{-q^2 + {\rm m_c}^2}{2p\cdot q} \\
\xi &\simeq \frac{Q^2 + {\rm m_c}^2}{2M\nu} = \frac{Q^2 + {\rm m_c}^2}{Q^2/x} \\
\xi &\simeq x\cdot\left(1 + \frac{{\rm m_c}^2}{Q^2}\right)
\end{aligned}$$

where x is the usual Bjorken scaling variable, $x = {\rm Q}^2/2{\rm M}\nu$. For the massless quark case, $\xi = x$. In this derivation, terms in $x^2{\rm M}^2$ have been neglected. Target mass terms are also not included in the Monte Carlo simulation[††]

[††]Letting $\xi = x\cdot(1+\frac{{\rm m_c}^2}{Q^2})\,(1-\frac{x^2M^2}{Q^2})$ in the Monte Carlo confirms the effect is small: -0.00007, -0.00008, and -0.00009, in $R^{\nu}_{\rm exp}$, $R^{\overline{\nu}}_{\rm exp}$, and $\sin^2\theta_W$, respectively.

The heavy quark threshold effects are contained in the following modifications to the structure functions:

$$\begin{aligned} 2xF_1(x,Q^2) &\rightarrow \frac{x}{\xi}2\xi F_1(\xi,Q^2) \\ F_2(x,Q^2) &\rightarrow F_2(\xi,Q^2) \\ xF_3(x,Q^2) &\rightarrow \frac{x}{\xi}\xi F_3(\xi,Q^2) \end{aligned}$$

Using this substitution, the charged current differential cross section (Equation 1.25) can be rewritten in terms of the new ξ–dependent structure functions:

$$\frac{d^2\sigma^{\nu,\overline{\nu}}}{dx\,dy} = \frac{G_F^2 ME}{\pi}\left[\begin{array}{l} \frac{y^2}{2}\frac{x}{\xi}\,2\xi F_1(\xi,Q^2) + \left(1-y-\frac{Mxy}{2E}\right)F_2(\xi,Q^2) \\ \pm\, y\,\left(1-\frac{y}{2}\right)\frac{x}{\xi}\,\xi F_3(\xi,Q^2) \end{array}\right] \tag{5.54}$$

Further, including violation of the Callan-Gross relation:

$$F_2(\xi,Q^2) = \frac{1+R_L(\xi,Q^2)}{1+4M^2\xi^2/Q^2}\,2\xi F_1(\xi,Q^2) \tag{5.55}$$

where $\mathrm{R_{Whitlow}}(\xi,\mathrm{Q}^2)$ is assumed here for $R_L(\xi,\mathrm{Q}^2)$, it then follows that:

$$\begin{aligned} \frac{d^2\sigma^{\nu,\overline{\nu}}}{dx\,dy} = \frac{G_F^2 ME}{\pi}[&\left(\frac{y^2}{2}\frac{x}{\xi} + \frac{1+R_L(\xi,Q^2)}{1+4M^2\xi^2/Q^2}\,\left(1-y-\frac{Mxy}{2E}\right)\right)\,2\xi F_1(\xi,Q^2) \\ &\pm\, y\,(1-\frac{y}{2})\frac{x}{\xi}\,\xi F_3(\xi,Q^2)] \end{aligned} \tag{5.56}$$

In terms of quark distributions, the charm production cross sections for neutrino scattering off of a proton and neutron target are each given by:

$$\begin{aligned} \frac{d^2\sigma(\nu\,p\rightarrow c\,\mu^-)}{dx\,dy} = \frac{G_F^2 ME}{\pi}&\left[\frac{1+R_L(\xi,Q^2)}{1+4M^2\xi^2/Q^2}\left(1-y-\frac{Mxy}{2E}\right)+\frac{xy}{\xi}\right]\cdot \\ &2\xi\,\left[\,|V_{cd}|^2\,d_v(\xi)+|V_{cd}|^2\,\overline{d}(\xi)+|V_{cs}|^2\,s(\xi)\,\right] \end{aligned} \tag{5.57}$$

$$\frac{d^2\sigma(\nu\, n \to c\,\mu^-)}{dx\,dy} = \frac{G_F^2 ME}{\pi}\left[\frac{1+R_L(\xi,Q^2)}{1+4M^2\xi^2/Q^2}\left(1-y-\frac{Mxy}{2E}\right)+\frac{xy}{\xi}\right]\cdot$$
$$2\xi\left[\,|V_{cd}|^2\,u_v(\xi)+|V_{cd}|^2\,\overline{u}(\xi)+|V_{cs}|^2\,s(\xi)\,\right] \qquad (5.58)$$

Hence, for an isoscalar target, the neutrino charm production cross section is:

$$\frac{d^2\sigma(\nu\, N \to c\,\mu^-)}{dx\,dy} = \frac{G_F^2 ME\,\xi}{\pi}\left[\frac{1+R_L(\xi,Q^2)}{1+4M^2\xi^2/Q^2}\left(1-y-\frac{Mxy}{2E}\right)+\frac{xy}{\xi}\right]$$
$$\cdot\left[\begin{array}{l} |V_{cd}|^2\,\Theta(W-M_{\Lambda_C})\;(d_v(\xi)+u_v(\xi))\;+ \\ |V_{cd}|^2\,\Theta(W-M_{\Lambda_C}-M_\pi)\;\left(\overline{d}(\xi)+\overline{u}(\xi)\right)\;+ \\ 2\,|V_{cs}|^2\,\Theta(W-M_{\Lambda_C}-M_K)\,s(\xi) \end{array}\right] \qquad (5.59)$$

The analogous equation for antineutrinos is obtained by substituting $q \longleftrightarrow \overline{q}$ for each quark flavor in the above expression:

$$\frac{d^2\sigma(\overline{\nu}\, N \to \overline{c}\,\mu^+)}{dx\,dy} = \frac{G_F^2 ME\,\xi}{\pi}\left[\frac{1+R_L(\xi,Q^2)}{1+4M^2\xi^2/Q^2}\left(1-y-\frac{Mxy}{2E}\right)+\frac{xy}{\xi}\right]$$
$$\cdot\left[\begin{array}{l} |V_{cd}|^2\,\Theta(W-M_p-M_D-M_\pi)\;\left(\overline{d}(\xi)+\overline{u}(\xi)\right)\;+ \\ 2\,|V_{cs}|^2\,\Theta(W-M_p-M_D-M_K)\,\overline{s}(\xi) \end{array}\right] \qquad (5.60)$$

Fast–rescaling threshold factors, $\Theta(W)$, are implemented as step functions. This requirement on the invariant mass of the hadronic system ensures that the production of the final state charm quark (i.e., charmed meson or baryon) is kinematically possible. In the absence of Callan–Gross violation, the charm suppression is simply contained in the threshold factor:

$$1-y+\frac{xy}{\xi} = 1-\frac{{\rm m_c}^2}{2ME\,\xi} \qquad (5.61)$$

which, for example, is the multiplicative factor appearing in the charm sea scattering expressions in Section 5.1.6.

In addition, the charm production cross sections are limited by several kinematic thresholds. The struck quark momentum must not exceed the total proton momentum ($\xi \leq 1$), ensuring that $F_2(\xi)$ is non–zero:

$$x \leq 1 - \frac{{m_c}^2}{2MEy} \leq 1 - \frac{{m_c}^2}{2ME} \tag{5.62}$$

$$y \geq \frac{{m_c}^2}{2ME(1-x)} \geq \frac{{m_c}^2}{2ME} \tag{5.63}$$

Charm production is thus kinematically suppressed at large x and small y. However, this does not mean that the struck quark carries away only a small fraction of momentum. Because $x \geq 0$,

$$\xi \geq \frac{{m_c}^2}{2ME\,y} \geq \frac{{m_c}^2}{2ME} \tag{5.64}$$

sea quarks with smaller ξ are less effective at producing heavy charm than valence quarks [47]. As a result of the kinematic thresholds and overall x/ξ structure function rescaling (Equation 5.54), the effect is largest at small y and small x (where x/ξ is smallest).

The parameters of the slow rescaling model are well constrained. They are extracted from opposite–sign dimuon data [48], because roughly 10% of the time the charm quark can semi–leptonically decay resulting in events with two oppositely charged muons (Figure 5.21). The leading muon comes from the neutrino vertex, the second muon results from the semileptonic decay of the charm quark:

In this case, the dimuon cross section is given by:

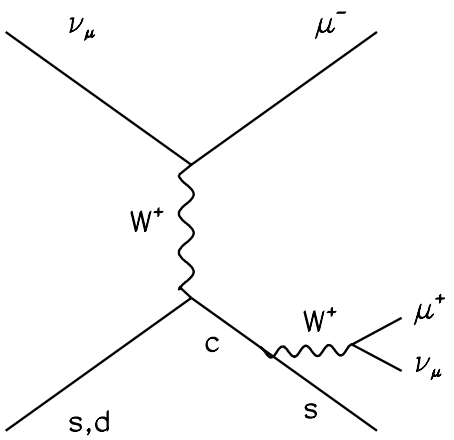

$$\nu_\mu + \begin{pmatrix} d \\ s \end{pmatrix} \longrightarrow \mu^- + \quad c \quad + X$$
$$\hookrightarrow \quad \mu^+ + \nu_\mu + X'$$
$$\overline{\nu}_\mu + \begin{pmatrix} \overline{d} \\ \overline{s} \end{pmatrix} \longrightarrow \mu^+ + \quad \overline{c} \quad + X$$
$$\hookrightarrow \quad \mu^- + \overline{\nu}_\mu + X'$$

Figure 5.21: Opposite–sign dimuon production diagrams.

$$\frac{d^2\sigma(\nu\, N \to \mu^-\mu^+ X)}{dx\, dy} = \frac{d^2\sigma(\nu\, N \to c\, \mu^-)}{dx\, dy} \cdot D(z) \cdot B_c(c \to \mu\nu X) \qquad (5.65)$$

where $B_c(c \to \mu\nu X) = 0.092$ is the branching ratio for $c \to \mu$ averaged over the charmed particles produced at the hadronic vertex and $D(z)$ describes the fragmentation of the charm quark into a charmed hadron. Specifically, the hadronization process is described using the Collins–Spiller [44] heavy quark fragmentation function[‡‡]

$$D(z) = \frac{(\frac{1-z}{z} + \epsilon\, \frac{2-z}{1-z})(1+z^2)}{(1 - \frac{1}{z} - \frac{\epsilon}{1-z})^2} \qquad (5.66)$$

where ϵ is a free parameter and z is the fraction of the charm quark's momentum carried by the charmed hadron.

In the slow rescaling model, the production of $\mu^+\mu^-$ pairs is determined by an effective charm mass parameter (m_c), the level of the strange sea (κ), the shape of

[‡‡]There is a typo in References [42] and [43]. The correct form, $(1 + z^2)$, as given by Equation (14.3) in Reference [44] is what is used in the charm fragmentation model in the MC.

the strange sea (α), and $V_{c\,d}$ (Section 5.1.2). In the Monte Carlo, the slow rescaling parameters from the fit to CCFR dimuon data are used (Table 5.6); the parameters are each varied within their experimental uncertainties in determining the final model uncertainty on $\sin^2\theta_W$ (Chapter 7).

κ	0.373 ± 0.049
α	2.50 ± 0.65
V_{cd}	0.2205 ± 0.012
m_c	1.32 ± 0.024 GeV

Table 5.6: Values of the parameters used in the Monte Carlo slow rescaling model as measured from CCFR dimuon data [48].

The dimuon data is well–described [48, 42, 43] by the LO heavy charm production model described here, and provides an important test of the slow rescaling hypothesis. The slow rescaling parameter which maintains the greatest impact on the $\sin^2\theta_W$ analysis is, of course, m_c (Section 7.3.1). Figure 5.22 shows the size of the charm threshold suppression for various values of m_c. The heavier the charm mass, the greater the suppression. Figure 5.23 displays the result of assuming a non–zero charm mass on the Monte Carlo predictions for $R^{\nu}_{\rm exp}$ and $R^{\overline{\nu}}_{\rm exp}$. Setting the charm mass to zero in the Monte Carlo gives an estimate of the size of the effect: approximately* –0.0052, –0.0117, –0.0033 in $R^{\nu}_{\rm exp}$, $R^{\overline{\nu}}_{\rm exp}$, and $\sin^2\theta_W$, respectively.

* Estimating the effect of massless charm is partially an ill–defined exercise because of the effects of fast–rescaling, thresholds, and non–existing charm production events.

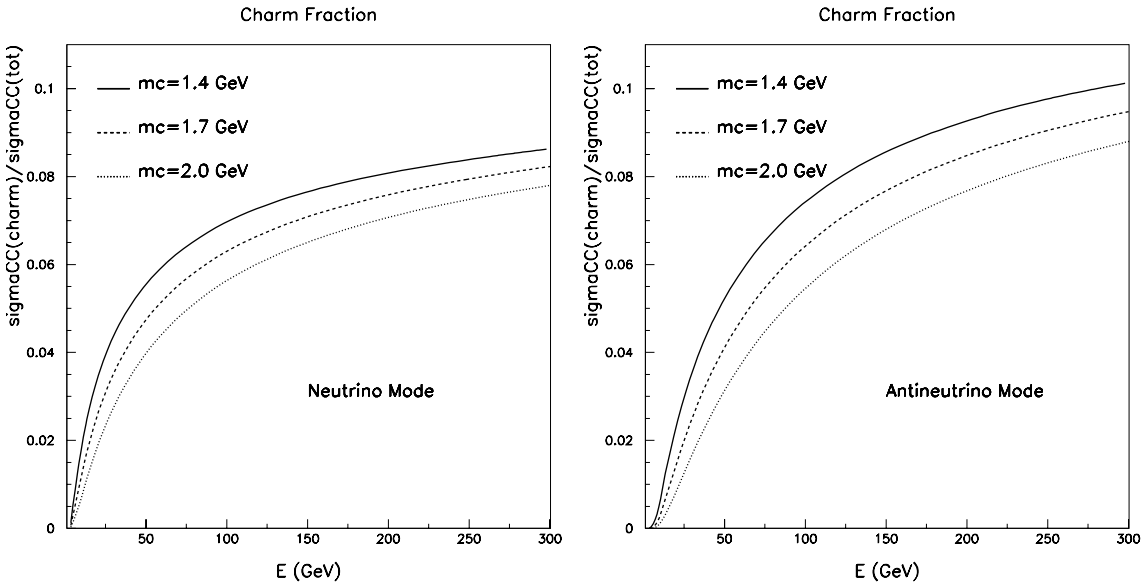

Figure 5.22: Effect of the slow rescaling model threshold suppression on the predicted charm fractions, $\sigma_{CC}^{\rm charm}/\sigma_{CC}^{\rm tot}$, shown over a varying range of m_c.

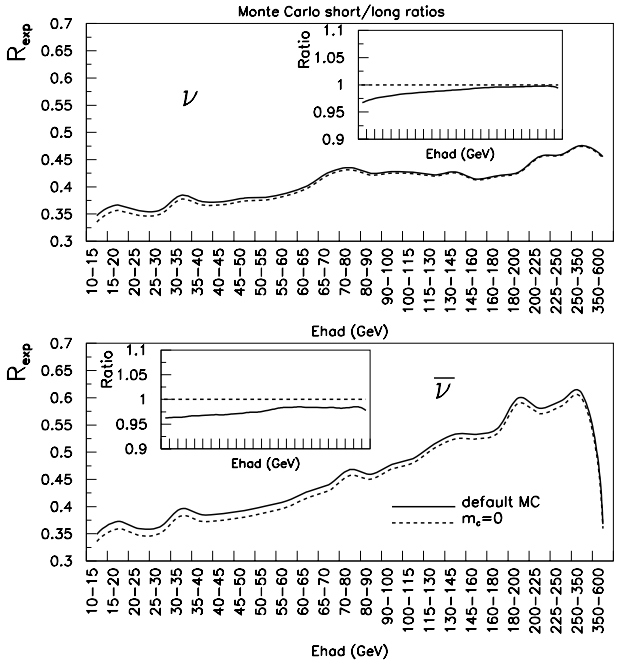

Figure 5.23: Effect of heavy charm on the MC predictions for $R_{\rm exp}^{\nu}$ and $R_{\rm exp}^{\overline{\nu}}$ assuming $m_c = 1.32$ GeV (*solid*) and $m_c \simeq 0$ GeV (*dotted*).

Assuming lepton universality, the charm quark can also decay into an electron roughly half of the time:

$$\nu_\mu + \begin{pmatrix} d \\ s \end{pmatrix} \longrightarrow \mu^- + \quad c \quad + X \qquad (5.67)$$
$$\hookrightarrow \quad e^+ + \nu_e + X'$$

Such processes are included in the Monte Carlo simulation with the same branching ratio as for the muon case, $B_c(c \to e\nu X) = B_c(c \to \mu\nu X) = 0.092$, and result in the production of long events with mostly soft electrons. In the case of ν_e scattering, processes involving the production of wrong sign muons:

$$\nu_e + \begin{pmatrix} d \\ s \end{pmatrix} \longrightarrow e^- + \quad c \quad + X \qquad (5.68)$$
$$\hookrightarrow \quad \mu^+ + \nu_\mu + X'$$

and secondary electrons:

$$\nu_e + \begin{pmatrix} d \\ s \end{pmatrix} \longrightarrow e^- + \quad c \quad + X \qquad (5.69)$$
$$\hookrightarrow \quad e^+ + \nu_e + X'$$

are also included in the Monte Carlo simulation. Together they constitute roughly 1% of the total ν_e events passing cuts.

5.1.5 Strange Sea Scattering

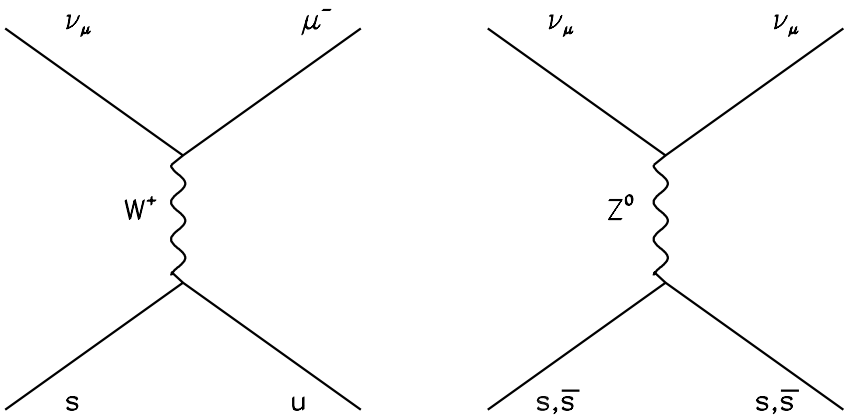

Figure 5.24: Diagrams for CC and NC strange sea scattering processes which do not yield a heavy charm quark in the final state.

The Monte Carlo also includes strange sea scattering processes which do not yield a charmed final state (Figure 5.24). In this case, the corresponding doubly differential CC and NC cross sections are:

$$\frac{d^2\sigma_S(\nu_\mu + p \to \mu^- + X)}{dx\,dy} = 2\,|V_{us}|^2\,xs(x) + \sigma_S^L(CC) \tag{5.70}$$

$$\begin{aligned}\frac{d^2\sigma_S(\nu_\mu + p \to \nu_\mu + X)}{dx\,dy} &= [2\,xs(x)(s_L^2 + s_R^2(1-y)^2) + 2\,x\overline{s}(x)\,(s_L^2(1-y)^2 + s_R^2) \\ &\quad + \sigma_S^L(NC)] \cdot \Theta(W - M_\Lambda - M_K)\end{aligned} \tag{5.71}$$

The terms containing longitudinal contributions are:

$$\begin{aligned}\sigma_S^L(CC) &= \left[\left(\frac{1+R_L}{1+4M^2x^2/Q^2} - 1\right)(1-y) - \frac{Mxy}{2E}\left(\frac{1+R_L}{1+4M^2x^2/Q^2}\right)\right] \\ &\quad \cdot 2\,|V_{us}|^2\,xs(x)\end{aligned} \tag{5.72}$$

$$\begin{aligned}\sigma_S^L(NC) &= (1-y)\left(\frac{1+R_L}{1+4M^2x^2/Q^2} - 1\right)(s_L^2 + s_R^2)\,2xF_1(x) \\ &\quad -\frac{Mxy}{2E}\left(\frac{1+R_L}{1+4M^2x^2/Q^2}\right)(s_L^2 + s_R^2)\,2xF_1(x)\end{aligned} \tag{5.73}$$

where $2xF_1(x) = 2\left[xs(x) + x\overline{s}(x)\right]$ and the NC coupling factors are $s_L = d_L = -\frac{1}{2} + \frac{1}{3}\sin^2\theta_W$, $s_R = d_R = \frac{1}{3}\sin^2\theta_W$. The strange sea distributions, $s(x) = \overline{s}(x)$, come from the measurement of CCFR and NuTeV opposite–sign dimuon events (Section 5.1.2). Algebra further reduces these expressions to:

$$\begin{aligned}\frac{d^2\sigma_S(\nu_\mu + p \to \mu^- + X)}{dx\,dy} &= \frac{d^2\sigma_S(\nu_\mu + n \to \mu^- + X)}{dx\,dy} \\ &= \frac{G_F^2 ME}{\pi}\left[y + \left(1 - y - \frac{Mxy}{2E}\right)\left(\frac{1 + R_L(x,Q^2)}{1 + 4M^2x^2/Q^2}\right)\right] \\ &\quad \cdot 2\left|V_{us}\right|^2 xs(x) \end{aligned} \tag{5.74}$$

$$\begin{aligned}\frac{d^2\sigma(\nu_\mu + p \to \nu_\mu + X)}{dx\,dy} &= \frac{d^2\sigma(\nu_\mu + n \to \nu_\mu + X)}{dx\,dy} \\ &= \frac{G_F^2 ME}{\pi}\left[\begin{array}{l} \left(1 - y - \frac{Mxy}{2E}\right)\left(\frac{1+R_L(x,Q^2)}{1+4M^2x^2/Q^2}\right) \\ \quad \cdot 2(s_L^2 + s_R^2)[xs(x) + x\overline{s}(x)] \\ \quad + 2\,xs(x)\,y\,[s_L^2 - (1-y)s_R^2] \\ \quad + 2\,x\overline{s}(x)\,y\,[s_R^2 - (1-y)s_L^2] \end{array}\right] \end{aligned} \tag{5.75}$$

The same expressions hold in the case of antineutrino scattering with the replacement $s(x) \to \overline{s}(x)$. The CC cross sections written above include only the non–charm–producing remnant. As a result, the dominant effect of including this contribution to the total cross section is an increase in the number of neutral current events because the NC cross section for scattering off d, $\overline{d}$, s, and $\overline{s}$ quarks is slightly larger than for u and $\overline{u}$ quarks.

5.1.6 Charm Sea Scattering

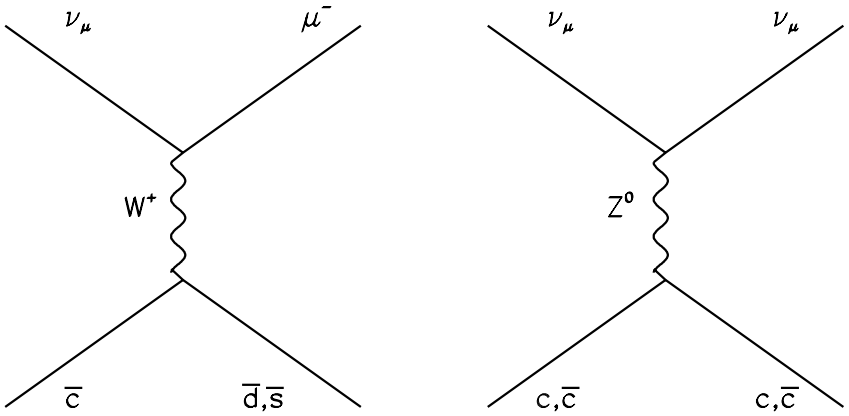

Figure 5.25: LO diagrams for CC and NC charm sea scattering.

Neutrinos can also directly scatter off of the charm sea (Figure 5.25). The cross sections for CC and NC charm sea scattering are:

$$\begin{aligned}
\frac{d^2\sigma_H(\nu_\mu + p \to \mu^- + X)}{dx\,dy} &= \frac{G_F^2 ME}{\pi} \cdot \Theta\left(W - M_{\Lambda_C} - M_K - M_\pi\right) \\
&\cdot \left(1 - \frac{{\rm m_c}^2}{2ME\,\xi}\right) \cdot \left(|V_{cd}|^2 + |V_{cs}|^2\right) 2\,\xi\overline{c}(\xi)\,(1-y)^2 \\
\frac{d^2\sigma_H(\nu_\mu + p \to \nu_\mu + X)}{dx\,dy} &= \frac{G_F^2 ME}{\pi} \cdot \Theta\left(W - M_{\Sigma_C}\right) \cdot \left(1 - \frac{{\rm m_c}^2}{2ME\,\xi}\right) \\
&\cdot \left[(c_L^2 + c_R^2(1-y)^2)\,2\,\xi c(\xi) + (c_L^2(1-y)^2 + c_R^2)\,2\,\xi\overline{c}(\xi)\right]
\end{aligned}$$

assuming $F_2(x,Q^2) = 2xF_1(x,Q^2)$ and neglecting target mass terms. In the above expressions, the NC quark couplings are $c_L = u_L = \frac{1}{2} - \frac{2}{3}\sin^2\theta_W$ and $c_R = u_R = -\frac{2}{3}\sin^2\theta_W$. Note that the antineutrino cross sections are simply obtained by substituting $c(x) \longleftrightarrow \overline{c}(x)$. Despite the underlying LO treatment, the cross sections have been augmented to account for higher order boson–gluon fusion processes; for

example, production of $c\overline{c}$ pairs from gluons in the nucleon such as those shown in Figure 5.26. To account for such higher order contributions, which lead to a massive c quark in the final state, the LO cross sections include additional slow rescaling thresholds via the substitution $x \rightarrow \xi$ (Equation 5.53) and through the threshold factor $1 - \frac{\mathrm{m}_c{}^2}{2ME\xi}$ (Equation 5.61). As in the LO charm production formalism outlined in Section 5.1.4, the charm sea scattering processes are also subject to the same kinematic thresholds as presented in Equations (5.63) and (5.64). As a result, the NC interaction is suppressed relative to its CC counterpart because the NC final state contains two charm quarks; hence, for NC events, ξ is modified by the substitution $\mathrm{m}_c \rightarrow 2 \cdot \mathrm{m}_c$.

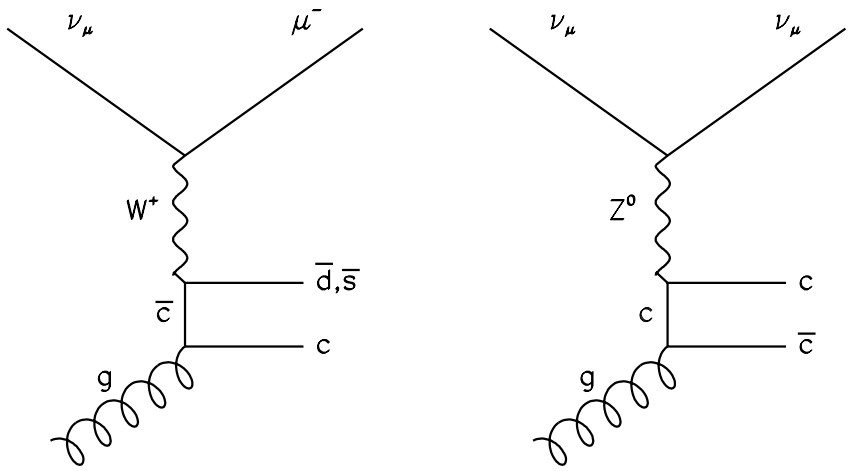

Figure 5.26: Higher order (NLO) diagrams for CC and NC charm sea scattering.

Unfortunately, measurement of the charm sea content of the nucleon is not very precise. In our chosen LO charm sea model, CTEQ4LO pdfs provide an initial estimate of the level of the charm sea, the charm sea shape is assumed to be the same as that for the strange sea, and finally the substitution $\mathrm{m}_c \rightarrow 2{\cdot}\mathrm{m}_c$ is employed

in the slow rescaling formalism for NC events. This simple model is then tuned to match European Muon Collaboration (EMC) $c\overline{c}$ production data [49]. EMC data is chosen because it populates a region in x most relevant to our experimental data, and because it is obtained from an iron target. The tuning procedure involves comparing the measured charm contribution to F_2 to our slow-rescaled prediction assuming a heavy charm sea:

$$F_2^{c\overline{c}} = 4/9\,[\xi\, c(\xi) + \xi\, \overline{c}(\xi)] = 8/9\,\xi\, c(\xi) \tag{5.76}$$

$$\xi = x \cdot (1 + \frac{{m_c}^2}{Q^2}) \tag{5.77}$$

To reproduce the EMC data with this model, a 50% enhancement of the CTEQ4LO charm sea level is required. Figure 5.27 compares the tuned model prediction, i.e., after the 50% charm level enhancement, to all available data on $F_2^{c\overline{c}}$. The final charm content, $C(x) = \int x\, c(x)\, dx$, is found to be less than 0.5%, a factor two smaller than the strange sea.

Finally, the charm sea is also measured at NuTeV through neutral current production of wrong sign single muons, processes such as those shown in Figure 5.28. Despite offering a less precise constraint than the EMC data, our charm model is found to be consistent with the NuTeV measurement of the total NC charm cross section, $\sigma_{NC}^{c\overline{c}} = 2.1 \pm 1.8$ fb at $\langle E_\nu \rangle = 154$ GeV [52].

Fortunately, $\sin^2\theta_W$ is not very sensitive to the charm sea. The result of including charm sea scattering at this level is +0.00005 (-0.00004) in $R_{\rm exp}^{\nu}$ ($R_{\rm exp}^{\overline{\nu}}$), which translates into a small +0.00010 effect in $\sin^2\theta_W$.

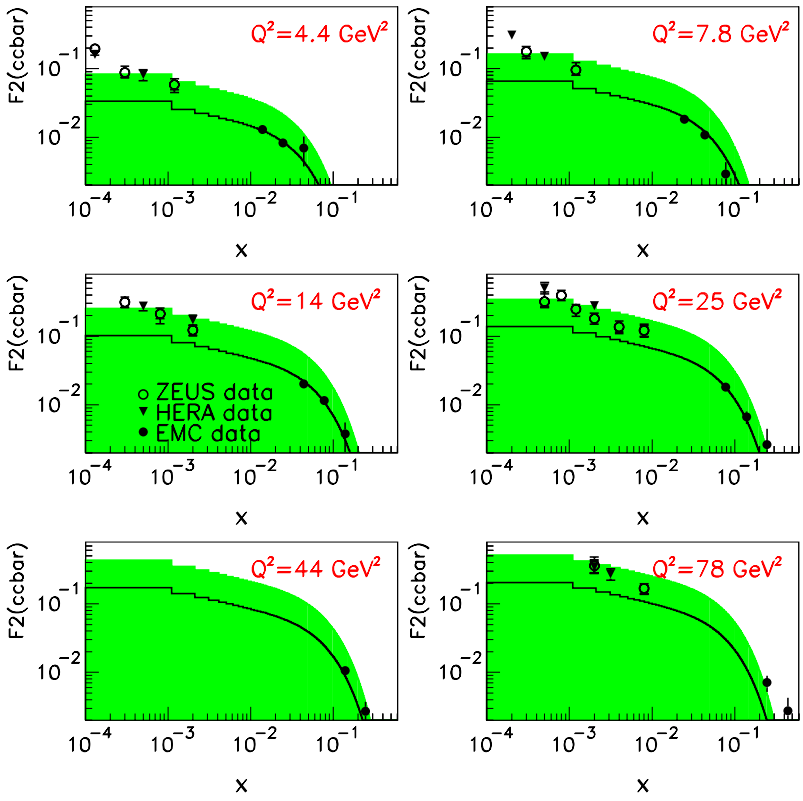

Figure 5.27: Comparison of the tuned charm sea model to EMC [49], ZEUS [50], and HERA [51] $F_2^{c\bar{c}}$ data in various Q^2 bins. The shaded band indicates the systematic error assigned to the intrinsic charm model (Section 7.3.5).

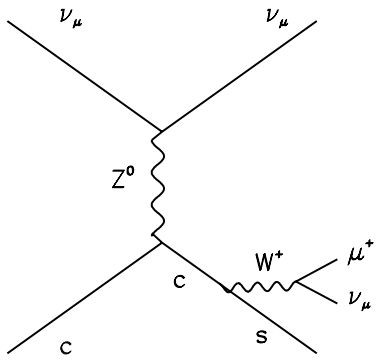

Figure 5.28: Wrong–sign single muon production from NC charm scattering.

5.1.7 Quasi–Elastic Scattering

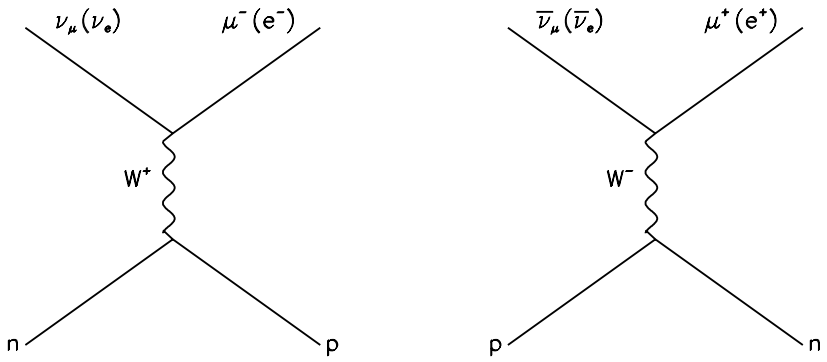

Figure 5.29: Diagrams depicting ν (left) and $\overline{\nu}$ (right) quasi–elastic scattering.

Quasi–elastic events result from nucleon scattering in which the nucleon remains a single particle in the final state:

$$\begin{aligned} \nu_\mu + n &\longrightarrow \mu^- + p, \qquad \nu_e + n \longrightarrow e^- + p \\ \overline{\nu}_\mu + p &\longrightarrow \mu^+ + n, \qquad \overline{\nu}_e + p \longrightarrow e^+ + n \end{aligned}$$

These $x = 1$ events lack a hadronic shower and have zero inelasticity, $y = 0$. While ν_μ quasi–elastic events are not energetic enough to pass the minimum E_{had} requirement, ν_e quasi–elastics can enter the sample because of the energy deposited by the final state electron. Therefore, the Monte Carlo includes ν_e quasi–elastics, which constitute approximately 1.3% (2.9%) of ν_e ($\overline{\nu}_e$) events passing analysis cuts. The fractional contribution of quasi–elastic (QE) events to the total CC cross section is assumed to be:

$$\begin{aligned} \sigma^{\nu}_{QE} &= 1.441 \cdot \sigma^{\nu}_{CC}/E \quad (10^{-38}\,\mathrm{cm}^2) \\ \sigma^{\overline{\nu}}_{QE} &= 2.963 \cdot \sigma^{\overline{\nu}}_{CC}/E \quad (10^{-38}\,\mathrm{cm}^2) \end{aligned}$$

and then checked against available data on neutrino quasi–elastic scattering [53] (Figure 5.30). The total size of the quasi–elastic contribution to the predicted short/long

ratios is +0.00032 for $R^{\nu}_{\rm exp}$ and +0.00089 for $R^{\overline{\nu}}_{\rm exp}$. Hence, the inclusion of ν_e quasi–elastic events leads to a net +0.00015 increase in $\sin^2\theta_W$.

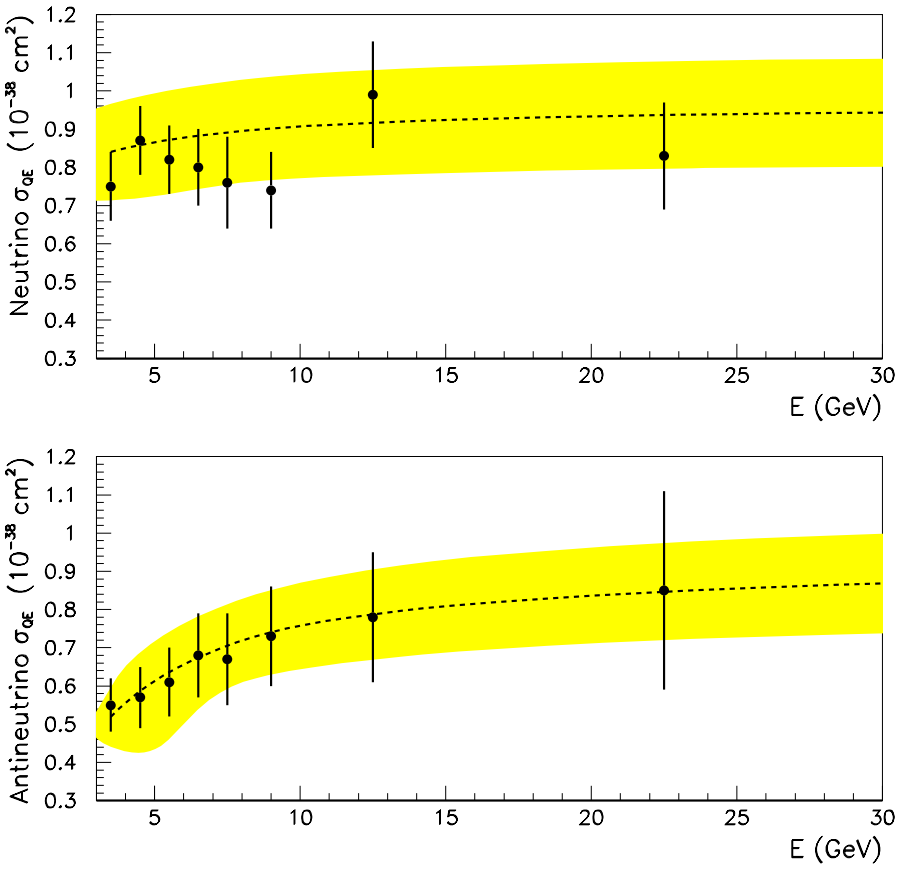

Figure 5.30: Monte Carlo ν and $\overline{\nu}$ quasi–elastic cross section predictions plotted as a function of neutrino energy. The data points are from Serpukhov [53]. The yellow band indicates the 15% uncertainty assigned to this model.

5.1.8 Neutrino–Electron Scattering

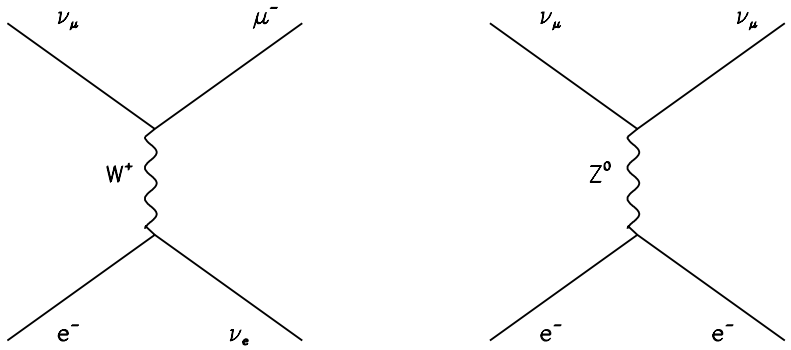

Figure 5.31: Diagrams depicting CC and NC ν_μ–electron scattering.

Neutrinos striking the NuTeV detector will not only interact with the target nucleons but also with atomic electrons (Figure 5.31). The purely leptonic process of neutrino scattering off target electrons is included in our Monte Carlo cross section model. These processes can proceed through both charged current (s-channel):

$$\nu_\mu + e^- \rightarrow \nu_e + \mu^- \tag{5.78}$$

$$\overline{\nu}_e + e^- \rightarrow \overline{\nu}_\mu + \mu^- \tag{5.79}$$

and the elastic interactions:

$$\nu_\mu + e^- \rightarrow \nu_\mu + e^- \tag{5.80}$$

$$\overline{\nu}_\mu + e^- \rightarrow \overline{\nu}_\mu + e^- \tag{5.81}$$

$$\nu_e + e^- \rightarrow \nu_e + e^- \tag{5.82}$$

$$\overline{\nu}_e + e^- \rightarrow \overline{\nu}_e + e^- \tag{5.83}$$

The CC processes, given by Equations (5.78) and (5.79), typically do not deposit enough energy to pass the minimum energy requirement for the analysis; hence, only the elastic case ($\nu + \mathrm{e}^- \rightarrow \nu + \mathrm{e}^-$) contributes, where:

$$\frac{d\sigma(\nu_\mu\, e)}{dy} = \frac{G_F^2 m_e E}{2\pi}\left[(g_V^e + g_A^e)^2 + (g_V^e - g_A^e)^2\,(1-y)^2)\right] \quad (5.84)$$

$$\frac{d\sigma(\overline{\nu}_\mu\, e)}{dy} = \frac{G_F^2 m_e E}{2\pi}\left[(g_V^e - g_A^e)^2 + (g_V^e + g_A^e)^2\,(1-y)^2)\right] \quad (5.85)$$

$$\frac{d\sigma(\nu_e\, e)}{dy} = \frac{G_F^2 m_e E}{2\pi}\left[(g_V^e + g_A^e + 2)^2 + (g_V^e - g_A^e)^2\,(1-y)^2)\right] \quad (5.86)$$

$$\frac{d\sigma(\overline{\nu}_e\, e)}{dy} = \frac{G_F^2 m_e E}{2\pi}\left[(g_V^e - g_A^e)^2 + (g_V^e + g_A^e + 2)^2\,(1-y)^2)\right] \quad (5.87)$$

$$g_V^e = 2\sin^2\theta_W - \frac{1}{2}, \quad g_A^e = -\frac{1}{2}$$

Note that in contrast to the NC $\nu_\mu\, e^- \to \nu_\mu\, e^-$ reactions, $\nu_e\, e^- \to \nu_e\, e^-$ elastic scattering is mediated by both NC and CC interactions; the $(g_V^e + g_A^e + 2)^2$ term accounts for the interference between these two contributions. Here, y is defined to be the momentum fraction of the outgoing lepton ($y \equiv E_e/E$), E is the incident neutrino energy, and g_V^e, g_A^e are the vector and axial-vector couplings of the weak current to the electron. Given Fermilab Tevatron energies, $E \gg m_e$, left-right interference terms involving factors of m_e/E vanish. Due to the light mass of the target, such reactions have very little available center of mass energy, $s = 2m_eE$, which implies a small cross section. The scale of $\sigma(\nu + e^-)$ is on the order of 10^{-42} cm^2 GeV^{-1}, such that scattering off target electrons is roughly four orders of magnitude less likely than scattering off nucleons.

The bound $0 < y < 1$ imposes a further restriction on the kinematics of elastic neutrino-electron scattering events. If we let k, k' be the 4-momentum vectors of the incoming and outgoing neutrino, respectively, and likewise p, p' for the electron, then by energy and momentum conservation it follows that:

$$(k - p')^2 = (k' - p)^2$$

$$
\begin{aligned}
E_e E - E p_e \cos\theta_e &= m_e E' \\
E_e E - E p_e \cos\theta_e &= m_e (E - E_e + m_e) \\
E_e E (1 - \cos\theta_e) &= m_e (E - E_e) \\
E_e (1 - \cos\theta_e) &= m_e (1 - y) \\
E_e \theta_e^2 &= 2 m_e (1 - y)
\end{aligned}
$$

Here, E is the incoming neutrino energy, E' is the outgoing neutrino energy ($E' = E + m_e - E_e$ by energy conservation), E_e and p_e are the outgoing electron energy and momentum, and θ_e is the angle of the outgoing electron with respect to the incoming neutrino direction. From the kinematic constraint, $0 < y < 1$, it follows that the electron is emitted in a very forward direction:

$$E_e \, \theta_e^2 < 2 \, m_e \tag{5.88}$$

Hence, elastic neutrino scattering events manifest themselves with small likelihood as a single forward–scattered electron in the detector.

5.1.9 The Propagator Term

The neutrino NC and CC cross sections in the simulation include the effect of the massive Z or W boson propagator via the multiplication:

$$\frac{d^2\sigma_{NC}^{\nu,\overline{\nu}}}{dx\,dy} = \frac{d^2\sigma_{NC}^{\nu,\overline{\nu}}}{dx\,dy} \cdot \frac{1}{(1 + Q^2/M_Z^2)^2} \tag{5.89}$$

$$\frac{d^2\sigma_{CC}^{\nu,\overline{\nu}}}{dx\,dy} = \frac{d^2\sigma_{CC}^{\nu,\overline{\nu}}}{dx\,dy} \cdot \frac{1}{(1 + Q^2/M_W^2)^2} \tag{5.90}$$

The effect of the propagator correction is a +0.00023 shift in R^{ν} and a +0.00015 shift in $\mathrm{R}^{\overline{\nu}}$, resulting in a net +0.00031 shift in $\sin^2\theta_W$.

5.1.10 Non-Isoscalar Target

An idealized isoscalar target consists of equal numbers of protons and neutrons; however, the NuTeV detector is an iron target containing a 5.67% neutron excess:

$$\frac{N-Z}{A} = \frac{N-Z}{N+Z} = 0.0567 \tag{5.91}$$

where N, Z, and A=N+Z are the number of neutrons, protons, and nucleons in the iron nucleus. Because a proton is composed of uud valence quarks, and a neutron of ddu quarks, the neutron excess implies an unequal number of u and d quarks in the target. In particular, assuming isospin symmetry, $u^p = d^n$ and $d^p = u^n$, this translates into roughly a 2% excess of d quarks relative to u quarks. The dominant effect is in the CC cross section. From charge conservation, neutrinos preferentially scatter off of d quarks, and antineutrinos off of u quarks (see Appendix D). The result is an enhancement in the CC neutrino cross section combined with a corresponding reduction in the CC antineutrino cross section[†]. The NC cross section is also enhanced, but by a smaller percentage.

The average nucleon cross section for our non-isoscalar target is obtained by explicitly calculating the proton and neutron cross sections and correcting their contributions by the weighted average of their densities:

$$\frac{d^2\sigma^{\nu N}}{dx\,dy} = \frac{1}{A}\cdot\left(Z\,\frac{d^2\sigma^{\nu p}}{dx\,dy} + N\,\frac{d^2\sigma^{\nu n}}{dx\,dy}\right) \tag{5.92}$$

The non-isoscalarity of the NuTeV target results in a -0.0039 decrease in $R^{\nu}_{\rm exp}$ and an +0.0043 increase in $R^{\overline{\nu}}_{\rm exp}$. The result is a large -0.0080 shift in $\sin^2\theta_W$ arising mainly due to the fact that $d_v \simeq u_v(1-x)$.

[†] The decrease in $\sigma^{\overline{\nu}}$ is slightly less than the increase in σ^{ν} due to the add'l $(1-y)^2$ dependence.

5.1.11 Lepton Mass Terms

The Monte Carlo includes terms in the charged current neutrino cross section that are proportional to the lepton mass, m. The form for the additional cross section is derived in Section 1.3 and follows the formalism of Reference [60][‡]:

$$\begin{aligned}\frac{d^2\sigma_{CC}^{\nu,\overline{\nu}}}{dx\,dy} = \left(\frac{d^2\sigma_{CC}^{\nu,\overline{\nu}}}{dx\,dy}\right)_{m=0} &+ \frac{G_F^2 ME}{\pi}\left[\frac{m^2 y}{4MEx}2xF_1(x,Q^2) - \frac{m^2}{4E^2}F_2(x,Q^2)\right.\\ &\mp \frac{m^2 y}{4MEx}xF_3(x,Q^2) + \frac{m^2}{M^2}\left(\frac{Mxy}{2E}+\frac{m^2}{4E^2}\right)F_4(x,Q^2)\\ &- \left.\frac{m^2}{2MEx}xF_5(x,Q^2)\right] \qquad (5.93)\end{aligned}$$

where $\left(\frac{d^2\sigma_{CC}^{\nu,\overline{\nu}}}{dx\,dy}\right)_{m=0}$ is given by Equation (1.25), and m is either m_μ or m_e depending on the flavor of the interacting neutrino. In computing this contribution to the inclusive cross section, it is further assumed that $2xF_1(x,Q^2) = F_2(x,Q^2)$, $F_4(x,Q^2) = 0$, and $xF_5(x,Q^2) = F_2(x,Q^2)$. The latter two constraints are known as the Albright-Jarlskog relations. The effect of the inclusion of non-zero lepton mass terms results in small shifts in $R^{\nu}_{\rm exp}$, $R^{\overline{\nu}}_{\rm exp}$, and $\sin^2\theta_W$ of $+0.00024$, $+0.00050$, and $+0.00018$, respectively.

[‡] Beware, there is a sign mistake in the F_3 term in Equation (3.4) in Reference [60] and a factor of $1/x$ missing in the F_1 and F_3 terms in Equation (6.3) in Reference [61].

5.1.12 Higher Twist Effects

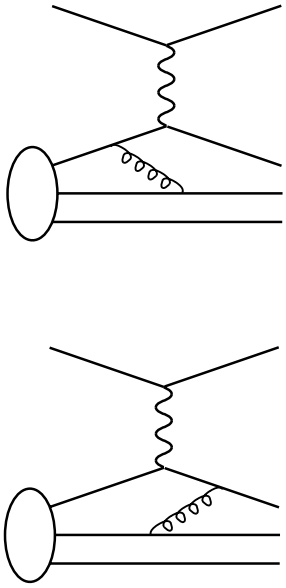

Figure 5.32: Diagrams illustrating several higher twist processes.

Non-perturbative higher twist effects arise from inter–quark interactions in the nucleon, resulting in a kind of "cross-talk" between the struck and spectator quarks. Because the quark involved in the hard scatter communicates via a gluon propagator, the effect is suppressed by powers of $1/\mathrm{Q}^2$. Therefore, higher twist effects are only important at low Q^2. Several Feynman diagrams illustrate higher twist processes in Figure 5.32.

Because neither CCFR nor NuTeV has sufficient low Q^2, high x differential cross section data to constrain the BGPAR fit, the Q^2 evolution of the F_2 and xF_3 structure functions must be augmented to account for such possible color interactions among quarks. Remaining higher twist effects are measured by comparing SLAC electron scattering and BCDMS muon scattering measurements of $F_2(x,\mathrm{Q}^2)$ to the model expectation and fitting deviations to the form $1 + \mathrm{ht(x)}/\mathrm{Q}^2$ [62]. The fit finds:

$$\mathrm{ht}(x) = \max\left[0.672\left(\frac{x^{1.893}}{1-1.138\,x} - 0.236\right), 10\right], \quad x > 0.4 \tag{5.94}$$

The resultant corrections increase the CC and NC cross section predictions at high x and low Q^2:

$$\frac{\sigma^2_{NC,CC}}{dx\,dy} = \frac{\sigma^2_{NC,CC}}{dx\,dy}\cdot\left(1+\frac{\mathrm{ht(x)}}{\mathrm{Q}^2}\right), \quad x > 0.4 \tag{5.95}$$

Figure 5.33 shows the improved agreement with SLAC and BCDMS $F_2(x,\mathrm{Q}^2)$ data as a result of the modification to the BGPAR prediction at high x. The net effects are +0.00012, +0.00013, +0.00014 increases in R^{ν}_{exp}, $R^{\overline{\nu}}_{\mathrm{exp}}$, and $\sin^2\theta_W$, respectively.

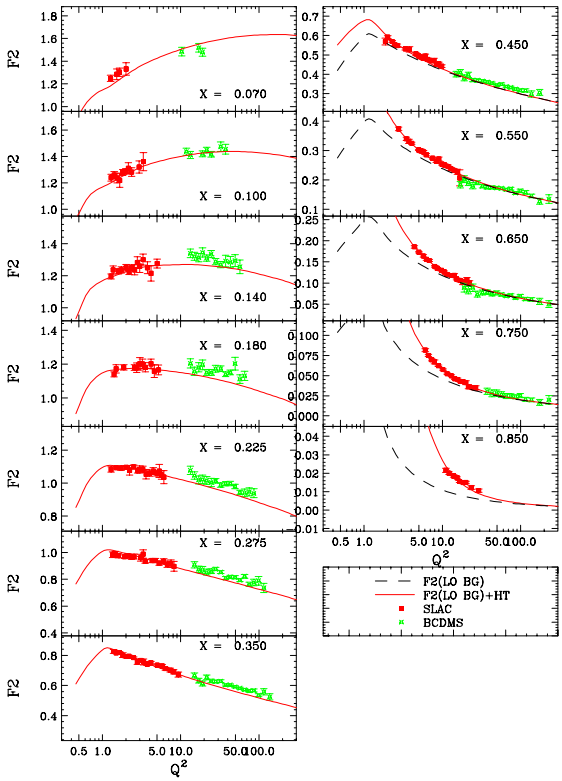

Figure 5.33: LO BGPAR $F_2(x,\mathrm{Q}^2)$ predictions before (dotted) and after (solid) applying the higher twist correction as compared to SLAC and BCDMS $F_2(x,\mathrm{Q}^2)$ data. Plot courtesy of U.K. Yang [63].

5.1.13 Long Exit Correction

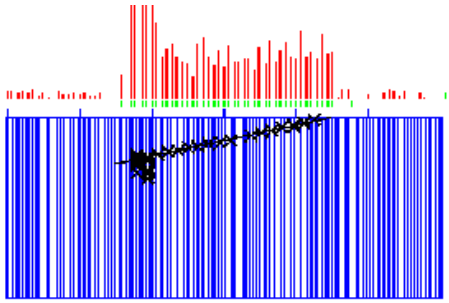

Figure 5.34: A typical long exit event that has exited the NuTeV calorimeter.

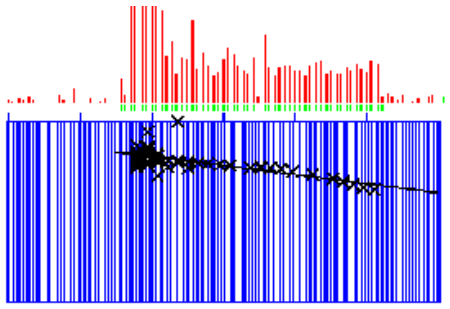

Figure 5.35: A typical long exit event that has ranged out in the NuTeV calorimeter.

The cross section data used in the BGPAR fit requires a toroid analyzed muon, hence we must verify applicability to highly inelastic events, $y \to 1$, which lack a toroid analyzed muon (see, for example, Figures 5.41 – 5.44). Given that the largest background to the NC sample are these high y CC events (17% of short events in ν mode, 7% in $\overline{\nu}$ mode), it is crucial to verify the high y Monte Carlo simulation to roughly a percent accuracy. For this purpose, we choose a control sample of "long exit" events. Long exits have lengths greater than or equal to 31 counters, originate in the calorimeter, but do not penetrate into the toroid. The length cut at 31 safely ensure that there are no ν_e events and essentially no NC events in the sample ($< 0.1\%$ contamination). As a result, long exit events include CC events in which the muon exits out the side of the detector (Figure 5.34), with wide angle:

$$\theta_\mu^2 = \frac{2Mx\left(E_\nu - \mathrm{E_{had}}\right)}{E_\mu E_\nu} = \frac{2Mxy}{E_\mu} \tag{5.96}$$

and also CC events with a low energy muon that "ranges out" in the calorimeter (Figure 5.35). Figure 5.36 shows the kinematics of these events in comparison to

CC events with a toroid muon; long exits are high y, moderate x events.

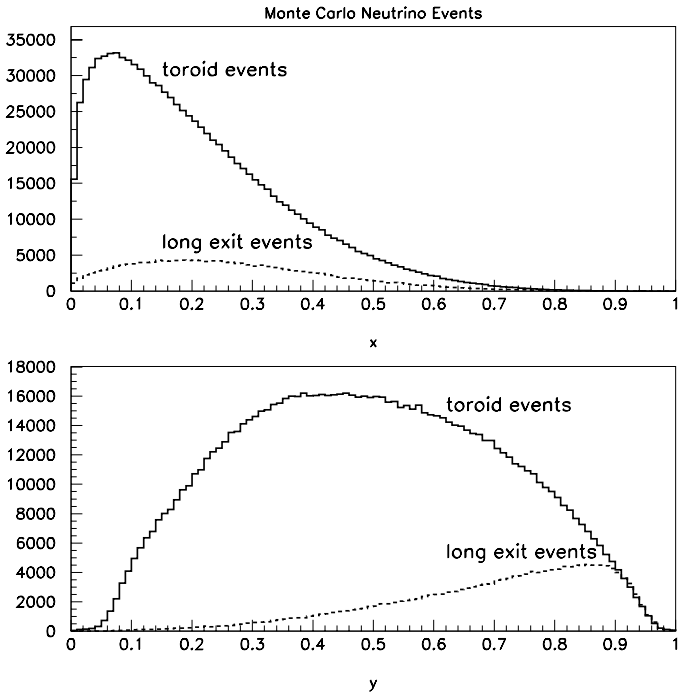

Figure 5.36: Comparison of event kinematics for CC neutrino long exit (dashed) and more common toroid events (solid).

Energy distribution comparisons reveal that the Monte Carlo reasonably predicts the shape of long exits populating the outer region of the detector (30-50 inches), but not the inner volume (0–30 inches). As shown in Figure 5.37, the Monte Carlo systematically overpredicts the number of inner radius long exits at moderate energies (E_{had} = 40–115 GeV), while underpredicting their level at higher energies (E_{had} = 115–160 GeV). The transition at 115 GeV occurs where the long exit distribution falls most rapidly. Because the disagreement is localized in x and Q^2, modifications can be made directly to the high Q^2, moderate x PDFs. The CCFR cross section data does not include high y events, so the PDF is not otherwise constrained in this

region. The adopted procedure is to decrease the BGPAR valence distributions by 2.6% in the region $0.005\,Q^2 < x < 0.0133\,Q^2$ and increase their contribution by 2.0% in the region $0.003\,Q^2 < x < 0.005\,Q^2$. Simultaneously, the total quark content $(q + \overline{q})$ must be conserved, and the correction is limited to regions in which there is appreciable valence content, namely $x > 0.1$. Given that the same correction is applied to both u and d distributions, the ratio d/u is preserved to maintain agreement with d_v/u_v from NMC data and $\overline{d}/\overline{u}$ from E866 data, as presented in Section 5.1.2.

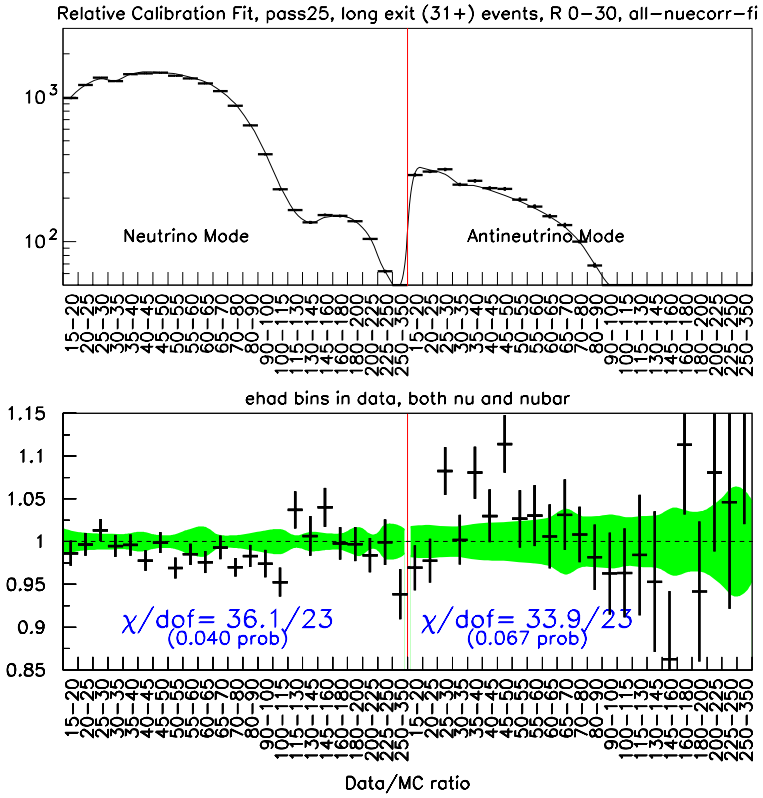

Figure 5.37: Comparison of data and Monte Carlo E_{had} distributions for **inner radius** (0–30 inches) long exit events **before** correction. The ν ($\overline{\nu}$) distribution is displayed on the left (right). The band indicates the $\pm 1\sigma$ systematic uncertainty.

This correction fixes the inner radius long exit disagreement, requires only small changes to the LO BGPAR parton distributions, maintains Monte Carlo predictive

power for the CC cross section both in shape and normalization, results in a well-behaved flux, and leads to small changes in R^{ν} and $R^{\overline{\nu}}$ with no observed radial dependence. The effect of the long exit correction is a shift of –0.00021 (+0.00035) in $R^{\nu}_{\rm exp}$ ($R^{\overline{\nu}}_{\rm exp}$), for a net –0.00048 shift in the measured $\sin^2\theta_W$. Figure 5.38 displays the resultant energy distributions for inner radius long exit events, which agrees with data to within the assigned systematic uncertainties. Figure 5.39 displays the level of agreement for all long exit events in the sample. Further information on this correction can be found in Reference [54].

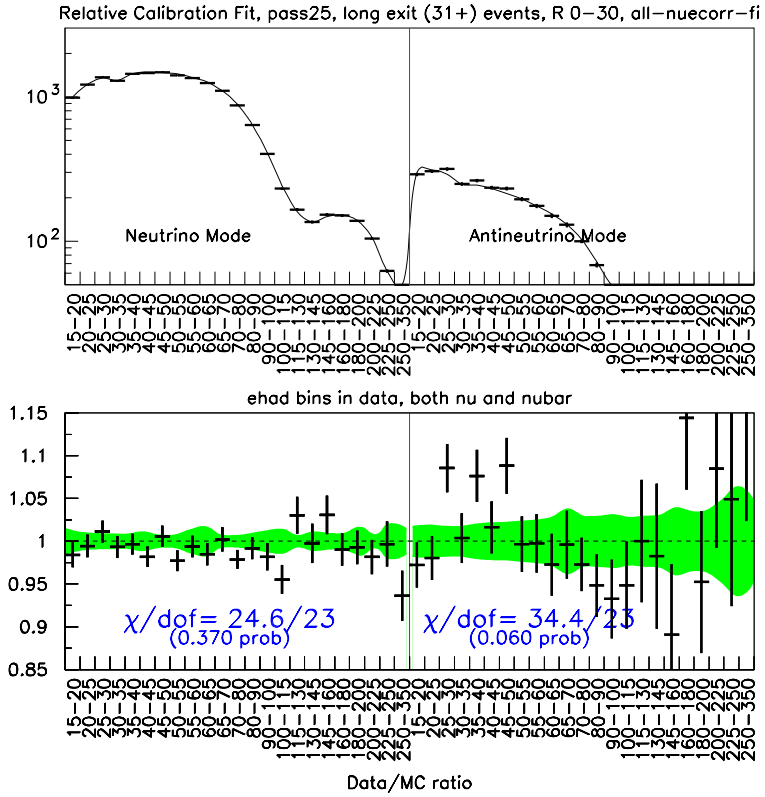

Figure 5.38: Comparison of data and Monte Carlo $E_{\rm had}$ distributions for **inner radius** (0–30 inches) long exit events **after** correction. The ν ($\overline{\nu}$) distribution is displayed on the left (right). The band indicates the $\pm 1\sigma$ systematic uncertainty.

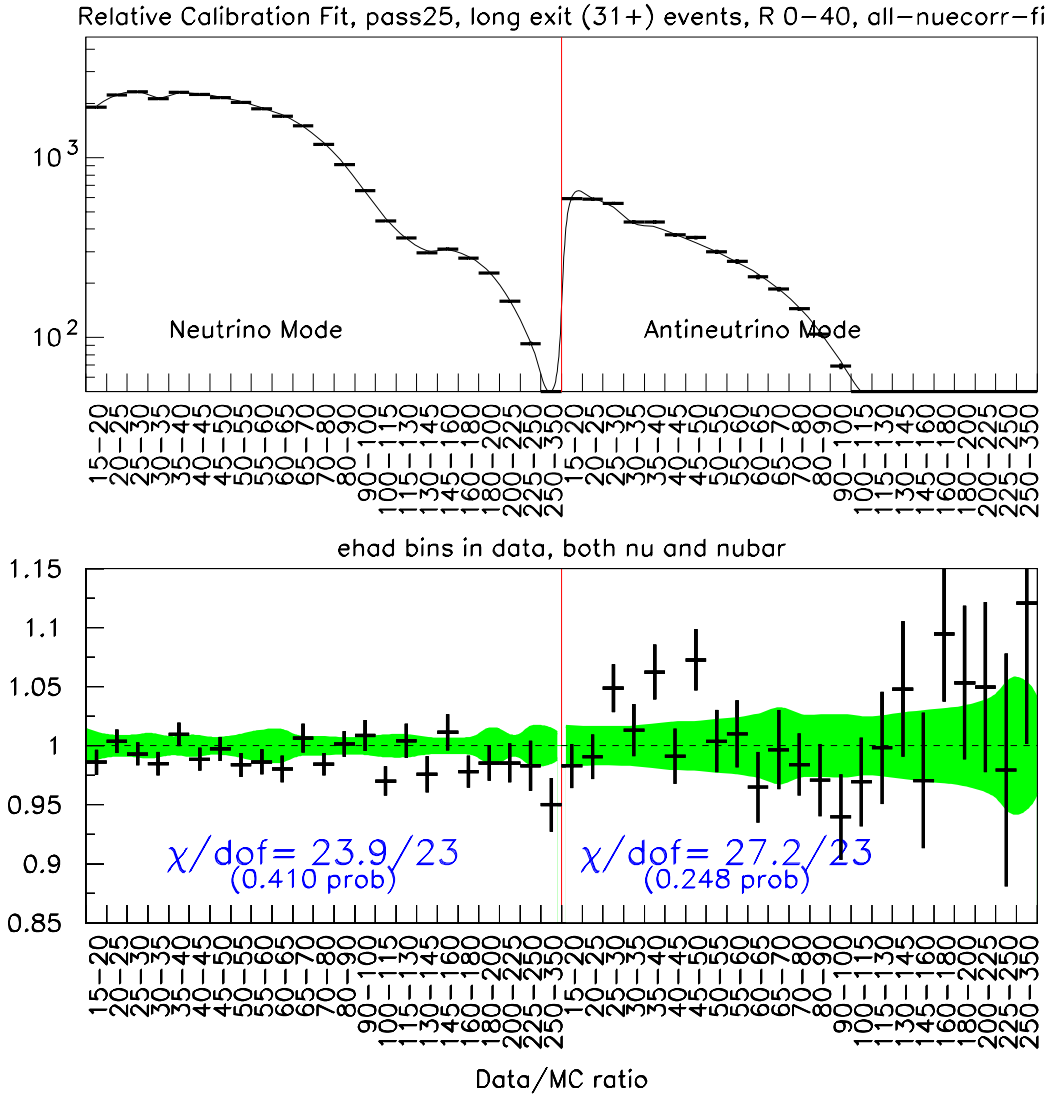

Figure 5.39: Comparison of data and Monte Carlo E_{had} distributions for **all** long exit events in the analysis sample **after** correction. The neutrino (antineutrino) distribution is displayed on the left (right) hand side of the plot. The band indicates the $\pm 1\sigma$ systematic uncertainty.

5.1.14 Data/MC Cross Section Comparison

This self consistent, QCD–inspired, enhanced LO model describes our data extraordinarily well. Figures 5.41 – 5.44 compare the final Monte Carlo and the CCFR charged current differential cross section data after all of the aforementioned components have been included in the Monte Carlo model. The comparisons are shown both at the pion peak, $E_\nu = 75$ GeV, and at the kaon peak, $E_\nu = 190$ GeV. Excellent agreement is in fact exhibited across the full kinematic range. The χ^2/dof for $x < 0.7$, $E_\nu < 360$ GeV is 2741/2770 which equates to a probability of 65%. Figure 5.40 subdivides the contributions to the net χ^2 in regions of x, y, and E_ν.

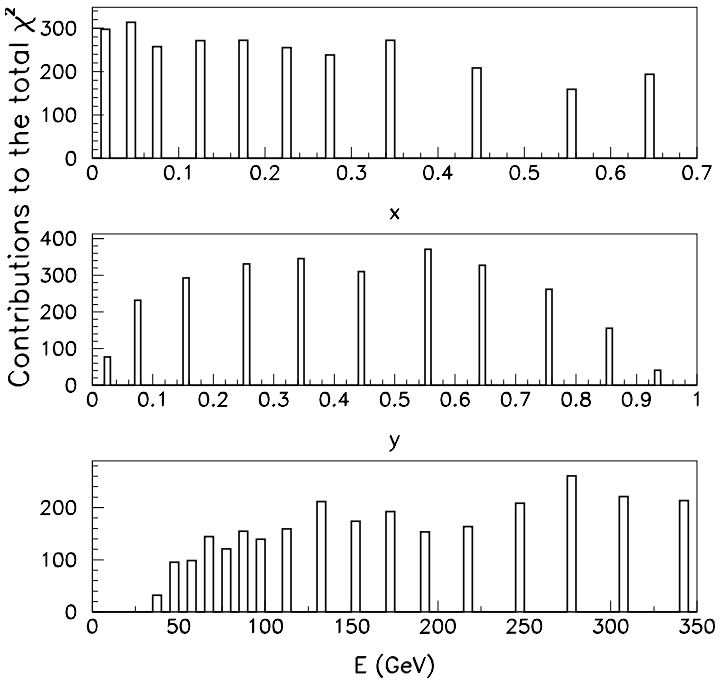

Figure 5.40: Contributions to the total $\chi^2 = \left(\frac{\frac{d^2\sigma^{Data}}{dx\,dy} - \frac{d^2\sigma^{MC}}{dx\,dy}}{\delta \frac{d^2\sigma^{Data}}{dx\,dy}} \right)^2$ in bins of x, y, E_ν.

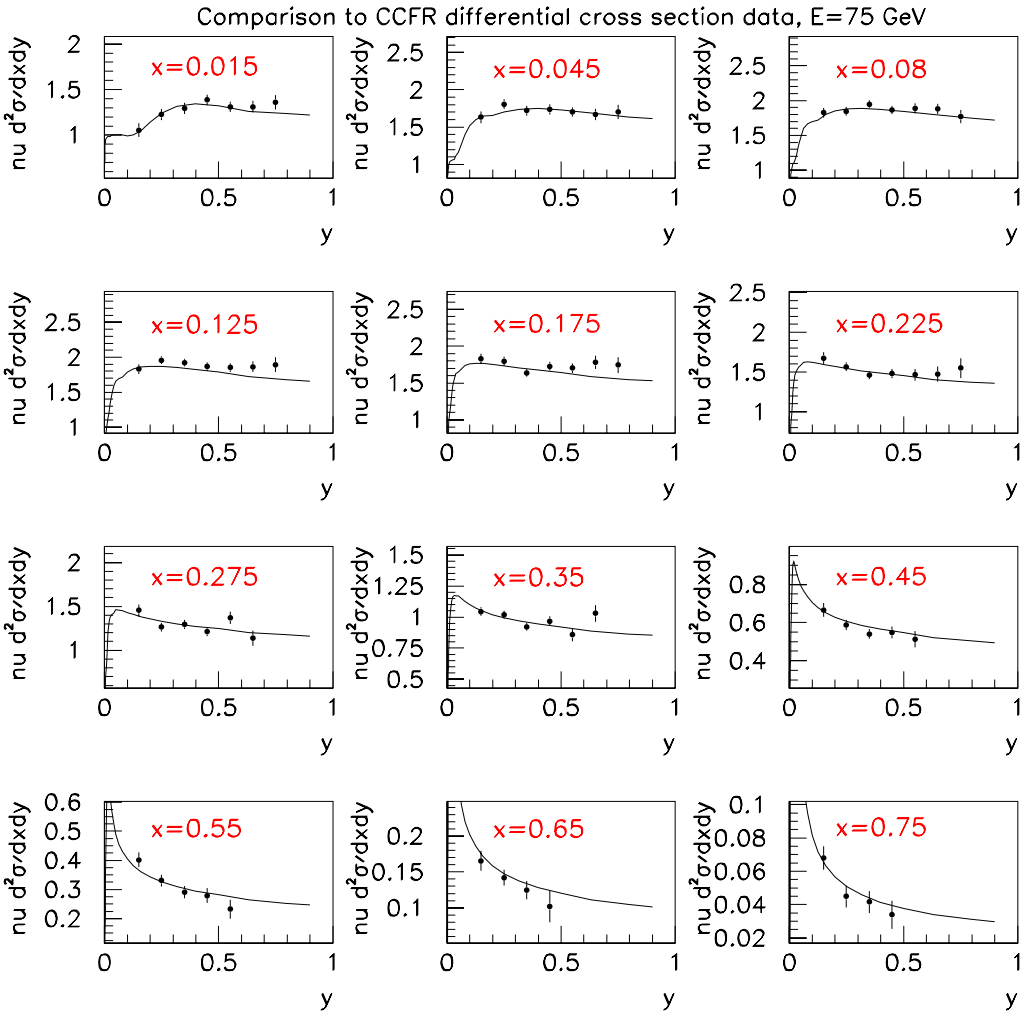

Figure 5.41: Final Monte Carlo prediction compared to CCFR **neutrino** CC differential cross section data at E_ν=75 GeV.

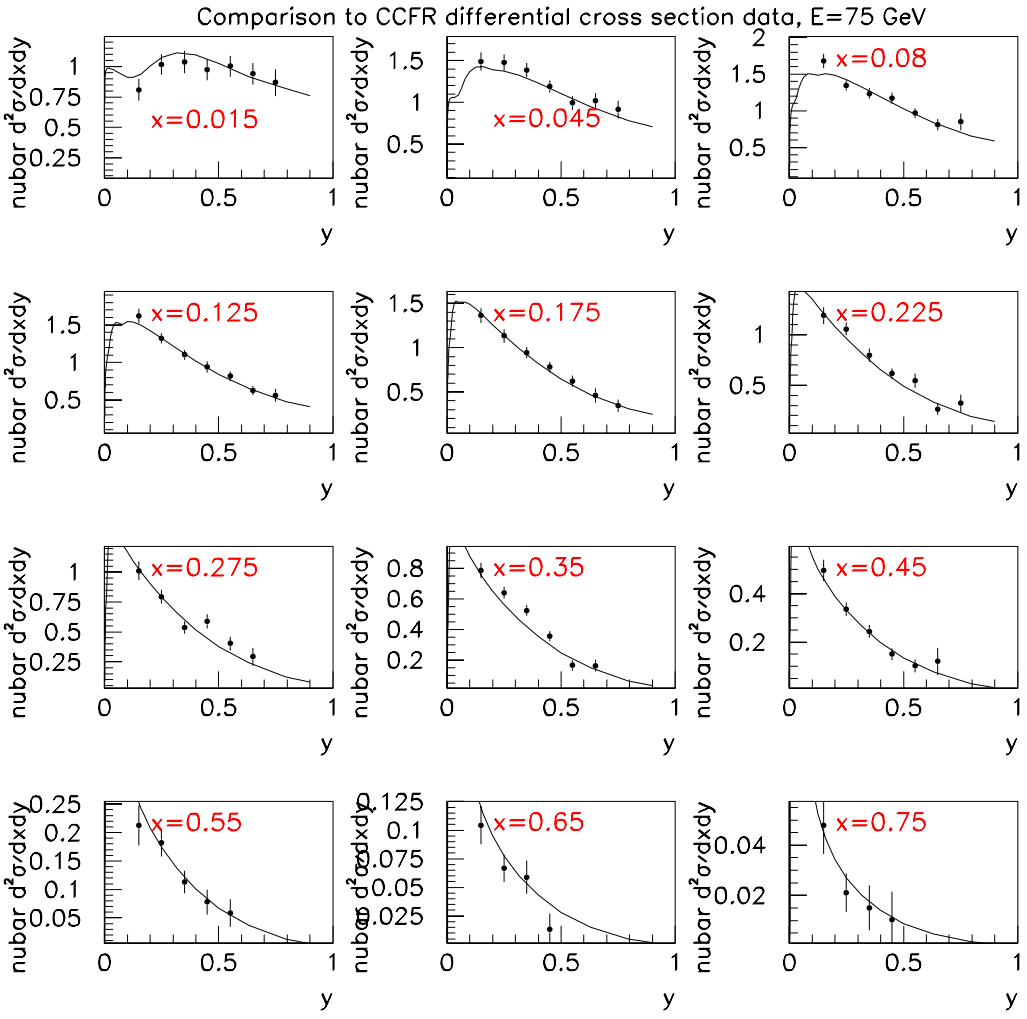

Figure 5.42: Final Monte Carlo prediction compared to CCFR **antineutrino** CC differential cross section data at E_ν=75 GeV.

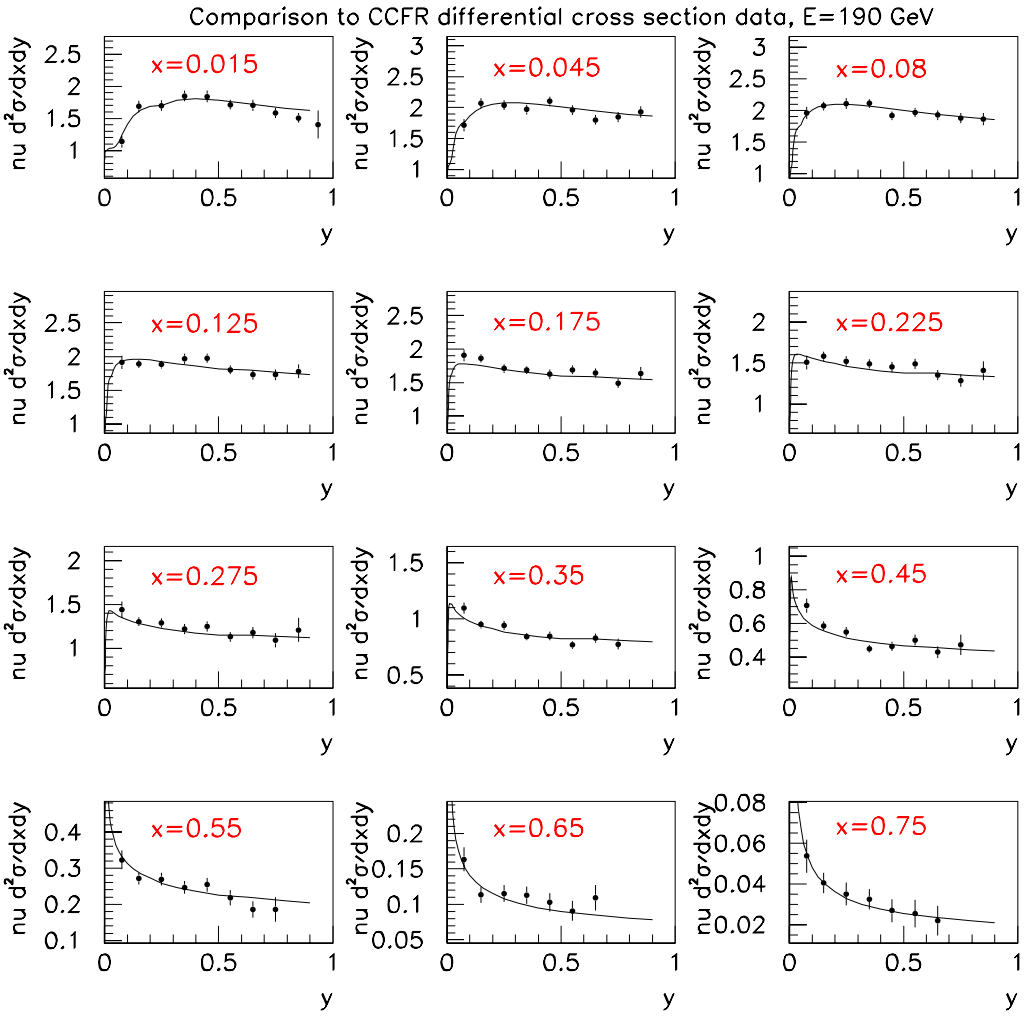

Figure 5.43: Final Monte Carlo prediction compared to CCFR **neutrino** CC differential cross section data at E_ν=190 GeV.

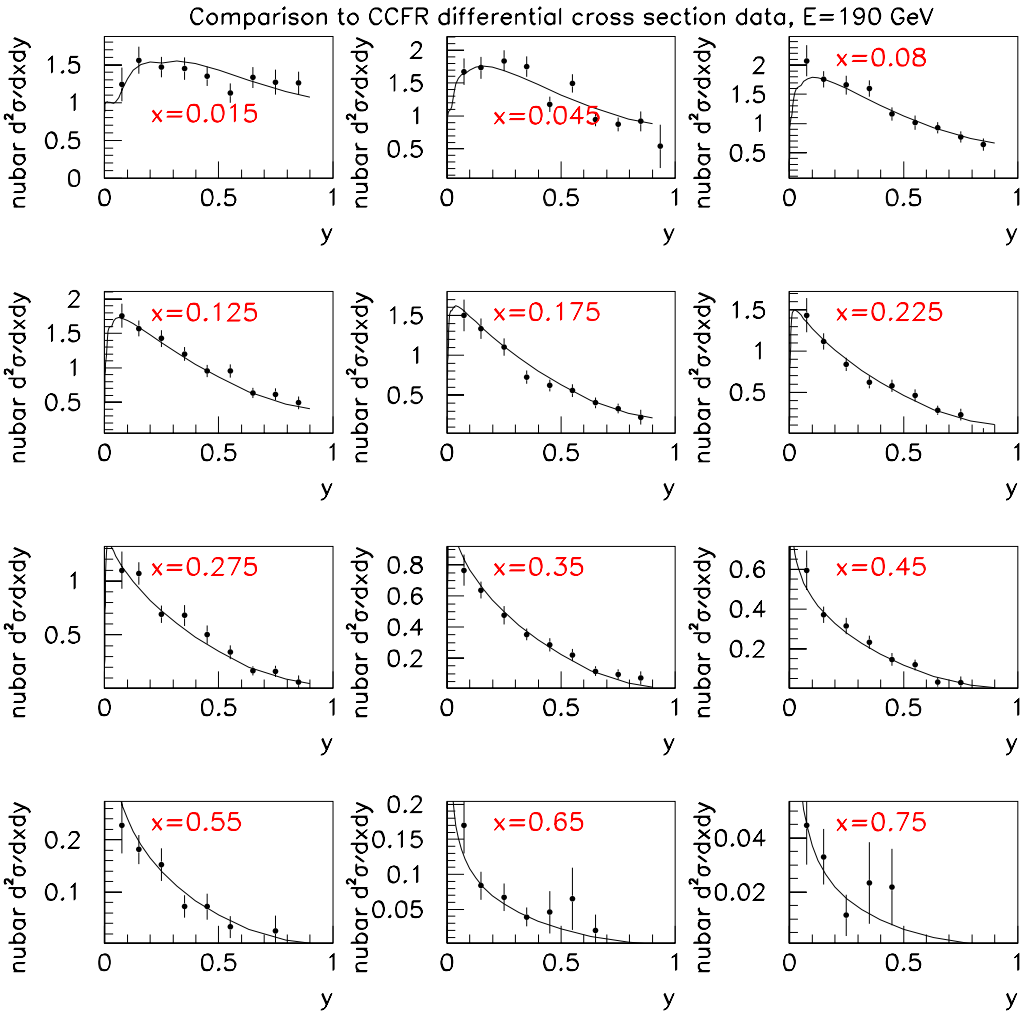

Figure 5.44: Final Monte Carlo prediction compared to CCFR **antineutrino** CC differential cross section data at E_ν=190 GeV.

5.1.15 Cross Section with External PDFs

External PDFs do not fare nearly as well as our tuned BGPAR parameterization in describing the neutrino data. Figures 5.46 and 5.47 demonstrate the poor performance of the leading order CTEQ and GRV PDFs in reproducing the CCFR differential cross section data after correcting the external PDFs for heavy target effects (Figure 5.45). The χ^2/dof using external PDFs is a factor 2–3 worse than our default fit: 7250/2570 for CTEQ4LO and 4420/2570 for GRV94LO. The deficiency in the CTEQ and GRV PDFs results from their use of R_L, higher twist, and strange sea parameters that are incompatible with our LO cross section model; hence, using more recent CTEQ or GRV fits would not alter this conclusion. This the reason why NuTeV must use its own internal parton distributions.

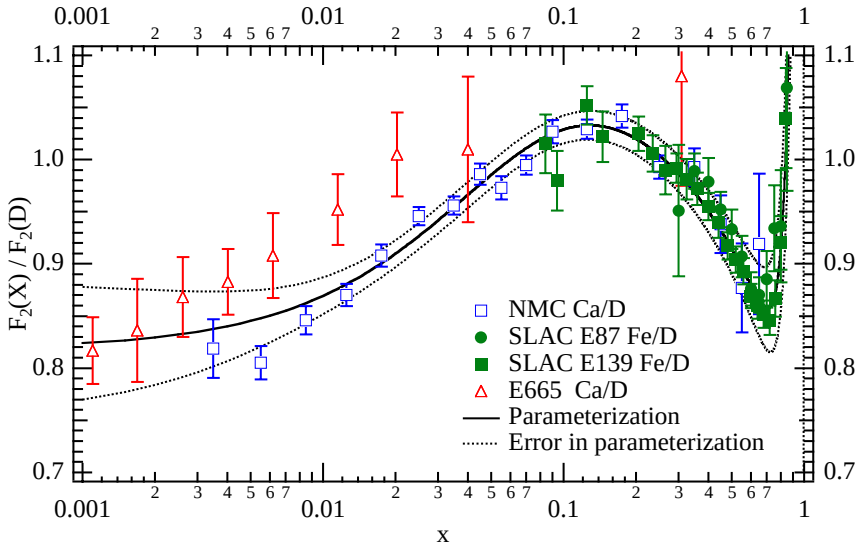

Figure 5.45: The ratio of F_2 on heavy nuclei to F_2 on deuterium as measured from charged lepton scattering data (SLAC [55], NMC [56], E665 [57]). The data is parametrized by the functional form: $F_2(N)/F_2(D) = 1.0963 - 0.36427\,x - 0.27805\exp^{-21.936\,x} + 2.7715\,x^{14.417}$ [58].

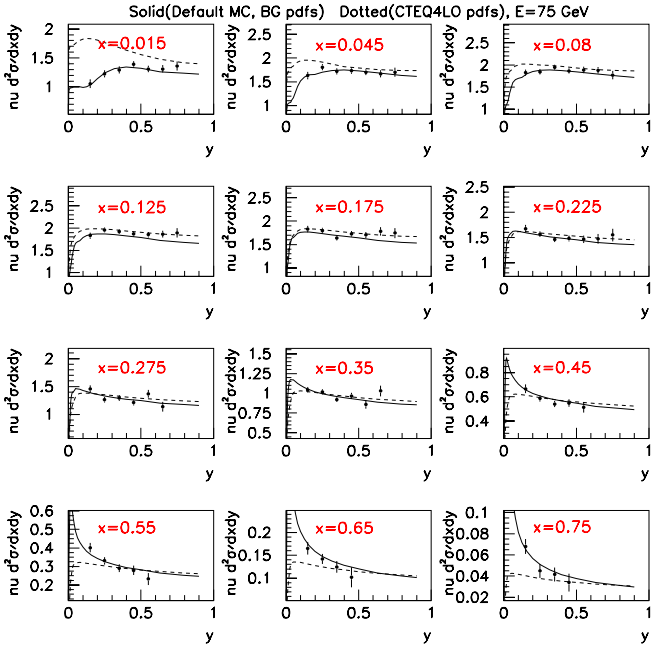

Figure 5.46: LO cross section prediction using **CTEQ4LO** (dotted curve) versus default BGPAR (solid curve) compared to CCFR data at $E_\nu = 75$ GeV.

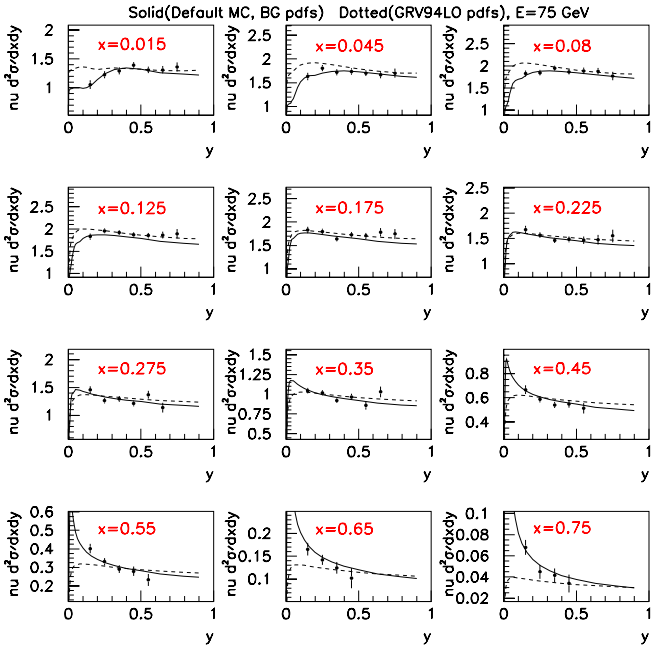

Figure 5.47: LO cross section prediction using **GRV94LO** (dotted curve) versus default BGPAR (solid curve) compared to CCFR data at $E_\nu = 75$ GeV.

5.2 Neutrino Flux

NuTeV produced separate neutrino and antineutrino beams that were roughly 98% ν_μ and $\overline{\nu}_\mu$, respectively, with small fluxes of electron and "wrong–sign" neutrinos (Figure 5.48). A detailed beam Monte Carlo is used to predict the various sources of neutrinos, whose numerical contributions are provided for reference in Table 5.7. The following sections describe the simulation and tuning of the ν_μ and ν_e beam predictions.

Source	Neutrino Mode	Antineutrino Mode
$\pi^\pm, K^\pm \to \mu^\pm \nu_\mu\,(\overline{\nu}_\mu)$	0.982	0.973
$K^\pm_{e3}$	0.01570 ± 0.00030	0.01150 ± 0.00020
K_{Le3}, K_{Se3}	0.00065 ± 0.00007	0.00290 ± 0.00030
Charmed Meson $\to \nu_e$	0.00042 ± 0.00006	0.00155 ± 0.00020
$\mu \to \nu_e$	0.00007 ± 0.00001	0.00010 ± 0.00001
$\Lambda_c, \Lambda, \Sigma$	0.00003 ± 0.00003	0.00023 ± 0.00020

Table 5.7: Fraction of observed neutrino interactions by production process.

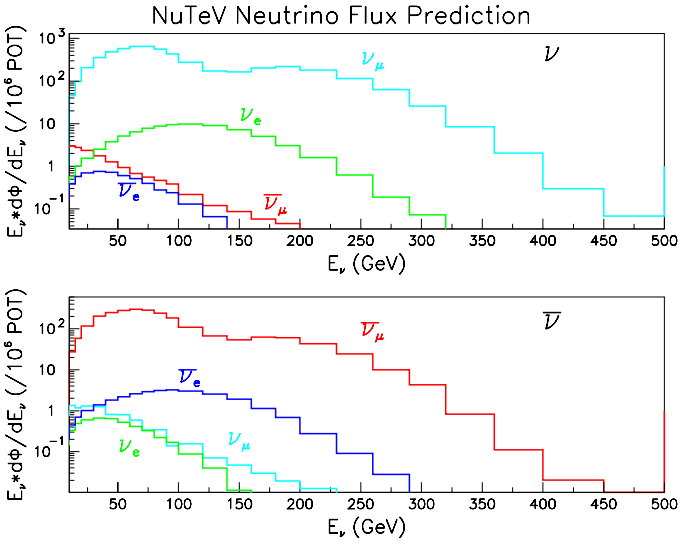

Figure 5.48: Spectra of various contributions to the NuTeV neutrino beam.

5.2.1 Muon Neutrino Flux

The dichromatic muon neutrino beam is dominated by the two–body decays of pions and kaons in the NuTeV SSQT:

$$\pi^+ \rightarrow \mu^+ + \nu_\mu, \quad \pi^- \rightarrow \mu^- + \overline{\nu}_\mu \qquad (\mathrm{BR} = 100\%) \tag{5.97}$$

$$K^+ \rightarrow \mu^+ + \nu_\mu, \quad K^- \rightarrow \mu^- + \overline{\nu}_\mu \qquad (\mathrm{BR} = 63.5\%) \tag{5.98}$$

The beam also includes three–body decays of both charged and neutral kaons to muons and electrons.

$$K^+ \rightarrow \pi^0 \mu^+ \nu_\mu, \quad K^- \rightarrow \pi^0 \mu^- \overline{\nu}_\mu \tag{5.99}$$

$$K^+ \rightarrow \pi^0 e^+ \nu_e, \quad K^- \rightarrow \pi^0 e^- \overline{\nu}_e \tag{5.100}$$

$$K_L \rightarrow \pi^- \mu^+ \nu_\mu, \quad K_L \rightarrow \pi^+ \mu^- \overline{\nu}_\mu \tag{5.101}$$

$$K_L \rightarrow \pi^- e^+ \nu_e, \quad K_L \rightarrow \pi^+ e^- \overline{\nu}_e \tag{5.102}$$

The $K^\pm \rightarrow \pi^0 e^\pm \nu_e \, (\overline{\nu}_e)$ decay are the dominant source of electron neutrinos in the experiment. The neutrino flux simulation is based on the TURTLE beam transport program [66] with charged pion and kaon production data from Atherton [67], parametrized for thick targets by Malensek [68]. Provided with information on the surveyed positions of the magnets, beam apertures, collimators, and measured magnetic fields in the SSQT, TURTLE uses ray tracing to project the trajectories of particles to their decay point. As can be seen from Figure 5.49, the TURTLE–based Monte Carlo does a reasonable job describing the energy distribution of ν_μ CC events in the data. The agreement is not perfect as a consequence of uncertainties in parent particle production.

To compensate for these uncertainties, the Monte Carlo spectrum is tuned to

the observed neutrino flux by varying the mean neutrino energies, both from π and K decays, and the relative K/π production rates. The ν_μ flux tuning procedure selects a high statistics sample of CC toroid events, not unlike the sample used in the NuTeV structure function analyses. Table 5.8 reports the adjustments required to fit the data, while Figures 5.50 and 5.51 display the comparisons after applying these small but necessary corrections to the Monte Carlo flux predictions.

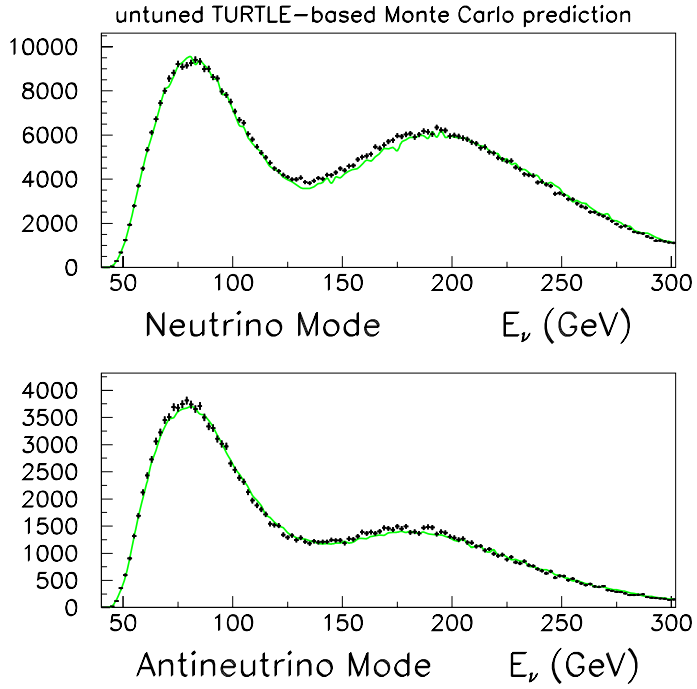

Figure 5.49: Neutrino energy spectrum for ν_μ CC events compared to the untuned TURTLE–based Monte Carlo prediction (solid curve).

Beam Type	E_π	E_K	K/π
ν_μ	–0.2%	–1.3%	+2.7%
$\overline{\nu}_\mu$	–0.4%	–0.9%	+2.8%

Table 5.8: Flux parameter adjustments required to fit the data.

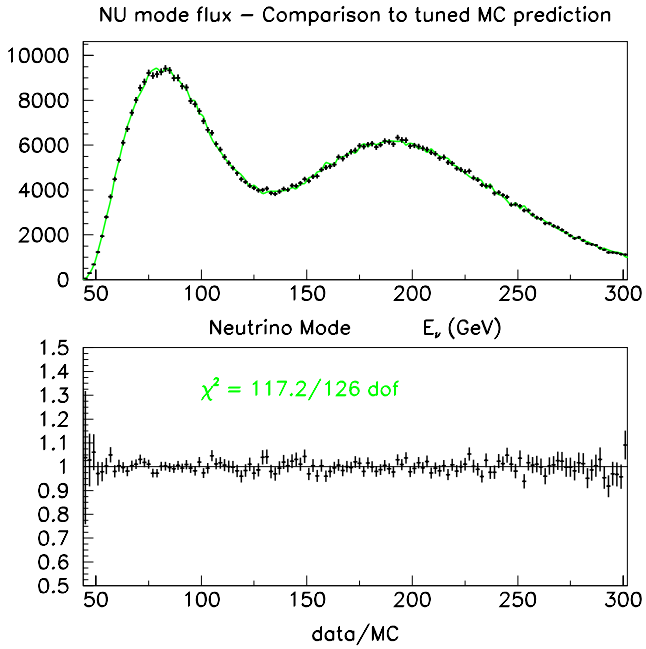

Figure 5.50: Comparison of CC ν_μ data events in the flux tuning sample to the Monte Carlo prediction (solid curve) after tuning.

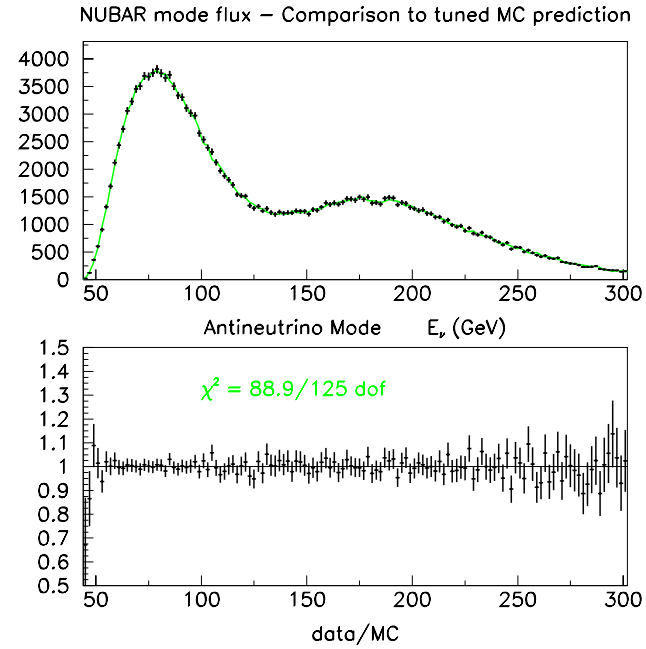

Figure 5.51: Comparison of CC $\overline{\nu}_\mu$ data events in the flux tuning sample to the Monte Carlo prediction (solid curve) after tuning.

5.2.2 Electron Neutrino Flux

Accurate modeling of the electron neutrino contamination in the NuTeV beam is a necessity given our inability to discriminate between ν_μ NC interactions and ν_e CC interactions, both of which register as short events in the detector. Despite comprising only $\sim 2\%$ of the neutrino beam, the ν_e's are a significant background, constituting roughly 5% of short events in both the ν and $\overline{\nu}$ samples. As a direct consequence, uncertainties in the ν_e content of the beam contribute the largest source of experimental error in the $\sin^2\theta_W$ analysis (Chapter 7).

The vast majority, 93% of the electron neutrino interactions in ν mode and 71% in $\overline{\nu}$ mode, of electron neutrinos result from $K^\pm_{e3}$ decays:

$$\begin{aligned} K^+ &\rightarrow \pi^0 + e^+ + \nu_e \\ K^- &\rightarrow \pi^0 + e^- + \overline{\nu}_e \end{aligned} \tag{5.103}$$

The Monte Carlo beam simulation is tuned to describe ν_e and $\overline{\nu}_e$ fluxes produced from charged kaon decay with high accuracy because the $K^\pm$ decay contribution is tightly constrained by the flux tuning procedure described in the previous section. Small corrections to the predicted flux, measured from the tuning procedure, are applied to the beam Monte Carlo prediction for ν_e's from charged kaon decays (Table 5.8). Other smaller sources of ν_e's, such as neutral kaon, charmed meson, μ, Λ_c, Λ, and Σ^- decays are also included. These contributions are displayed in Figure 5.52 and discussed in turn below.

Neutral Kaon Contribution

$K_L \rightarrow \pi^\pm e^\mp \nu_e$ (K_{Le3}) decays are also considered as a source of electron neutrinos; however, because of the low acceptance for neutral particles in the NuTeV SSQT,

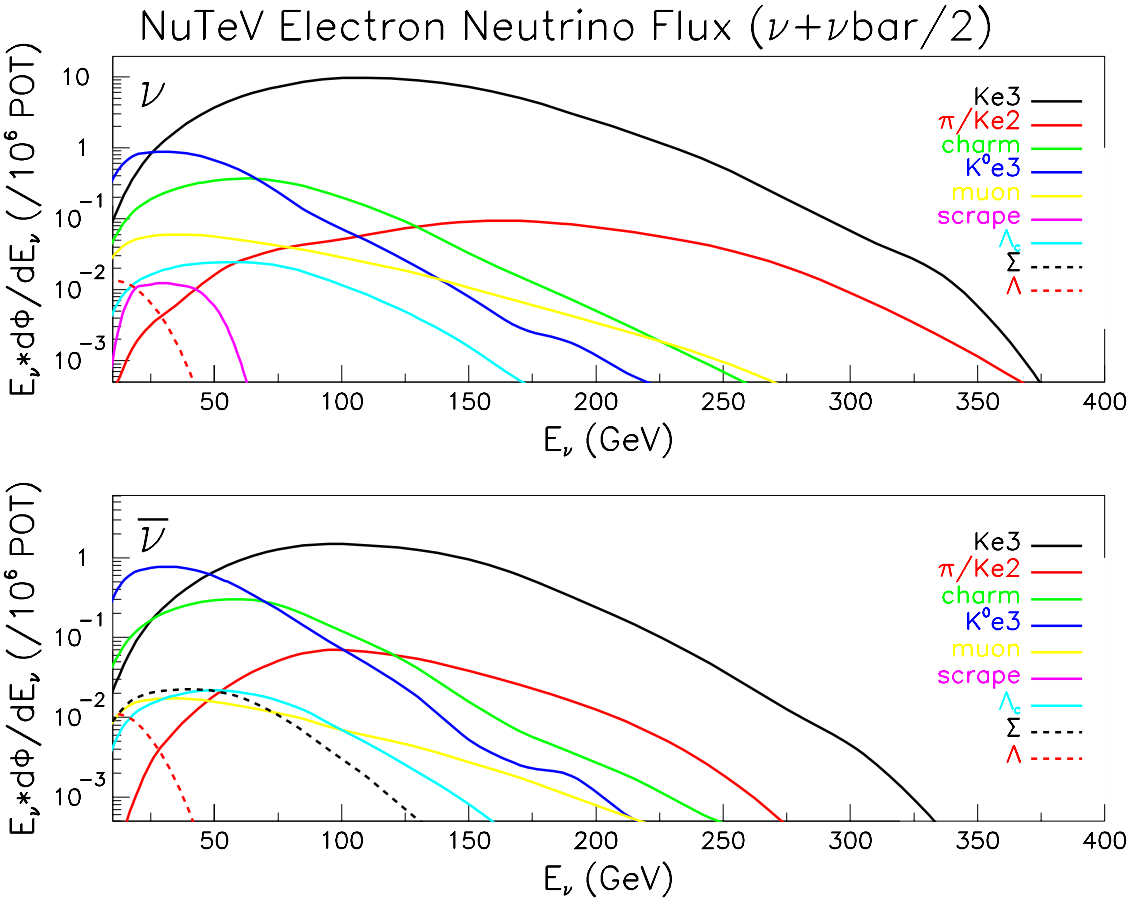

Figure 5.52: Contributions to the NuTeV ν_e flux as a function of neutrino energy for both neutrino (top) and antineutrino (bottom) running.

they contribute to electron neutrino rates only 4% (25%) of their charged counterparts in neutrino (antineutrino) running.

Given that kaon production is dominated by the strong interaction, the production rate for neutral kaons is obtained from the charged kaon rates. Quark counting yields:

$$N_{K^0} = \frac{1}{2}\left(N_{K^+} + N_{K^-}\right) \tag{5.104}$$

$$N_{\overline{K^0}} = N_{K^-} \tag{5.105}$$

This implies that the K_L production distribution, N_{K_L}, is approximately equal to $\frac{3}{4}N_{K^-} + \frac{1}{4}N_{K^+}$. The Malensek parameterization for $K^{\pm}$ production from protons on a Beryllium target [68] provides an estimate of the K^+ and K^- production spectra.

The Fermilab E731 experiment [69] has directly measured K_L production at 5 mrad and observed a deviation from the Malensek predicted spectrum parametrized by a multiplicative factor:

$$\begin{aligned} &1 + (6.033 \times 10^{-3})\,p - (4.283 \times 10^{-6})\,p^2 \\ &-(1.016 \times 10^{-7})\,p^3 + (1.802 \times 10^{-10})\,p^4 \end{aligned} \tag{5.106}$$

where p is the kaon momentum. This correction increases the predicted number of K_L's by roughly 50%. The E731 constraint together with the addition of K_{Se3} decays, which contribute $\sim$ 5% of the total number of ν_e's from neutral kaons, results in a -0.00022 shift in the measured value of $\sin^2\theta_W$ relative to the pure–Malensek–K_{Le3} model. Figure 5.53 shows the resultant momentum and angular spectra of parent K_L's whose descendent electron neutrinos hit the NuTeV detector. The mean K_L angle and energy are roughly 7 mrad and 100 GeV, respectively. An estimate of the uncertainties in the K_L production model is provided in Chapter 7.

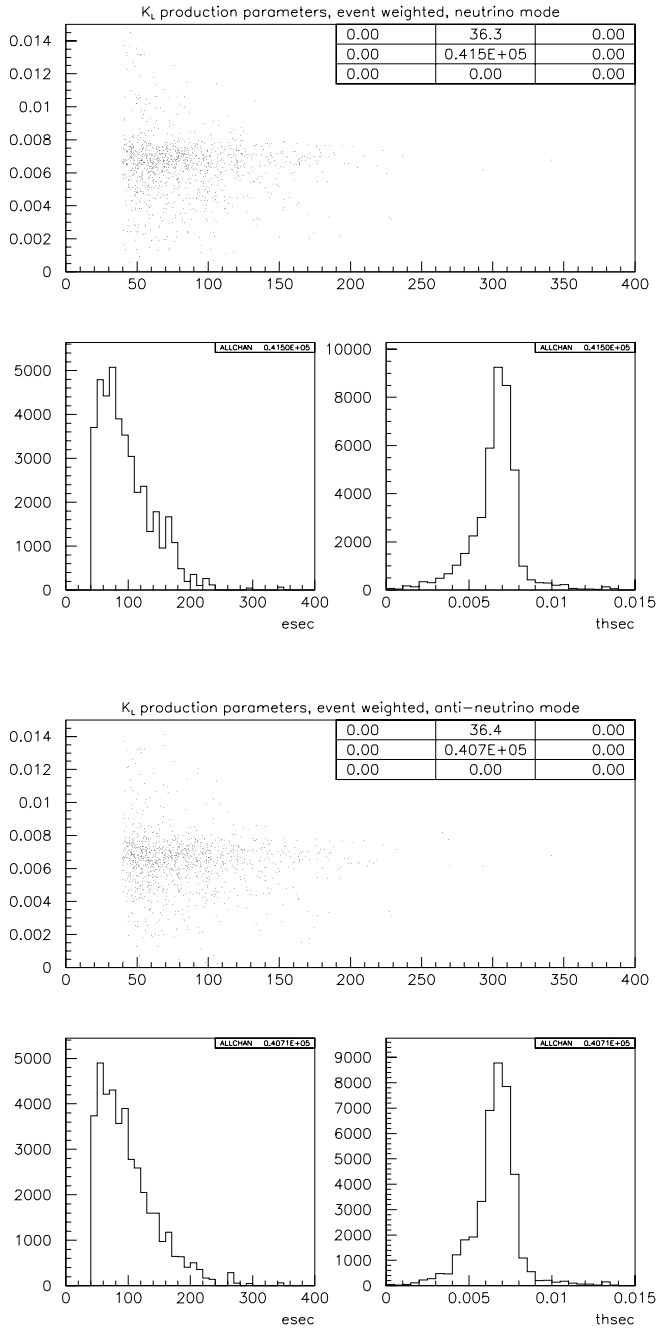

Figure 5.53: ν (top) and $\overline{\nu}$ (bottom) mode K_L production parameters. Top plot in each case is the angle versus momentum spectrum for K_L's producing ν_e's in the NuTeV detector. The bottom two plots show the K_L momentum and angular distributions. The plots are weighted by the probability for producing a ν_e which interacts in the detector.

Charmed Mesons

Charmed mesons are also a source of electron neutrinos. Both protons that interact in the BeO target and non–interacting protons that strike the beam dump have some finite probability of producing a $c\overline{c}$ pair that can fragment into a charmed meson ($D^{\pm}$, D^{0}). Their inclusive production was measured by two Fermilab experiments. Ammar *et al.* [70] reports total production cross sections measurements of $22^{+9}_{-7} \pm 5.5$ μb for D^0 and $26 \pm 4 \pm 6.5$ μb for D^+, both for 800 GeV protons incident on a liquid hydrogen target. Kodama *et al.* [71] finds higher total cross sections: $38 \pm 3 \pm 13$ μb for D^0 and $38 \pm 9 \pm 14$ μb for D^+, both for 800 GeV protons incident on emulsion. Combining the charged and neutral D production measurements,

$$\sigma(D^{\pm}) \cdot \mathrm{BR}(\mathrm{D}^{\pm} \to \mu) + \sigma(\mathrm{D}^{0}) \cdot \mathrm{BR}(\mathrm{D}^{0} \to \mu) \tag{5.107}$$

using $\mathrm{BR}(\mathrm{D}^{\pm} \to \mu) = 0.17$ and $BR(D^0 \to \mu) = 0.07$, yields $5.9^{+1.5}_{-1.4}$ μb for Ammar and 9.0 ± 3.0 μb for Kodama. The resultant Kodama–Ammar weighted average is therefore 6.5 ± 1.3 μb. Table 5.9 summarizes these computations. While the pure–Kodama estimate is used to predict the rate of D meson production in the NuTeV beamline simulation, the prediction is reweighted by a factor $6.5\,\mu\mathrm{b}/9.0\,\mu\mathrm{b} = 0.72$ to yield a total cross section in accord with this weighted average. Changing from the Kodama central value to the Kodama–Ammar average increases the $\sin^2\theta_W$ measurement by 0.00016.

Because the charmed mesons decay quickly, they leave no time for the wrong–sign mesons to bend out of the beamline. Therefore, measurement of wrong–sign muons in the NuTeV $\overline{\nu}$ sample provides a second constraint on the charm content of the beam. Fits to the NuTeV wrong–sign data yield $\sum_i \sigma(D_i) \cdot BR(D_i \to \nu_\mu) = 9.6 \pm 2.4$

	$\sigma(p+p \to D^{\pm}+X)$	$\sigma(p+p \to D^{0}+X)$	$\sum \sigma \cdot \mathrm{BR}$
Ammar	26 ± 7.6	$22^{+10.5}_{-8.9}$	$5.9^{+1.5}_{-1.4}$
Kodama	38 ± 16.6	38 ± 13.3	9.0 ± 3.0
Kodama–Ammar			6.5 ± 1.3
NuTeV WS μ			9.6 ± 2.4
All Combined			$7.3^{+1.2}_{-1.1}$

Table 5.9: Combination of the measurements of inclusive D meson production cross sections (in units of μb) for 800 GeV proton data [70, 71, 52].

μb [52]. Although the NuTeV measurement is not as precise as the production measurements it is included in evaluating the ν_e systematics (Chapter 7).

Other Smaller Sources

Other smaller sources of electron neutrinos, which contribute at the sub–percent level include decays of muons, Λ, Λ_c, and Σ particles. Roughly 0.4% (0.6%) of the ν_e's in the neutrino (antineutrino) data result from the decays of muons:

$$\mu^+ \to e^+ + \nu_e + \overline{\nu}_\mu, \quad \mu^- \to e^- + \overline{\nu}_e + \nu_\mu \tag{5.108}$$

produced in the decays of pions and kaons. Combined, the decays of Λ, Λ_c, and Σ^-'s constitute approximately 0.2% (0.4%) of the ν_e flux in ν ($\overline{\nu}$) mode. The charmed baryons are a potential source of both ν_e's and $\overline{\nu}_e$'s, through the decays:

$$\begin{aligned} \Lambda_c^+ \to \quad & \Lambda \quad + e^+ + \nu_e \qquad (\mathrm{BR} = 2.3\%) \\ \hookrightarrow \quad & p^+ + e^- + \overline{\nu}_e \qquad (\mathrm{BR} = 8.32 \times 10^{-4}) \end{aligned} \tag{5.109}$$

The Σ^- decays are a source of $\overline{\nu}_e$'s:

$$\Sigma^- \to n + e^- + \overline{\nu}_e \qquad (\mathrm{BR} = 1.02 \times 10^{-3}) \tag{5.110}$$

Their contributions negligibly affect the $\sin^2\theta_W$ measurement ($\delta \sin^2\theta_W = 0.00007$).

5.2.3 Direct Measurement of the ν_e Flux

Rather than rely solely on the Monte Carlo, three direct measurements of the ν_e content in the beam verify the simulation. As seen in the previous section, the analysis of wrong–sign events in the antineutrino data checks the lower energy K_L and charmed meson contributions [52]. This section discusses two additional direct data constraints on the ν_e flux. In the region $80 < \mathrm{E_{had}} < 180$ GeV, a shower shape analysis provides a statistical determination of the ν_e flux [64]. Above 180 GeV, length distribution fits provide the most precise determination of the ν_e content.

Shower Shape Analysis

A shower shape analysis statistically determines the total number of CC ν_e interactions in the detector by exploiting the difference between the longitudinal energy development in electromagnetic and hadronic showers (Figure 5.54).

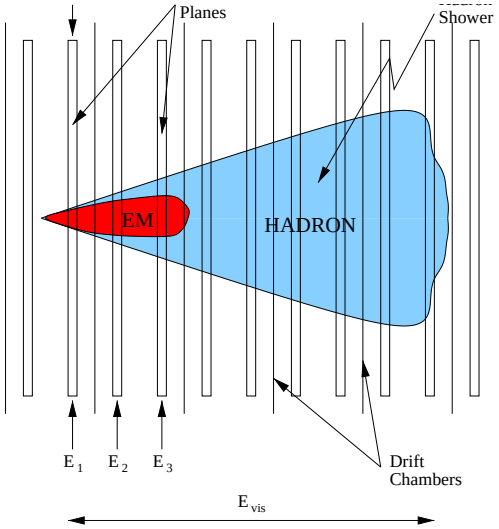

Figure 5.54: Illustration of the shower profile for a CC ν_e interaction, $\nu_e + N \rightarrow e^- + X$. The electromagnetic shower develops more quickly than the overall hadronic shower, typically depositing energy only in the first three scintillation counters.

To describe the energy profile, we define the fractional quantity:

$$\eta_3 = \frac{E_1 + E_2 + E_3}{\mathrm{E_{had}}} \tag{5.111}$$

where E_i is the energy deposited in the i^{th} scintillation counter downstream of the neutrino interaction. The η_3 distributions for CC ν_e events, sharply peaked near unity, differ dramatically from their ν_μ counterparts. Fitting the observed η_3 distributions to a combination of ν_μ and ν_e events, yields a direct measure of the ν_e component. The measurement has the greatest statistical power in the region from $80 < \mathrm{E_{had}} < 180$ GeV (Figure 5.55); it is less precise, though consistent, with the prediction from the beam Monte Carlo:

$$N_{\mathrm{meas}}/N_{\mathrm{pred}}\,(\nu_e) = 1.05 \pm 0.03 \tag{5.112}$$

$$N_{\mathrm{meas}}/N_{\mathrm{pred}}\,(\overline{\nu}_e) = 1.01 \pm 0.04 \tag{5.113}$$

The data indicate a slightly larger number of ν_e's than the prediction. The weighted average of the two results forms a combined measurement, which increases the predicted number of ν_e's from $K^{\pm}_{e3}$ decays by 2% in ν mode and $< 1\%$ in $\overline{\nu}$ mode.

Length Fits

Initial comparisons between data and Monte Carlo revealed a $\sim$10% excess in the number of short events observed in the data above 180 GeV (Figure 5.56) that was not seen in the long event sample. Masked by a detector effect, the excess had also not been observed in the preliminary $\sin^2\theta_W$ analysis [26]. Before switching to the SUPERLOWs, saturation of the ADCs caused these events to migrate to lower energies where they were not visible (Chapter 3). The effect accounts for the entire 0.8σ shift in $\sin^2\theta_W$ ($\delta\sin^2\theta_W = +0.0024$) between the preliminary (1998) and

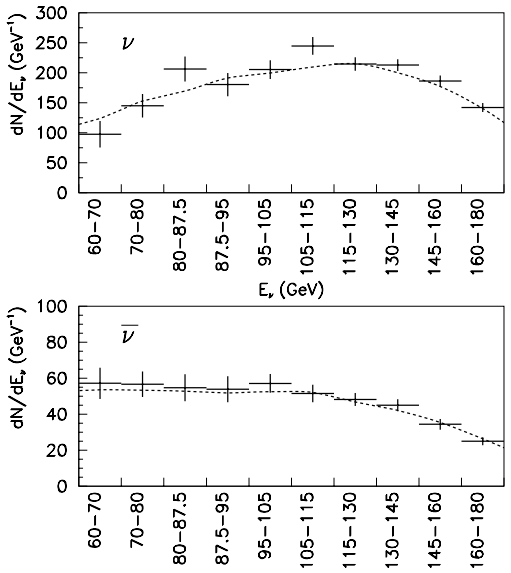

Figure 5.55: Number of ν_e's per GeV as a function of energy for ν (top) and $\overline{\nu}$ (bottom) modes compared to the beam MC prediction (dotted curve).

final (2002) analyses. The excess events were eventually identified as high energy ν_e interactions.

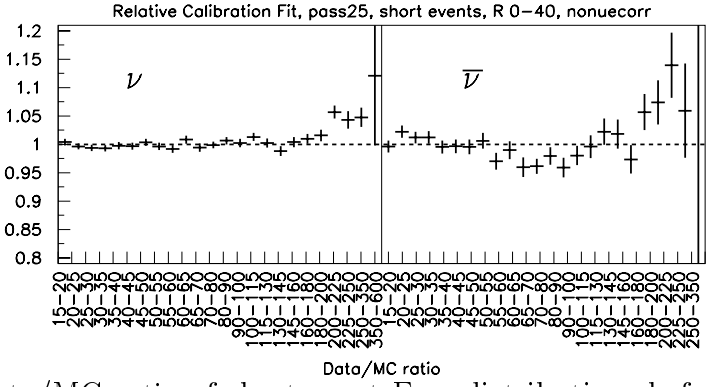

Figure 5.56: Data/MC ratio of short event E_{had} distributions before including the measurement of high energy ν_e's from the data. The excess in the data exists above 180 GeV in both modes.

Very high energy ν_e's are produced in the decays of wide angle, high transverse momentum kaons. Such kaons populate the extreme high energy tail of the flux spectrum (Figure 5.48) where no external production data exists. A check of the ν_μ

flux distributions (Figure 5.57) reveals the inadequacy of the beam Monte Carlo to predict these extremely high energy kaons to better than 20–30%.

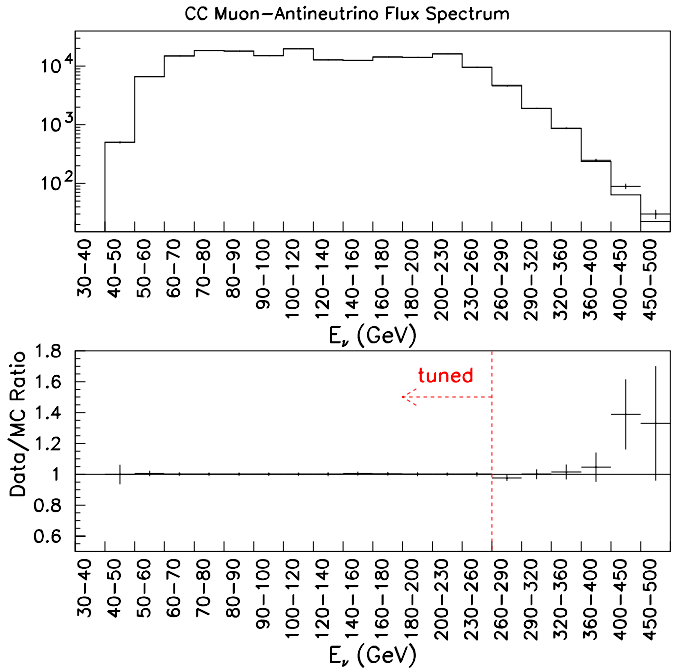

Figure 5.57: Energy distribution of CC $\overline{\nu}_\mu$ data events compared to the beam Monte Carlo prediction. The peak regions are tuned below 300 GeV (Section 5.2.1).

Although the ν_μ flux tuning and shower shape analyses described previously do not have the statistical power to constrain the highest energy kaons, a precise measurement of the ν_e content in the high energy tail of the flux results from fits to NC length distributions. Fitting for additional ν_e content is possible because the length distributions are very well modeled in all energy regions. See Figure 5.58 for the length distributions for antineutrino events with $E_{had} > 180$ GeV. The ν_e's clearly dominate extremely short events at high energy. Fitting the length distributions for an overall NC level, in addition to a ν_e rescaling factor, yields a measurement of $38 \pm 9\%$ more ν_e events observed in the $\overline{\nu}$ beam, and $32 \pm 4\%$ in the ν beam. An

additional 4% systematic uncertainty is assigned based on discrepancies in the short length agreement at low energy.

Such fits do not perform as well at low energies, where there are fewer ν_e events. Fits in the lower energy region are consistent with zero ν_e enhancement, which confirms the choice to use the shower shape results below 180 GeV.

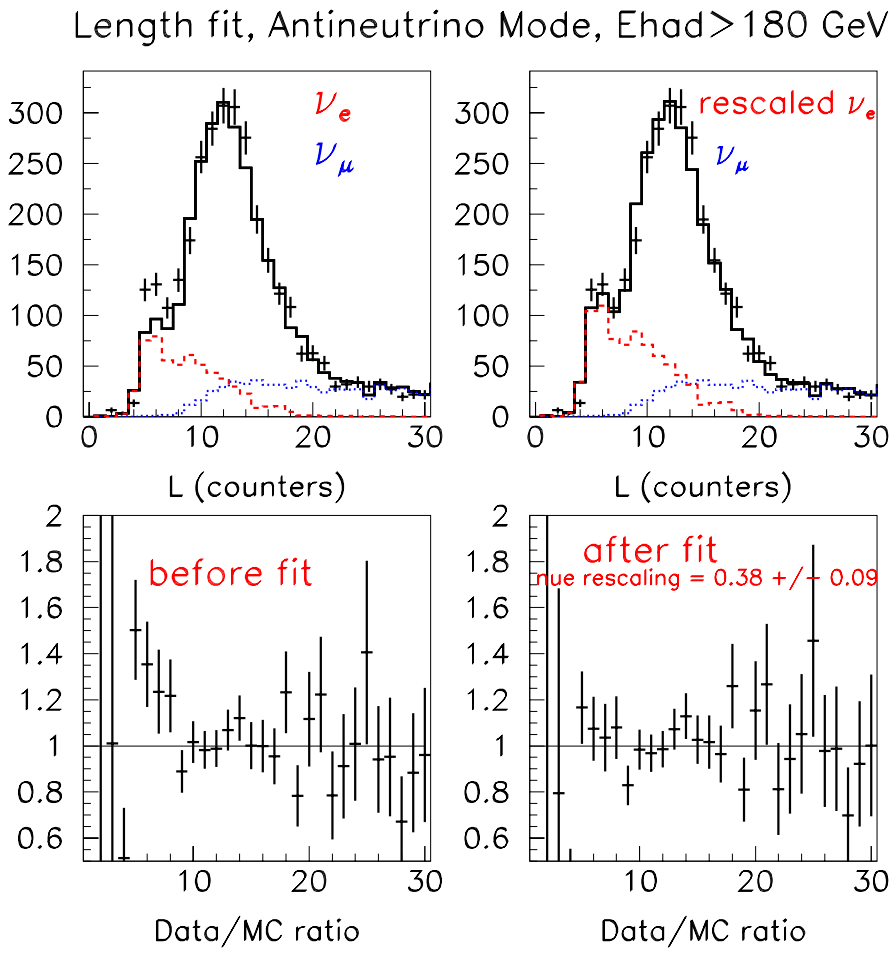

Figure 5.58: Length distributions for $\overline{\nu}$ events above 180 GeV. The plots on the left show the beam Monte Carlo prediction before the fit. The plots on the right show the result after fitting for a level change in the predicted number of ν_e's.

Despite the fact that the high energy ν_e content can be measured, NuTeV made

the conservative decision to cut events with $E_{had} > 180$ GeV from the analysis. After incorporating the high energy ν_e measurement from the data, the short event ratios flatten at high E_{had} (Figure 5.59), and moreover, the $\sin^2\theta_W$ fit results become consistent whether or not an upper E_{had} cut is applied[§].

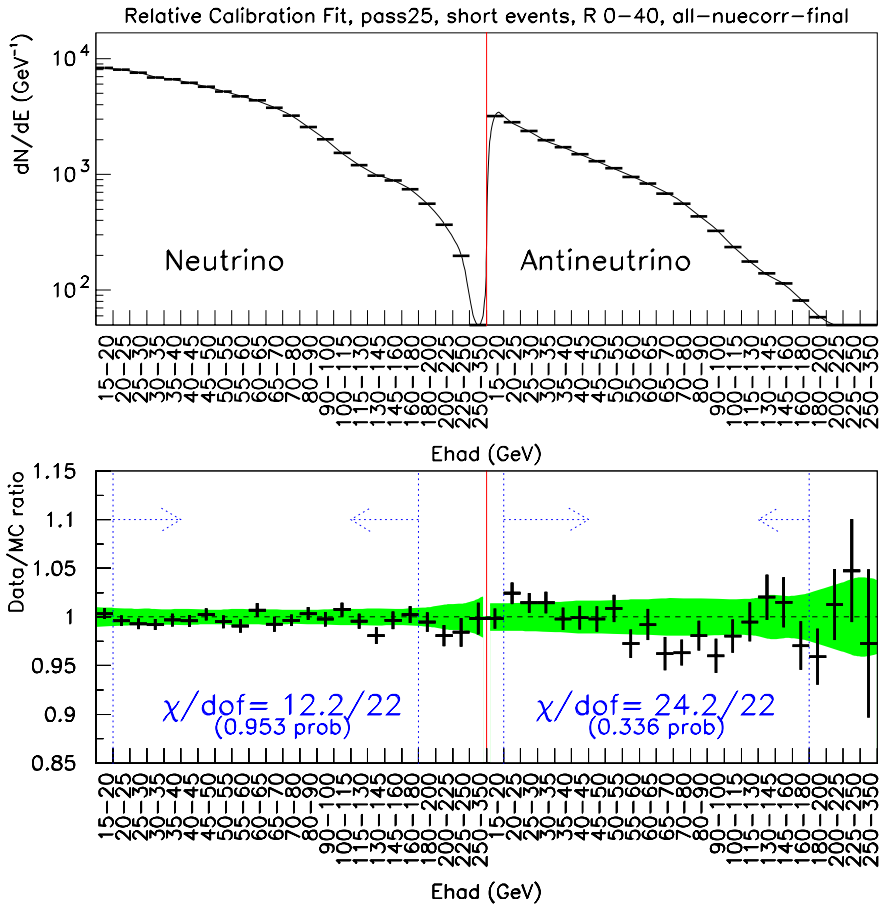

Figure 5.59: Short event E_{had} distributions after including the measurement of high energy ν_e's from the data. The bands display the $\pm 1\sigma$ systematic uncertainty.

[§] The 1C fits yield $\sin^2\theta_W = 0.22773 \pm 0.00163$ for $20 < E_{had} < 180$ GeV compared to $\sin^2\theta_W = 0.22795 \pm 0.00162$ for $E_{had} > 20$ GeV. The difference in the fit values is only 0.00022.

5.3 Detector Response

The Monte Carlo not only includes a cross section and flux model, but must also closely simulate the response of the NuTeV detector to the products of neutrino interactions. To this end, the Monte Carlo includes all the calibration information that affects the measurement of energy deposition in the calorimeter. The first four subsections in this section describe the Monte Carlo model for hadron energy deposition, muon energy loss, electromagnetic energy deposition, and potential energy leakage out the side of the calorimeter.

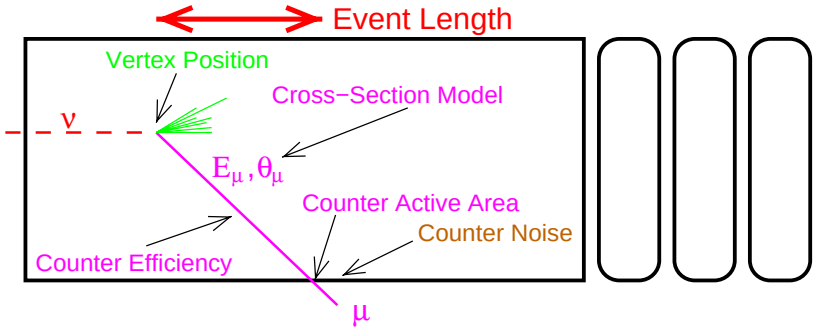

Figure 5.60: Detector modeling most important to the $\sin^2\theta_W$ analysis.

Furthermore, anything that affects the length of an event is also important (Figure 5.60). Therefore, the Monte Carlo accurately simulates the determination of the event vertex and end position. In order to mimic the data analysis as closely as possible, the Monte Carlo simulates biases in the PLACE algorithm in addition to pulls in the transverse vertex determination. For CC events, the Monte Carlo includes a muon simulation that accounts for detector effects such as counter positions, and ineffiencies which can alter the end point of the event. Noise is included in both NC and CC events. The Monte Carlo includes a shower length model which sets

the length of most NC events. The bulk of the effects are modeled using either real neutrino data or events from our extensive hadron, muon, and electron testbeam. The remaining sections in this chapter describe these elements of the Monte Carlo detector response model in detail.

5.3.1 Hadron Energy Determination

The hadronic energy generated for a given Monte Carlo process is dictated by the kinematics of the event:

$$\mathrm{E_{hadg}} = y \cdot E_\nu \tag{5.114}$$

where the inelasticity, y, is randomly generated according to a flat distribution from 0.0 to 1.0, and the neutrino energy, E_ν, is set by beam Monte Carlo inputs. The generated energy is first calibrated by correcting for the measured non–linearity of the NuTeV calorimeter:

$$\begin{aligned} \mathrm{E_{had}} &= \mathrm{E_{hadg}} \cdot C_\pi \\ &= \mathrm{E_{hadg}} \cdot \left[\frac{e \cdot f_{\pi^0}(\mathrm{E_{hadg}}) + h \cdot [1 - f_{\pi^0}(\mathrm{E_{hadg}})]}{e \cdot f_{\pi^0}(75) + h \cdot [1 - f_{\pi^0}(75)]} \right] \end{aligned} \tag{5.115}$$

using Groom's parameterization [27] for $f_{\pi^0}(E)$ normalized to 75 GeV testbeam data with $e/h = 1.079 \pm 0.011$ (in exact analogy with the treatment of events in the data in Chapter 3). The Monte Carlo randomly smears the hadronic energy according to the energy resolution measured from hadron testbeam data:

$$\frac{\sigma}{E} = \frac{0.86 \pm 0.01}{\sqrt{E}} + 0.022 \pm 0.001 \tag{5.116}$$

The testbeam calibration constants and resolution smearing apply to an E_{had} definition using a fixed twenty counter sum. Recall that for data events in the $\sin^2\theta_W$ analysis, E_{had} is obtained by summing the pulse heights in an energy–dependent number of scintillation counters, not always twenty (Chapter 4). To account for this, shower libraries are generated from the same testbeam samples used in determining the 99% containment lengths for the data analysis (Equation 4.3). Stored in the shower libraries are the single counter testbeam hadron energies sampled starting at PLACE and normalized to the twenty counter energy sum. These shower library ratios are used to correct the Monte Carlo hadronic energy to form single counter responses:

$$E^{MC}_{cntr}(i) = E_{had} * \left(\frac{E_{had}(i)}{E_{had20}}\right)_{\text{TB shower library}} \tag{5.117}$$

were i = PLACE, PLACE–19. Although the energy sum for data events includes the energy in counter PLACE+1, no such information can be included in the testbeam shower libraries because of the entering charged hadron. An additional correction (measured from neutrino data) accounts for the missing upstream energy in testbeam events:

$$f_1 = \max\left(0, -0.002154 + \frac{0.02353}{\ln(\max(1.2, E_{hadg}))}\right) \tag{5.118}$$

$$E^{MC}_{cntr}(i = PLACE + 1) = E_{had} * \frac{f_1}{1 + f_1} \tag{5.119}$$

which is about 0.2 GeV for a 50 GeV shower. The single counter energies are corrected by the same counter map corrections as the data (Chapter 3) and are then summed in the exact same manner as the data, first forming a length based on the twenty counter quantity:

$$L'_{var}(NC) = int\left[4.4827 + 1.41042 \cdot \ln(E_{had})\right] \quad (5.120)$$

$$L'_{var}(CC) = int\left[4.4827 + 1.41042 \cdot \ln\left(E_{had} + \sum_{i=PLACE+1}^{PLACE-19} E_{\mu,e}(i)\right)\right] \quad (5.121)$$

The NC and CC events are treated distinctly because in the data, the hadron energy sum includes the additional energy from muons (in ν_μ CC interactions) and from electrons (in ν_e CC interactions). The models for muon and electron energy deposition are described in the following two sections. Based on the initial length estimate, L', a new energy sum and resultant length are calculated:

$$E_{hadvar}'(NC) = \sum_{i=PLACE+1}^{PLACE-L'_{var}(NC)+1} E_{cntr}^{MC}(i) \quad (5.122)$$

$$E_{hadvar}'(CC) = \sum_{i=PLACE+1}^{PLACE-L'_{var}(CC)+1} E_{cntr}^{MC}(i) + E_{\mu,e}(i) \quad (5.123)$$

$$L_{var}(NC) = int\left[4.4827 + 1.41042 \cdot \ln(E_{hadvar}'(NC))\right] \quad (5.124)$$

$$L_{var}(CC) = int\left[4.4827 + 1.41042 \cdot \ln(E_{hadvar}'(CC))\right] \quad (5.125)$$

L_{var} is chosen to the length that contains $\approx 99\%$ of the total recorded shower energy, on average. Finally, the variable–length energy definition, E_{hadvar}, is:

$$E_{hadvar}(NC) = \sum_{i=PLACE+1}^{PLACE-L_{var}(NC)+1} E_{cntr}^{MC}(i) \quad (5.126)$$

$$E_{hadvar}(CC) = \sum_{i=PLACE+1}^{PLACE-L_{var}(CC)+1} E_{cntr}^{MC}(i) + E_{\mu,e}(i) \quad (5.127)$$

This admittedly complicated iterative procedure ensures identical treatment for NC and CC events both in the data and in the Monte Carlo.

5.3.2 Muon Energy Deposition

The analysis is relatively insensitive to the hadronic shower energy determination because both NC and CC events have similar hadronic energy distributions; however, CC events differ in the presence of additional muon energy deposit in the shower region. The muons, which have energy:

$$E_\mu = (1 - y)\, E_\nu \tag{5.128}$$

can deposit energy either by ionization loss, bremsstrahlung, or pair production. The energy loss is simulated using measurements of the energy deposited by straight–through (trigger 6) muons. On average, the muon deposits roughly 250 MeV/counter.

5.3.3 Electron Response

For CC electron neutrino events, the electromagnetic energy deposited by the final state electron, $E_e = (1 - y)\, E_\nu$, contributes to the hadron shower. The Monte Carlo first corrects to a detector energy:

$$E_e \longrightarrow E_e \cdot \frac{C_\pi}{C_e} = E_e \cdot \left(\frac{0.212}{0.195}\right) = E_e \cdot (1.087 \pm 0.020) \tag{5.129}$$

and then map corrects the electron energy response in analogy to the treatment of events in the data (Chapter 3). Observed energy is smeared by a Gaussian with standard deviation:

$$\frac{\sigma}{E} = \frac{0.499}{\sqrt{E}} + 0.042 \tag{5.130}$$

The length of the electron shower in the Monte Carlo comes from the measurements of testbeam electrons, ranging in energy from 5 to 170 GeV (Figure 5.62). The electron shower lengths use the same length definition as data in the $\sin^2\theta_W$ analysis.

In most cases, the electron shower length is 4–5 scintillation counters, but fluctuates to longer or shorter lengths following the probability observed in the testbeam data.

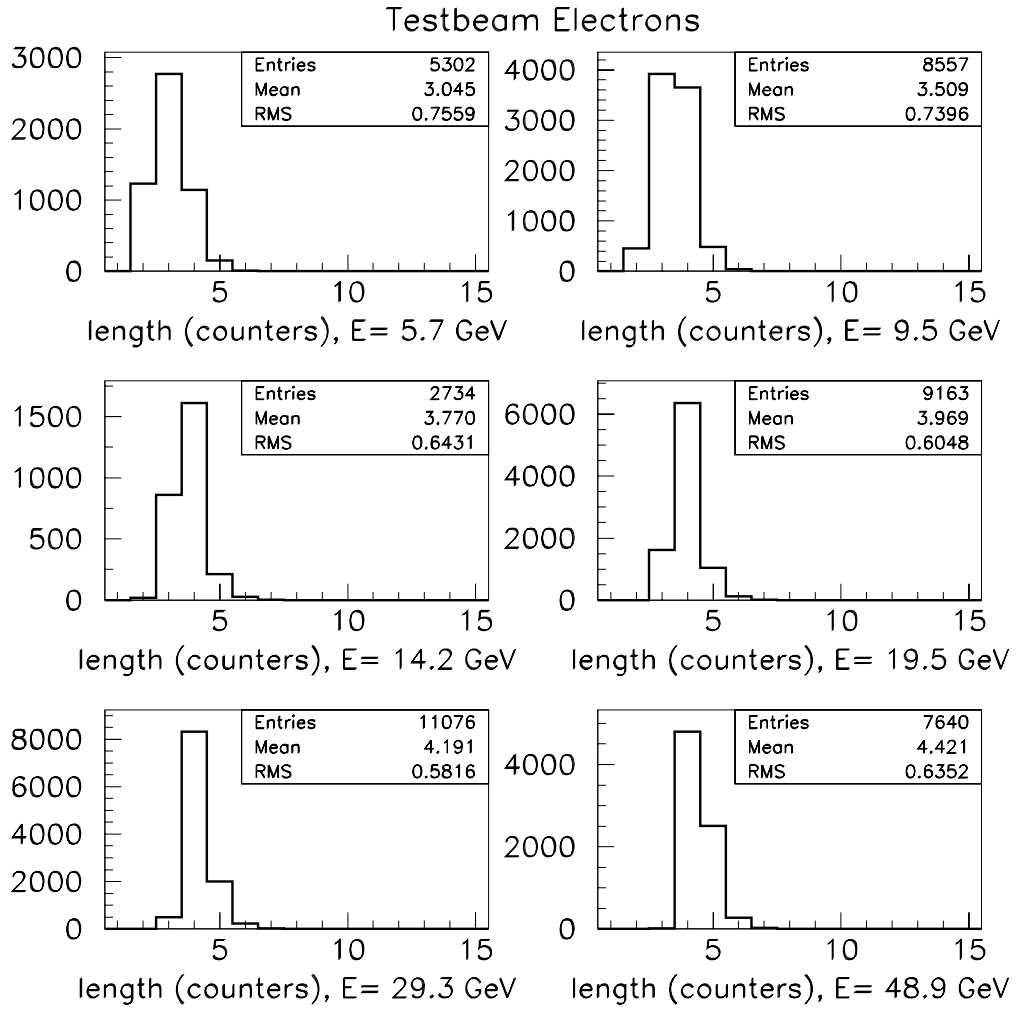

Figure 5.61: Shower lengths for testbeam e^-s ranging in energy from 5 to 50 GeV.

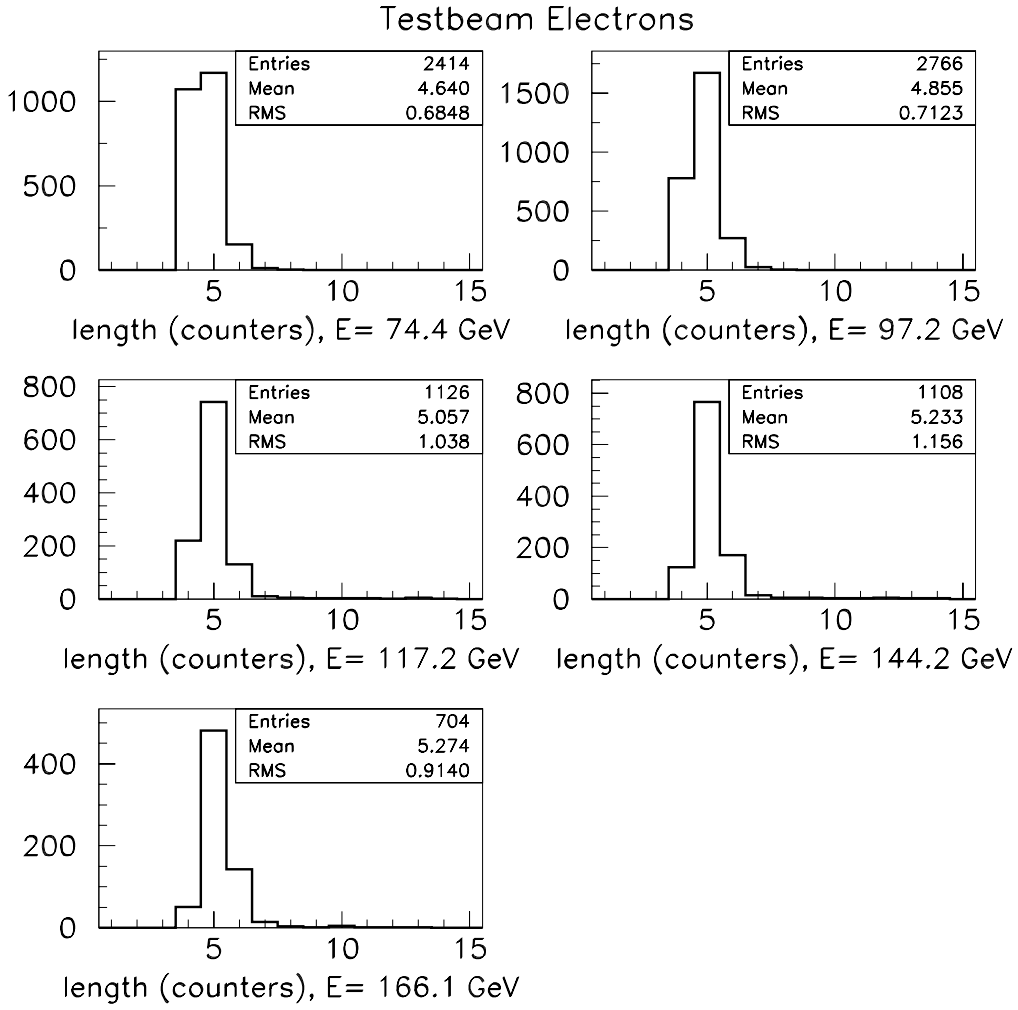

Figure 5.62: Shower lengths for testbeam e^-s ranging in energy from 75 to 170 GeV.

5.3.4 Shower Leakage

Because hadronic showers can be large in transverse size, shower particles can leak out of the detector laterally, causing events to appear less energetic. Correspondingly, the Monte Carlo must also simulate incomplete hadron shower containment in the calorimeter. Although fiducial cuts minimize this effect, Figure 5.63 shows an example of an event which may have had substantial leakage but passed the vertex criteria. This event did not pass the minimum E_{had} requirement and was cut from the data sample.

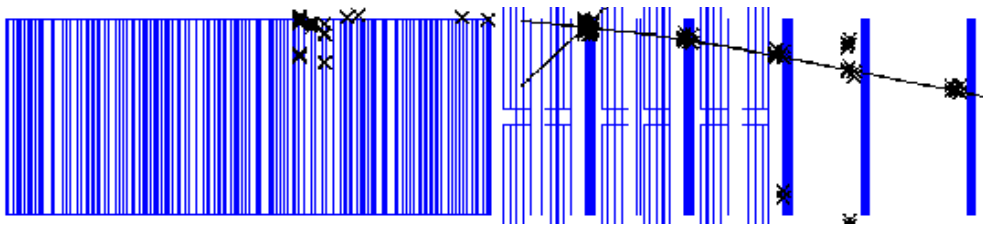

Figure 5.63: An event with significant lateral shower leakage out the side of the NuTeV detector. This event was recorded with E_{had}=17 GeV, PLACE=32, Vx=40 inches, Vy=–4 inches, and a length of 8 counters.

Modeling the effect of lateral shower leakage is important because it does not cancel in the ratio, R_{exp} = short/long. As an example, consider the cases of a long and a short CC event, both near the edge of the detector. To fit these descriptions, the long CC event tends to have its muon pointing toward the center of the detector, balanced by a hadronic shower that exits out the side (Figure 5.64). Short CC events have the opposite geometry, in which case, the shorter the muon, the more contained the hadron shower (Figure 5.65).

The leakage is parametrized as a function of energy and position using edge events generated in GEANT. Letting d denote the distance from the edge of the

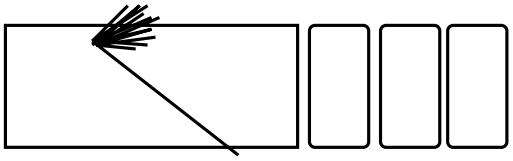

Figure 5.64: Illustration of a **long** event near the edge of the detector. The shower leaks out the side of the detector.

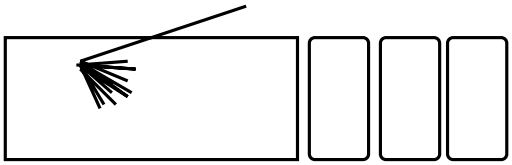

Figure 5.65: Illustration of a **short** event near the edge of the detector. The shower is contained in the detector.

detector and calculating a corrected distance:

$$D = d - \max(0, \sin\theta_{\rm h} \cdot ({\rm E}_{\rm hadg} + 10)) - 3 \cdot \sin\theta_{\rm h} \tag{5.131}$$

assuming the hadronic shower angle is positive if the shower is pointing towards the edge of the detector:

$$\theta_h = -\theta_\mu \left(\frac{1-y}{y}\right) \tag{5.132}$$

the GEANT–based fractional shower leakage, parametrized as a function of energy, position, and shower angle, is:

$$\begin{aligned} f_L = 0.206 \quad & \cdot \quad \left(e^{-0.189 \cdot D} + e^{-0.0702 \cdot D - 2.004}\right) \\ & \cdot \quad \left[1 - 0.23 \cdot \ln({\rm E}_{\rm hadg}) + 0.0213 \cdot \ln({\rm E}_{\rm hadg})^2\right] \end{aligned} \tag{5.133}$$

where f_L is the fraction of missing energy for $7 \leq d < 40$ inches. The hadronic energies for edge events in the Monte Carlo become ${\rm E}_{\rm had} = {\rm E}_{\rm had}(1 - f_L)$. Hence, for a 20 GeV event 10 inches from the edge of the detector with a 0.1 radian shower angle, the correction is roughly 5%. The effect of cutting off showers that go over the edge of the detector is an increase in the predicted short/long ratios as a result of the reduced number of long events passing the minimum ${\rm E}_{\rm had}$ requirement: $\delta R^{\nu}_{\rm exp} = +0.00011$,

$\delta R^{\overline{\nu}}_{\rm exp} = +0.00010$. In addition to reducing the energy of edge events that are not fully contained in the detector, their lengths are also adjusted, on average, by -0.10 counter for $40 \leq \max(\mathrm{Vx}, \mathrm{Vy}) < 45$ inches, and -0.35 counter for $\max(\mathrm{Vx}, \mathrm{Vy}) \geq 45$ inches. The effect of the length correction, however, is small due to our choice of fiducial volume: $\delta R^{\nu}_{\rm exp} = +3.0 \times 10^{-6}$, $\delta R^{\overline{\nu}}_{\rm exp} = +2.5 \times 10^{-5}$.

5.3.5 Longitudinal Vertex Determination

The Monte Carlo generates the location of the neutrino interaction according to the distribution of material in the NuTeV detector. To simulate the determination of the longitudinal event vertex in the data, the Monte Carlo includes the effects of biases in the PLACE–finding algorithm, NC/CC differences, and mis–cabling. These contributions are discussed in the following sections.

Even/Odd PLACE Effect

The NuTeV detector is not perfectly uniform, having additional material in front of even–numbered scintillation counters (Figure 3.6). An even/odd PLACE difference results from the slightly higher probability that a neutrino will interact in the increased material in front of an even–numbered scintillation counter and register as an even PLACE event. Figure 6.4 exhibits our resultant ability to model this effect, where it can be seen that the Monte Carlo accurately tracks the dips in the PLACE distribution from the data. However, it is not entirely important to model this effect precisely because the even/odd counter difference is correlated between NC and CC events and cancels in the ratio, $R^{\nu} = \sigma^{NC}/\sigma^{CC}$.

PLACE Shift

The counter-based PLACE algorithm does not necessarily find the exact location of a neutrino interaction. PLACE can shift upstream if hadrons back–scatter (albedo effect) or shift downstream if the shower develops slowly and leaves too little energy in the first counter. The accuracy of the PLACE algorithm can be measured with dimuon events, such as those shown in Figure 5.7 because an independent estimation of the event vertex can be made by projecting the muon tracks back to their point of intersection.

First, the full sample of CCFR dimuon data is reduced by a number of quality cuts, including a restriction that the opening angle of the two muons be greater than 20 milliradians in at least one view. The intersection point of the two muons is determined by performing a linearized, vertex–constrained fit to the two tracks. Accounting for multiple Coulomb scattering, the two tracks are forced to intersect in both x and y by adjusting the track slopes and intercepts within errors until the distance between the two tracks is minimized. The process is iterated until the fit χ^2 converges. The point of intersection is then calculated from the resultant track positions. The difference between the muon track intersection and the vertex determined by the PLACE algorithm is shown in Figure 5.66. The three energy bins have roughly equal dimuon statistics in each. Table 5.10 summarizes the mean differences in each bin. The units have been converted into inches using 8.319 inches as the nominal counter separation in the NuTeV detector. The comparison shows that, on average, the PLACE algorithm finds the vertex roughly one inch upstream of the dimuon track intersection.

A GEANT–based, hit-level simulation, known as McNuTeV determines how ac-

	dimuon intersection - PLACE
$E_{had} < 50$ GeV	0.658 ± 0.169
$50 \leq E_{had} < 100$ GeV	1.140 ± 0.164
$E_{had} \geq 100$ GeV	1.266 ± 0.211

Table 5.10: Mean difference (in inches) between the dimuon vertex and PLACE.

curately the dimuon track fitting routine finds event vertices. Analysis of McNuTeV dimuon events with known vertex positions and opening angles, reveals that the constrained fit systematically pulls the vertex approximately two inches downstream of the true interaction point. Figure 5.67 and Table 5.11 summarize the results of the track–fitting accuracy study.

	dimuon intersection – true vertex
$E_{had} < 50$ GeV	1.762 ± 0.142
$50 \geq E_{had} < 100$ GeV	2.111 ± 0.119
$E_{had} \geq 100$ GeV	2.151 ± 0.167

Table 5.11: Difference between the dimuon vertex calculated from the intersection of the two muon tracks and the GEANT–generated event vertex in **inches**.

Combining the two results, we conclude that, on average, the PLACE algorithm shifts the vertex approximately one inch downstream of the true interaction point (Figure 5.68). Table 5.12 displays the final PLACE shift results implemented in the Monte Carlo in units of scintillation counters. Discussion of the systematics associated with the PLACE shift determination can be found in Chapter 7.

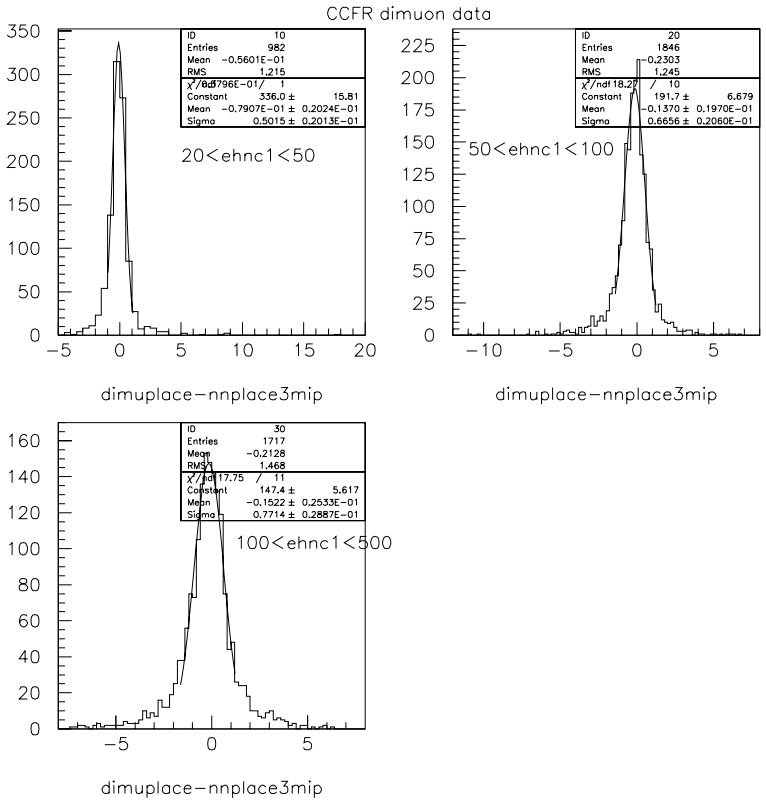

Figure 5.66: CCFR dimuon data. Comparison of the longitudinal vertex determined from the intersection of two muon tracks to that obtained from the counter–based PLACE algorithm. The difference, measured in units of scintillation counters, is shown in bins of E_{had}.

	Mean PLACE shift
$E_{had} < 50$ GeV	0.132 ± 0.026 (stat)
$50 \geq E_{had} < 100$ GeV	0.117 ± 0.024 (stat)
$E_{had} \geq 100$ GeV	0.106 ± 0.032 (stat)

Table 5.12: Mean number of **counters** PLACE is shifted downstream of the true neutrino interaction. Error is statistical only.

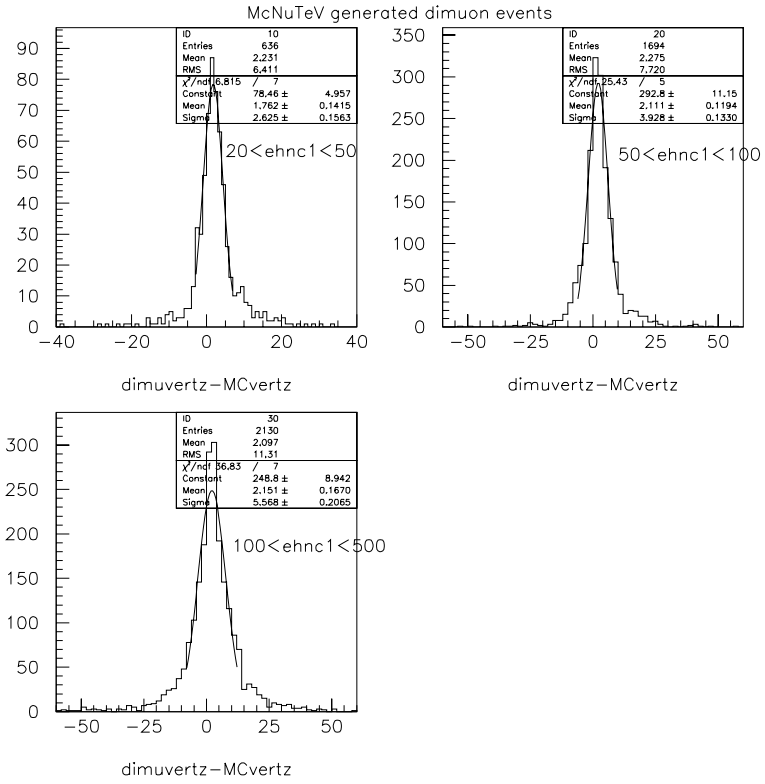

Figure 5.67: McNuTeV generated dimuon events. Test of the muon track extrapolation. Comparison of the vertex determined from the intersection of two muon tracks to the generated McNuTeV vertex. The horizontal axis is in units of inches.

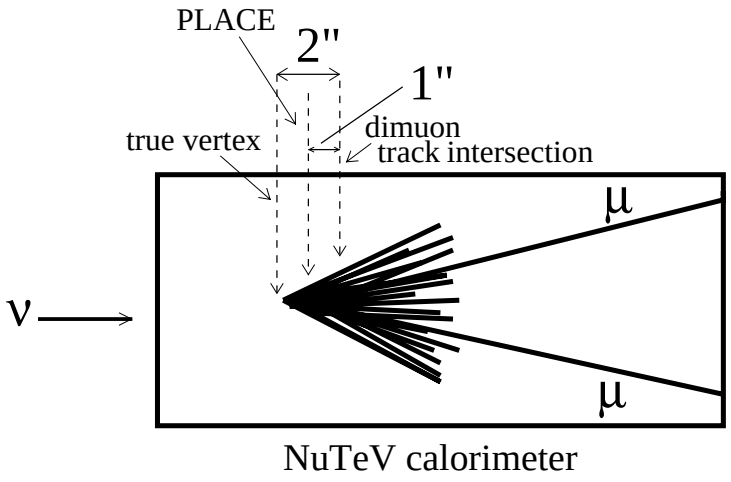

Figure 5.68: Illustration of the PLACE shift results. Diagram is not shown to scale.

NC/CC Correction

The muon energy deposit present in CC interactions provides a small but measurable bias to the PLACE determination, sometimes shifting it upstream. To simulate the effect, the Monte Carlo vertex for CC events is corrected using the PLACE shift measured from studies of NC events with an artificially added muon [64]. Figure 5.69 shows the size of the effect as a function of energy. The smaller the shower energy, the larger the effect of the added muon pulse height in pushing the single counter response above the threshold (Section 4.1). Accounting for an NC/CC PLACE difference in the Monte Carlo results in -0.00009, +0.00019, -0.00021 shifts in the predictions for $R^{\nu}_{\rm exp}$, $R^{\overline{\nu}}_{\rm exp}$, and $\sin^2\theta_W$, respectively.

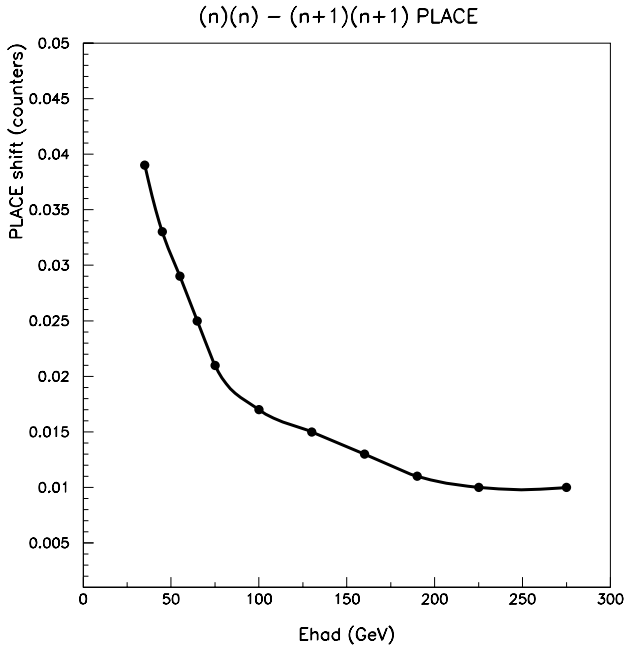

Figure 5.69: PLACE correction for CC events in the Monte Carlo. The correction accounts for the added pulse height from the muon in CC events. The difference between $(n)(n)$ and $(n+1)(n+1)$ PLACE for NC events is equivalent to the shift from the addition of a muon to the event.

Cable Swaps

The Monte Carlo reproduces cabling mistakes that affect the longitudinal vertex determination. For a large portion of the NuTeV run, phototubes from counters 73 and 74 (as well as counters 9 and 12) were interchanged in the HIGH/Sbit summation. This meant any event with PLACE=73 automatically registered as PLACE=74. We randomly throw for this probability in the Monte Carlo. Figure 6.4 displays how well the Monte Carlo reproduces the effect; especially note the dip and peak at counters 73 and 74.

5.3.6 Muon Simulation

The event energy profile determines the length of an event. In the data, EXIT is the first counter downstream of PLACE which is followed by three or more counters each with less than 0.25 mip of energy (Section 4.1). This end point results from either the muon in the case of most CC interactions or the hadronic shower in the case of NC interactions. Here, we discuss the case in which the muon sets the event length. The hadron shower length model will be addressed at the end of this chapter.

In the simulation of CC events, the muon is propagated through the calorimeter in one counter increments, accounting for muon energy loss and multiple scattering in each step. Proper simulation of the end of the muon track depends on accurate modeling of the NuTeV scintillation counters. For CC events in which the muon exits out the side of the detector, knowledge of the positions and effective sizes of the counters is crucial. In addition, the Monte Carlo must simulate the effects of counter inefficiency, which can potentially shorten the length of an event, and counter noise, which can artificially extend the length of an event. Modeling of the

counter widths, positions, efficiency, and noise are each discussed in turn below.

Counter Width

Simulation of the fiducial volume of the detector requires measurement of both the position and effective dimensions of the scintillation counters. Determination of the counter locations and edges allows accurate estimation of the short CC background to the NC event sample. To determine their active area and location, the counters are imaged with both neutrino–induced and testbeam muons. Hits in the drift chambers provide a precise estimate of the location of the muon track which is then projected to determine the location of the muon in each scintillation counter. Requiring the response in the counter to be greater than 0.25 mip (i.e., Sbit–on) thus allows the counter response to be mapped out, or "X–rayed", in x and y.

The primary analysis of the counter edges and their internal structure used neutrino–induced muons, specifically a high statistics sample of trigger 1, 3, and 6 muons (Chapter 3). Figure 5.70 shows a typical counter X–ray. The active region of the counter is a 119 $\times$ 119 inch square surrounded by a two inch thick acrylic support frame and a 5/8 inch wide wavelength shifter bar (Figure 3.12). The overall efficiency of the counter is nearly 100% throughout its active region and nearly–so for muons passing through the wavelength shifter bars, but is close to zero for muons hitting the acrylic supports. The X–ray also very clearly shows the position of the support ribs. The Monte Carlo assumes the acrylic supports are insensitive to muons and sets the efficiency of both the scintillator oil and the wavelength shifter bars to 100% pending a possible correction for counter inefficiency (Section 5.3.6).

The measured edges determine the total active size of the counters. Assuming all of the counters have the same width, and using the position measurements

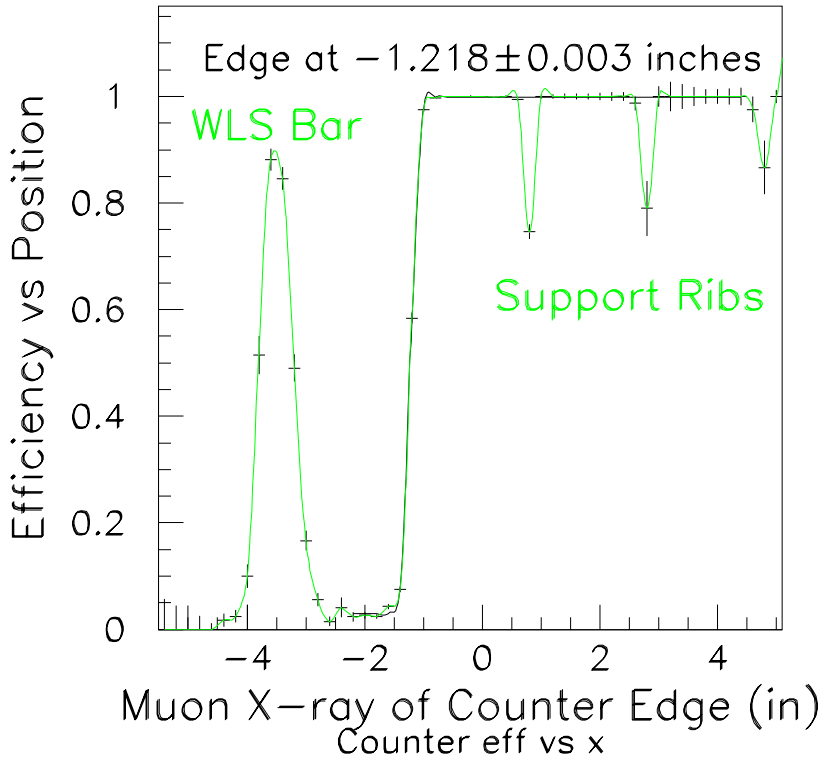

Figure 5.70: X–ray of counter edge using muons. Plotted is the counter efficiency as a function of x–position in inches. An offset of 58.5 inches from the x–coordinate allows the counter edge to appear within a ±5 inch window around 0.

from only the first two (most downstream) calorimeter carts[◇], the counter width is $119.24 \pm 0.02\,(\text{stat}) \pm 0.05\,(\text{syst})$ inches. The systematic uncertainty includes half of the spread in all of the individual counter width measurements, combined with an overall 0.03 inch uncertainty from the track projection. X–ray data from a sample of 50 GeV testbeam muons hitting the extreme eastern edge of the calorimeter provide only a partial cross–check because they illuminated only one edge of counters upstream of counter 38. The counter width from the testbeam measurement,

◇ The downstream counters in carts 1 and 2 have the smallest projection errors and most sharply defined edges.

$119.10 \pm 0.02\,(\text{stat}) \pm 0.03\,(\text{syst})$ inches, is consistent with the neutrino data measurement. Combining the two, the resultant counter width is 119.12 ± 0.08 inches, where half of the discrepancy between the neutrino and testbeam data measurements has been included a systematic.

Counter Position

Counter X–rays also determine the locations of the scintillation counters in the NuTeV coordinate system (Appendix B). Figure 5.71 shows the counter coordinates as measured in inches from the east, west, top, and bottom edges of each counter. On average, the counters are very close to the center of the NuTeV coordinate system in x, and roughly one inch above the center in y. The final values for the counter x and y coordinates (Tables 5.13 and 5.14) are averages of the measurements from the two sides.

The z positions of each counter were measured by hand[△] and verified using Survey and Alignment data. The counter z positions were tied into the Lab E coordinate system (Appendix B) using the relative distance between the most downstream counter and drift chamber in the calorimeter. The measured z positions employed for both data and Monte Carlo reconstruction appear in Table 5.15.

[△] The counter z positions in NuTeV differ from CCFR due to the movement of the carts; for NuTeV, the counters were moved several inches upstream and spread further apart.

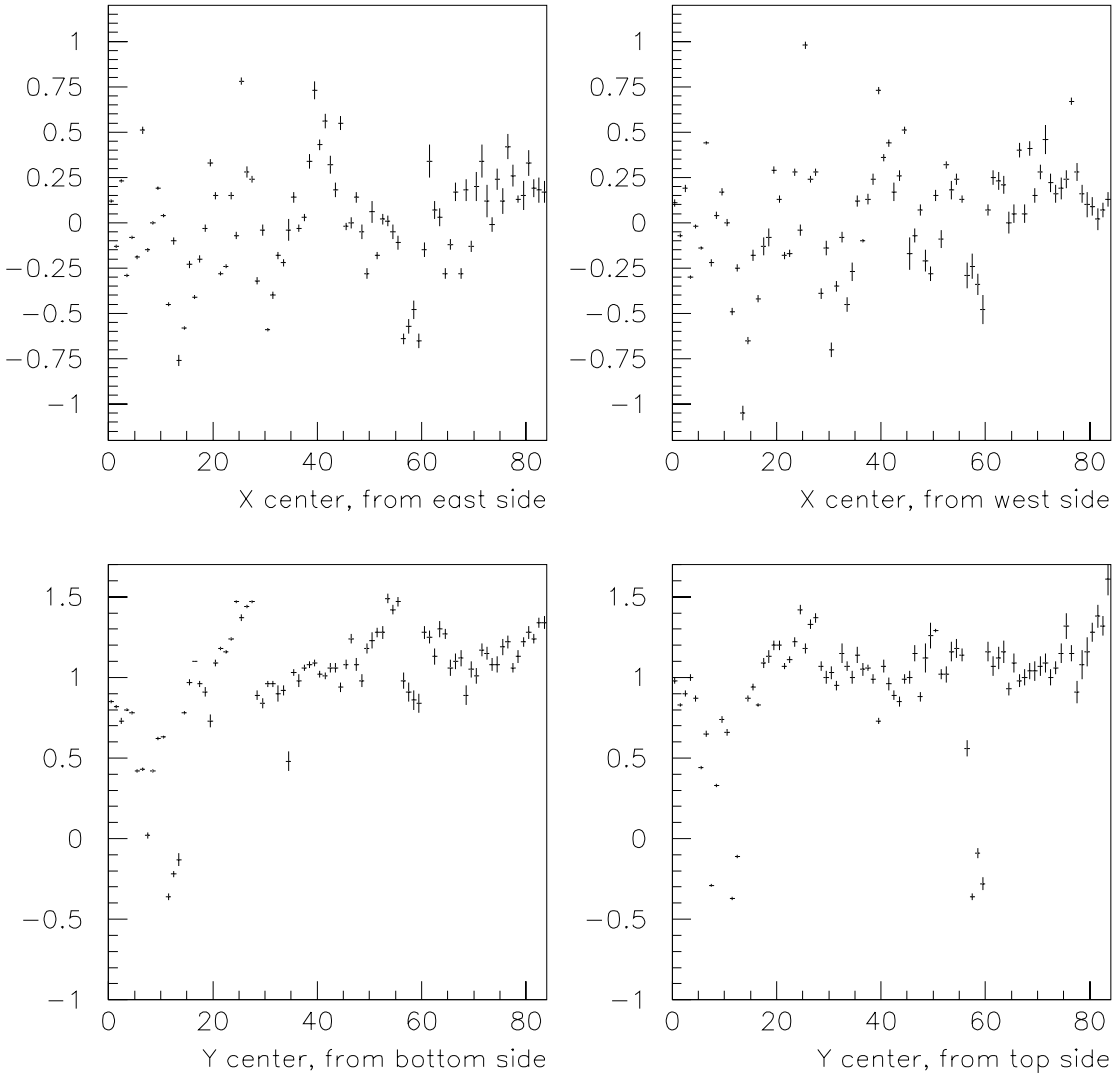

Figure 5.71: x and y coordinates of each counter center. Note: an offset of 59.6 inches (the measured counter half width) has been subtracted from each coordinate.

Counter	X center	Counter	X center
1	0.12	43	0.25
2	-0.10	44	0.22
3	0.21	45	0.53
4	-0.30	46	-0.09
5	-0.05	47	-0.04
6	-0.16	48	0.11
7	0.47	49	-0.13
8	-0.18	50	-0.28
9	0.02	51	0.11
10	0.18	52	-0.13
11	0.02	53	0.17
12	-0.47	54	0.10
13	-0.17	55	0.10
14	-0.90	56	0.01
15	-0.62	57	-0.47
16	-0.20	58	-0.41
17	-0.42	59	-0.41
18	-0.17	60	-0.57
19	-0.05	61	-0.04
20	0.31	62	0.30
21	0.14	63	0.15
22	-0.23	64	0.12
23	-0.20	65	-0.14
24	0.22	66	-0.03
25	-0.05	67	0.28
26	0.88	68	-0.11
27	0.26	69	0.30
28	0.26	70	0.01
29	-0.35	71	0.24
30	-0.09	72	0.40
31	-0.64	73	0.17
32	-0.38	74	0.08
33	-0.13	75	0.22
34	-0.33	76	0.18
35	-0.15	77	0.55
36	0.13	78	0.27
37	-0.07	79	0.14
38	0.08	80	0.12
39	0.29	81	0.21
40	0.73	82	0.10
41	0.40	83	0.12
42	0.50	84	0.15

Table 5.13: **x–coordinate** of the center of each scintillation counter in inches.

Counter	Y center	Counter	Y center
1	0.91	43	0.98
2	0.82	44	0.96
3	0.81	45	0.97
4	0.90	46	1.04
5	0.82	47	1.19
6	0.43	48	0.98
7	0.54	49	1.05
8	-0.14	50	1.22
9	0.38	51	1.26
10	0.68	52	1.15
11	0.64	53	1.15
12	-0.37	54	1.33
13	-0.16	55	1.30
14	-0.58	56	1.31
15	0.82	57	0.77
16	0.95	58	0.27
17	0.97	59	0.39
18	1.02	60	0.28
19	1.02	61	1.22
20	0.97	62	1.16
21	1.14	63	1.12
22	1.12	64	1.23
23	1.13	65	1.10
24	1.23	66	1.08
25	1.45	67	1.04
26	1.28	68	1.06
27	1.38	69	0.96
28	1.42	70	1.05
29	0.98	71	1.04
30	0.92	72	1.13
31	1.00	73	1.08
32	0.95	74	1.07
33	1.02	75	1.12
34	1.00	76	1.26
35	0.74	77	1.18
36	1.09	78	0.99
37	1.01	79	1.11
38	1.06	80	1.19
39	1.04	81	1.28
40	0.91	82	1.31
41	1.05	83	1.33
42	0.99	84	1.48

Table 5.14: **y–coordinate** of the center of each scintillation counter in inches.

Counter	Z center	Counter	Z center
1	-17.18	43	-370.80
2	-23.81	44	-377.53
3	-33.68	45	-387.80
4	-39.31	46	-394.43
5	-50.18	47	-404.18
6	-56.68	48	-410.80
7	-66.56	49	-420.68
8	-72.93	50	-427.30
9	-83.31	51	-437.05
10	-89.56	52	-443.18
11	-99.31	53	-453.55
12	-106.18	54	-460.30
13	-116.18	55	-470.30
14	-122.68	56	-476.80
15	-135.05	57	-489.05
16	-141.68	58	-495.68
17	-151.55	59	-505.68
18	-158.18	60	-512.30
19	-168.05	61	-522.05
20	-174.55	62	-528.55
21	-184.30	63	-538.55
22	-191.05	64	-544.93
23	-200.93	65	-554.93
24	-207.68	66	-561.68
25	-217.55	67	-571.55
26	-224.30	68	-578.18
27	-233.80	69	-588.05
28	-240.43	70	-594.55
29	-253.18	71	-606.80
30	-259.68	72	-613.55
31	-269.80	73	-623.30
32	-276.43	74	-629.93
33	-285.80	75	-639.80
34	-292.68	76	-646.55
35	-302.55	77	-656.18
36	-309.18	78	-662.93
37	-319.30	79	-672.93
38	-325.80	80	-679.68
39	-335.68	81	-689.55
40	-342.18	82	-696.55
41	-351.93	83	-706.55
42	-358.55	84	-713.18

Table 5.15: **z–coordinate** of the center of each scintillation counter in inches.

Counter Efficiency

Next, the simulation checks for inefficiencies along the muon track. An inefficiency gap of three or more counters along the path of the single muon can signal a false event end, causing the event to appear artificially shorter. The Monte Carlo assumes no inefficiencies inside hadronic showers or when two or more muons overlap. Counter efficiencies are measured using straight–through muons (trigger 6's) which pass though all 84 scintillation counters. The muons are required to be momentum analyzed with at least 10 GeV of energy at the front face of the toroid, and the upstream and downstream ends of the muon track are required to lie within a 50 inch box cut. The efficiencies are measured separately for neutrino and antineutrino running by looking for gaps of one, two, or three or more counters along the muon track. Figure 5.72 shows the probability of a gap of three or more counters compared to the probability for a single counter gap. Because the response of neighboring counters is correlated, the average probability for three consecutive unresponsive counters is about 3×10^{-5}, compared to the $\mathcal{O}(10^{-6})$ expectation if counter responses were completely uncorrelated. A look–up table in the Monte Carlo stores the random probabilities for a gap of one, two, three or more counters for each of the 84 calorimeter counters. No position dependence is observed, so none is applied in the Monte Carlo.

Counter Noise

The counters also have some probability of firing even when a muon is not present. Noise in the scintillation counters can artificially extend the length of an event causing a short event to become long. The counter simulation is further complicated

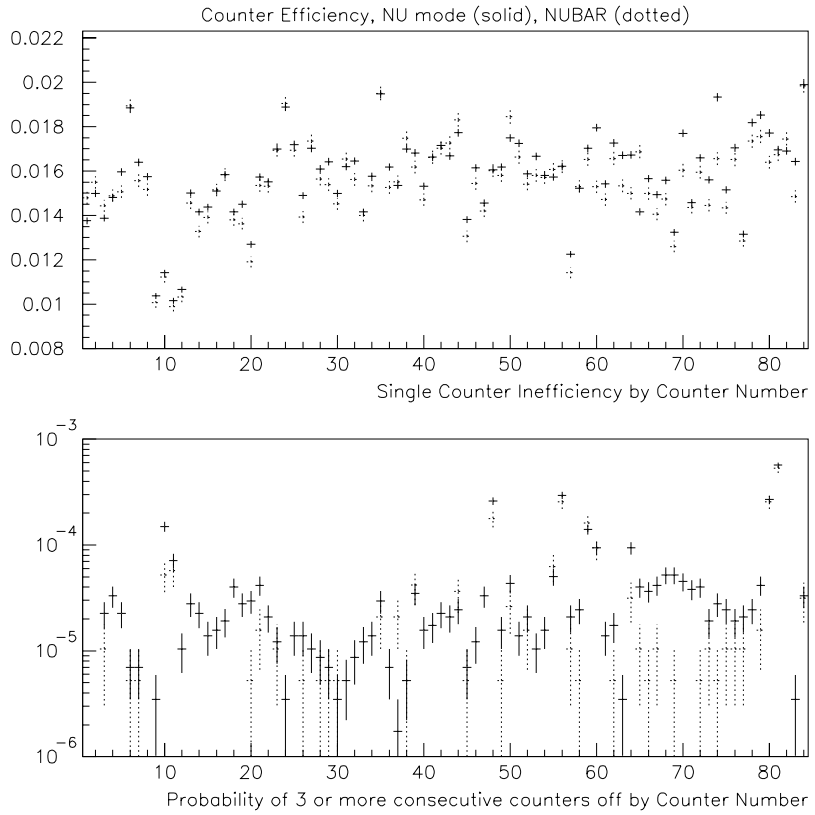

Figure 5.72: The top plot shows the measured single counter inefficiency for both ν (solid) and $\overline{\nu}$ (dotted) mode events. The bottom plot displays the probability of three or more consecutive counters not firing along the muon track. Both are plotted as a function of counter number.

by multiple interactions which can occur in the data (Figure 5.73). In this sense, "noise" loosely refers to anything that can extend the event length. Because such effects are correlated with neutrino activity, they are studied in high statistics samples of neutrino events by examining sections far from the interaction region.

The noise probabilities are measured using trigger 10 events (Chapter 3). Trigger 11 was originally designed for this purpose; however, the trigger occasionally fired due to neutrino activity in the calorimeter and not just from interactions in the

toroid as desired for noise studies. Since trigger 10 randomly fires during the fast gates and is not correlated with beam activity. The effect of beam pile–up must be added as a correction. A multiplicative pile–up correction is determined from the ratio of correlations between trigger 11 and trigger 10 events with in–time hits firing counter 84's Sbits but not the veto. To ensure that beam–uncorrelated noise is not scaled as consequence, cosmic ray gate trigger 10's are subtracted prior to the scaling procedure and then added back into the sample. The noise probabilities result from requiring greater than 0.25 mip (minimum ionizing particle) and an S–bit in each of three consecutive counters that are otherwise supposed to be quiet.

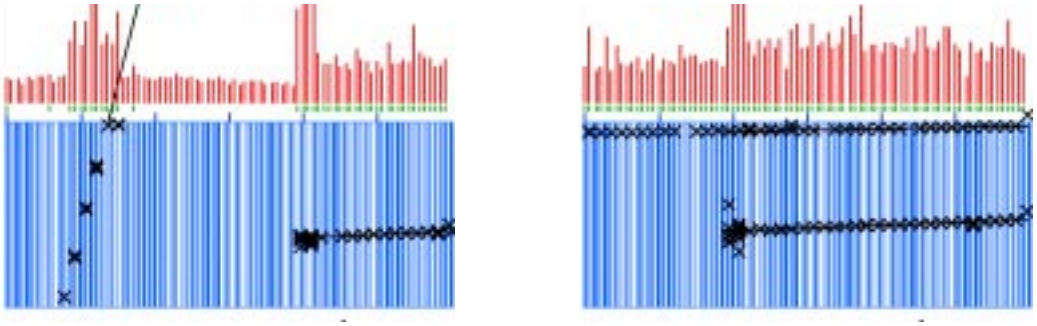

Figure 5.73: Examples of overlapping events in the NuTeV detector.

Like the counter efficiencies, separate noise files are generated for neutrino and antineutrino events. If three counters along the muon track are inefficient, then no noise is generated because the event necessarily terminated upstream of the noisy region. Figure 5.74 shows the multi–counter noise probabilities used in the Monte Carlo to determine the likelihood of noise hits extending the length of an event. The length can be extended up to a maximum number of 84 noisy counters, for instance, in the case of an overlay muon traversing the entire length of the calorimeter.

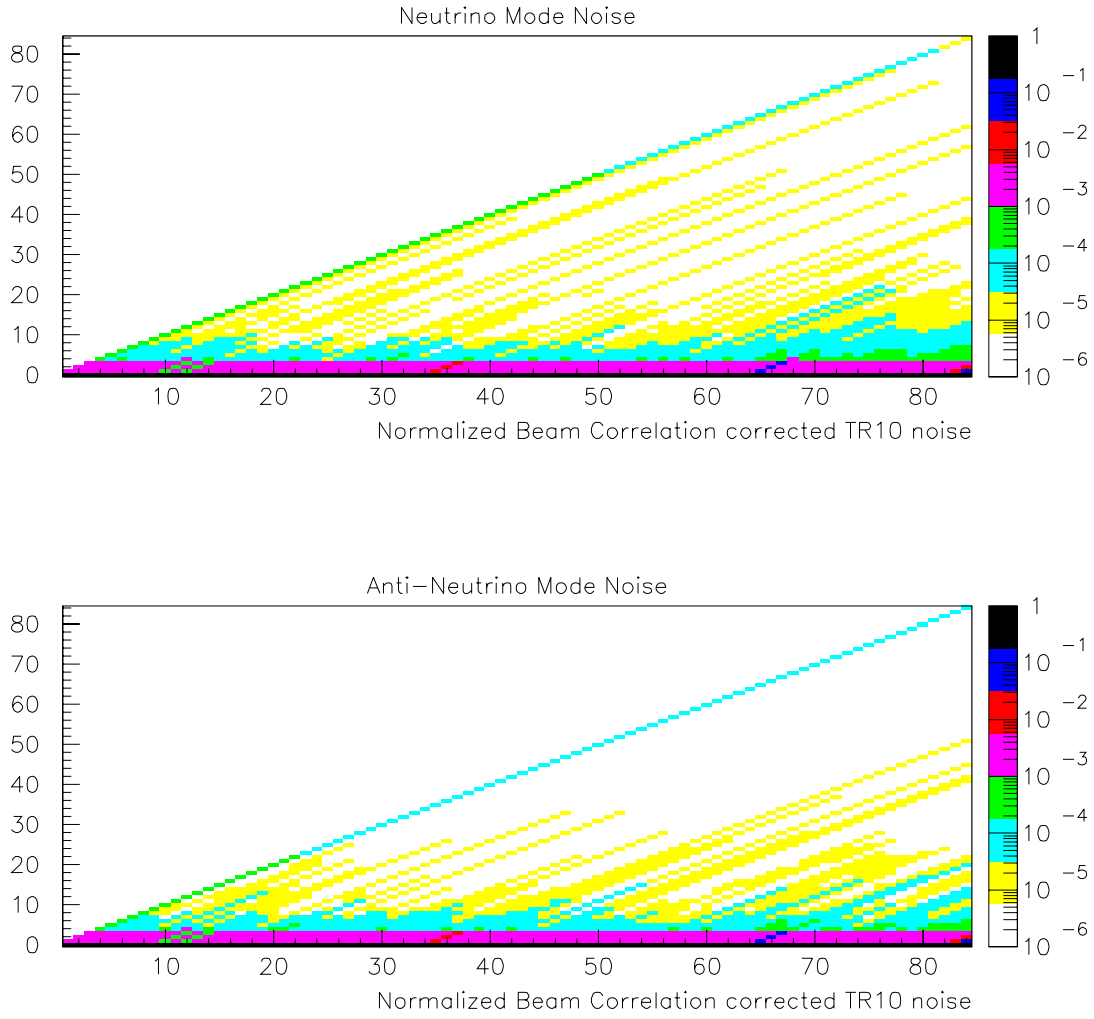

Figure 5.74: The final multi-counter noise probabilities used in the Monte Carlo. Plotted on the vertical axis is the number of counters the event length would be extended; on the horizontal axis is the counter number from which the search starts.

5.3.7 Hadron Shower Length

The hadronic shower determines the length of NC neutrino interactions in the detector. Approximately 0.7% of the NC events register as long events. This NC background to the CC sample, in which the shower "punches through" to longer lengths, must be modeled to roughly 10% to ensure small uncertainties in the final result. Single pion testbeam data measures shower lengths at discrete hadron energies but are insufficient alone to predict NC punch–through at the required level of precision. Instead, an augmented LEPTO simulation is employed to produce neutrino–induced hadron showers based on testbeam single pion and electron inputs. The procedure is as follows. LEPTO generates products of neutrino interactions, including electrons, γ's, and both charged and neutral hadrons. The distribution of lengths of electrons and γ's are set by testbeam electron data (e.g., Figure 5.62), while the distribution of hadron lengths is set by testbeam single pion data (Figures 5.75 and 5.76). All particles are allowed to propagate before they shower and are tracked based on their interaction probability. Neutral particles creating gaps of three or more consecutive scintillation counters truncate the length of the hadron shower, as in the data. A small modification to the LEPTO simulation prevents generation of charm final states ($c \rightarrow \mu$) so as not to duplicate the charm semileptonics that are already included in the primary Monte Carlo muon tracking model (Section 5.1.4).

Figure 5.77 compares the resultant Monte Carlo length predictions to the distributions in the data. Toroid events, comprising $\sim 60\%$ of the total sample, normalize the Monte Carlo events to the data, but have been excluded from the plot for clarity. In the remaining CC events, either the muon has a low energy and ranges out in the calorimeter or the muon has a large opening angle and exits out the side of the

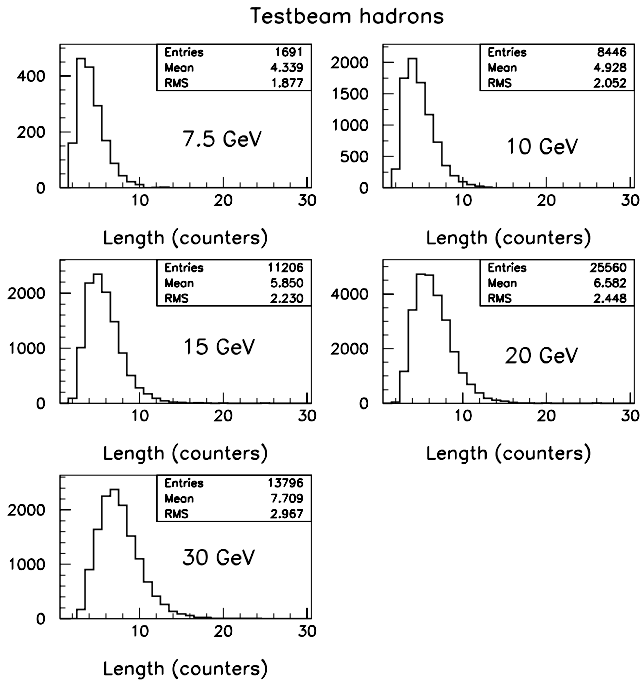

Figure 5.75: Shower lengths for testbeam π's ranging in energy from 7 to 30 GeV.

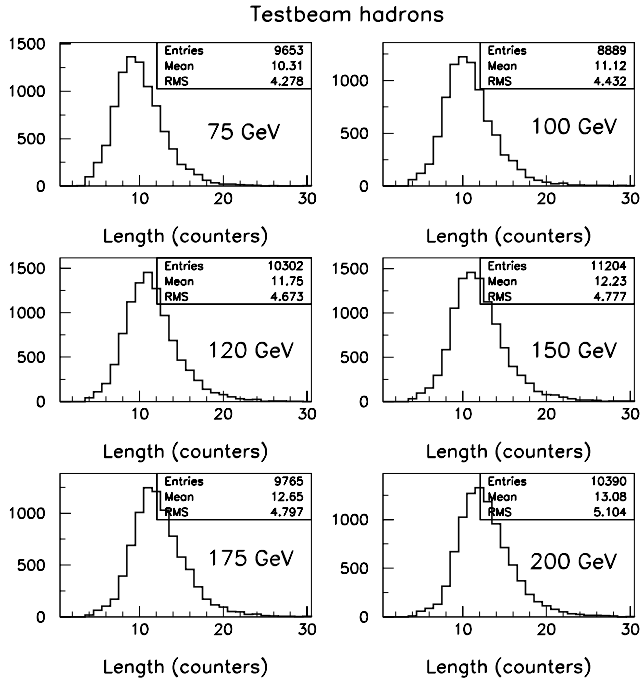

Figure 5.76: Shower lengths for testbeam π's ranging in energy from 75 to 200 GeV.

detector. Excellent agreement results in the region of the length cut, as indicated by the plot inlays, as well as in the L> 31 counter region. The later provides additional confidence in the Monte Carlo estimate of the ν_μ short CC background in the NC region.

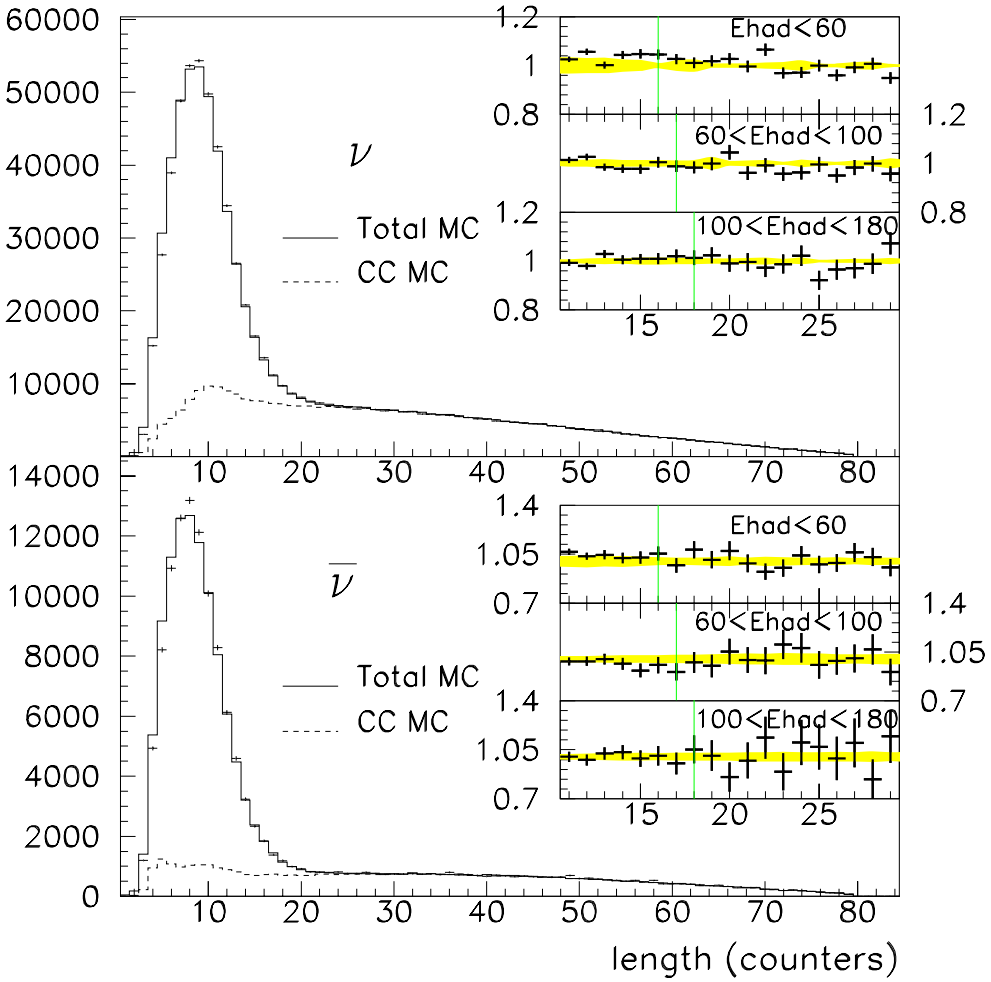

Figure 5.77: Comparison of data and MC length distributions for both ν (top) and $\overline{\nu}$ (bottom) events. The dashed curve shows the total CC Monte Carlo prediction $(\nu_\mu + \nu_e)$. The inlays display data/MC ratios in the region of the length cut. In each case, the length cut is represented by the pale vertical line. The bands indicate the $\pm 1\sigma$ systematic uncertainty.

Tables 5.16 through 5.19 list the number of events in each length bin for both data and Monte Carlo. The Monte Carlo listing includes a breakout of the individual ν_e, ν_μ NC, and ν_μ CC contributions in each bin.

Figure 5.78 displays the level of agreement between data and Monte Carlo at very short lengths. The marginal ability of the shower length model to describe hadronic showers spanning only a few counters to better than 10% is covered by systematics and does not affect the analysis.

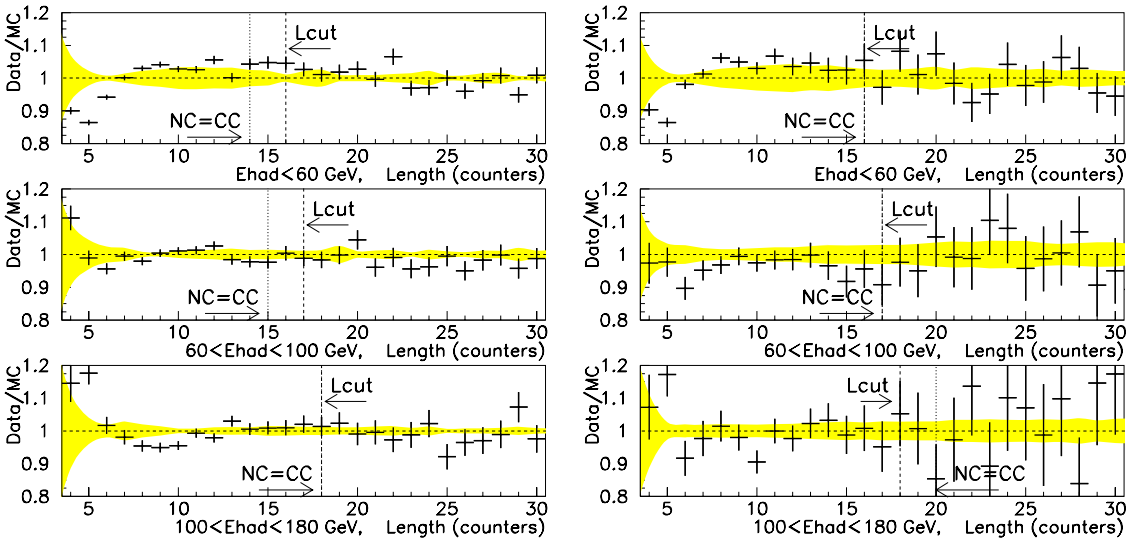

Figure 5.78: Short length data/MC agreement in several energy bins for both ν (left) and $\overline{\nu}$ (right) events. The locations of the length cut and the place where the NC and CC content are equal (as determined from MC) are also indicated. The shaded bands show the $\pm 1\sigma$ systematic uncertainty.

Length	Data	Monte Carlo Total	Monte Carlo $\nu_e + \overline{\nu}_e$	Monte Carlo $\nu_\mu^{\rm NC} + \overline{\nu}_\mu^{\rm NC}$	Monte Carlo $\nu_\mu^{\rm CC} + \overline{\nu}_\mu^{\rm CC}$
1	0	133	19	109	5
2	102	526	53	463	10
3	3040	4003	458	3435	110
4	15224	16310	2070	13692	548
5	27677	30650	3485	25813	1352
6	38948	41020	3357	35189	2474
7	48826	48919	3166	41835	3918
8	53647	53194	3344	44516	5334
9	54341	53494	3225	43567	6702
10	49774	49423	2911	38962	7550
11	42515	41946	2399	31757	7790
12	34459	33655	1826	24128	7701
13	26533	26416	1334	17457	7625
14	20801	20591	909	12428	7254
15	16543	16336	657	8463	7216
16	13576	13282	380	5598	7304
17	11211	11069	274	3689	7106
18	9727	9698	180	2410	7108
19	8674	8561	121	1521	6919
20	8150	7950	86	1002	6862
21	7478	7592	53	655	6884
22	7378	7203	32	428	6743
23	6977	7203	26	308	6869
24	6815	6974	26	217	6731
25	6745	6847	17	158	6672
26	6507	6793	11	118	6664
27	6623	6721	7	92	6622
28	6466	6456	5	76	6375
29	6253	6434	3	64	6367
30	6334	6356	6	52	6298
31	6159	6164	10	42	6112
32	6170	6184	4	40	6140
33	5850	6060	5	31	6024
34	5832	5827	4	32	5791
35	5722	5773	2	30	5741
36	5629	5765	6	22	5737
37	5497	5585	1	19	5565
38	5371	5352	2	22	5328
39	5144	5303	5	16	5282
40	5174	5143	3	23	5117

Table 5.16: Number of **neutrino** events in each length bin (L=0–40).

Length	Data	Monte Carlo Total	Monte Carlo $\nu_e + \overline{\nu}_e$	Monte Carlo $\nu_\mu^{\rm NC} + \overline{\nu}_\mu^{\rm NC}$	Monte Carlo $\nu_\mu^{\rm CC} + \overline{\nu}_\mu^{\rm CC}$
41	4849	5054	1	23	5030
42	4802	4853	2	22	4829
43	4716	4689	0	17	4672
44	4635	4590	4	23	4563
45	4498	4520	3	16	4501
46	4476	4435	1	17	4417
47	4176	4256	2	9	4245
48	4141	4133	1	12	4120
49	3961	3864	1	10	3853
50	3734	3859	2	7	3850
51	3646	3678	1	8	3669
52	3465	3639	1	6	3632
53	3458	3434	3	5	3426
54	3204	3314	2	6	3306
55	3102	3092	1	4	3087
56	3026	3004	0	4	3000
57	2814	2858	0	3	2855
58	2757	2729	1	3	2725
59	2634	2581	1	1	2579
60	2515	2548	0	2	2546
61	2419	2416	0	1	2414
62	2291	2263	2	1	2260
63	2109	2140	0	0	2140
64	2039	2015	1	2	2013
65	1936	1927	0	1	1926
66	1743	1847	0	2	1845
67	1680	1647	0	1	1646
68	1520	1564	0	0	1564
69	1410	1480	0	0	1479
70	1318	1340	0	2	1338
71	1182	1195	0	0	1194
72	1034	1032	0	0	1032
73	1025	1027	0	0	1027
74	847	862	0	0	861
75	751	766	0	0	766
76	629	683	0	0	683
77	572	572	0	0	572
78	417	481	0	0	481
79	279	319	0	0	319
80	0	0	0	0	0
toroid	912739	912742	112	768	911854

Table 5.17: Number of **neutrino** events in each length bin (L=41+).

Length	Data	Monte Carlo Total	Monte Carlo $\nu_e + \overline{\nu}_e$	Monte Carlo $\nu_\mu^{\rm NC} + \overline{\nu}_\mu^{\rm NC}$	Monte Carlo $\nu_\mu^{\rm CC} + \overline{\nu}_\mu^{\rm CC}$
1	0	53	10	42	1
2	33	184	25	157	3
3	1198	1403	224	1163	16
4	4927	5370	947	4353	69
5	8209	9165	1232	7804	129
6	10922	11293	1028	10048	217
7	12597	12579	813	11422	344
8	13179	12683	748	11464	471
9	12120	11782	652	10558	572
10	10082	10108	560	8902	647
11	8284	8039	423	6968	648
12	6121	6073	297	5103	673
13	4593	4478	213	3601	664
14	3231	3205	143	2441	621
15	2338	2381	94	1653	634
16	1853	1826	66	1077	683
17	1376	1451	40	703	708
18	1189	1139	24	442	674
19	989	996	12	287	696
20	916	887	10	187	690
21	813	826	8	122	696
22	796	821	5	82	734
23	791	803	4	59	740
24	815	770	2	40	727
25	756	769	1	32	735
26	755	764	2	24	739
27	798	759	1	21	738
28	764	749	2	16	731
29	731	762	1	14	747
30	736	760	1	12	747
31	738	747	2	10	736
32	754	784	1	8	775
33	744	747	0	7	739
34	749	750	1	8	741
35	730	736	1	5	730
36	794	732	1	5	726
37	711	745	0	5	740
38	723	705	0	5	699
39	693	691	0	5	686
40	665	719	1	6	712

Table 5.18: Number of **antineutrino** events in each length bin (L=0–40).

Length	Data	Monte Carlo Total	Monte Carlo $\nu_e + \overline{\nu}_e$	Monte Carlo $\nu_\mu^{\rm NC} + \overline{\nu}_\mu^{\rm NC}$	Monte Carlo $\nu_\mu^{\rm CC} + \overline{\nu}_\mu^{\rm CC}$
41	715	689	1	5	683
42	678	696	1	6	689
43	660	691	0	5	685
44	681	665	1	4	661
45	651	668	0	3	665
46	647	637	0	4	632
47	636	643	1	2	640
48	635	634	0	2	632
49	696	595	0	3	592
50	593	599	0	2	597
51	605	573	0	1	571
52	574	568	0	1	567
53	555	553	0	1	553
54	537	526	0	1	525
55	509	504	0	1	503
56	527	506	0	2	504
57	490	473	0	1	472
58	527	466	0	1	465
59	423	452	1	0	452
60	431	413	0	0	413
61	425	420	0	1	419
62	407	397	0	0	397
63	394	360	0	1	360
64	355	358	0	0	357
65	370	337	0	0	337
66	332	326	0	0	326
67	288	307	0	0	307
68	288	305	0	0	305
69	293	283	0	0	283
70	245	244	0	0	244
71	240	224	0	0	223
72	194	202	0	0	201
73	210	202	0	0	202
74	180	189	0	0	188
75	162	158	0	0	158
76	152	134	0	0	134
77	124	118	0	0	118
78	121	100	0	0	100
79	65	77	0	0	77
80	0	0	0	0	0
99	214644	214669	25	167	214477

Table 5.19: Number of **antineutrino** events in each length bin (L=40+).

Chapter 6

Data–Monte Carlo Comparisons

6.1 Comparison of Event Variable Distributions

To demonstrate that the Monte Carlo accurately simulates neutral and charged current neutrino interactions in our detector, we compare data and Monte Carlo distributions of all event variables in the analysis. In all cases, the Monte Carlo assumes the best–fit $\sin^2\theta_W$ of Chapter 8 and has been normalized to the data using the total number of events reaching the toroid. The data is cosmic ray subtracted in all figures. The χ^2 calculations of this chapter include only the statistical errors, which have been rescaled to account for Monte Carlo statistics. Of interest are comparisons of:

- $\mathbf{E_{had}}$: Figure 6.2 shows shower energy distributions for the entire analysis sample and including events above 180 GeV (the measurement of ν_e events above 180 GeV is included in the Monte Carlo prediction). Good agreement is exhibited across the entire energy range. The Monte Carlo also accurately simulates changes in the number of counters used in the variable–length hadronic energy summation, E_{hadvar}. These dips appear because most events have a final state

muon which contributes, on average, 0.2 GeV of energy to each counter. To illustrate the effect, Figure 6.1 shows the ratio of E_{hadvar}/E_{had20} for Monte Carlo events.

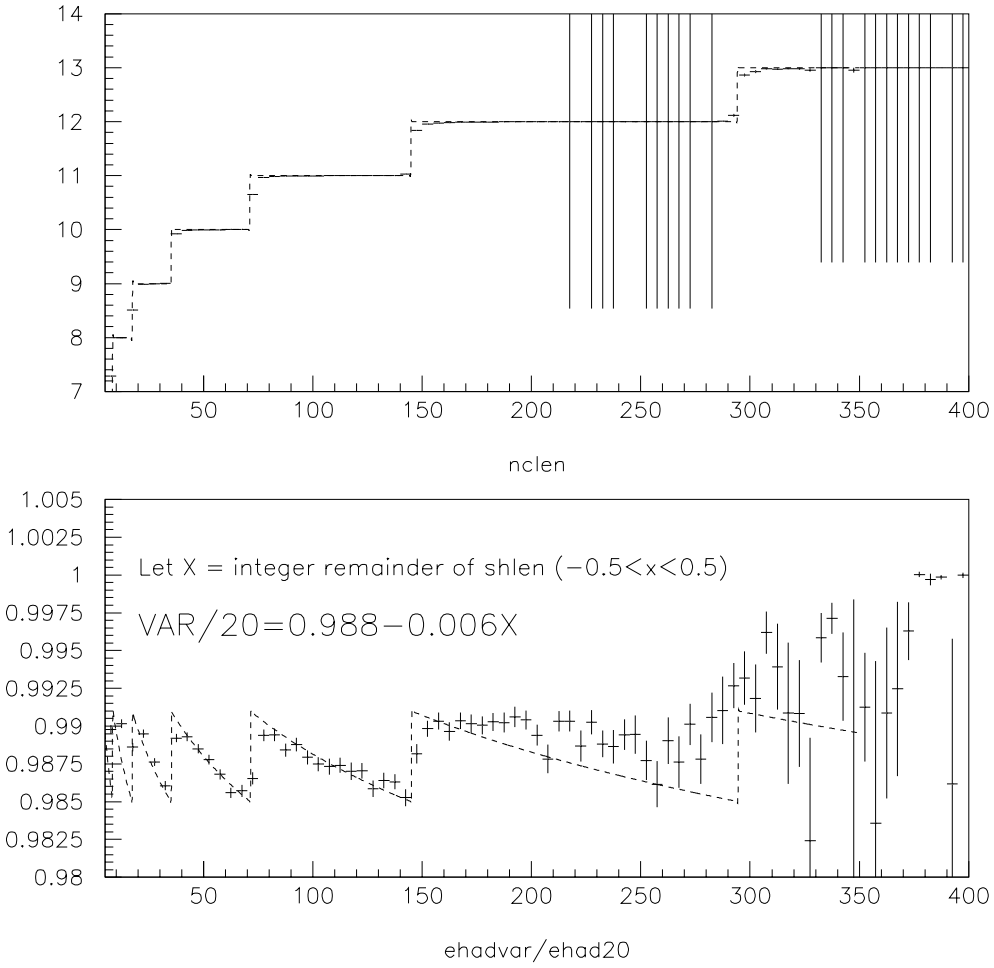

Figure 6.1: The top plot shows the number of counters employed in the variable length E_{had} sum as a function of energy. The bottom plot shows the resultant ratio of E_{hadvar}/E_{had20}, again for Monte Carlo events. The discontinuities reveal the boundaries where the length sum changes.

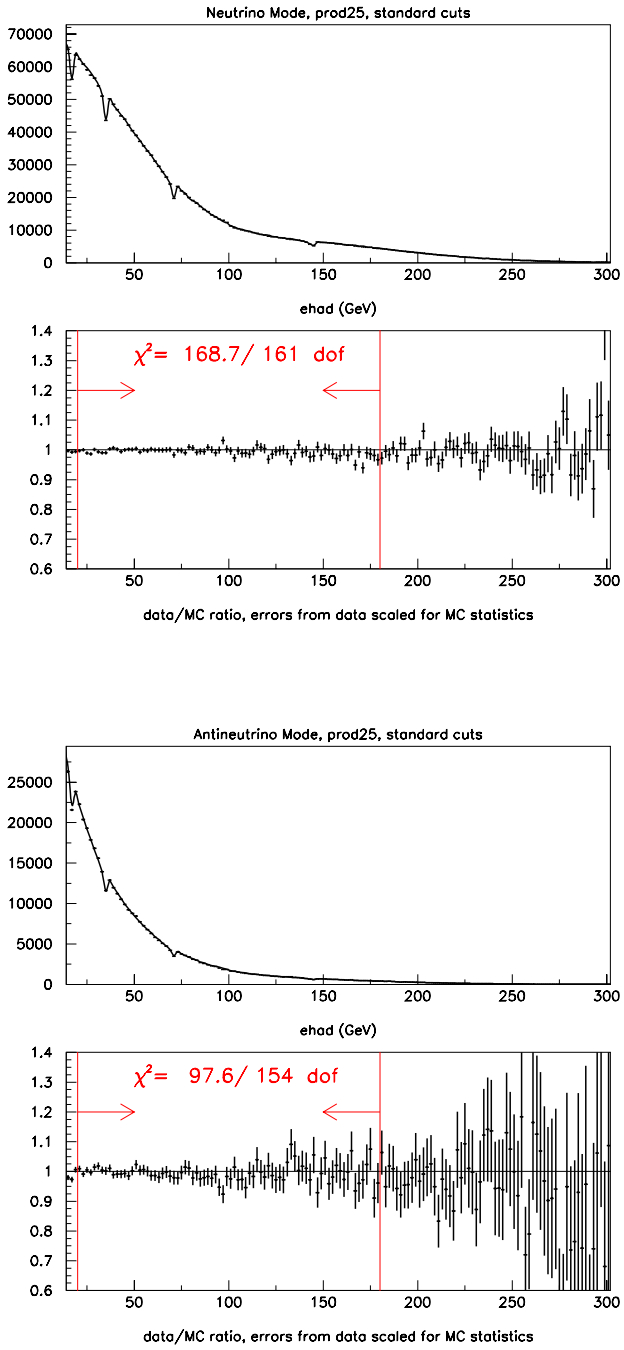

Figure 6.2: Comparison of data and Monte Carlo (solid curve) $\mathbf{E_{had}}$ distributions for both ν (top) and $\overline{\nu}$ (bottom) events. The vertical lines with arrows indicate the range of data included in the analysis, $20 \leq \mathrm{E_{had}} \leq 180$ GeV.

- **Length**: Figure 6.3 compares the length distributions in the data and Monte Carlo for events that pass the analysis requirements. Of primary importance is the excellent agreement in the region of the length cut (L=16–18) and for short ν_μ CC events where the muon either ranges out or left the detector at a wide angle ($31 \leq \mathrm{L} < 99$). The marginal statistical agreement between data and Monte Carlo near the NC peak and at very low lengths ($\mathrm{L} \lesssim 10$) does not affect the determination of R_{exp} because it is within assigned systematics. The disagreement probably results from uncertainties in the modeling of very short hadron shower lengths, not from an error in the estimation of the short ν_μ CC events (as evinced by the excellent agreement in the $31 \leq \mathrm{L} < 99$ region), and not from the level of ν_e contamination (which has been constrained by direct measurements).

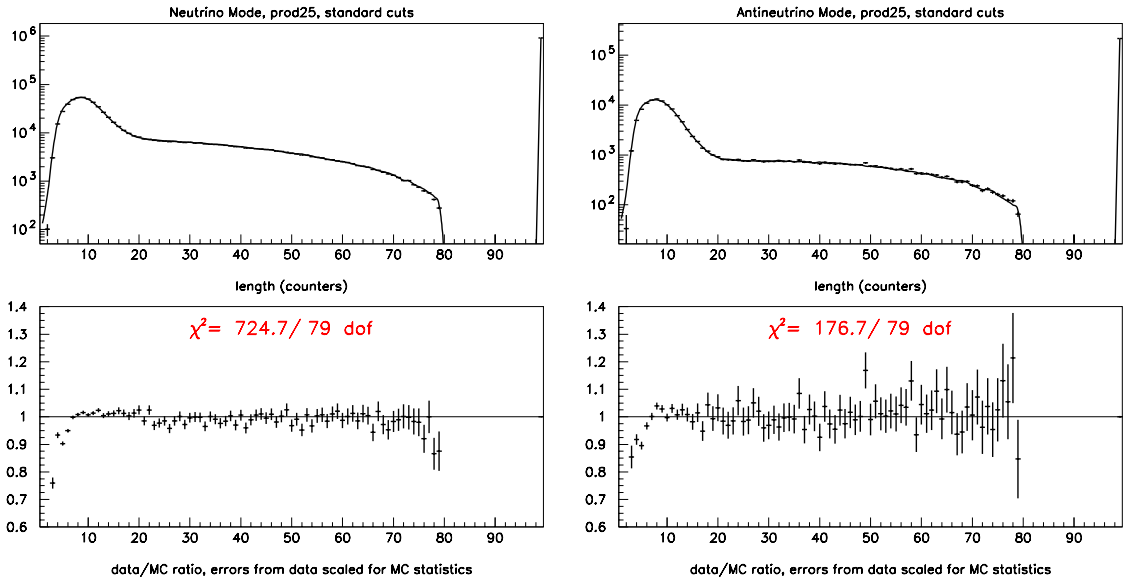

Figure 6.3: Comparison of data and Monte Carlo (solid curve) **length** distributions for both neutrino (left) and antineutrino (right) events passing analysis cuts. Toroid events are assigned a length of 99 counters by default.

- **PLACE**: The Monte Carlo accurately tracks the even/odd differences and single counter dips observed in the PLACE distribution in the data (Figure 6.4). Modeling of the PLACE determination was discussed in detail in Chapter 5.

- **Vx,Vy**: Figures 6.5 and 6.6 display vertex distributions in both x and y for data and Monte Carlo. Good agreement is observed even beyond the analysis cuts at 40 inches in x and 45 inches in y.

In general, the agreement between data and Monte Carlo shown in these figures is quite good; without exception the agreement is more than satisfactory for the purposes of the present analysis. The agreement certainly inspires confidence in the ability of the Monte Carlo model to simulate the distribution of events in the data. However, to ensure that the apparent accuracy of the Monte Carlo is not accidental in some way, the next section probes the stability of the agreement relative to changes in the analysis cuts.

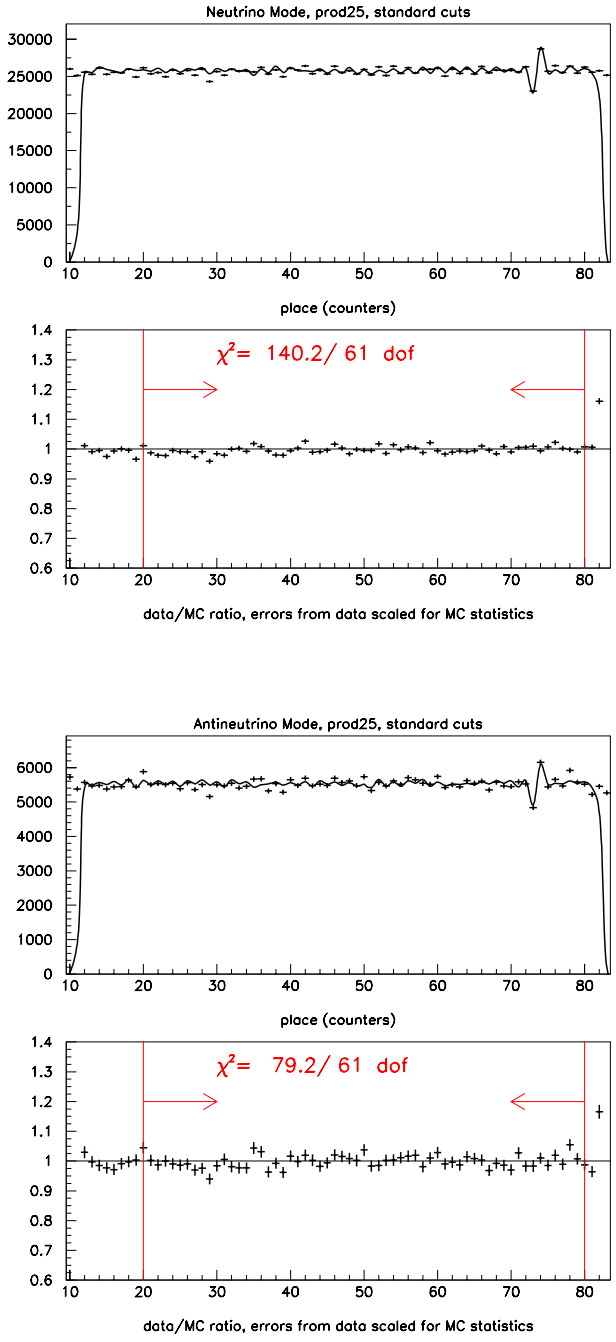

Figure 6.4: Data and MC (solid curve) **PLACE** distributions for both ν (top) and $\overline{\nu}$ (bottom) events. The calorimeter counters are numbered from 1 to 84, counter 1 being the most downstream. MC events are generated from PLACE = 12 to 82.

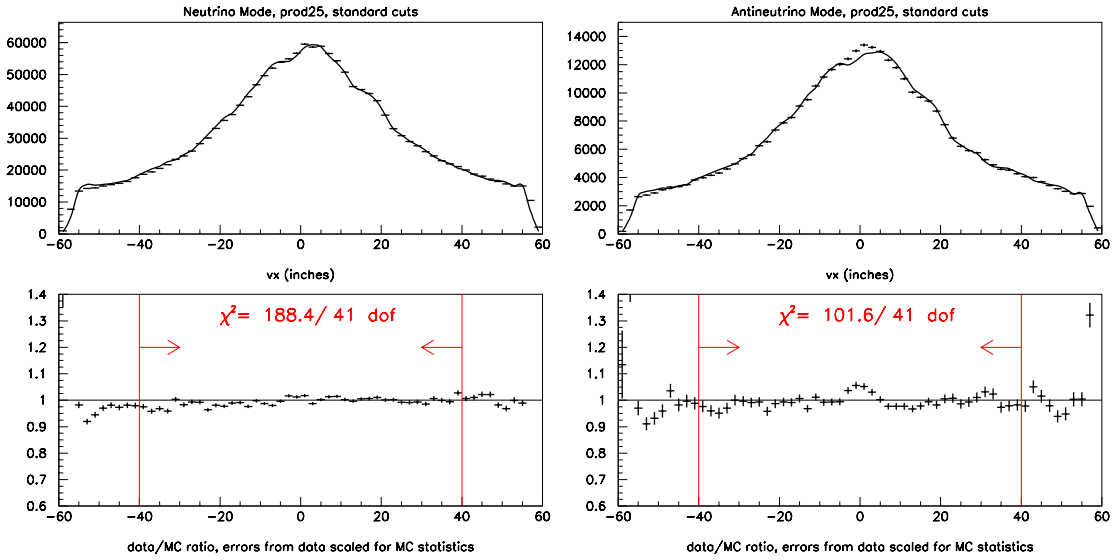

Figure 6.5: Comparison of data and MC (solid curve) **Vx** distributions for both ν (left) and $\overline{\nu}$ (right) events. The arrows indicate the range included in the analysis.

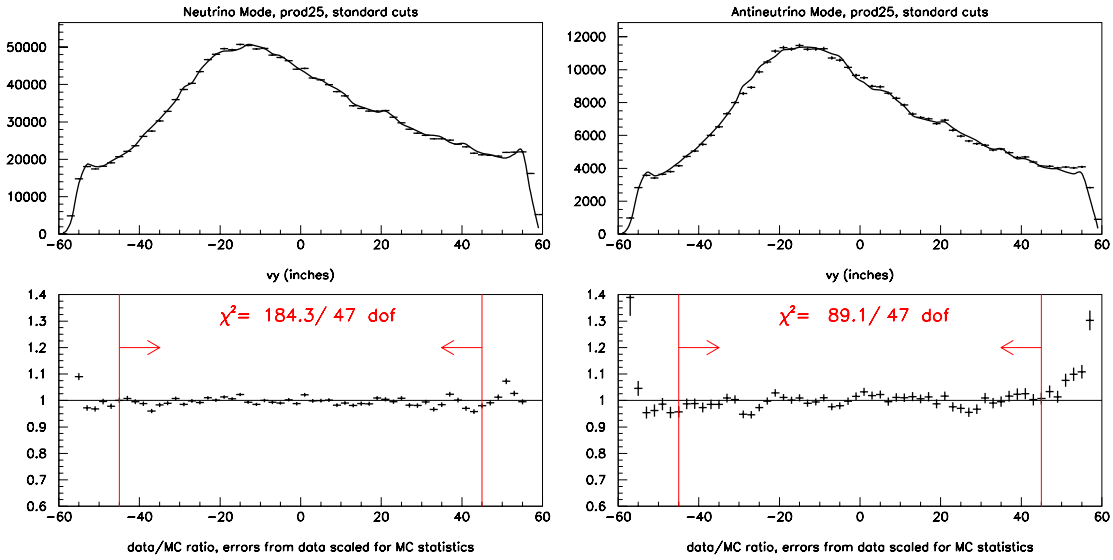

Figure 6.6: Comparison of data and MC (solid curve) **Vy** distributions for both ν (left) $\overline{\nu}$ (right) events. The arrows indicate the range included in the analysis.

6.2 Stability Checks

Careful checks of possible systematic effects due to detector instabilities verify the consistency of the ratios under changes in fiducial cuts and over different ranges of event variables. The following sections discuss the stability of $R_{\rm exp}$ as a function of time, length cut, vertex position, and hadronic energy.

6.2.1 Time Dependence

Figure 6.7 displays the time dependence of $R_{\rm exp}$ in the data during both neutrino and antineutrino running. No single ν ($\overline{\nu}$) run differs by more than 3σ (3.5σ) from the average. Furthermore, the ratios exhibit no trend over time (the slopes are less than 10^{-4} in each case).

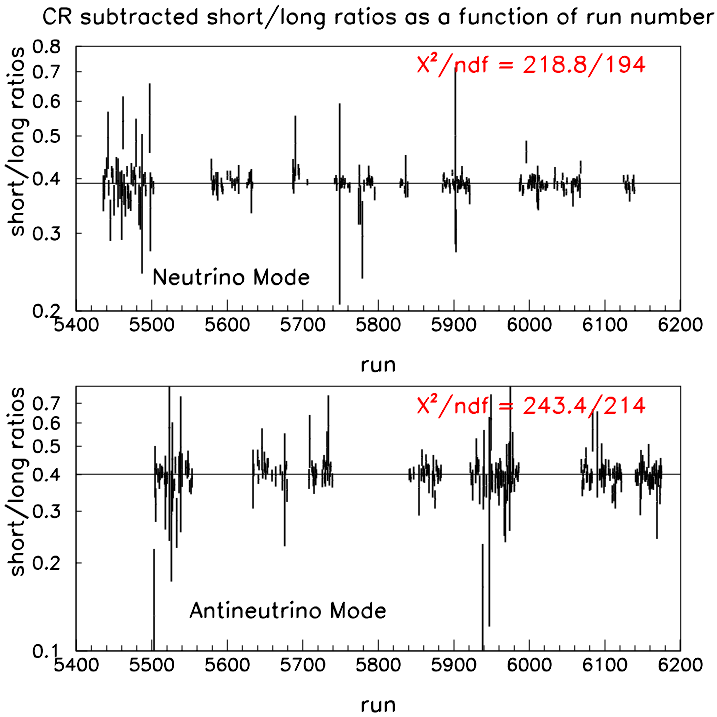

Figure 6.7: $R_{\rm exp}$ plotted as a function of run number for runs accepted in the analysis. The data have been cosmic ray subtracted.

6.2.2 Length Cut Variation

To check the chosen NC/CC separation, the short/long ratios are extracted under several choices of length cuts. Figure 6.8 compares $R_{\rm exp}$ in the data and Monte Carlo as a function of length cut, varying from a NC/CC separation that contains less than 0.5% CC background to one which contains roughly 99% CC events. Data and Monte Carlo agree well over this entire range.

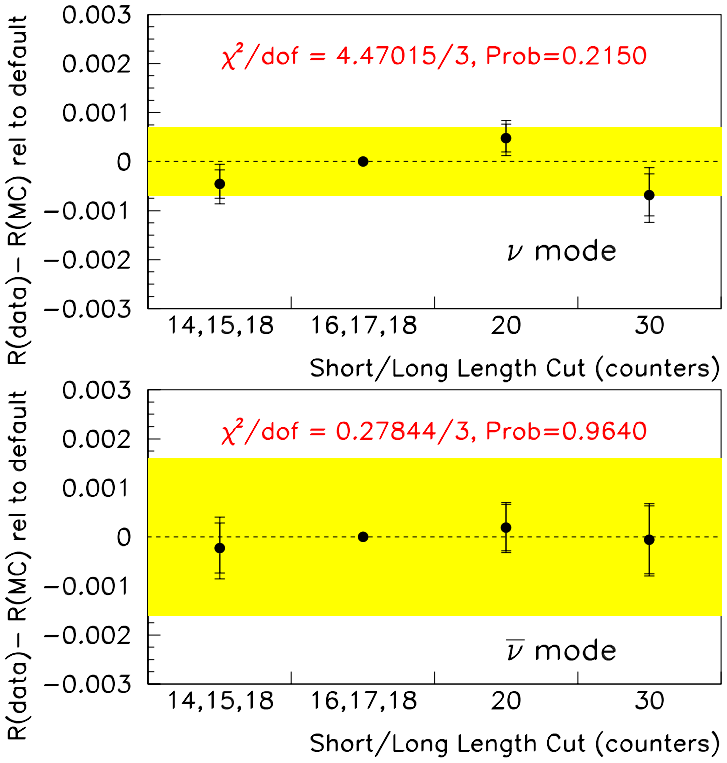

Figure 6.8: Variation in the agreement between $R_{\rm exp}$ in data and MC under various length cut choices. The data point with no error bars indicates the default length cut at 16,17,18 counters (Section 4.3). The point to the left indicates a tighter length cut; cutting closer to the NC peak. The two points to the right indicate looser cuts; cutting further away from the NC peak. The errors on these points are relative to the default length cut and include both statistical uncertainties as well as the largest systematic uncertainties which affect the length determination. The large bands indicate the statistical error on the measurement of $R_{\rm exp}$ in the data.

6.2.3 Position Dependence

A comparison of $R_{\rm exp}$ in data and Monte Carlo as a function of longitudinal event vertex checks the uniformity of the detector (Figure 6.9). The agreement is flat as a function of PLACE with high probability as expected for neutrino interactions. This would not be the case, for example, if there were a neutron background present in the data sample that had not been properly accounted for. Such neutrons would preferentially populate the upstream end of the detector because the neutron interaction length is small compared to the dimensions of the detector. In this were the case, one would observe an exponential falloff consistent with neutron interactions rather than the observed flat behavior expected for neutrinos.

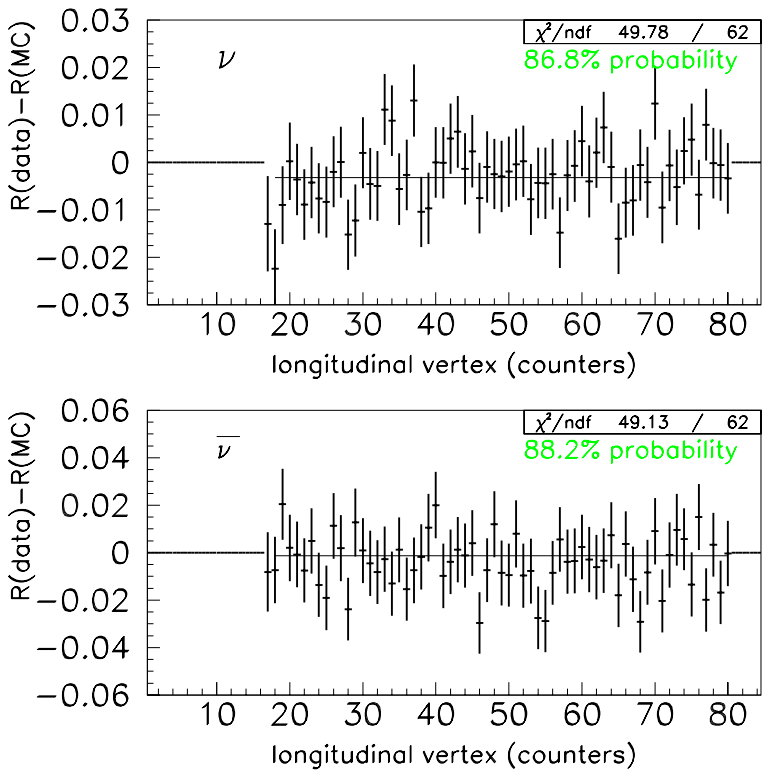

Figure 6.9: Plot of the agreement between $R_{\rm exp}$ in data and Monte Carlo as a function of longitudinal vertex position, PLACE. The incoming neutrino direction is from right to left in this plot. Errors are statistical only.

The short/long ratios in data and Monte Carlo are also extracted as a function of the transverse vertex of the event. Figure 6.10 compares $R_{\rm exp}$ in data and Monte Carlo for four independent 10 inch frame bins. The bin numbering is as indicated in Chapter 4: bins 1-4 are included in the analysis while bin 5 is included as a cross-check. Such a comparison validates the NC background predictions, both ν_e and short CC, which preferentially populate the outer edges of the detector. Reasonable, flat agreement spans the entire fiducial region. The χ^2 probability for these results is 26% in ν mode, 76% in $\overline{\nu}$ mode.

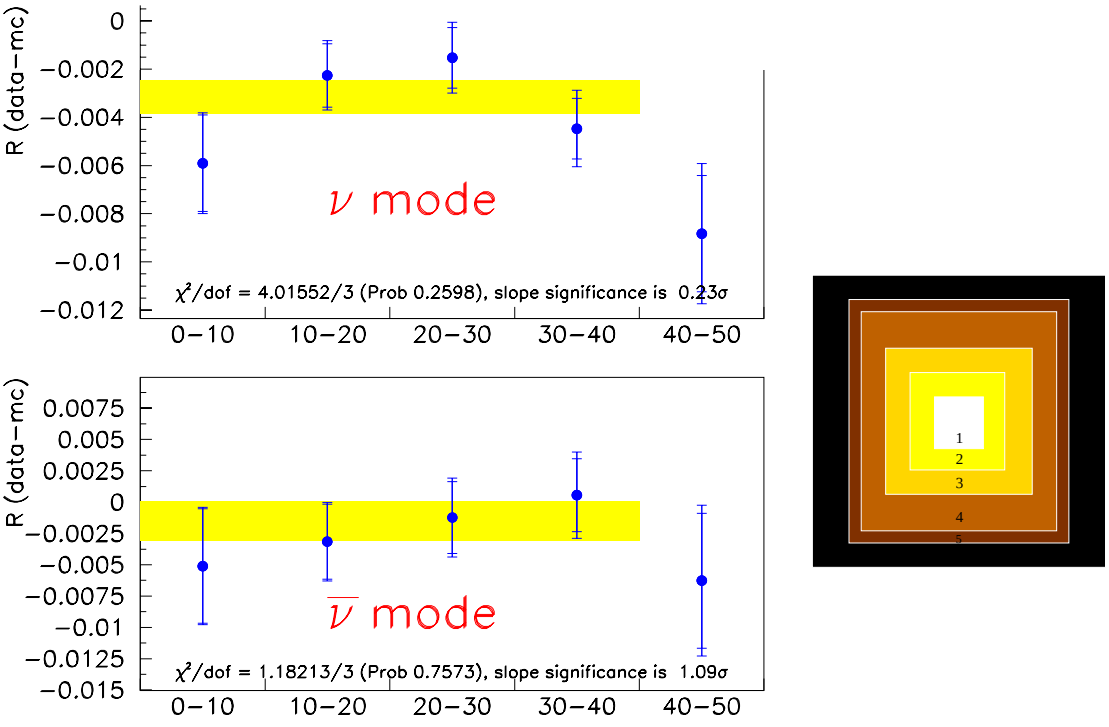

Figure 6.10: Plot of the variation $R_{\rm exp}$ in data and Monte Carlo as a function of frame box bins, moving from the inner region of the detector (left) to the outer edge of the detector (right). The bins are mutually exclusive, for example, bin 2 does not contain events from bin 1 and vice versa. The error bars represent the statistical and systematic uncertainties. The band indicates the statistical uncertainty on the measurement of $R_{\rm exp}$ in the data.

Moreover, the agreement is not unreasonable if a fiducial bin beyond the standard analysis region were to be included in the comparison (Figure 6.11). Including the additional outer–most bin, actually improves the agreement in $\overline{\nu}$ mode, the probability in ν mode remains acceptable at 11%.

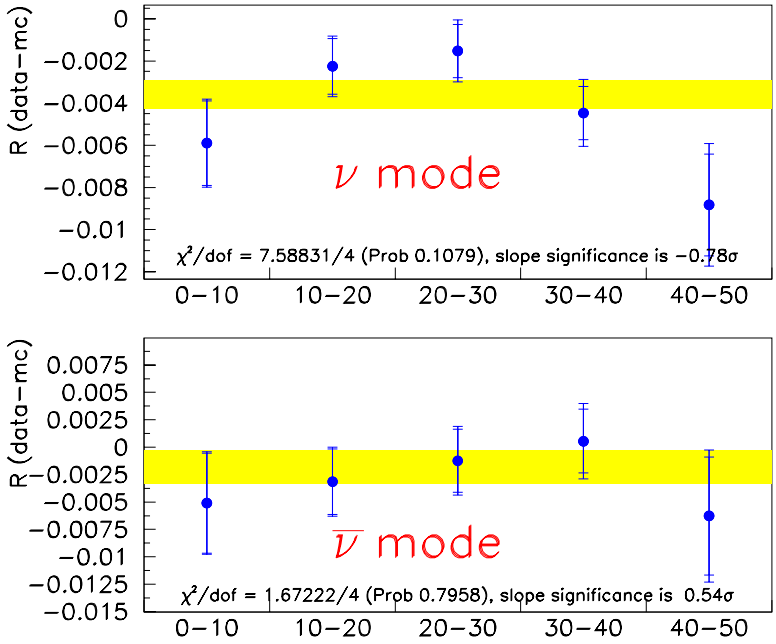

Figure 6.11: Fit results after including one bin beyond the standard fiducial region.

6.2.4 Energy Dependence

Finally, the result is stable as a function of energy. Figures 6.12 and 6.13 display the agreement between the hadronic energy distributions in the data and Monte Carlo for short and long events, respectively. This comparison checks the sum of all effects: backgrounds, neutrino flux, detector modeling, cross section model, etc. Reasonable agreement is exhibited. In all cases, the systematics have been added in

quadrature and are included in the calculation of the χ^2's. The χ^2's include bin to bin correlations, and the structure in these plots is not outside systematics.

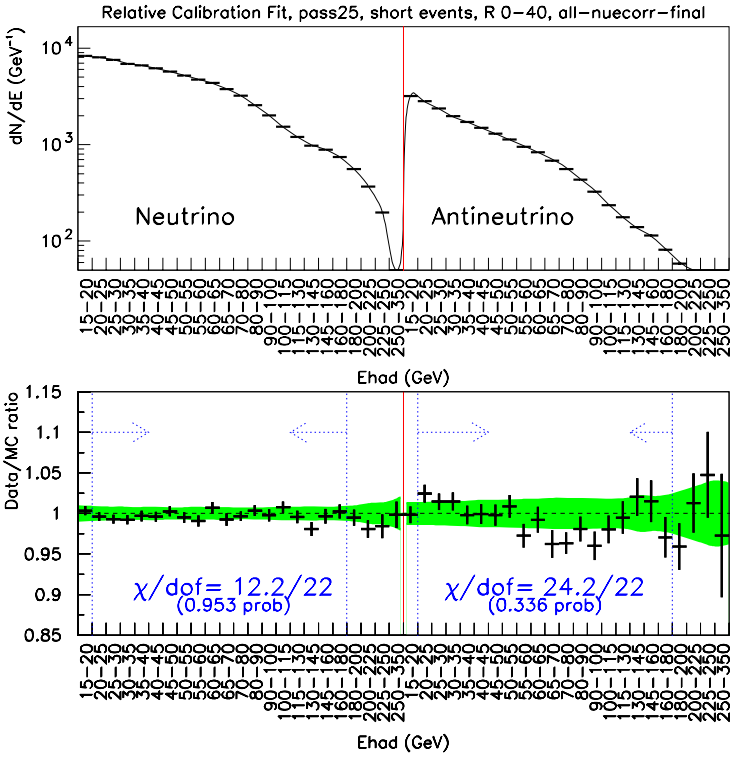

Figure 6.12: E_{had} distributions in data and Monte Carlo for **short** (NC candidate) events. The band on the lower data/MC ratio plot indicates the $\pm$ 1 σ systematic uncertainty. The arrows indicate the range of data included in the final analysis, namely $20 \leq E_{had} \leq 180$ GeV. Note that the measurement of ν_e events above 180 GeV has been included in the MC (Section 5.2.3).

Because the Monte Carlo accurately simulates the individual short and long energy distributions, the short/long ratios are also in good agreement. (Figure 6.15).

A summary of the χ^2 probabilities from the stability tests presented in this section shows no obvious indication of a problem. Figure 6.14 plots the probabilities for both the neutrino and antineutrino mode tests. The mean probability is 55%.

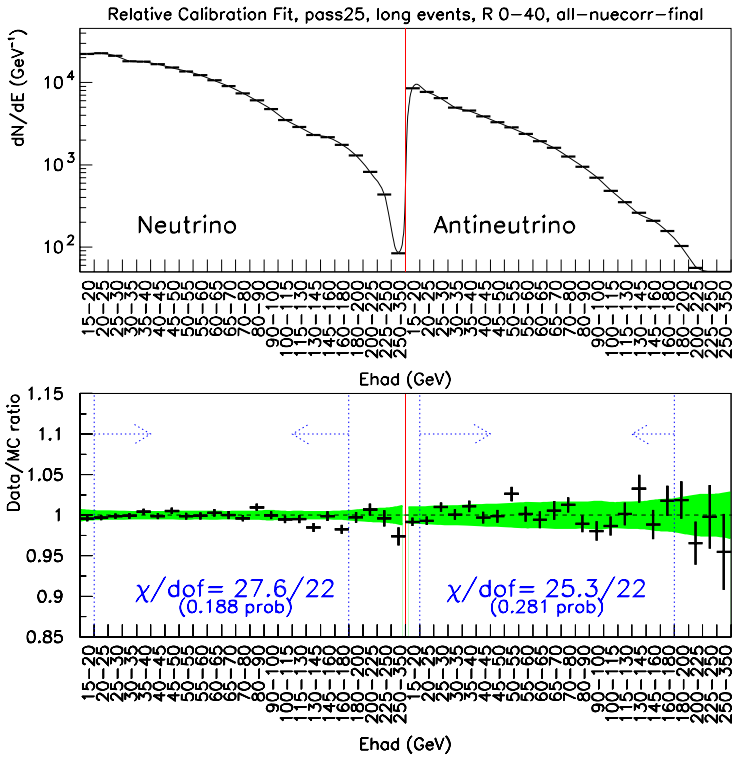

Figure 6.13: E_{had} distributions in data and Monte Carlo for **long** (CC candidate) events. The band on the lower data/MC ratio plot indicates the $\pm$ 1 σ systematic uncertainty. The arrows indicate the range of data included in the final analysis.

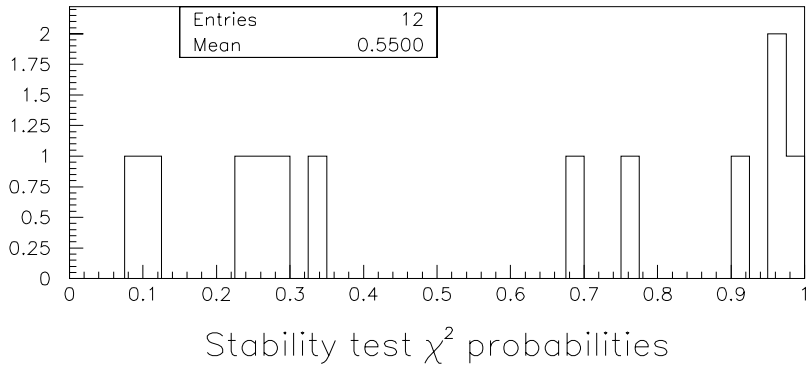

Figure 6.14: χ^2 probabilities from the stability checks presented in this section.

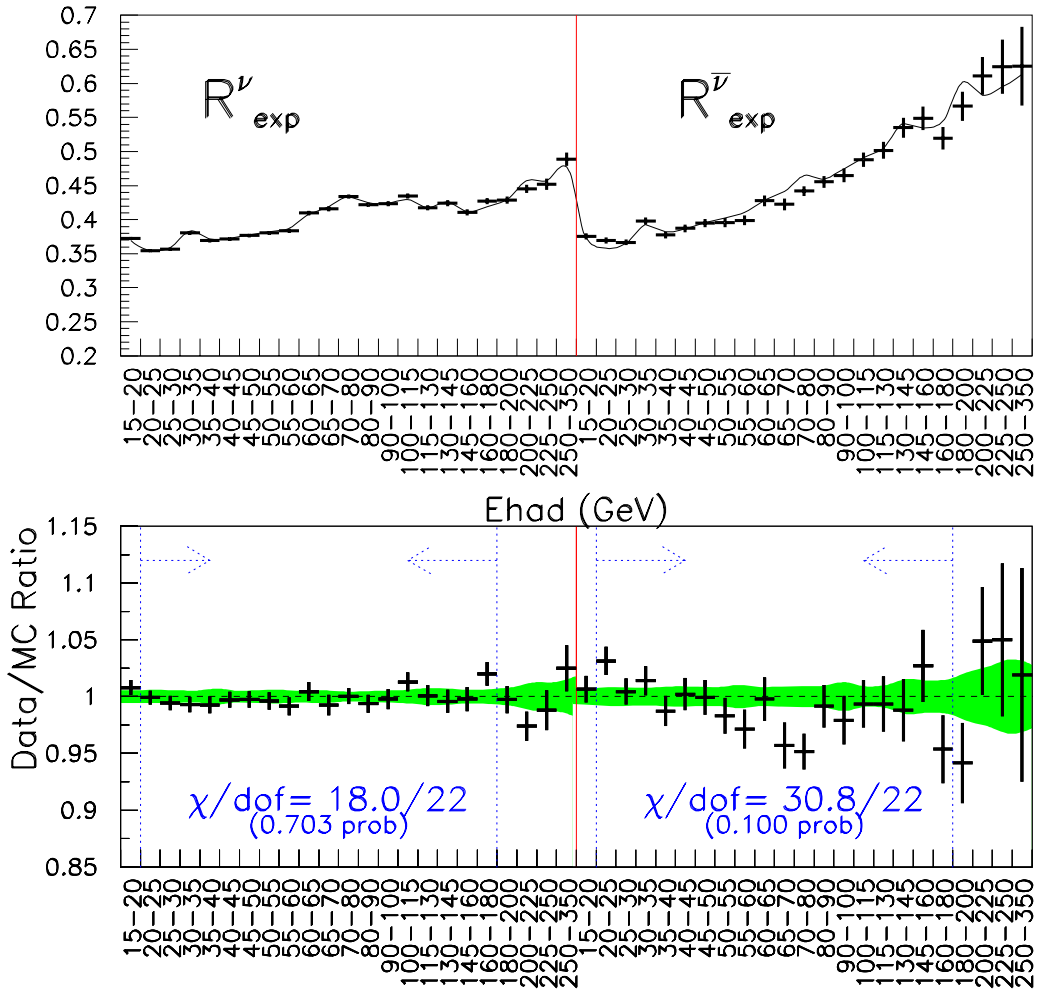

Figure 6.15: $R_{\rm exp}$ distributions in data and Monte Carlo as a function of $\rm E_{had}$. The band on the bottom data/MC ratio plot indicates the $\pm$ 1 σ systematic uncertainty. The arrows indicate the range of data included in the final analysis, namely 20 $\leq$ $\rm E_{had}$ $\leq$ 180 GeV.

Chapter 7

Uncertainties

This chapter discusses the determination of the statistical and systematic uncertainties relevant to the present analysis. The numerical values pertain to the default, single parameter 1C fit to $\sin^2\theta_W$. Evaluation of the uncertainties for the alternative 0C $\sin^2\theta_W$, $\sin^2\theta_W - \rho_0$, and $g_L^{\mathrm{eff}\,2} - g_R^{\mathrm{eff}\,2}$ fits reside in Chapter 8.

7.1 Statistical Uncertainties

7.1.1 Data Statistics

The largest single source of uncertainty in this measurement is statistical. The total numbers of short and long events observed in the final data sample,

$$R^{\nu} = \frac{456,838}{1,166,640} = 0.3916 \pm 0.0007 \tag{7.1}$$

$$R^{\overline{\nu}} = \frac{101,222}{249,911} = 0.4050 \pm 0.0016 \tag{7.2}$$

imply a statistical uncertainty on $\sin^2\theta_W$ of 0.00135. This statistical uncertainty from the 1C fit, which also determines m_c does not include the effect of the statistical uncertainty on m_c; that is included as a systematic (Table 7.10).

7.1.2 Monte Carlo Statistics

To ensure a negligibly small Monte Carlo statistical uncertainty, a grand total of 32×10^6 neutrino and 21×10^6 antineutrino events comprise the final sample. After cuts, the Monte Carlo contains roughly 9 times the neutrino data statistics, and 22 times the antineutrino data statistics.

The total Monte Carlo neutrino event sample consists of a summation of sixteen dst samples, each generated with 2×10^6 events. Similarly, the final antineutrino event sample results from six 1.5×10^6 event dsts combined with twelve 1×10^6 event dsts. Because our Monte Carlo events are generated simultaneously as correlated NC and CC events, it is not appropriate to take statistical errors as an estimate of the uncertainty. The Monte Carlo statistical uncertainty is instead calculated by evaluating the spread in the $R_{\rm exp}$ values obtained for each of these subsamples. Figure 7.1 shows the distribution of $R_{\rm exp}$ values, which is a Gaussian distribution with an RMS spread of 0.00029 for the ν samples and 0.00045 for the $\overline{\nu}$ samples. Hence, the uncertainties in $R^{\nu}_{\rm exp}$ and $R^{\overline{\nu}}_{\rm exp}$:

$$\delta R^{\nu}_{MC} = 0.00029/\sqrt{16} = 0.00007 \tag{7.3}$$

$$\delta R^{\overline{\nu}}_{MC} = 0.00045/\sqrt{17} = 0.00011 \tag{7.4}$$

imply an error on $\sin^2\theta_W$ of 0.00011 resulting from the statistics of the final MC.

7.2 Experimental Uncertainties

The experimental uncertainties relate to the simulation of the NuTeV neutrino beam and detector. The largest source of experimental error in the measurement of $\sin^2\theta_W$ results from the determination of the electron neutrino background. Smaller uncer-

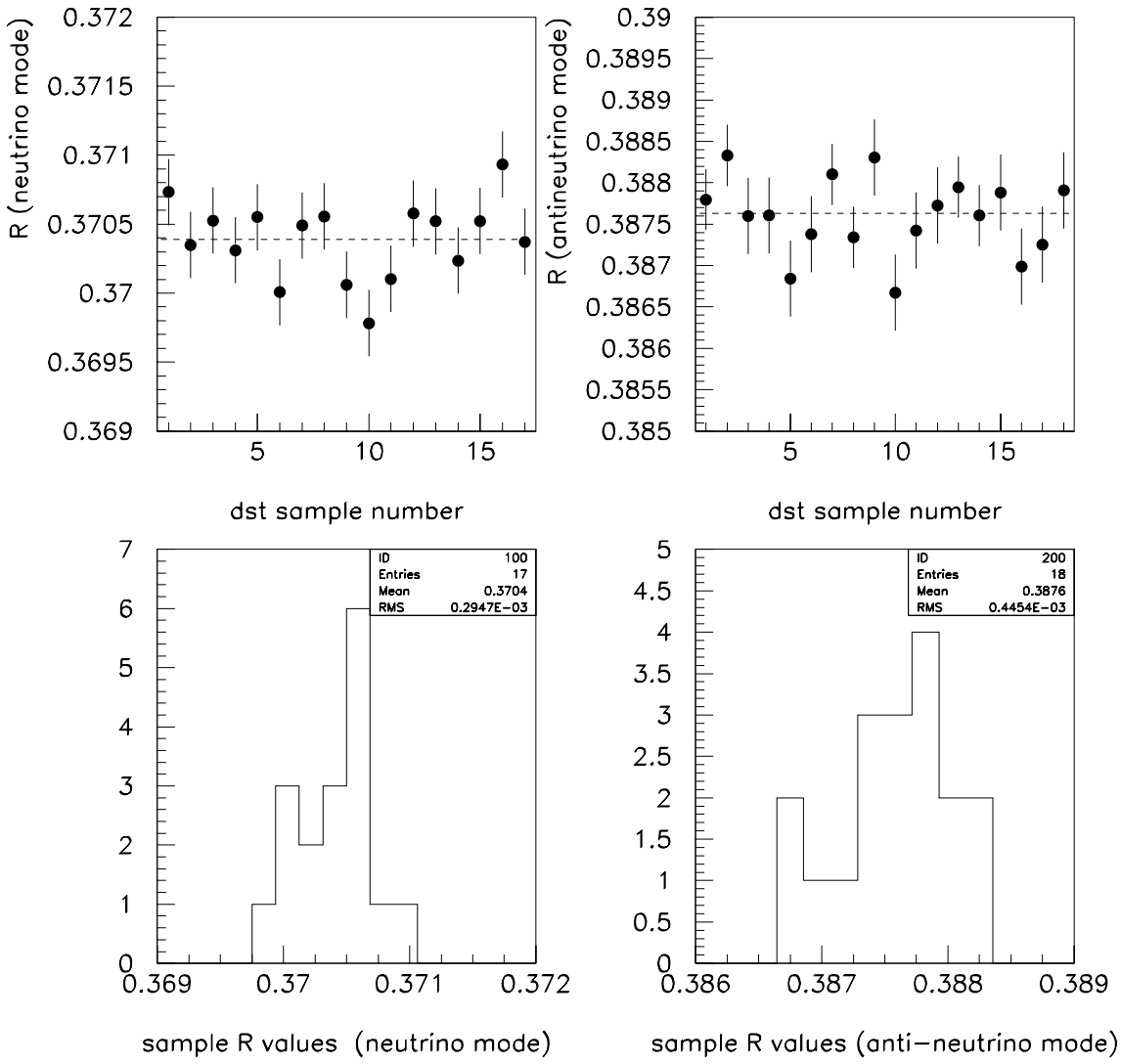

Figure 7.1: Spread in dst sample $R_{\rm exp}$ values used to determine the Monte Carlo statistical uncertainty. Plots on the left (right) are from the ν ($\overline{\nu}$) dsts.

tainties arise from the energy, ν_μ flux, length, and vertex determinations. Table 7.14 provides a breakdown of the individual error sources which are also discussed below. In each case, the systematic is evaluated by shifting the relevant parameters by $\pm 1\sigma$ in the Monte Carlo and measuring the difference before and after the shift.

7.2.1 Energy Measurement and the ν_μ Flux

The largest uncertainty in the ν_μ flux determination arises from the calibration of the hadron and muon energy scales. The absolute sizes of the uncertainties are determined either from testbeam and/or neutrino flux constraints.

Using NuTeV calibration data, the absolute hadron energy scale is determined to within $\pm 0.43\%$. The $\sin^2\theta_W$ analysis is affected by possible miscalibration in two ways. First, a variation in $\mathrm{E_{had}}$ changes the number of short and long events that pass the energy cut (remember the length cut depends on energy). This accounts for roughly 70% of the total error. Second, changes in the energy scale modify the neutrino flux. For example, a +1% hadron energy mismeasurement in the data changes the flux parameters by a few tenths of a percent (Table 7.1).

Flux Parameter	Neutrino Mode	Antineutrino Mode
δE_π	+0.31%	+0.23%
δE_K	+0.40%	+0.31%
$\delta K/\pi$	-0.11%	+0.11%

Table 7.1: Change in the flux parameters for a +1% $\mathrm{E_{had}}$ shift in the data.

Given a +0.43% hadron energy miscalibration along with the associated ν_μ flux changes, the shift in R^{ν}_{exp} ($R^{\overline{\nu}}_{\mathrm{exp}}$) is 0.00009 (0.00008), which produces an overall uncertainty in $\sin^2\theta_W$ of 0.00012. The quoted shifts apply only to the ν_μ flux deter-

mination, the resultant changes in the ν_e flux prediction are discussed in the next section.

Although the muon energy measured in the toroid is not directly used in this analysis, the effect of a miscalibration enters indirectly through the ν_μ flux tuning procedure. Calibration data determines the absolute E_μ scale to approximately 1%. Requiring the flux to be y–independent further constrains the relative $\mathrm{E_{had}}/E_\mu$ scale to $\pm$ 0.25% in neutrino mode, and $\pm$ 0.4% in antineutrino mode. The effect of the ν_μ flux change associated with this level of muon miscalibration (Table 7.2) produces shifts in R^{ν}_{exp} and $R^{\overline{\nu}}_{\mathrm{exp}}$ of 0.00006 and 0.00011, respectively, which are conservatively assumed to be uncorrelated. The resultant uncertainties in $\sin^2\theta_W$ for each mode (0.00009 for ν and 0.00005 for $\overline{\nu}$) yield a combined error of 0.00010.

Flux Parameter	Neutrino Mode	Antineutrino Mode
δE_π	+0.62%	+0.42%
δE_K	+0.56%	+0.54%
$\delta K/\pi$	+0.01%	+0.32%

Table 7.2: Change in the flux parameters for a +1% E_μ shift in the data.

Table 7.3 summarizes the energy uncertainties affecting the determination of the ν_μ and $\overline{\nu}_\mu$ fluxes. The errors from the hadron and muon energy scale uncertainties are comparable.

Hadron Energy Resolution

Energy resolution describes how observed energies are affected by random event–to–event fluctuations in showering behavior. These fluctuations can "smear" the measured energy distributions as described in Chapter 3. The hadron energy smearing correction is conservatively varied by $\pm$10% of itself, yielding small 0.00003

Energy Scale Systematic	$\delta R^{\nu}_{\rm exp}$	$\delta R^{\overline{\nu}}_{\rm exp}$	$\delta \sin^2\theta_W$
$E_{\rm had}$ ($\pm 0.43\%$)	0.00009	0.00008	0.00012
E_μ, ν ($\pm 0.25\%$)	0.00006	———	0.00009
E_μ, $\overline{\nu}$ ($\pm 0.40\%$)	———	0.00011	0.00005
Total :	0.00011	0.00014	0.00016

Table 7.3: Contributions to the ν_μ flux systematic resulting from uncertainties in the hadron and muon energy calibrations.

(0.00006) shifts in $R^{\nu}_{\rm exp}$ ($R^{\overline{\nu}}_{\rm exp}$), which imply a mere 0.00002 uncertainty in $\sin^2\theta_W$.

Muon Energy Deposition

A 1% uncertainty is assigned to the energy deposited by muons in CC events. The muon contribution to the shower is coherently shifted by ± 2 MeV/counter, resulting in a 0.00009 (0.00019) shift in $R^{\nu}_{\rm exp}$ ($R^{\overline{\nu}}_{\rm exp}$), which translates into a 0.00007 uncertainty in $\sin^2\theta_W$.

7.2.2 Electron Neutrino Background

$R_{\rm exp}$ is sensitive to uncertainties in the absolute flux of electron neutrinos because almost all of the ν_e–induced CC interactions qualify as short events, and therefore affect only the numerator of the ratio. Uncertainties in the $K^\pm \to \pi^0 e^\pm \nu_e$ ($K^\pm_{e3}$) branching ratio and energy calibrations dominate the error in the ν_e background prediction. Based on a constrained fit to $K^\pm$ branching ratios, the Particle Data Group (PDG) [12] estimates the fractional uncertainty in the $K^\pm_{e3}$ branching ratio to be:

$$\frac{\Gamma\left(K^\pm \to \pi^0 e^\pm \nu_e(\overline{\nu}_e)\right)}{\Gamma\left(K^\pm \to \pi^\pm \nu_\mu(\overline{\nu}_\mu)\right)} = 0.0759 \pm 0.0011 \qquad (7.5)$$

including a scale factor of 1.4 to account for the poor fit χ^2. The final 1.5% error assignment arises from this fractional uncertainty estimate from the PDG combined

with a 0.5% uncertainty from SSQT alignment tolerances. Propagation of the 1.5% error in the $K^{\pm}_{e3}$ branching ratio results in a 0.00034 uncertainty in $\sin^2\theta_W$.

The second largest ν_e error results from energy scale uncertainties. As described in Chapter 5, the ν_e flux prediction is inherently tied to the ν_μ flux determination; hence, energy scale uncertainties that affect the ν_μ flux prediction also affect the ν_e prediction. Propagating the 0.43% hadron energy scale uncertainty to the $\nu'_e s$ in combination with the associated changes to the flux prediction (Table 7.1) yields 0.00014, 0.00002, 0.00022 uncertainties in $R^{\nu}_{\rm exp}$, $R^{\overline{\nu}}_{\rm exp}$, and $\sin^2\theta_W$, respectively. The flux changes resulting from a 0.25% (0.40%) mismeasurement of the muon energy in ν ($\overline{\nu}$) mode (Table 7.2), propagate to give another net 0.00022 error in $\sin^2\theta_W$. In comparing with Table 7.3, note that the calibration errors primarily impact $\sin^2\theta_W$ through the resultant changes to the ν_e flux prediction (and to a much lesser degree through changes in the ν_μ flux).

Despite having large fractional uncertainties, other sources of ν_e's, such as K_L, charmed meson, and muon decays, contribute to a much lesser degree because they constitute much smaller contributions to the total ν_e flux. Although an estimated 20% uncertainty in K_L production dominated the CCFR ν_e systematics, this contribution is suppressed for NuTeV because of the low acceptance for neutral particle propagation in the SSQT. In addition, the K_L uncertainty is re–evaluated for NuTeV to reflect the new beam geometry. In the NuTeV beamline simulation, the K_L prediction from Malensek [68] is tuned to match data from E731 [69] (Chapter 5). The overall accuracy of the K_L production rate prediction considers three sources of error. First, a 6% normalization error accounts for the range in the number of protons on target recorded during the running of E731. Second, a 2.5% uncertainty covers

the extrapolation of the E731 results above 160 GeV. The E731 kaon momentum spectrum is very well constrained in the region 40–160 GeV (c.f. Figure 90 in Reference [69]). Given that 11% of NuTeV's events result from kaons above 160 GeV, and assuming a conservative 25% uncertainty in the K_L fraction above 160 GeV, yields the 2.5% estimate. Third, the E731 data had a fixed production angle of 5.5 mrad, whereas NuTeV has a mean production angle of roughly 7 mrad. Assuming the E731 5.5 mrad production angle changes the predicted number of ν_e's by $\sim 16\%$ (Figure 7.2).

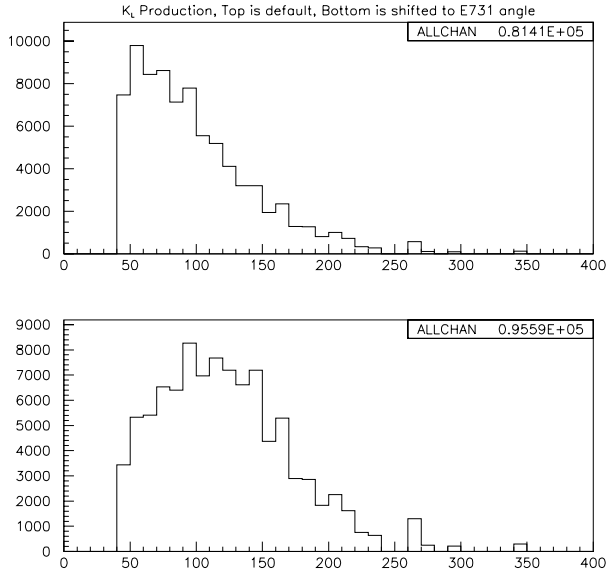

Figure 7.2: Change in K_L production after correcting to the 5.5 mrad E731 production angle (bottom). Top plot is the default K_L prediction ($< \theta > \simeq 7$ mrad).

If the angular dependence is known to 50%, an 8% uncertainty results from the angular extrapolation from E731 to NuTeV. Table 7.4 summarizes the three contributing K_L production uncertainties, which combined yield an overall 10% error assignment.

E731 normalization	6.0%
Extrapolation above 160 GeV	2.5%
Angular extrapolation	8.0%
Total :	10%

Table 7.4: Calculation of the total uncertainty in K_L production at NuTeV.

Muon decays receive a very conservative 10% uncertainty* Charm contributions receive a 15% fractional uncertainty based on $c\overline{c}$ cross section measurements from 800 GeV p–N data [70, 71] and the analysis of wrong–sign events in $\overline{\nu}$ mode at NuTeV [52] (Chapter 5). Table 7.5 summarizes the contributions to the total ν_e systematic error.

Energy Scale Systematic	$\delta R^{\nu}_{\rm exp}$	$\delta R^{\overline{\nu}}_{\rm exp}$	$\delta \sin^2\theta_W$
$K^{\pm}_{e3}$ ($\pm$1.2%)	0.00028	0.00027	0.00034
$E_{\rm had}$ ($\pm$0.43%)	0.00014	0.00002	0.00022
ν, E_{μ} ($\pm$0.25%)	0.00012	———	0.00019
$\overline{\nu}, E_{\mu}$ ($\pm$0.40%)	———	0.00006	0.00003
K_L ($\pm$10%)	0.00010	0.00051	0.00005
μ decay ($\pm$10%)	0.00003	0.00004	0.00003
Charm ($\pm$15%)	0.00011	0.00048	0.00001
Total :	0.00037	0.00075	0.00045

Table 7.5: Uncertainties in the determination of the ν_e and $\overline{\nu}_e$ backgrounds.

Constraints from the analysis of wrong–sign events [52] and direct measurements of the ν_e content of the beam [64] further reduces the ν_e uncertainties. The correlation matrix is built numerically by finding the change in χ^2 that results from 1σ variations in each of the ν_e systematics and combinations of systematics. Combining the two independent analyses with the apriori constraint from the beam Monte

* Reference [52] cites a 3% variation resulting from changes in the average muon polarization. The fit to $\overline{\nu}$ WS data constrains μ decay sources to better than 7% [52].

Carlo, and assuming no apriori correlations except for the very weak correlation (–0.085) between charm and K_L from the wrong–sign analysis, yields the following covariance matrix:

$$\begin{pmatrix} \delta K_{e3} & \delta \mathrm{E_{had}} & \delta E_\mu(\nu) & \delta E_\mu(\overline{\nu}) & \delta \mathrm{charm} & \delta K_L \\ +0.627 & -0.087 & +0.062 & -0.061 & -0.161 & -0.055 \\ -0.087 & +0.974 & -0.046 & -0.027 & +0.034 & +0.022 \\ -0.062 & -0.045 & +0.985 & +0.008 & +0.022 & +0.010 \\ -0.061 & -0.028 & +0.008 & +0.976 & +0.010 & +0.016 \\ -0.161 & +0.034 & +0.021 & -0.001 & +0.807 & -0.180 \\ -0.055 & +0.022 & +0.010 & +0.015 & -0.180 & +0.882 \end{pmatrix} \tag{7.6}$$

Simultaneous use of all of the ν_e information, in both neutrino and antineutrino running, reduces the total $\sin^2\theta_W$ uncertainty in Table 7.5 from 0.00045 to 0.00039.

Electron Response

The electron response systematic includes two contributions. First, a $\pm 2\%$ electron energy scale uncertainty applied to electrons in CC ν_e events accounts for uncertainties in the energy response of counters 83 and 84. Testbeam electrons deposit energy only in the most upstream counters; therefore the uncertainty in the calibration of these counters relative to the average gain of the remaining calorimeter counters adds to the overall electron energy calibration uncertainty. This leads to very small shifts in both R^{ν}_{exp} and $R^{\overline{\nu}}_{\mathrm{exp}}$, implying a negligible uncertainty in $\sin^2\theta_W$ of 4×10^{-6}. Second, a 1.1% hadron non-linearity uncertainty accounts for the relative response of the calorimeter to electromagnetic versus hadronic showers. This yields a compa-

rably small 2×10^{-6} uncertainty in $\sin^2\theta_W$. Both of these uncertainties are negligible because only a handful of ν_e events have hadron energies close to the 20 GeV cut.

7.2.3 Event Length

Uncertainties associated with the event length determination include errors associated with the hadron shower length model, the PLACE determination, and the calorimeter counter simulation. The later includes contributions resulting from modeling of the counter efficiencies, noise, and size. This subsection discusses each of the contributions to the length systematic.

Hadron Shower Length

The hadron shower length model receives an energy dependent uncertainty based on varying tuning parameters of the model within reasonable range suggested by data in the long NC region. These variations cause shifts in the high length tail of the distribution which are then parametrized as additive shifts to the predicted shower length. The contributions are tabulated in Table 7.6.

energy bin	length uncertainty	$\delta R^{\nu}_{\rm exp}$	$\delta R^{\overline{\nu}}_{\rm exp}$	$\delta\sin^2\theta_W$
$E_{had} \leq 20$ GeV	0.20 counter	0.00001	1×10^{-6}	0.00002
$20 < E_{had} \leq 60$ GeV	0.10 counter	0.00016	0.00018	0.00018
$E_{had} > 60$ GeV	0.05 counter	0.00015	0.00008	0.00020
	Total :	0.00021	0.00020	0.00027

Table 7.6: Contributions to the hadron shower length systematic in bins of E_{had}.

PLACE Determination

As presented in Chapter 5, dimuon events provide a measure of the accuracy of the PLACE algorithm; however, PLACE is sensitive to the presence or absence of

muons in an event (Figure 5.69). A systematic thereby arises from the additional muons present in the study sample. The effect of the two muons is measured using a high statistics sample of NC events. Figure 7.8 shows the difference between $(n)(n)$ and $(n+2)(n+2)$ PLACE for short neutrino events passing analysis cuts. The difference between $(n)(n)$ and $(n-2)(n-2)$ place provides a symmetry check. The mean difference estimates the 1σ effect of the two muons on the PLACE shift determination[†]. From this, we determine that the accuracy of the interaction point is measured to 0.08 counter for $E_{had} < 50$ GeV, 0.04 counter for $50 \leq E_{had} < 100$ GeV, and 0.02 counter for $E_{had} \geq 100$ GeV. Half of the difference is taken as a correction to our original measurement and the other half as a systematic. Table 7.7 summarizes the contributions to the final PLACE systematic.

energy bin	PLACE systematic	δR^{ν}_{exp}	$\delta R^{\overline{\nu}}_{exp}$	$\delta \sin^2\theta_W$
$E_{had} < 50$ GeV	0.04 counter	0.00018	0.00011	0.00024
$50 \leq E_{had} < 100$ GeV	0.02 counter	0.00011	0.00007	0.00015
$E_{had} \geq 100$ GeV	0.01 counter	0.00002	0.00003	0.00003
	Total :	0.00021	0.00013	0.00028

Table 7.7: Contributions to the PLACE systematic in bins of E_{had}. Shown are the resultant uncertainties in R^{ν}_{exp}, $R^{\overline{\nu}}_{exp}$ and $\sin^2\theta_W$.

[†] Raising the threshold in the PLACE algorithm by two mips is equivalent to the addition of two muons which deposit, on average, two mips per counter.

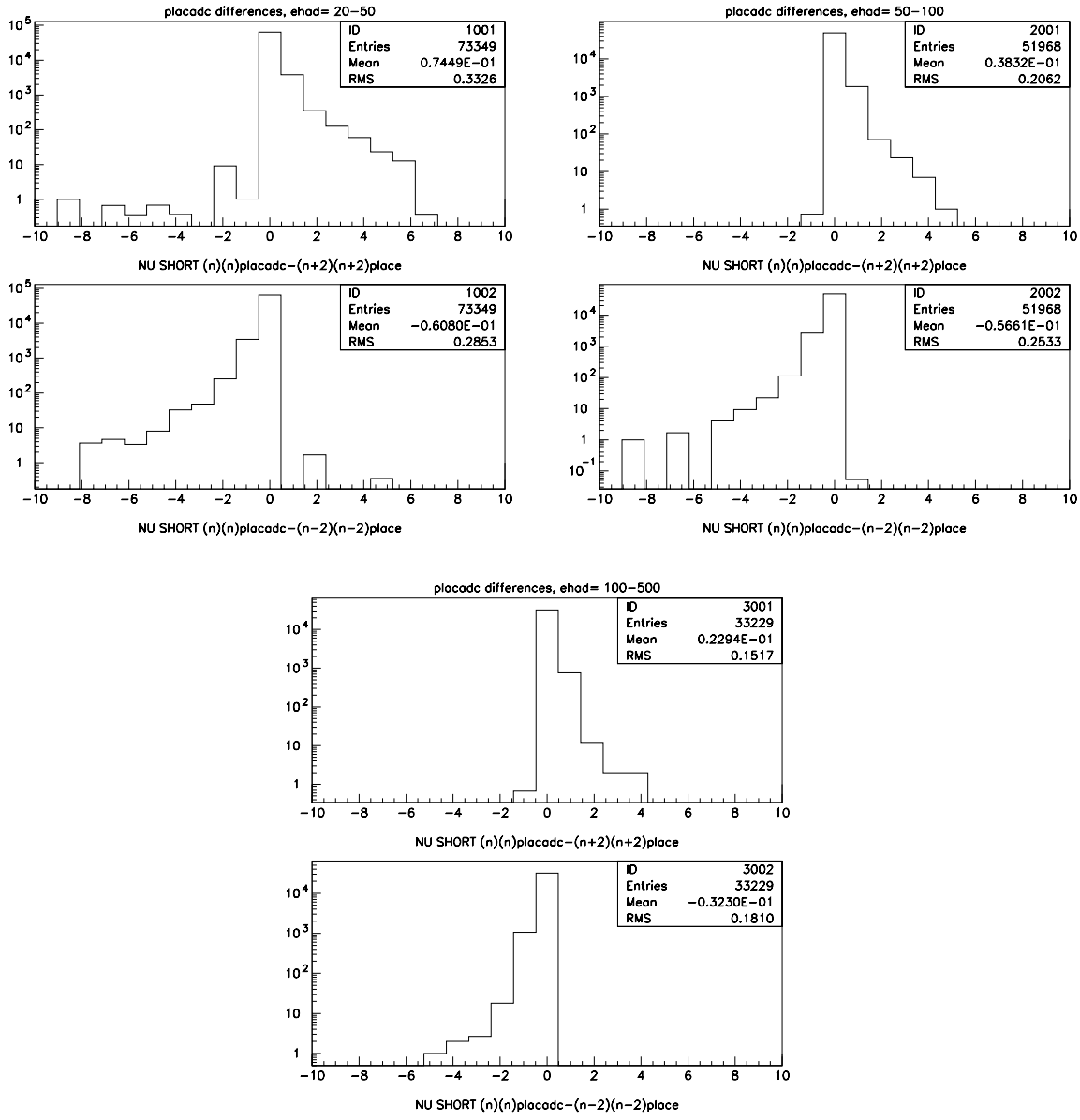

Table 7.8: The effect of the presence of two muons on the PLACE algorithm measured for a sample of short ν events in three energy bins: E_{had}=20–50 GeV, 50–100 GeV, and 100–500 GeV. Plotted on the top in each case is the difference between $(n)(n)$ and $(n+2)(n+2)$ PLACE; on the bottom is the difference between $(n)(n)$ and $(n-2)(n-2)$ PLACE. Horizontal axis is in units of counters.

Counter Noise and Efficiency

We estimate that we have measured counter inefficiencies leading to gaps of three or more counters and counter noise probabilities to better than 3%. The choice of length ($L_{\rm cut} = 16, 17, 18$) and PLACE ($P_{\rm cut}$=17,18,21) cuts force a reliance on the noise and efficiency in the most downstream counter to distinguish between short and long events in the lowest two energy bins. As a result, the noise and efficiency uncertainties are not negligible. Both uncertainties are conservatively assumed to be uncorrelated between neutrino and antineutrino mode running. The 3% counter noise uncertainty leads to 0.00013, 0.00005, 0.00022 uncertainties in $R^{\nu}_{\rm exp}$, $R^{\overline{\nu}}_{\rm exp}$, and $\sin^2\theta_W$, respectively. The 3% counter efficiency systematic implies 0.00003, 0.00003, 0.00005 uncertainties in $R^{\nu}_{\rm exp}$, $R^{\overline{\nu}}_{\rm exp}$, and $\sin^2\theta_W$, respectively.

Counter Width

The $\sin^2\theta_W$ result is sensitive to the active area of the scintillation counters. As described in Chapter 5, the effective counter widths are measured to an accuracy of 0.08 inch using muons to illuminate the counter edges. The uncertainty comes from the the spread in the individual counter width measurements combined with the difference between the measurements obtained from neutrino data and from testbeam. This covers any uncertainty in the assumption that all counters have the exact same width, as well as any unaccounted systematic effects from the fitting procedure [65]. Changing the counter half widths by 0.08 inch in the Monte Carlo results in a 0.00003 (0.00001) shift in $R^{\nu}_{\rm exp}$ ($R^{\overline{\nu}}_{\rm exp}$), and a resultant 0.00004 uncertainty in $\sin^2\theta_W$.

7.2.4 Transverse Vertex Determination

The transverse vertex determination has three sources of error related to the pull of the hadron shower, the muon, and the detector edge. The hadron shower and muon pulls are varied independently according to the multiplicative form:

$$\text{shower pull} = \text{shower pull} \cdot [1 + \text{a} + \text{b} \cdot (\ln(\text{E}_{\text{hadg}}) - 3.4)] \quad (7.7)$$

$$\text{muon pull} = \text{muon pull} \cdot [1 + \text{a} + \text{b} \cdot (\ln(\text{E}_{\text{hadg}}) - 3.6)] \quad (7.8)$$

The offset (a) and slope (b) are uncorrelated for independent variations in the muon and hadron shower pulling, so their effects are added in quadrature; however, because the muon and hadron shower pulling are highly correlated their individual uncertainties are summed. Table 7.9 tabulates the contributions for 1σ limits on the contributing shifts.

	VPULL systematic	$\delta R^{\nu}_{\text{exp}}$	$\delta R^{\overline{\nu}}_{\text{exp}}$	$\delta \sin^2 \theta_W$
muon pulling	a = 0.02	0.00002	0.00002	0.00003
muon pulling	b = 0.03	0.00001	0.00001	0.00001
		0.00002	0.00002	0.00003
shower pulling	a = 0.005	5×10^{-6}	0.00009	0.00003
shower pulling	b = 0.007	6×10^{-6}	3×10^{-6}	8×10^{-6}
		8×10^{-6}	0.00009	0.00003
	Total :	0.00003	0.00011	0.00006

Table 7.9: Contributions to the transverse vertex pulling systematic. Shown are the resultant uncertainties in R^{ν}_{exp}, $R^{\overline{\nu}}_{\text{exp}}$ and $\sin^2 \theta_W$.

The uncertainty of the detector edge correction receives a very conservative estimate: a correlated 1σ shift to each one inch bin across the detector. The effect,

parametrized as a function of position in the detector, shifts the shower–pulled vertices in each view by:

$$\begin{aligned} \mathrm{Vx} &= \mathrm{Vx} + \frac{\mathrm{Vx}}{|\mathrm{Vx}|}(0.015 + 6 \times 10^{-6} \cdot \mathrm{Vx}^2) \\ \mathrm{Vy} &= \mathrm{Vy} + \frac{\mathrm{Vy}}{|\mathrm{Vy}|}(0.015 + 6 \times 10^{-6} \cdot \mathrm{Vy}^2) \end{aligned} \tag{7.9}$$

The result of the systematic, which on average moves the vertex $\sim 0.015 - 0.03$ inches further towards the edge of the detector, is a change of 0.00006 and 0.00005 in R^{ν}_{exp} and $R^{\overline{\nu}}_{\mathrm{exp}}$, which translates into a 0.00007 uncertainty in $\sin^2\theta_W$.

7.3 Physics Model Uncertainties

Theoretical errors are induced by uncertainties in the Monte Carlo parameterization. Charm production remains the largest model uncertainty in the present measurement of $\sin^2\theta_W$. Smaller sources of error arise from uncertainties in R_L, $\sigma_{\overline{\nu}}/\sigma_{\nu}$, higher twist, radiative corrections, the charm sea, and the non–isoscalar target. In each case, the systematic is evaluated by shifting the relevant parameters in the Monte Carlo by $\pm 1\sigma$ and measuring the difference in the results after the shift. In some cases, the PDFs are re–extracted to ensure consistent treatment within the Monte Carlo cross section model.

7.3.1 Charm Production and Strange Sea

Because the production of a charm quark from an s or d quark only occurs via a charged–current process, it is not susceptible to cancellation in the ratio R^{ν}=NC/CC. As a result, uncertainties in the production model contributed the single largest source of error in the previous CCFR $\sin^2\theta_W$ analysis [17]. Unlike CCFR, NuTeV's

use of separate, high statistics ν and $\overline{\nu}$ samples greatly reduces sensitivity to uncertainties in cross sections resulting from scattering off $q - \overline{q}$ symmetric seas. Specifically, the νs and $\overline{\nu s}$ contributions cancel, leaving only a residual charm producing component from d_v scattering. This remaining component is not only Cabbibo suppressed[‡] but also less affected by m_c threshold effects because d_v quarks typically carry a large fraction of the nucleon's momentum. NuTeV enjoys a factor **six** reduction in the $\sin^2\theta_W$ uncertainty due to charm production relative to CCFR.

Determination of the total charm production uncertainty requires evaluation of several contributions. The systematics include $\pm 1\sigma$ variations in the effective charm mass (m_c), the strange sea level (κ), the strange sea shape (α), and the CKM matrix element (V_{cd}). For each parameter variation, the PDFs are re–extracted so as to constrain the generated charged–current cross section to data. The resultant shifts in $R^{\nu}_{\rm exp}$, $R^{\overline{\nu}}_{\rm exp}$, and $\sin^2\theta_W$ are listed below in Table 7.10.

	$\delta R^{\nu}_{\rm exp}$	$\delta R^{\overline{\nu}}_{\rm exp}$	$\delta \sin^2\theta_W$
1C fit $m_c = 1.34 \pm 0.09$ GeV	0.00086	0.00186	0.00045
$\alpha = 2.50 \pm 0.65$	0.00017	0.00041	0.00011
$\kappa = 0.373 \pm 0.049$	0.00010	0.00017	0.00009
$V_{cd} = 0.2205 \pm 0.012$	0.00008	0.00008	0.00010
	0.00089	0.00191	0.00048

Table 7.10: Uncertainties in $R^{\nu}_{\rm exp}$, $R^{\overline{\nu}}_{\rm exp}$, and $\sin^2\theta_W$ for 1σ variations in the charm production model and strange sea parameters [48, 42].

The correlations between the strange sea parameters, m_c, κ, and α, are measured from CCFR/NuTeV dimuon data [72] (Table 7.11). The $\alpha - \kappa$ correlation reduces the combined $\sin^2\theta_W$ uncertainty from 0.00048 (obtained by naıvely adding the

[‡] Scattering off d quarks is suppressed by the factor $|V_{cd}|^2 \sim 0.05$ whereas scattering off s quarks is favored by the factor $|V_{cs}|^2 \sim 0.95$.

uncertainties in quadrature) to 0.00047.

	m_c	κ	α
m_c	1.0	0.445	0.036
κ	0.445	1.0	-0.465
α	0.036	-0.465	1.0

Table 7.11: Correlation coefficients obtained in the joint CCFR/NuTeV dimuon fit with $s(x) = \overline{s}(x)$ [72].

7.3.2 Longitudinal Structure Function, R_L

The second largest theoretical uncertainty arises from imprecise knowledge of the longitudinal structure function, R_L. Rather than follow the CCFR [17] convention of assigning a $\pm 15\%$ systematic, R_L is shifted by a constant offset so as not to underestimate the effect in regions where R_L is zero. At low x and Q^2, where there are large differences between the model predictions for R_L, the data indicate a ± 0.03 uncertainty (Figure 5.18). A smaller shift is applied in the high x and moderate Q^2 region, which is well constrained by SLAC and NMC data. Here, the difference between the NLO and NNLO predictions, which appears to be less than 0.01 in this region, provides the magnitude of the systematic (Figure 7.3).

$$\begin{aligned} R_L &\pm 0.01, \quad x > 0.15,\ Q^2 > \frac{x}{0.15} \\ R_L &\pm 0.03, \quad \text{otherwise} \end{aligned} \tag{7.10}$$

Applying the above offsets to R_L and re-fitting the CCFR differential cross section data results in large shifts in the predicted short/long ratios: 0.00045 in $R^{\nu}_{\rm exp}$ and 0.00101 in $R^{\overline{\nu}}_{\rm exp}$. Because of the inherent $\nu - \overline{\nu}$ cancellation, the resulting uncertainty in $\sin^2\theta_W$ is reduced to 0.00032.

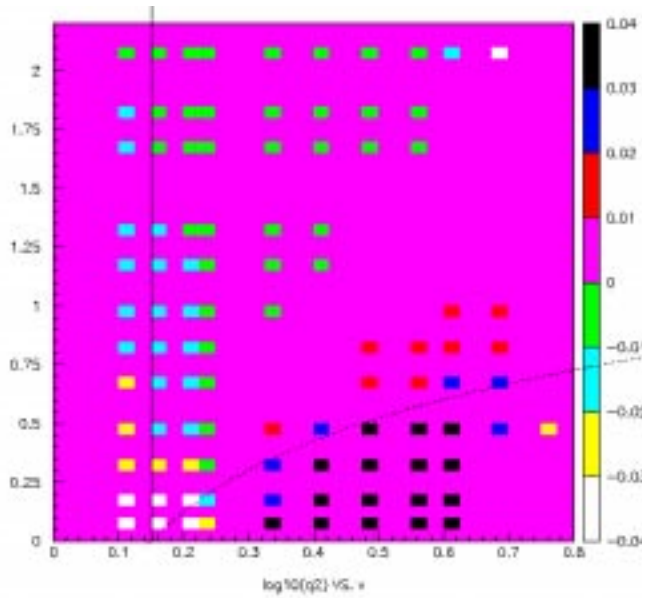

Figure 7.3: Difference between the NLO and NNLO predictions for R_L plotted as a function of x and $\log_{10}(Q^2)$. The lines indicate the boundaries where $x = 0.15$ and $Q^2 = x/0.15$. Data is courtesy of U.K. Yang [63].

7.3.3 Relative ν, $\overline{\nu}$ Cross Sections

Because we are relying on a combination of neutrino and antineutrino data to extract $\sin^2\theta_W$, the measurement is sensitive to differences in the ratio of antineutrino–nucleon and neutrino–nucleon total cross sections. The world average from neutrino measurements, $\sigma^{\overline{\nu}}/\sigma^{\nu} = 0.499 \pm 0.007$ [36], provides an estimate of the uncertainty. Varying $\sigma^{\overline{\nu}}/\sigma^{\nu}$ by $\pm 1.4\%$ results in a 0.00022 uncertainty in $\sin^2\theta_W$.

7.3.4 Higher Twist

Higher twist contributions are constrained by fits to SLAC and BCDMS F_2 data on hydrogen and deuterium targets (Chapter 5). The model is assigned a 100% uncertainty. The systematic is estimated by turning off the higher twist correction in the Monte Carlo, resulting in a 0.00014 shift in $\sin^2\theta_W$.

7.3.5 Radiative Corrections

The uncertainties in the Bardin/ZFITTER electroweak radiative corrections [30, 31] result from the variation of all[§] possible parameters and settings in the radiative correction code. The variations which produce non-negligible ($\geq 10^{-6}$) shifts appear in Table 7.12. These include changes in the handling of M_{top}^4 corrections and in choices of the hadronic vacuum polarization. Varying the final state quark masses from the constituent to current scale ($\sim$10 MeV–1 GeV) produces large changes in the NC and CC cross sections individually, which cancel in the ratio. Finally, recall that the radiative corrections are a combination of QED corrections calculated by Bardin [30] and weak corrections computed from ZFITTER [31] (Chapter 5). Our approximation that the corrections to the effective NC couplings can be factored from the remainder of the electroweak corrections, however, is not exact. We approximate the systematic uncertainty in this procedure by the numerical difference between the two procedures. This error is the largest of the radiative correction uncertainties.

	$\delta R^{\nu}_{\rm exp}$	$\delta R^{\overline{\nu}}_{\rm exp}$	$\delta \sin^2\theta_W$
M_{top}^4 terms (IAMT4)	0.00002	7×10^{-6}	0.00003
QED vacuum polarization (IHVP)	8×10^{-6}	2×10^{-6}	0.00001
final state quark masses (QPMFI)	0.00007	0.00016	0.00001
Weak–QED separation	0.00005	0.00006	0.00010
Total :	0.00009	0.00017	0.00011

Table 7.12: Uncertainties resulting from the Bardin/ZFITTER electroweak radiative corrections. Where applicable, the variables in parentheses indicate the parameters that are varied in the radiative correction code.

[§] Believe me, this was no picnic.

Charm Sea

The $c\,\overline{c}$ production model in the Monte Carlo is tuned to match EMC measurement of $F_2^{c\overline{c}}$ on iron [49] (Chapter 5). The charm sea model is assigned a 100% uncertainty. In addition, a 50% uncertainty is attributed to the level of the charm sea, effectively attributing a 100% uncertainty to the tuning procedure itself. The resultant $\sin^2\theta_W$ uncertainty is tabulated in Table 7.13. Fortunately, the present analysis is not particularly sensitive to large fractional uncertainties in the charm sea.

	$\delta R^{\nu}_{\rm exp}$	$\delta R^{\overline{\nu}}_{\rm exp}$	$\delta\sin^2\theta_W$
charm sea model (100%)	0.00005	0.00004	0.00010
charm sea level (50%)	0.00002	0.00001	0.00003
Total :	0.00005	0.00004	0.00010

Table 7.13: Uncertainties in the LO Monte Carlo charm sea model.

7.3.6 Non–Isoscalar Target

Corrections to d_v/u_v and $\overline{d}/\overline{u}$ are obtained from fits to NMC and E866 data (Chapter 5). To estimate uncertainties associated with this evaluation, a 1σ scale factor of 1.4 is applied to both the valence and sea functions, $d/u-1$. The resultant shifts in $R^{\nu}_{\rm exp}$ and $R^{\overline{\nu}}_{\rm exp}$ are both 0.00004, implying a 0.00005 uncertainty in $\sin^2\theta_W$.

7.3.7 Quasi–Elastic Cross Section

Quasi–elastic ν_e–N reactions produce electromagnetic showers that can satisfy the minimum $\rm E_{had}$ criteria for the analysis. The ν_e quasi–elastic cross section model is tuned to match Serpukhov data [53] and assigned a 15% uncertainty (Figure 5.30). Varying the quasi–elastic prediction by this amount results in 0.00005 and 0.00013

shifts in $R^{\nu}_{\rm exp}$ and $R^{\overline{\nu}}_{\rm exp}$, implying a small 0.00002 uncertainty in $\sin^2\theta_W$.

7.4 Table of Uncertainties

Table 7.14 summarizes the contributions to the total $\sin^2\theta_W$ error. The values listed here pertain to the single–parameter 1C $\sin^2\theta_W$ fit, as described in the next Chapter. The uncertainties are generally combined in quadrature except in the few cases outlined in the text.

7.5 Comparison with CCFR

As a proof of principle, Figure 7.4 compares the final NuTeV $\sin^2\theta_W$ errors relative to those obtained in CCFR [17]. The largest systematic plaguing the CCFR analysis, the uncertainty in the charm production model, is reduced by a factor of six for NuTeV because of the use of separate neutrino and antineutrino inputs. In addition, the ν_e flux systematic decreased by a factor of four because of the reduced K_L acceptance in the NuTeV beamline. Many of the experimental uncertainties are minimized as a result of rigorous constraints from extensive NuTeV calibration data. NuTeV also enjoys a cancellation in many of the theoretical uncertainties that are common to both neutrino and antineutrino interactions.

SOURCE OF UNCERTAINTY	$\delta R^{\nu}_{\rm exp}$	$\delta R^{\overline{\nu}}_{\rm exp}$	$\delta \sin^2\theta_W$
Data Statistics	0.00069	0.00159	0.00135
Monte Carlo Statistics	0.00007	0.00011	0.00010
TOTAL STATISTICS	**0.00069**	**0.00159**	**0.00135**
ν_e, $\overline{\nu}_e$ Flux:	0.00025	0.00044	0.00039
ENERGY: Hadron Calibration ($\pm$0.43%, ν_μ)	0.00009	0.00008	0.00012
Muon Calibration ($\pm$0.25% ν_μ, $\pm$0.4% $\overline{\nu}_\mu$)	0.00006	0.00011	0.00010
Energy Resolution (10%)	0.00003	0.00006	0.00002
Muon Energy Deposition (2 MeV/cntr)	0.00009	0.00019	0.00007
e/h ($\pm$1.1%), E_e ($\pm$2%)	2×10^{-6}	2×10^{-6}	4×10^{-6}
EVENT LENGTH: Shower Length Model	0.00021	0.00020	0.00027
PLACE Determination	0.00021	0.00013	0.00028
Counter Noise (3%)	0.00013	0.00005	0.00022
Counter Efficiency (3%)	0.00003	0.00003	0.00005
Counter Half Width ($\pm$0.08 inch)	0.00003	0.00001	0.00004
TRANSVERSE VERTEX: μ, Shwr Pulling	0.00003	0.00011	0.00006
Edge Correction	0.00006	0.00005	0.00007
TOTAL EXPERIMENTAL	**0.00044**	**0.00057**	**0.00063**
Charm Production, Strange Sea	0.00089	0.00184	0.00047
R_L ($\pm$0.03, $\pm$0.01)	0.00045	0.00101	0.00032
$\sigma^{\overline{\nu}}/\sigma^{\nu}$ ($\pm$1.4%)	0.00007	0.00026	0.00022
Higher Twist (100%)	0.00012	0.00013	0.00014
Radiative Corrections	0.00009	0.00017	0.00011
Charm Sea (100%)	0.00005	0.00004	0.00010
Non-Isoscalar Target (1σ)	0.00004	0.00004	0.00005
ν_e Quasi–Elastics ($\pm$15%)	0.00005	0.00013	0.00002
TOTAL PHYSICS MODEL	**0.00101**	**0.00212**	**0.00065**
TOTAL UNCERTAINTY	**0.00130**	**0.00272**	**0.00162**

Table 7.14: Uncertainties for the single parameter $\sin^2\theta_W$ 1C fit.

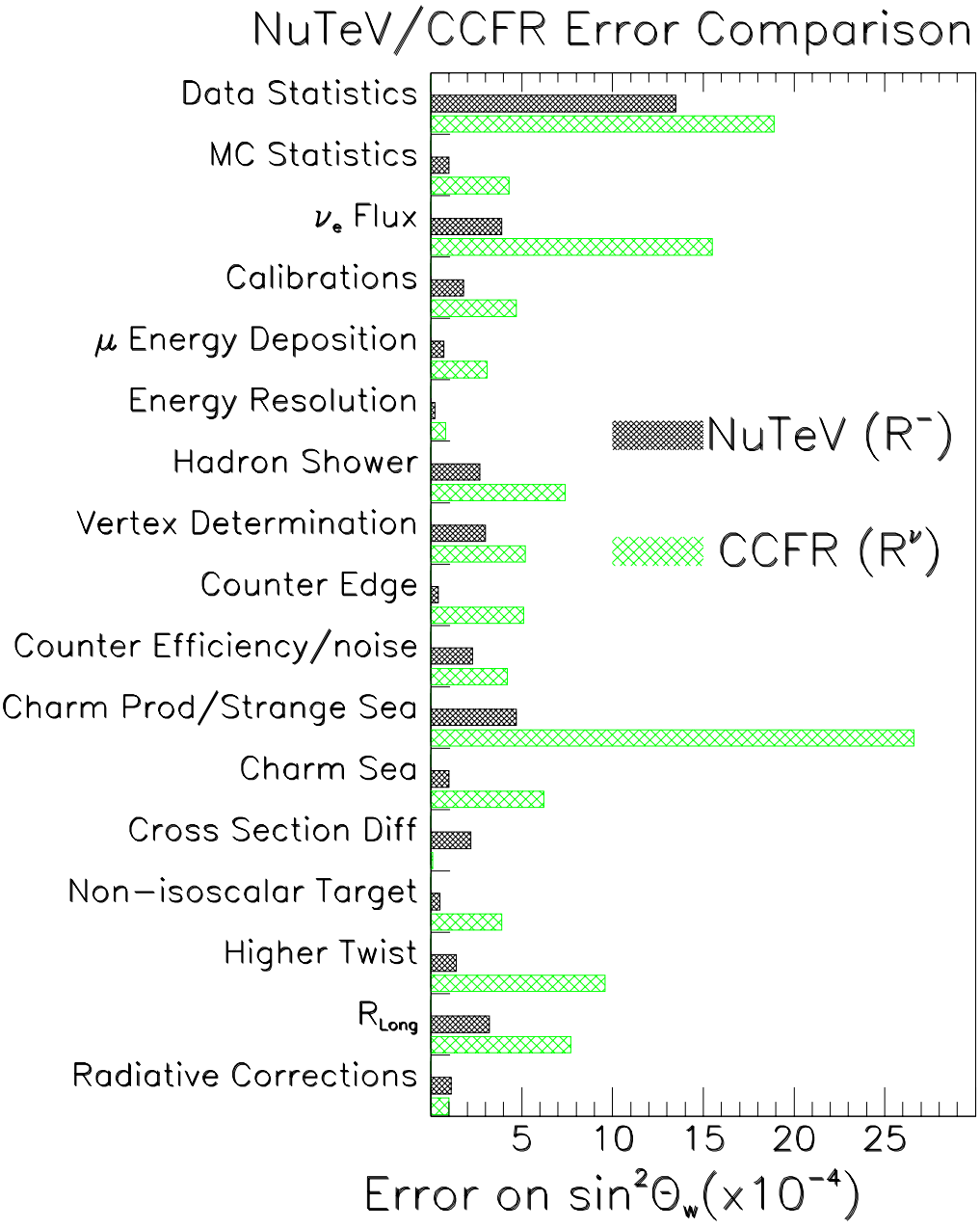

Figure 7.4: Itemized comparison between the NuTeV and CCFR $\sin^2\theta_W$ errors.

Chapter 8

Electroweak Fits

> *"Only a few important particles remain to be discovered and many of their properties are alleged to be known in advance. Surely this is not the way things will be, for Nature must still have some surprises in store for us."*
>
> — S.L. Glashow (1980)

This section describes the procedure for extracting electroweak parameters from the precise measurements of $R^{\nu}_{\rm exp}$ and $R^{\overline{\nu}}_{\rm exp}$. Single parameter fits for $\sin^2\theta_W$ and ρ_0 appear in the beginning of the section. To explore the disagreement with the standard model, we also perform two parameter fits for $(\sin^2\theta_W - \rho_0)$ and $(g_L^{\rm eff})^2 - (g_R^{\rm eff})^2$. The chapter concludes with a comparison of the results to measurements from other experiments around the world.

8.1 The 1C $\sin^2\theta_W$ Fit

The default electroweak fit is a single parameter fit for $\sin^2\theta_W$, chosen apriori before NuTeV took data because it can take full advantage of the cancellation afforded in the Paschos–Wolfenstein technique. This section describes the results of the fit of the precisely determined ratios, $R^{\nu}_{\rm exp}$ and $R^{\overline{\nu}}_{\rm exp}$, to their predictions as a function of electroweak parameters.

Recall that NuTeV does not measure ratios of NC to CC cross total sections, R^{ν} and $R^{\overline{\nu}}$, but instead measures experimental ratios of short to long events, $R^{\nu}_{\rm exp}$ and $R^{\overline{\nu}}_{\rm exp}$. The detailed Monte Carlo simulation of the experiment predicts these ratios for both neutrinos and antineutrinos as well as their dependence on electroweak parameters. The fit relies on a first order Taylor expansion of the $R_{\rm exp}$ prediction about its expected central value:

$$R_{\rm exp}^{\rm MC} \approx R_{\rm exp}^{\rm data} + \frac{\partial R_{\rm exp}}{\partial \sin^2\theta_W}\Delta\sin^2\theta_W + \frac{\partial R_{\rm exp}}{\partial {\rm m}_c}\Delta {\rm m}_c \tag{8.1}$$

In this (1C) case, m_c, the phenomenological parameter determining the threshold for heavy charm production, is explicitly included as a fit parameter. Because $R^{\overline{\nu}}_{\rm exp}$ has a very weak dependence on $\sin^2\theta_W$ (Table 8.1), the antineutrino data effectively "measures" m_c. The result is improved sensitivity to $\sin^2\theta_W$. The single parameter fit relies on the minimization of:

$$\chi^2 = \left[\sum_{\nu,\overline{\nu}} \frac{(R_{\rm exp}^{\rm MC} - R_{\rm exp}^{\rm data})^2}{\sigma(R_{\rm exp}^{\rm data})^2}\right] + \frac{({\rm m}_c - {\rm m}_c^{\rm data})^2}{\sigma({\rm m}_c^{\rm data})^2} \tag{8.2}$$

with respect to shifts in $\sin^2\theta_W$ and m_c from their central values. Because the effect of m_c is so significant, two further corrections are made. First, to account for terms quadratic in m_c:

$$R_{\rm exp}^{\rm MC} \longrightarrow R_{\rm exp}^{\rm MC} + \frac{\partial^2 R_{\rm exp}}{\partial {\rm m_c}^2}\Delta {\rm m_c}^2 \tag{8.3}$$

multiplicative factors obtained from quadratic fits to $R_{\rm exp}$ as a function of m_c are applied to the predicted ratios (Figure 8.1). The quadratic corrections are $0.945 + 0.055\left(\frac{\mathrm{m}_c - 1.4}{0.4}\right)$ for $R^{\nu}_{\rm exp}$ and $0.966 + 0.029\left(\frac{\mathrm{m}_c - 1.4}{0.4}\right)$ for $R^{\overline{\nu}}_{\rm exp}$. Second, the non–negligible m_c–κ correlation (Table: 7.11) is treated as a constant factor (0.975

for $R^{\nu}_{\rm exp}$ and 0.991 for $R^{\overline{\nu}}_{\rm exp}$) multiplying the m_c dependence of $R_{\rm exp}$.

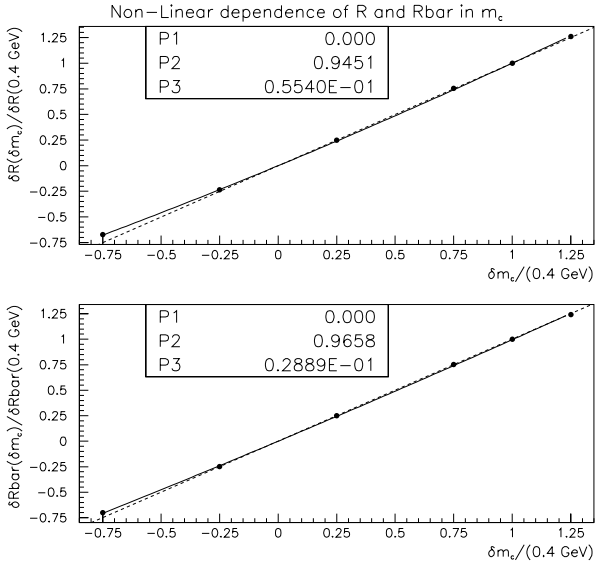

Figure 8.1: The non–linear dependence of $R^{\nu}_{\rm exp}$ (top) and $R^{\overline{\nu}}_{\rm exp}$ (bottom) on m_c.

MINUIT performs the fit to the data. Table 8.1 summarizes the inputs to the fit. The partial derivatives are determined numerically by shifting the relevant parameters, in this case $\sin^2\theta_W$ and m_c, in the Monte Carlo and evaluating the changes in the predictions for $R^{\nu,\overline{\nu}}_{\rm exp}$. In addition to the data measurements of $R^{\nu}_{\rm exp}$ and $R^{\overline{\nu}}_{\rm exp}$, the charm mass required to reproduce the experimental data on neutrino–induced dimuon production serves as an additional constraint, $m_c = 1.38 \pm 0.14$ GeV [42]. The simultaneous fit to $\sin^2\theta_W$ and m_c yields:

$$\sin^2\theta_W = 0.22773 \pm 0.00135\,(\text{stat}) \pm 0.00091\,(\text{syst}) \tag{8.4}$$

$$m_c = 1.34 \pm 0.09\,(\text{stat}) \pm 0.06\,(\text{syst})\ \text{GeV} \tag{8.5}$$

$$(\text{uncertainty correlation},\ \rho = 0.638) \tag{8.6}$$

The χ^2 for the fit is 0.334/1 equating to a probability of 56.3%. Figure 8.2 shows the variation in the $\sin^2\theta_W$ fit result as a function of input m_c. We also quote the

dependence of the result on $M_{\rm top}$ and $M_{\rm Higgs}$. Leading terms in the one–loop electroweak radiative corrections to the W and Z self–energies produce a weak residual dependence that is quadratic in $M_{\rm top}$ and logarithmic in $M_{\rm Higgs}$:

$$\begin{aligned} \sin^2\theta_W &= 0.22773 \pm 0.00163 \qquad (8.7) \\ &- 0.00022 \cdot \left(\frac{{M_{\rm top}}^2 - (175\ {\rm GeV})^2}{(50\ {\rm GeV})^2} \right) \\ &+ 0.00032 \cdot \ln\left(\frac{M_{\rm Higgs}}{150\ {\rm GeV}} \right) \qquad (8.8) \end{aligned}$$

The prediction from the standard model, with parameters determined by a fit to all other electroweak measurements, is 0.2227 ± 0.0004 [73, 74]. The NuTeV measurement lies approximately 3σ above the standard model expectation.

	Neutrino Mode	Antineutrino Mode
Data Measurement	0.39158 ± 0.00069	0.40503 ± 0.00159
Reference MC	0.39251	0.40673
$\partial R_{\rm exp}/\partial \sin^2\theta_W$	–0.630	-0.040
$\partial R_{\rm exp}/\partial {\rm m}_c$	0.0066	0.0137
${\rm m}_c^{\rm data}$ (GeV)	1.38 ± 0.014	1.38 ± 0.014

Table 8.1: Inputs to the 1C $\sin^2\theta_W$ fit. The data are compared to a reference Monte Carlo which assumes $\sin^2\theta_W = 0.227$ and ${\rm m}_c = 1.4$ GeV as starting values.

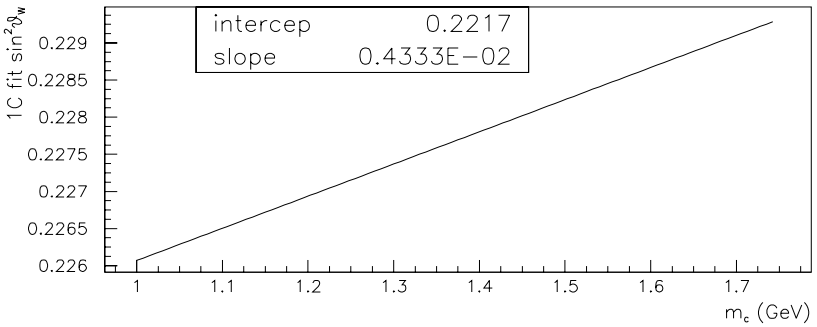

Figure 8.2: $\sin^2\theta_W$ from the 1C fit as a function of input charm mass.

8.2 The 0C $\sin^2\theta_W$ Fit

A 0C fit is also performed by dropping the charm mass constraint from the dimuon measurement and allowing m_c to vary as a free parameter in the fit. This gives a result based on a combination more similar to the Paschos–Wolfenstein quantity, R^-, than the aforementioned fit. In these fits, $\sin^2\theta_W$ is effectively determined from a quantity, $\tilde{R}^- \equiv R^\nu_{\rm exp} - xR^{\overline{\nu}}_{\rm exp}$. Recalling that the Paschos–Wolfenstein quantity, $R^- = (R^\nu - rR^{\overline{\nu}})/(1-r) = (R^\nu - 0.5R^{\overline{\nu}})/0.5 = 1/2 - \sin^2\theta_W$, one might expect $x = 0.5$ and $d\tilde{R}^-/d\sin^2\theta_W = -0.5$ if the fit is indeed similar to a pure Paschos–Wolfenstein determination. Table 8.2 compares these values for the 1C and 0C fits.

	x	$d\tilde{R}^-/d\sin^2\theta_W$
1C fit	0.249	–0.617
0C fit	0.453	–0.612

Table 8.2: The R^- approximation to the NuTeV 1C and 0C fits. In each case, $\sin^2\theta_W$ is determined from a quantity much like $\tilde{R}^- \equiv R^\nu_{\rm exp} - xR^{\overline{\nu}}_{\rm exp}$. The 0C fit is based on a combination more like the Paschos–Wolfenstein ratio.

The χ^2 minimization in this case becomes:

$$\chi^2 = \sum_{\nu,\overline{\nu}} \frac{(R^{\rm MC}_{\rm exp} - R^{\rm data}_{\rm exp})^2}{\sigma(R^{\rm data}_{\rm exp})^2} \tag{8.9}$$

The results for the 0C fit to $\sin^2\theta_W$ yield:

$$\begin{aligned} \sin^2\theta_W &= 0.22738 \pm 0.00164\,(\text{stat}) \pm 0.00076\,(\text{syst}) \\ &\quad - 0.00037 \cdot \left(\frac{{M_{\rm top}}^2 - (175\ \text{GeV})^2}{(50\ \text{GeV})^2} \right) \\ &\quad + 0.00050 \cdot \ln\left(\frac{M_{\rm Higgs}}{150\ \text{GeV}} \right) \end{aligned} \tag{8.10}$$

$$m_c = 1.30 \pm 0.13\,(\text{stat}) \pm 0.11\,(\text{syst})\ \text{GeV} \tag{8.11}$$

The effective charm mass from this fit, $m_c = 1.30 \pm 0.17$ GeV, provides a consistency check on the measurement from the dimuon data, $m_c = 1.38 \pm 0.14$ GeV. Dropping the m_c constraint, however, increases the overall uncertainty in $\sin^2\theta_W$ by $\sim 10\%$. The change is dominated by a 20% increase in the statistical error as a result of using more $\overline{\nu}$ data (Table 8.2), which is insensitive to $\sin^2\theta_W$, to reduce systematics.

8.3 The ρ_0 Fit

Although the primary goal of the experiment is to measure $\sin^2\theta_W$, we can fix $\sin^2\theta_W$ to the standard model value and instead fit for an overall NC coupling strength. In this case, all of the squared NC quark couplings receive a scale factor ρ_0^2 (see, for example, Equation 1.30 in Chapter 1). The fit for ρ_0 yields:

$$\begin{aligned} \rho_0 &= 0.99420 \pm 0.00132\,(\text{stat}) \pm 0.00162\,(\text{syst}) \\ &- 0.00084 \cdot \left(\frac{{M_{\text{top}}}^2 - (175\ \text{GeV})^2}{(50\ \text{GeV})^2} \right) \\ &+ 0.00130 \cdot \ln\left(\frac{M_{\text{Higgs}}}{150\ \text{GeV}} \right) \end{aligned} \tag{8.12}$$

Unlike the $\sin^2\theta_W$ fit, both the neutrino and antineutrino data are sensitive to ρ_0 ($\partial R^{\nu}_{\text{exp}}/\partial\rho_0 = 0.612$ and $\partial R^{\overline{\nu}}_{\text{exp}}/\partial\rho_0 = 0.710$), so there is less control over the charm production systematics, and the systematic uncertainties are much larger.

8.4 The $\sin^2\theta_W - \rho_0$ Fit

Two parameter fits dilute the discrepancy by increasing both the statistical and systematic uncertainties*. Despite the degeneracy of the two sets of parameters

* Correlated systematics cancel between ν and $\overline{\nu}$ modes in the one parameter fits, i.e., R^-, but do not cancel in the two parameter fits.

($R^{\nu}_{\rm exp}$, $R^{\overline{\nu}}_{\rm exp}$), we quote both model–dependent and "model–independent" fit results. The former is a simultaneous fit for $\sin^2\theta_W$ and ρ_0, described here. The later is a chiral coupling fit, described in the next section.

Because there is no apriori constraint on m_c, the two parameter fits reduce to a linearized problem in a given set of parameters, $\vec{X}$, where:

$$\vec{X} \equiv \begin{pmatrix} x_1 \\ x_2 \end{pmatrix} = \begin{pmatrix} \sin^2\theta_W \\ \rho_0 \end{pmatrix} \text{ or } \begin{pmatrix} g_L^{\rm eff\,2} \\ g_R^{\rm eff\,2} \end{pmatrix} \tag{8.13}$$

A Jacobian, which relates the experimental observables, $R^{\nu}_{\rm exp}$ and $R^{\overline{\nu}}_{\rm exp}$, to the electroweak fit parameters allows solution for $\vec{X}$ without resorting to a full fit minimization:

$$J_R[\vec{X}] = \begin{pmatrix} \frac{\partial R^{\nu}_{\rm exp}}{\partial x_1} & \frac{\partial R^{\nu}_{\rm exp}}{\partial x_2} \\ \frac{\partial R^{\overline{\nu}}_{\rm exp}}{\partial x_1} & \frac{\partial R^{\overline{\nu}}_{\rm exp}}{\partial x_2} \end{pmatrix} \tag{8.14}$$

In analogy with Equation 8.1, $\delta\vec{X} = J_R[\vec{X}]^{-1}\delta\vec{R}$, where $\delta\vec{R} \equiv \vec{R}^{\rm data}_{\rm exp} - \vec{R}^{\rm MC}_{\rm exp}$. Similarly, assuming a covariance matrix for $R_{\rm exp}$:

$$V_R \equiv \begin{pmatrix} \sigma(R^{\nu}_{\rm exp})^2 & \rho\,\sigma(R^{\nu}_{\rm exp})\,\sigma(R^{\overline{\nu}}_{\rm exp}) \\ \rho\,\sigma(R^{\nu}_{\rm exp})\,\sigma(R^{\overline{\nu}}_{\rm exp}) & \sigma(R^{\overline{\nu}}_{\rm exp})^2 \end{pmatrix} \tag{8.15}$$

the approximate error matrix for $\vec{X}$ is then $V_X = (J_R[\vec{X}])^{-1} V_R (J_R[\vec{X}]^T)^{-1}$.

Solution for the central values and errors of the two parameter quantities, $\vec{X}$, requires knowledge of $\delta\vec{R}$. A reference Monte Carlo provides predictions for $R_{\rm exp}$ assuming $m_c = 1.4$ GeV, $M_{\rm top} = 175$ GeV, $M_{\rm Higgs} = 150$ GeV, and the standard model value for $\sin^2\theta_W$ from ZFITTER v6.34 [31]. The differences between the measurement in the data and the prediction from the reference Monte Carlo are:

$$\begin{aligned}
\delta R^{\nu}_{\rm exp} &= -0.00306 \pm 0.00069\,({\rm stat}) \pm 0.00074\,({\rm syst}) \\
&\quad + 0.00612\,({\rm m}_c - 1.4) + 0.00089\,({\rm m}_c - 1.4)^2 \qquad (8.16) \\
\delta R^{\overline{\nu}}_{\rm exp} &= -0.00135 \pm 0.00159\,({\rm stat}) \pm 0.00142\,({\rm syst}) \\
&\quad + 0.0133\,({\rm m}_c - 1.4) + 0.00100\,({\rm m}_c - 1.4)^2 \qquad (8.17)
\end{aligned}$$

Using the linear term to evaluate the error from the ± 0.14 GeV uncertainty on ${\rm m}_c$:

$$\begin{aligned}
\delta R^{\nu}_{\rm exp} &= -0.00319 \pm 0.00069\,({\rm stat}) \pm 0.00074\,({\rm syst}) \pm 0.00086\,({\rm m}_c) \qquad (8.18) \\
&= -0.00319 \pm 0.00131 \\
\delta R^{\overline{\nu}}_{\rm exp} &= -0.00162 \pm 0.00159\,({\rm stat}) \pm 0.00142\,({\rm syst}) \pm 0.00179\,({\rm m}_c) \qquad (8.19) \\
&= -0.00162 \pm 0.00278
\end{aligned}$$

$R^{\nu}_{\rm exp}$ has been measured to an accuracy of 0.3%, and $R^{\overline{\nu}}_{\rm exp}$ to an accuracy of 0.7%. Systematic uncertainties lead to a correlation between the two of 0.636. Figure 8.3 displays the experimental constraint on $R^{\nu}_{\rm exp}$ and $R^{\overline{\nu}}_{\rm exp}$. As can be seen from the plot, the antineutrino ratio is consistent with the standard model expectation, while the neutrino mode ratio is roughly 0.8% low at 2.4σ significance.

	$\partial R^{\nu}_{\rm exp}/\partial$	$\partial R^{\overline{\nu}}_{\rm exp}/\partial$
$\sin^2\theta_W$	–0.630	–0.040
ρ_0	0.612	0.710

Table 8.3: Inputs to the two parameter $\sin^2\theta_W - \rho_0$ fit.

Using the above formalism and the Jacobian entries as determined from the Monte Carlo (Table 8.3), one can solve for $\vec{X} = (\sin^2\theta_W, \rho_0)$. Relaxing the assumption that $\rho_0 = 1$, the simultaneous two parameter fit yields:

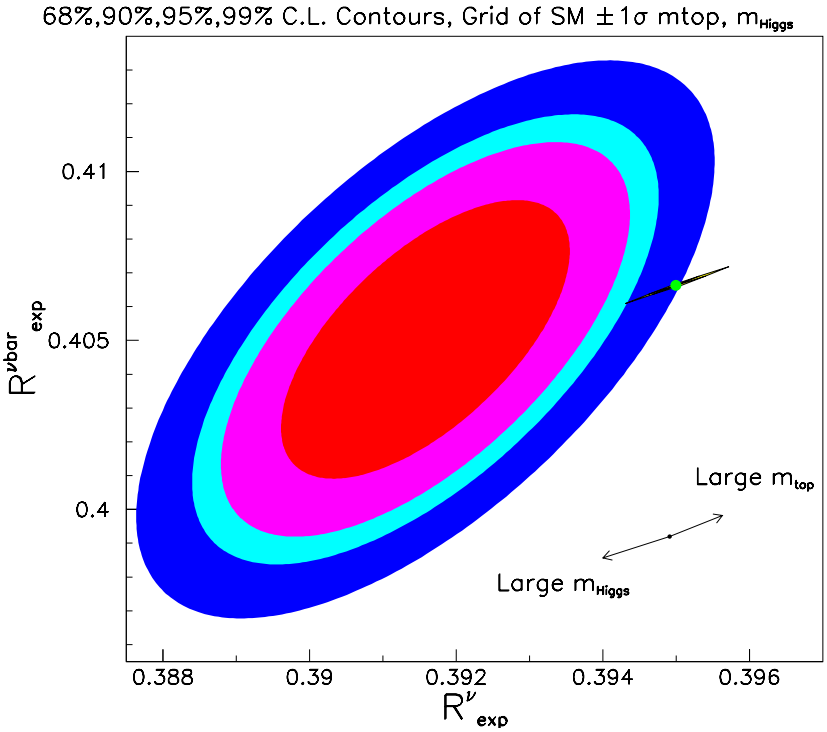

Figure 8.3: Experimental constraint on $R^{\nu}_{\rm exp}$ and $R^{\overline{\nu}}_{\rm exp}$. Ellipses indicate the allowed regions at 68%, 90%, 95% and 99% confidence levels. The standard model expectation is indicated by the small dot; the "wings" indicate how the standard model prediction would shift for $\pm 1\sigma$ variations in $M_{\rm top}$ and $M_{\rm Higgs}$. The large arrows indicate the direction of increasing $M_{\rm top}$ and $M_{\rm Higgs}$.

$$\sin^2\theta_W = 0.22647 \pm 0.00290 - 0.0080\,(\mathrm{m}_c - 1.38\ \mathrm{GeV}) \tag{8.20}$$

$$\rho_0 = 0.99789 \pm 0.00314 - 0.0183\,(\mathrm{m}_c - 1.38\ \mathrm{GeV}) \tag{8.21}$$

$$(\text{uncertainty correlation},\ \rho = 0.862)$$

If the charm mass dependence is explicitly incorporated into the systematics:

$$\sin^2\theta_W = 0.22647 \pm 0.00311 \tag{8.22}$$

$$\rho_0 = 0.99789 \pm 0.00405 \tag{8.23}$$

$$(\text{uncertainty correlation},\ \rho = 0.850)$$

Figure 8.4 shows the allowed regions for various levels of confidence. Given the standard model predictions, $\sin^2\theta_W = 0.2227 \pm 0.0004$ and $\rho_0 = 1$, either $\sin^2\theta_W$ or ρ_0 might be consistent with the standard model prediction, but not both.

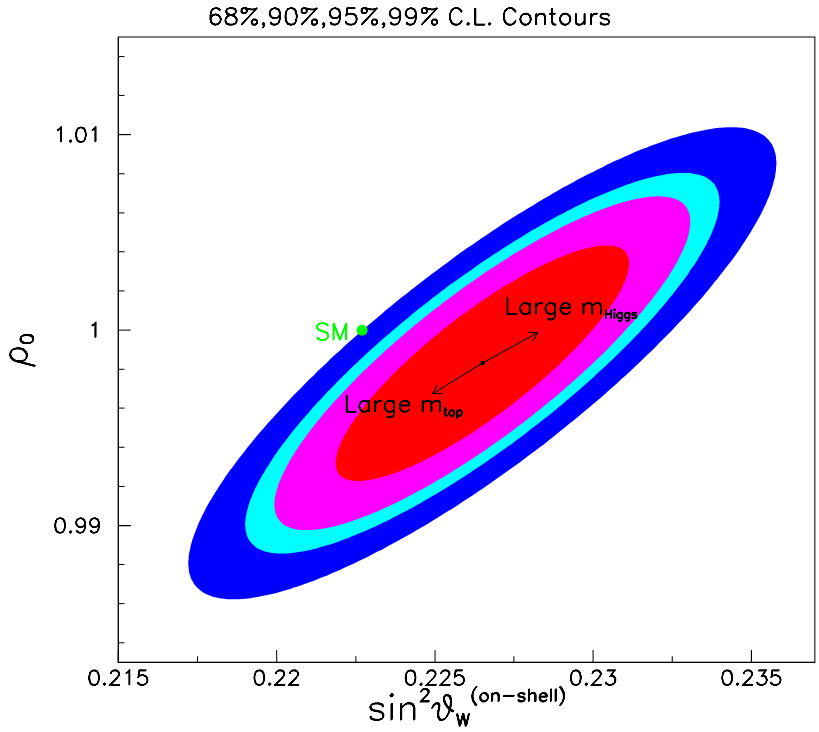

Figure 8.4: Experimental constraint on $\sin^2\theta_W$ and ρ_0. Ellipses indicate the allowed regions at 68% CL (inner ellipse) to 99% CL (outer–most ellipse). The arrows indicate how the fit result would shift for increasing $M_{\rm top}$ and $M_{\rm Higgs}$. The small dot marks the standard model expectation.

8.5 The $(g_L^{\rm eff})^2 - (g_R^{\rm eff})^2$ Fit

Model–independent two parameter fits, in terms of the isoscalar combinations of effective NC quark couplings, are also performed where:

$$(g_L^{\rm eff})^2 = (u_L^{\rm eff})^2 + (d_L^{\rm eff})^2, \qquad (g_R^{\rm eff})^2 = (u_R^{\rm eff})^2 + (d_R^{\rm eff})^2 \tag{8.24}$$

Scattering off an isoscalar target is essentially only sensitive to the isoscalar couplings. A weak dependence† on the isovector couplings, $\delta^2_{L,R} = {u^{\rm eff}_{L,R}}^2 - {d^{\rm eff}_{L,R}}^2$, arises from the strange and charm components in the nucleon sea, and from the slight non–isoscalarity of the NuTeV target. The fit uses the coupling dependences, $\partial R_{\rm exp}/\partial g^2_L$ and $\partial R_{\rm exp}/\partial g^2_R$, calculated under the assumption that δ^2_L and δ^2_R are constant:

$$\frac{\partial R_{\rm exp}}{\partial g^2_L} \equiv \frac{1}{2}\left(\frac{\partial R_{\rm exp}}{\partial u^2_L} + \frac{\partial R_{\rm exp}}{\partial d^2_L}\right), \qquad \frac{\partial R_{\rm exp}}{\partial g^2_R} \equiv \frac{1}{2}\left(\frac{\partial R_{\rm exp}}{\partial u^2_R} + \frac{\partial R_{\rm exp}}{\partial d^2_R}\right) \tag{8.25}$$

With these inputs (Table 8.4) and the measurements of $R^{\nu}_{\rm exp}$ and $R^{\overline{\nu}}_{\rm exp}$:

$$(g^{\rm eff}_L)^2 = 0.30005 \pm 0.00115 - 0.0053\,(\mathrm{m}_c - 1.38\ \mathrm{GeV}) \tag{8.26}$$

$$(g^{\rm eff}_R)^2 = 0.03076 \pm 0.00098 - 0.0036\,(\mathrm{m}_c - 1.38\ \mathrm{GeV}) \tag{8.27}$$

$$(\text{uncertainty correlation, } \rho = -0.355)$$

where these are the measured couplings after electroweak radiative corrections. Explicitly incorporating the charm mass dependence:

$$(g^{\rm eff}_L)^2 = 0.30005 \pm 0.00137 \tag{8.28}$$

$$(g^{\rm eff}_R)^2 = 0.03076 \pm 0.00110 \tag{8.29}$$

$$(\text{uncertainty correlation, } \rho = -0.017)$$

Figure 8.5 shows the solution in the $(g^{\rm eff}_L)^2 - (g^{\rm eff}_R)^2$ plane, for various confidence levels. The standard model values, as indicated on the plot, are $(g^{\rm eff}_L)^2 = 0.3042$ and $(g^{\rm eff}_R)^2 = 0.0301$. While the right–handed coupling appears to be compatible with the standard model, the NuTeV data clearly prefer a smaller left–handed effective coupling.

† Roughly 3% of the isoscalar sensitivity.

	$\partial R^{\nu}_{\rm exp}/\partial$	$\partial R^{\overline{\nu}}_{\rm exp}/\partial$
u_L	0.87297	0.73070
d_L	0.96909	0.90236
u_R	0.30748	2.19978
d_R	0.37783	2.42962
g_L^2	0.9210	0.8165
g_R^2	0.3427	2.3197

Table 8.4: Inputs to the two parameter ${g_L^{\rm eff}}^2 - {g_R^{\rm eff}}^2$ fit.

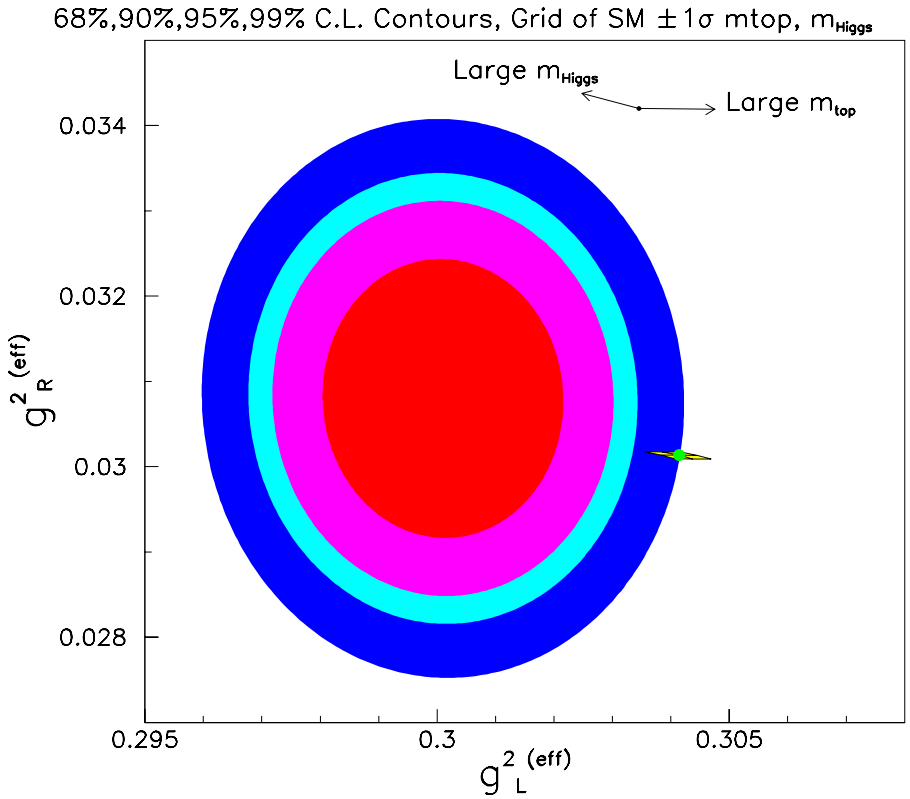

Figure 8.5: Experimental constraint on $(g_L^{\rm eff})^2$ and $(g_R^{\rm eff})^2$. Shown are the allowed regions at 68% CL out to 99% CL. The standard model expectation is indicated by the small dot; the "wings" indicate how that prediction would shift for $\pm 1\sigma$ variations in $M_{\rm top}$ and $M_{\rm Higgs}$. The large arrows indicate the direction of increasing $M_{\rm top}$ and $M_{\rm Higgs}$.

8.6 Comparisons to the Rest of the World

Comparisons to past neutrino–nucleon determinations of $\sin^2\theta_W$, direct measurements of M_W, and the world's current precision electroweak data place the NuTeV results into greater context.

8.6.1 Past νN Measurements of $\sin^2\theta_W$

The NuTeV result lies three standard deviations above the standard model expectation, however, it is in good agreement with previous neutrino–nucleon determinations of $\sin^2\theta_W$. Figure 8.6 demonstrates the consistency of the NuTeV result with past neutrino–nucleon determinations of the weak mixing angle. Combining the earlier measurements, after correcting the results for our improved knowledge of $M_{\rm top} = 175$ GeV and $\mathrm{m}_c = 1.38 \pm 0.14$ GeV, the average of the five most precise neutrino–nucleon measurements of $\sin^2\theta_W$ before NuTeV is:

$$\begin{aligned} {\sin^2\theta_W}^{\nu N}(\text{combined}) &= 0.2277 \pm 0.0024\,(\text{exp}) \pm 0.0019\,(\text{theory}) \\ &= 0.2277 \pm 0.0031 \end{aligned} \tag{8.30}$$

The statistics–dominated NuTeV measurement, which coincidentally has the same central value as the above combination, is twice as precise as the previous neutrino–nucleon experiments. It is interesting to note that all of the measurements lie systematically above the standard model expectation.

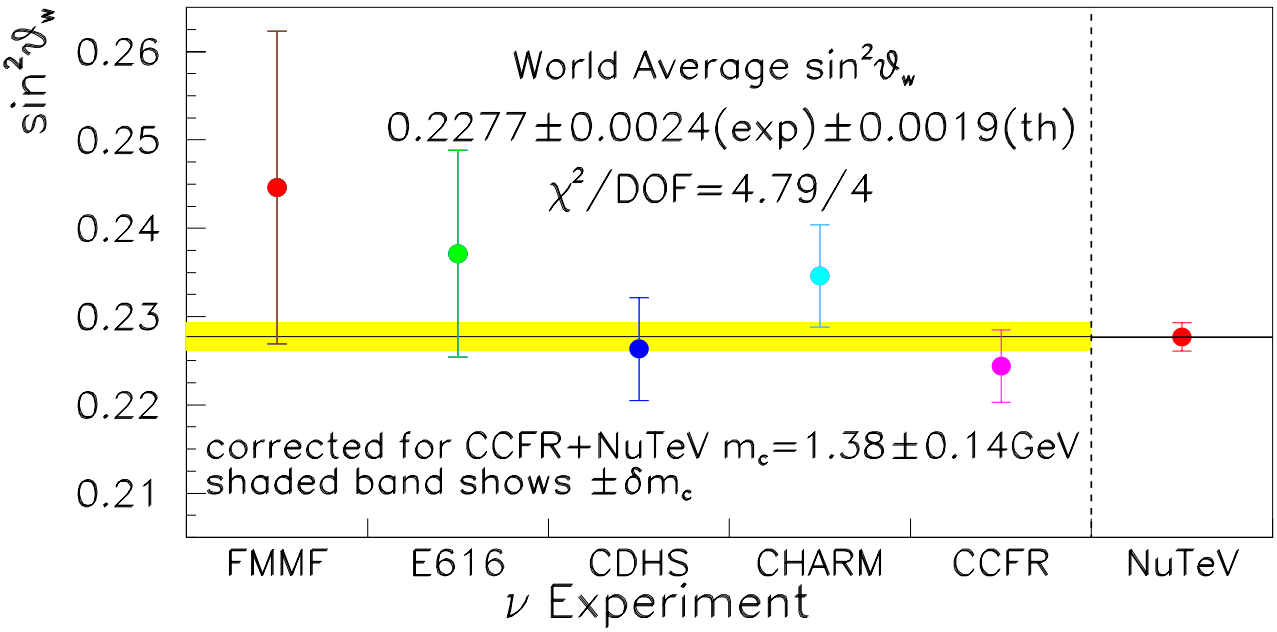

Figure 8.6: History of neutrino–nucleon measurements of $\sin^2\theta_W$. The band indicates the correlated charm production uncertainty (not present in NuTeV). Note: earlier experiments have been corrected for our improved knowledge: $m_c = 1.38$ GeV and $M_{\text{top}} > M_W$.

8.6.2 Direct M_W

In the on–shell renormalization scheme,

$$\sin^2 \theta_W^{\text{on-shell}} \equiv 1 - \frac{M_W^2}{M_Z^2} \tag{8.31}$$

where M_W and M_Z are the physical gauge boson masses, the NuTeV result implies $M_W = 80.14 \pm 0.08$ GeV. This value lies more than 3σ below the direct world average, $M_W = 80.45 \pm 0.03$ GeV [73]. Figure 8.7 compares the NuTeV result to the various direct measurements of M_W. The NuTeV measurement is just as precise as any other single measurement. The more precise indirect world average of $M_W = 80.38 \pm 0.02$ GeV is a combination of results from LEP I, SLD, APV, and direct M_{top} [74]. NuTeV is slightly less consistent with the direct measurements than with the indirect.

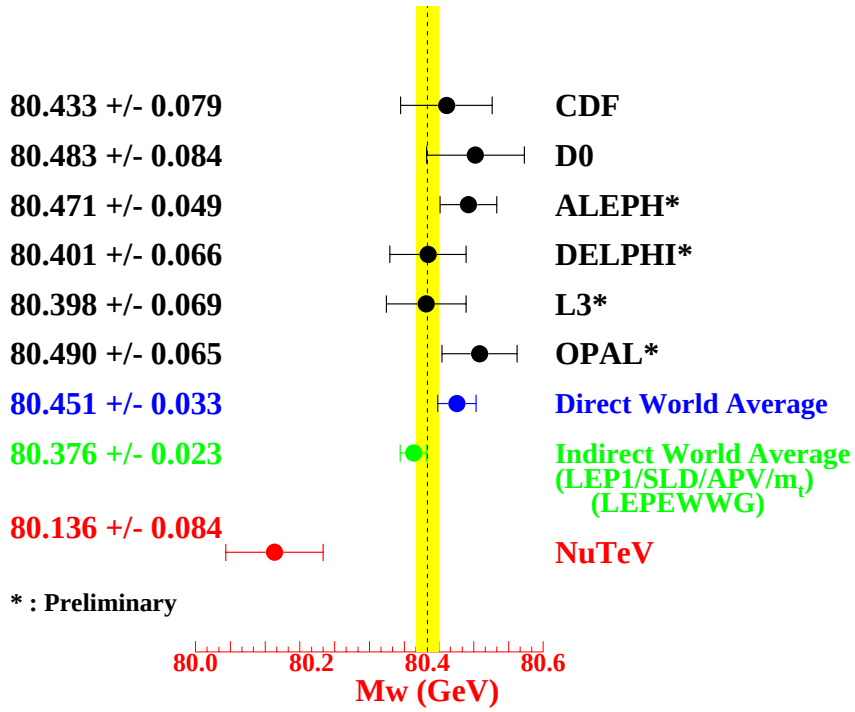

Figure 8.7: Comparison of the NuTeV result to direct measurements of M_W. Also shown is the indirect world average not including NuTeV [74].

Figure 8.8 shows the experimental constraints on M_W versus $M_{\rm top}$. The bulk of the data tend to collectively favor a light Higgs mass. The central value from recent global fits to all precision data is $M_{\rm Higgs} = 81^{+49}_{-32}$ GeV with an upper bound of $M_{\rm Higgs} < 196$ GeV at 95% CL [73]. The discrepancy in the NuTeV $\sin^2\theta_W^{\rm on-shell}$ from M_W, however, makes it difficult to reconcile the result with other precision data in terms of changes to $M_{\rm Higgs}$ or $M_{\rm top}$.

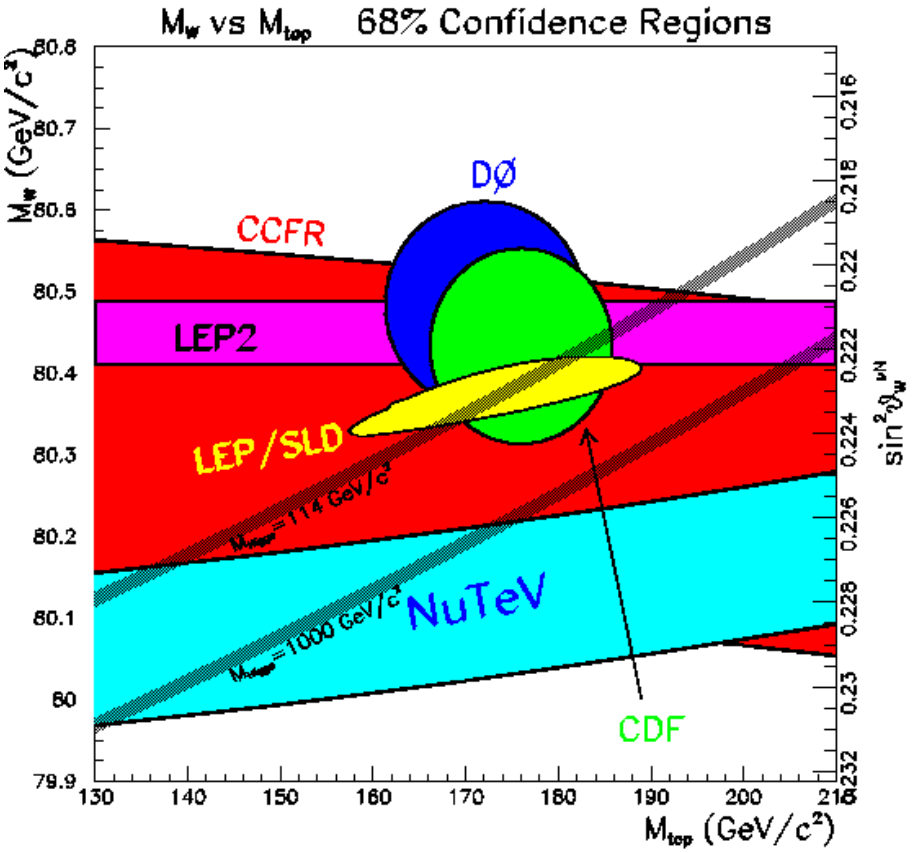

Figure 8.8: Comparison of 68% CL allowed regions for both direct and indirect measurements of M_W and $M_{\rm top}$. The shaded bands indicate the standard model predictions for $M_{\rm Higgs} = 114$ GeV and $M_{\rm Higgs} = 1$ TeV. The width of the bands is primarily due to the uncertainty in $\alpha(M_Z{}^2)$.

8.6.3 Global Standard Model Fits

Figure 8.9 exhibits the results of the LEP Electroweak Working Group (LEPEWWG) global fit to all precision electroweak data including the NuTeV measurement of $\sin^2\theta_W$ [73]. The largest pulls are coming from the NuTeV $\sin^2\theta_W$ result and the LEP II measurement of $A_{FB}^{0,b}$. The inclusion of the NuTeV measurement in the standard model fit increases the global χ^2/dof to 28.8/15. The probability of the χ^2 being worse than 28.8 is only 1.7%.

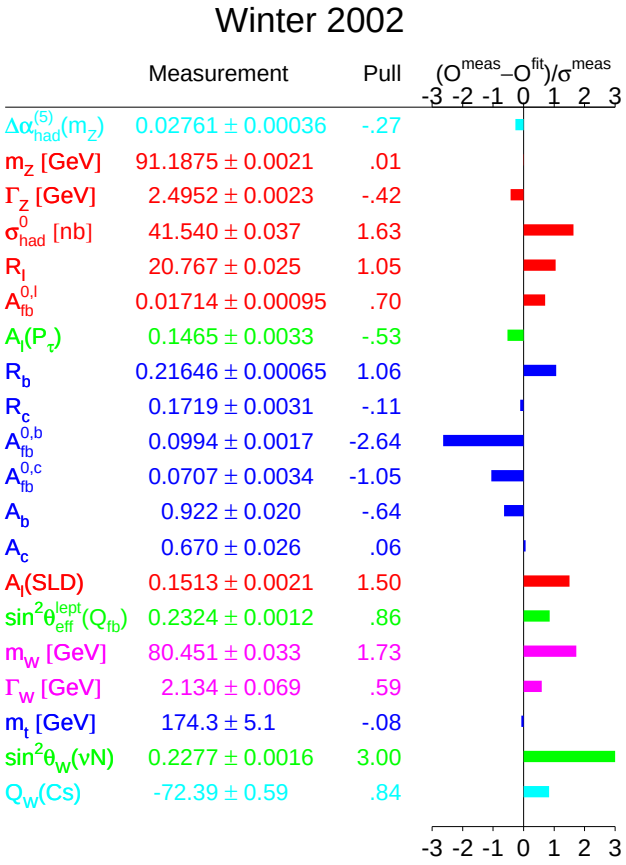

Figure 8.9: Current global electroweak fit including NuTeV $\sin^2\theta_W$. Bars indicate the pull of each measurement, in standard deviations, from its standard model expectation. The χ^2/dof is 28.8/15 (1.7% probability). Plot courtesy of LEPEWWG.

If one arbitrarily excludes the NuTeV results the fit is adequate. Without NuTeV,

the χ^2/dof is 19.6/14 which equates to a probability of 14.3%. This value is largely driven by the 3σ discrepancy between the two most precise determinations of $\sin^2\theta_W$ at the Z pole: the leptonic measurement, A_{LR} at SLD, and the hadronic measurement, $A_{FB}^{0,b}$ at LEP.

These results should, of course, be interpreted with caution. Discarding one or two measurements can improve the fit, but at the same time drastically change the predicted Higgs boson mass (Figure 8.10). If the two most discrepant measurements, $A_{FB}^{0,b}$ and NuTeV $\sin^2\theta_W$, are arbitrarily removed from the fit, the global χ^2 improves to 6.84/9, a robust 65% probability [75]; however, disregarding $A_{FB}^{0,b}$ implies that the favored value of the Higgs mass from the standard model fit drops to 43 GeV‡ [76], well below the direct search limits set by the non–discovery of the Higgs at LEP II, $M_{\text{Higgs}} > 114$ GeV [73].

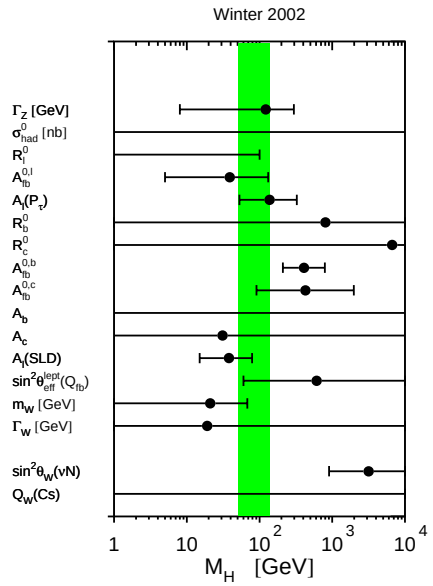

Figure 8.10: Sensitivity of the precision electroweak data to M_{Higgs}. Most of the data is consistent with a low M_{Higgs}, except for $A_{FB}^{0,b}$ and NuTeV $\sin^2\theta_W$. The NuTeV result favors large M_{Higgs}, but not with sufficient precision to pull the overall fit. Plot courtesy of LEPEWWG [73].

‡ At 90% confidence level, $17 < M_{\text{Higgs}} < 105$ GeV [75].

Figure 8.11 shows the global fit results if, instead of using the NuTeV $\sin^2\theta_W$ measurement, the results from the two parameter $(g_L^{\rm eff})^2$, $(g_R^{\rm eff})^2$ fit are included. In this case, the reported global agreement is similarly poor, $\chi^2/{\rm dof} = 29.2/16$ (2.2% probability). The NuTeV discrepancy is almost entirely in the left–handed effective coupling, $(g_L^{\rm eff})^2$, which lies 3σ below the standard model expectation.

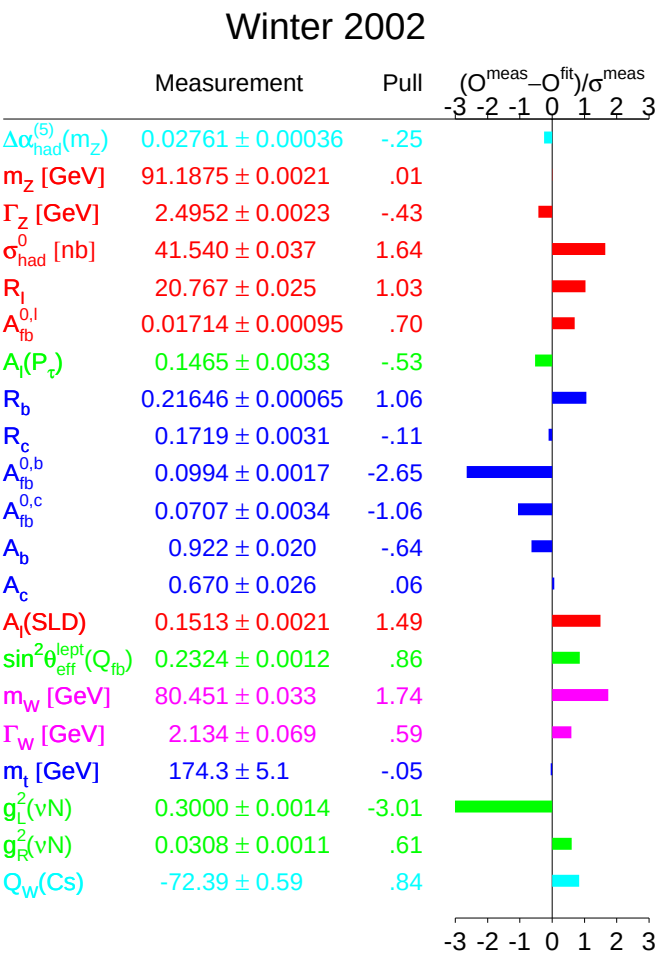

Figure 8.11: Winter 2002 global electroweak fit including NuTeV $(g_L^{\rm eff})^2$ and $(g_R^{\rm eff})^2$. Bars indicate the pull of each measurement, in standard deviations, from its standard model expectation. The $\chi^2/{\rm dof}$ is 29.2/16 (2.2% probability). Plot courtesy of the LEPEWWG [73].

Chapter 9

Conclusions

> *"Physics will change even more ... we think that the future will be only more radical and not less, only more strange and not more familiar, and that it will have its own new insights for the inquiring human spirit."*
>
> — J.R. Oppenheimer (1953)

The weak neutral current has long provided a quantitative test of the standard electroweak model. Continuing this tradition, this dissertation presents a precise determination of the weak mixing angle, from the measurement of ratios of neutral to charged current cross sections, using high statistics samples of neutrino and antineutrino events:

$$\sin^2\theta_W{}^{(\mathrm{on-shell})} = 0.2277 \pm 0.0013\,(\mathrm{stat}) \pm 0.0009\,(\mathrm{syst}) \tag{9.1}$$

which is currently the most precise determination of $\sin^2\theta_W$ from neutrino scattering. Although previous neutrino–nucleon measurements obtained a similar central value, the current determination is the first with sufficient precision to observe a deviation from the standard model. The result lies three standard deviations above the standard model prediction. Given this 3σ inconsistency, results are also extracted within a model–independent framework. NuTeV precisely measures effective left and right handed neutral current quark couplings:

$$(g_L^{\rm eff})^2 = 0.30005 \pm 0.00137 \quad (9.2)$$

$$(g_R^{\rm eff})^2 = 0.03076 \pm 0.00110 \quad (9.3)$$

which, when compared to the standard model expectations, $(g_L^{\rm eff})^2 = 0.3042$ and $(g_R^{\rm eff})^2 = 0.0301$, suggest that the data prefer a lower effective left–handed coupling. At present, both expressions of the result stand unchallenged.

9.1 Interpretations

Interpretations of the discrepant NuTeV result include the possibility of symmetry violating parton distributions, additional Z bosons, or unexpected neutral current neutrino interactions. Each is briefly considered below.

The NuTeV result is extracted assuming isospin symmetry in the nucleon, $u^p = d^n$, $d^p = u^n$, $\overline{u}^p = \overline{d}^n$, and $\overline{d}^p = \overline{u}^n$. While all global parton distribution fits (CTEQ, GRV, MRST) are performed under this assumption, the present analysis is sensitive because of the need to assign u and d flavors (which have different NC couplings) to the neutrino scatterers. Several classes of non–perturbative models calculate the potential effect of isospin violation in the nucleon [81, 82, 83]. Estimating the effect of the single quark mass difference ($m_d - m_u = 4.3$ MeV), the earliest calculation [81] predicts a large –0.0020 shift in $\sin^2\theta_W$, which could account for roughly 40% of the observed discrepancy. However, more complete calculations that include differences in the nucleon masses ($m_n - m_p = 1.3$ MeV), diquark masses ($m_{dd} - m_{uu}$), and nucleon radii predict much smaller shifts in the result. For example, the Thomas *et al.* bag model calculation [82] predicts $\delta\sin^2\theta_W(\text{NuTeV}) = -0.00010$ as a result of

the cancellation of opposing shifts at low and high x. A meson cloud model prediction [83] yields a similarly small +0.00020 shift in the NuTeV measurement. Figure 9.1 compares the various predictions. While the more recent calculations don't suggest a very large isospin violation, such a possibility cannot be firmly excluded as a potential explanation for the NuTeV results. However, a nucleon isospin violating model which successfully accounts for the NuTeV discrepancy needs to be evaluated in the context of a global fit so as not to violate existing experimental data in the attempt to accommodate NuTeV.

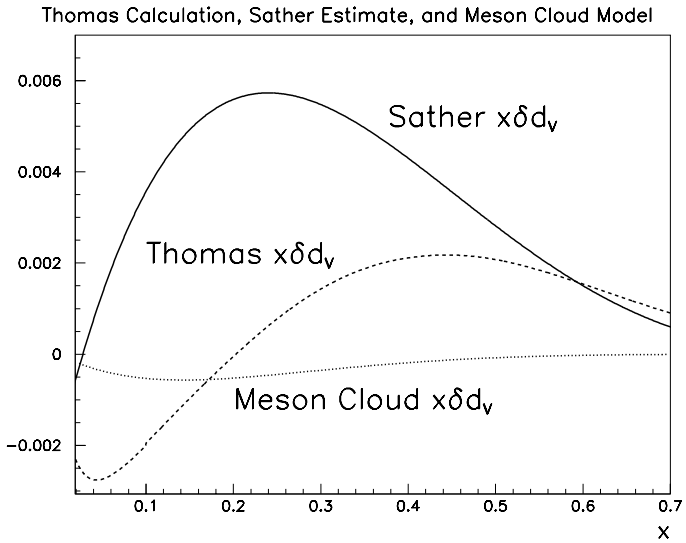

Figure 9.1: Various model predictions for an isospin violating difference in the minority quark distribution, $\delta d_v \equiv d_v^p - u_v^n$, as a function of x.

The analysis also assumes that the strange and antistrange seas are symmetric, $s(x) = \overline{s}(x)$; however it has been noted that non-perturbative QCD processes can potentially generate a momentum asymmetry between the strange and anti–strange seas [84]. Such an asymmetry can be directly measured using the same parton distribution formalism and cross section model as were employed in the $\sin^2\theta_W$ measurement. Leading order fits to the NuTeV neutrino and antineutrino dimuon

data samples [42] yield a negative asymmetry* (Figure 9.2):

$$\int x\, s(x) - x\, \overline{s}(x)\, dx = -0.0027 \pm 0.0013 \tag{9.4}$$

and a corresponding increase in the NuTeV measurement of $\sin^2\theta_W$:

$$\sin^2\theta_W = 0.2297 \pm 0.0019 \tag{9.5}$$

when compared to the result, $\sin^2\theta_W = 0.2277 \pm 0.0016$, assuming $s(x) = \overline{s}(x)$. Including the measured strange sea asymmetry increases the NuTeV discrepancy with the standard model to 3.7σ significance; hence, this is not a likely explanation.

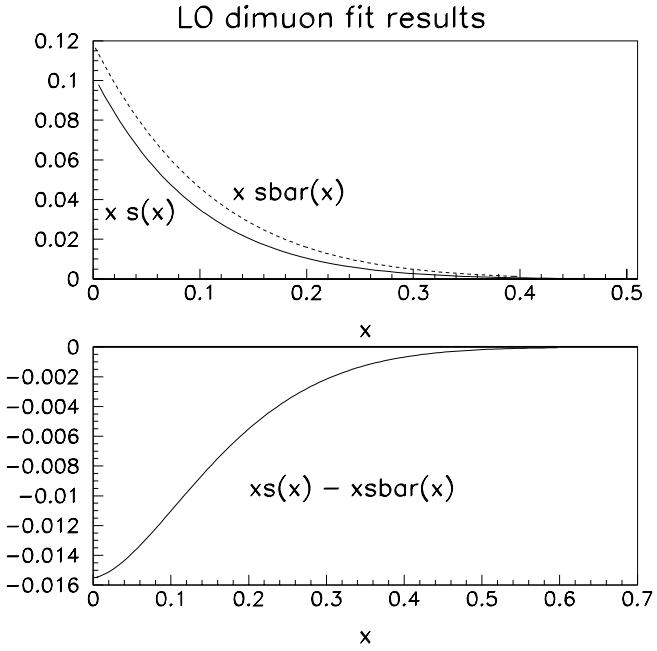

Figure 9.2: Measurement of the strange and anti–strange seas from the NuTeV LO analysis of dimuon processes $\nu N \to \mu^+\mu^- X$ and $\overline{\nu} N \to \mu^+\mu^- X$ [42]. The bottom plot displays the measured asymmetry $x\, s(x) - x\, \overline{s}(x)$ as a function of x.

* The result applies only within the specific PDF formalism and LO cross section model used in the NuTeV LO dimuon and $\sin^2\theta_W$ analyses and is not a more general statement about the existence of an asymmetric strange sea.

In addition to evaluating the effects of unexpected parton asymmetries (see the appended publication in Appendix F), we also consider several non–standard physics cases. The existence of an additional Z boson would impact the NuTeV measurement by shifting the effective neutrino–quark couplings away from their standard model values. These shifts can arise from both pure Z′ exchange as well as from Z–Z′ mixing. A popular class of Z′ models involves the introduction of extra U(1) symmetries. The E_6 model in particular has been considered as a candidate for grand unified theories. In this specific model, the coupling shifts are well determined [85], however because the NuTeV result requires an enhancement in the effective left–handed quark couplings (Figure 8.5), it is difficult to explain the entire discrepancy with the inclusion of such a Z′. While this specific model can produce large right–handed coupling shifts, appreciable Z–Z′ mixing is required to induce sizable shifts in the left–handed couplings. The size of the mixing is severely limited, at the $\sim 10^{-3}$ level, by measurements from LEP and SLD [86], hence making it difficult to accommodate the NuTeV measurement. On the other hand, it is possible to explain the entire NuTeV discrepancy with the inclusion of an "almost" sequential[†] Z′ with a mass in the $1.2^{+0.3}_{-0.2}$ TeV range. Both the Tevatron Run II and the LHC offer the hope of discovering such a Z′.

Finally, while such a solution is not model–independent or unique, it is interesting to interpret the entire NuTeV discrepancy as a deviation in the overall NC coupling strength ρ_0. The result, as presented in Section 8.3, is a neutral current rate that is 1% lower than the standard model expectation at almost 3σ significance:

$$\rho_0^2 = 0.9884 \pm 0.0026\,(\text{stat}) \pm 0.0032\,(\text{syst}) \tag{9.6}$$

[†] A Z′ with standard couplings but which interferes destructively with the standard model Z.

Figure 9.3 displays the NuTeV result in comparison to all other existing neutrino data. The only other precise experimental constraint, the LEP I measurement of Z decays into invisible channels, allows deduction of the number of light neutrino species. The result, $N_\nu = 3 \cdot \frac{\Gamma_{\rm meas}(Z\to\nu\overline{\nu})}{\Gamma_{\rm SM}(Z\to\nu\overline{\nu})} = 3 \cdot (0.9947 \pm 0.0028)$, is 2σ shy of the three known neutrino species [73]. Given this particular interpretation, one might suspect the neutral current couplings of neutrinos, since the only two precise measurements are both lower than the standard model expectation.

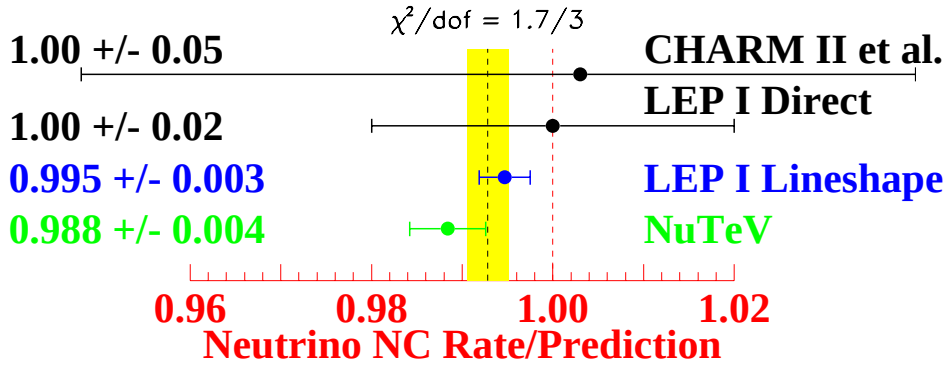

Figure 9.3: Experimental constraints on neutrino neutral current interaction rates relative to the standard model prediction. The two most precise measurements, LEP I $\Gamma(Z \to \nu\overline{\nu})$ and NuTeV ρ_0^2, are both below expectation.

Despite investigation of these avenues, the cause of the NuTeV discrepancy is not currently known. So what does the future hold? NuTeV was dismantled several years after data–taking and holds no hope of remeasuring electroweak parameters in neutrino scattering, but two future experiments are preparing to also test the low energy prediction of $\sin^2\theta_W$. To illustrate, Figure 9.4 shows the running of $\sin^2\theta_W$ in the $\overline{MS}$ scheme (Chapter 2).

Although very precise measurements of asymmetry parameters at the Z pole set the overall scale of the prediction, the two experimental constraints off the Z peak,

namely the atomic parity violation (APV) [77] and NuTeV $\sin^2\theta_W$ measurements, deviate from the predicted evolution of $\sin^2\theta_W$. Two polarized electron scattering experiments: an e^+e^- Møller scattering experiment, E158 at SLAC [78] and an electron–proton scattering experiment, QWEAK at Jefferson Lab [79] plan to probe this low Q^2 regime in the near future. These two experiments fall between the scales relevant for the APV and NuTeV measurements and propose to have improved precision. Any significant deviation in their measurements would provide striking evidence for new physics. However, if the deviation in the NuTeV measurement somehow results from new physics specific only to the neutrino or muon sector (i.e., beyond the Standard Model physics that is not flavor universal), then the discrepancy would surely not manifest itself in these two future experiments.

During the past three decades many experiments have performed a wealth of precision electroweak measurements to quantitatively test all aspects of the Standard Model. Unfortunately, the end of the decade precision measurements leave us with an incomplete picture. Despite current quests for ever higher energies, unexplained discrepancies still persist in existing data sets. While issues raised by the current data certainly heightens the excitment in high energy physics at the moment, this author hopes that in addition to pushing the experimental energy reach, there remains room in the high energy physics program for further exploration in the "low energy frontier".

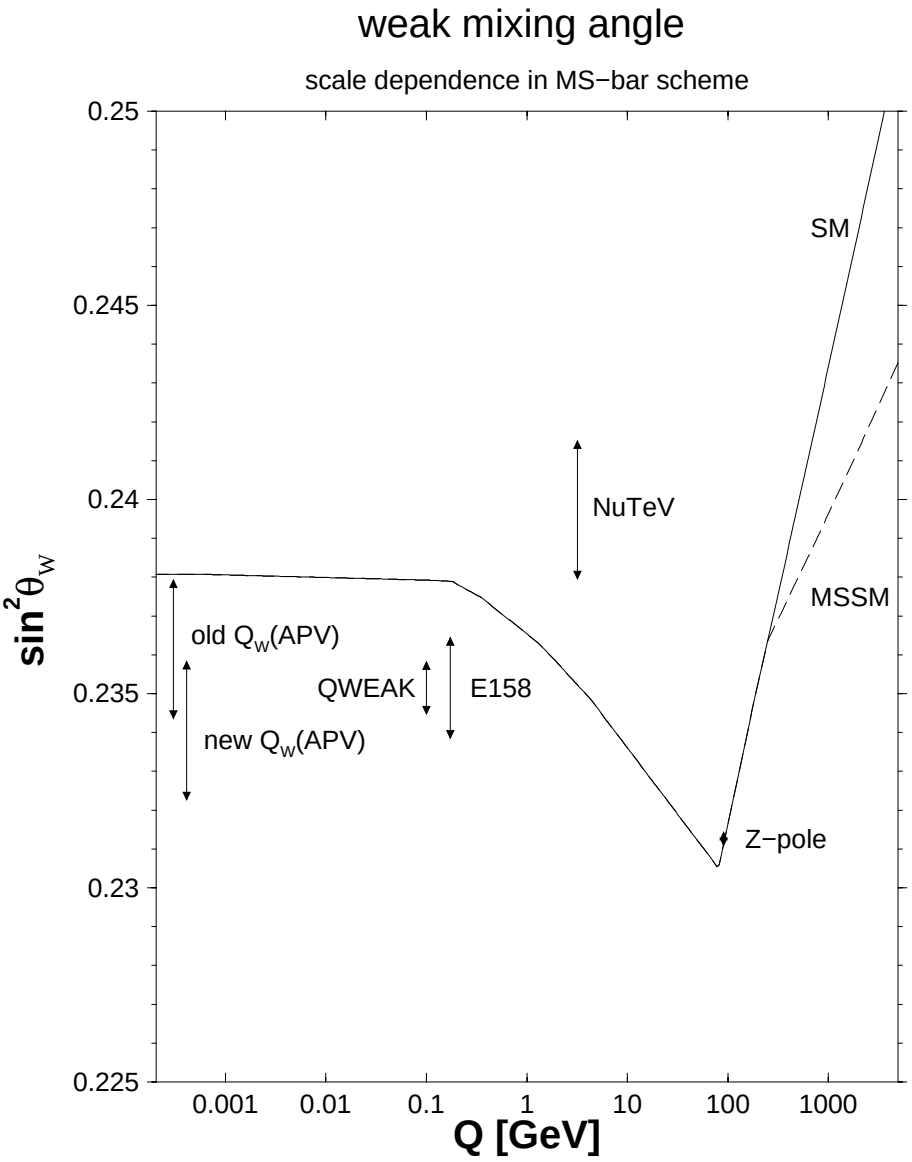

Figure 9.4: Scale dependence of $\sin^2\theta_W$ in the $\overline{MS}$ renormalization scheme (solid line). Shown are the experimental results from Z pole asymmetries (LEP, SLC), deep inelastic neutrino–nucleon scattering (NuTeV), and atomic parity violation (APV) measurements. The values for the APV measurement result from two recent recalculations of vacuum polarization effects. Expectations for E158 [78] and QWEAK [79] are also shown with arbitrary central values and projected uncertainties. Plot is courtesy of J. Erler [80].

Appendix A

The NuTeV Collaboration

R. A. Johnson, N. Suwonjandee, M. Vakili
University of Cincinnati

J. Conrad, B. T. Fleming, J.A. Formaggio, J. H. Kim, S. Koutsoliotas, C. McNulty, A. Romosan, M. H. Shaevitz, P. Spentzouris, E. G. Stern, A. Vaitaitis, E. D. Zimmerman
Columbia University

R. H. Bernstein, L. Bugel, M. J. Lamm, W. Marsh, P. Nienaber, J. Yu
Fermi National Accelerator Laboratory

T. Adams, A. Alton, T. Bolton, J. Goldman, M. Goncharov
Kansas State University

D. Buchholz, L. de Barbaro, H. Schellman, G. P. Zeller
Northwestern University

J. Brau, R. B. Drucker, R. Frey, D. Mason
University of Oregon

J. McDonald, D. Naples, M. Tzanov
University of Pittsburgh

S. Avvakumov, P. de Barbaro, A. Bodek, H. Budd, K. S. McFarland, D. A. Harris, W. K. Sakumoto, U. K. Yang
University of Rochester

Appendix B

Lab E Coordinate System

The lab E coordinate system is a right–handed cartesian coordinate system. The origin of the system resides roughly halfway between the calorimeter and the toroid, with the incoming neutrino beam direction chosen to be the +z direction. A diagram of the coordinate system is provided in Figure B.1.

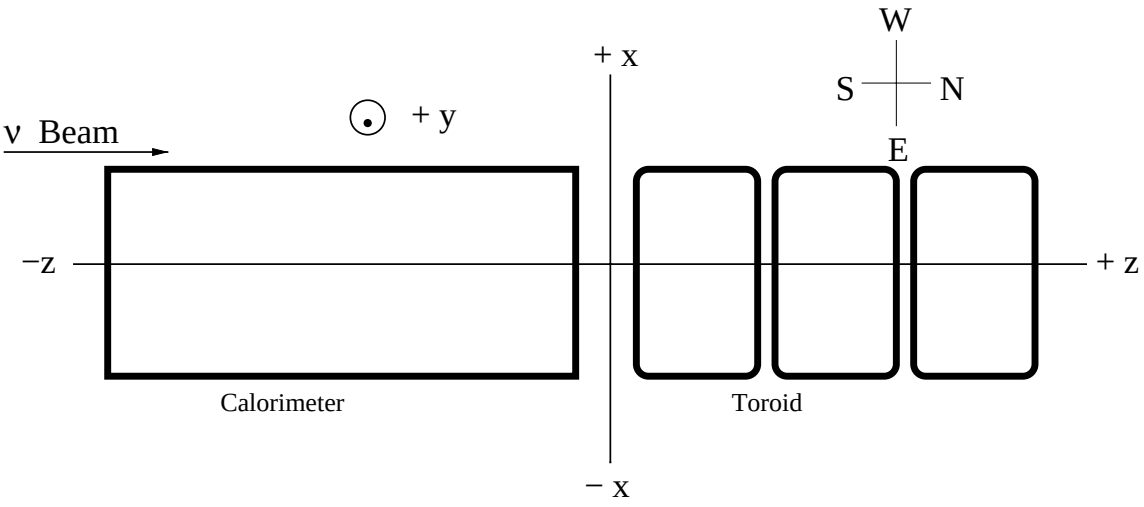

Figure B.1: Schematic of the Lab E coordinate system as illustrated by a bird's eye view of the NuTeV detector; +z is referred to as the downstream direction.

Appendix C

Protons on Target

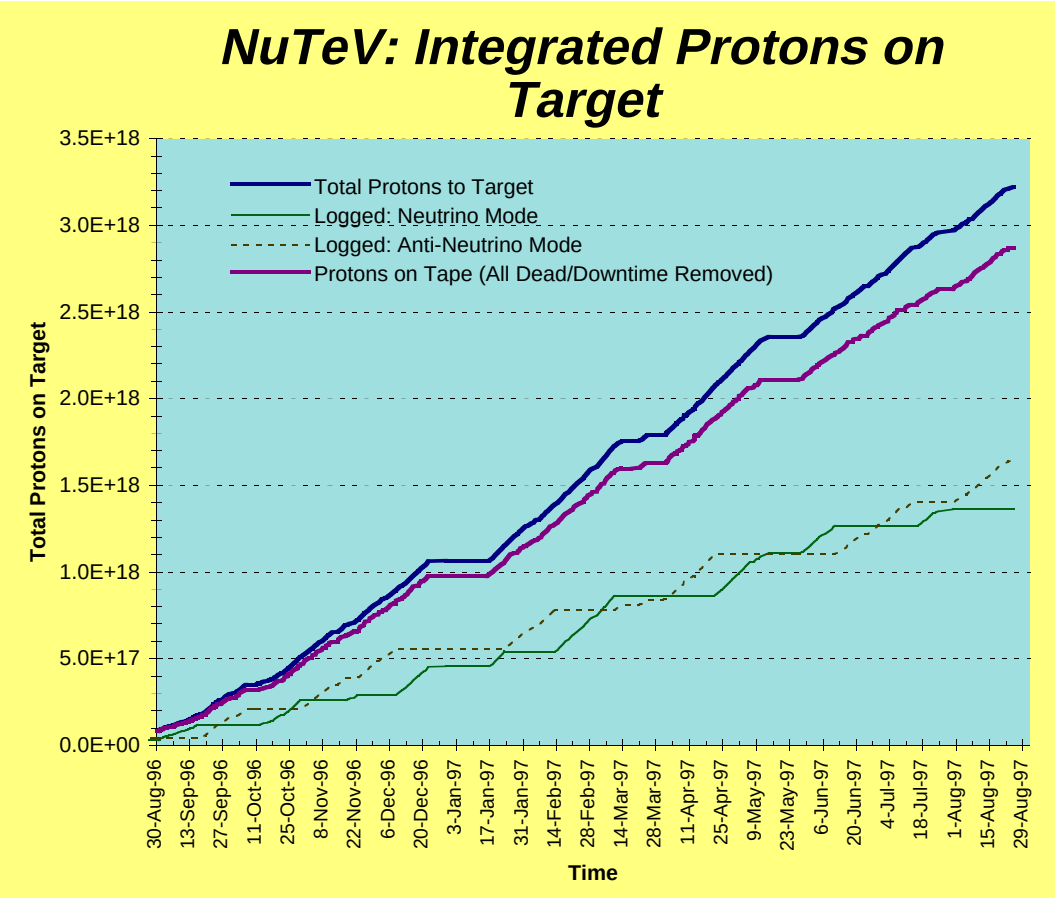

Figure C.1: Accumulation of protons on target as a function of time during NuTeV's 1996-1997 fixed target running. Also shown are the total number logged to tape in each mode.

Appendix D

CC Cross Section Facts

In charged current neutrino-nucleon interactions, the struck quark undergoes a flavor changing transition:

$$\begin{aligned} \nu_\mu + q &\longrightarrow \mu^- + q' \\ \overline{\nu}_\mu + q &\longrightarrow \mu^+ + q' \end{aligned} \tag{D.1}$$

Hence, charged current neutrino interactions proceed via exchange of a W^+, while antineutrino interactions proceed via exchange of a W^-. In order to conserve charge at the quark vertex, only negatively charged quarks participate in CC neutrino interactions while only positively charged quarks participate in CC antineutrino interactions. Hence, neutrinos can only scatter off of $d, s, \overline{u}$ and $\overline{c}$ quarks in CC interactions. Antineutrinos can only scatter off of $\overline{d}$, $\overline{s}, u$ and c quarks in CC interactions.

$$\nu \implies d, s, \overline{u}, \overline{c} \quad \text{CC scattering} \tag{D.2}$$

$$\overline{\nu} \implies \overline{d}, \overline{s}, u, c \quad \text{CC scattering} \tag{D.3}$$

Appendix E

Monte Carlo σ Normalization

It is worth noting that the NUMONTE Monte Carlo code returns a cross section value that is normalized by a factor $(G_F^2 ME/\pi)^{-1}$. Hence, to translate the output from the Monte Carlo routine, SIGMCQ, into a physical cross section an additional normalization factor of $\frac{G_F^2 ME}{\pi} = 15.8$ fb GeV^{-1} $\cdot$ E (GeV) $= 1.58 \times 10^{-38}$cm^2 GeV^{-1} $\cdot$ E (GeV) must be applied, such that:

$$\frac{d^2\sigma}{dx\,dy} = \frac{G_F^2 ME}{\pi} \cdot \left(\frac{d^2\sigma}{dx\,dy}\right)_{\text{SIGMCQ}} \tag{E.1}$$

As such, the Monte Carlo returns total isoscalar neutrino and antineutrino cross section values of:

$$\begin{aligned} \sigma^{\nu}/E &= 0.643 \times 10^{-38}\ \text{cm}^2 \cdot \text{GeV}^{-1} \\ \sigma^{\overline{\nu}}/E &= 0.319 \times 10^{-38}\ \text{cm}^2 \cdot \text{GeV}^{-1} \end{aligned}$$

Appendix F

Publications

The remainder of this dissertation contains articles on this topic that were submitted for publication. The first paper was accepted and published in *Physical Review Letters* in February 2002 [88]. The second paper, also appended, was submitted to *Physical Review D* in March 2002 and is still awaiting formal approval [89].

Precise Determination of Electroweak Parameters in Neutrino-Nucleon Scattering

G. P. Zeller,[5] K. S. McFarland,[8,3] T. Adams,[4] A. Alton,[4] S. Avvakumov,[8] L. de Barbaro,[5] P. de Barbaro,[8] R. H. Bernstein,[3] A. Bodek,[8] T. Bolton,[4] J. Brau,[6] D. Buchholz,[5] H. Budd,[8] L. Bugel,[3] J. Conrad,[2] R. B. Drucker,[6] B. T. Fleming,[2] R. Frey,[6] J. A. Formaggio,[2] J. Goldman,[4] M. Goncharov,[4] D. A. Harris,[8] R. A. Johnson,[1] J. H. Kim,[2] S. Koutsoliotas,[2] M. J. Lamm,[3] W. Marsh,[3] D. Mason,[6] J. McDonald,[7] C. McNulty,[2] D. Naples,[7] P. Nienaber,[3] A. Romosan,[2] W. K. Sakumoto,[8] H. Schellman,[5] M. H. Shaevitz,[2] P. Spentzouris,[2] E. G. Stern,[2] N. Suwonjandee,[1] M. Tzanov,[7] M. Vakili,[1] A. Vaitaitis,[2] U. K. Yang,[8] J. Yu,[3] and E. D. Zimmerman[2]

[1]*University of Cincinnati, Cincinnati, Ohio 45221*
[2]*Columbia University, New York, New York 10027*
[3]*Fermi National Accelerator Laboratory, Batavia, Illinois 60510*
[4]*Kansas State University, Manhattan, Kansas 66506*
[5]*Northwestern University, Evanston, Illinois 60208*
[6]*University of Oregon, Eugene, Oregon 97403*
[7]*University of Pittsburgh, Pittsburgh, Pennsylvania 15260*
[8]*University of Rochester, Rochester, New York 14627*

(Received 25 October 2001; published 12 February 2002)

The NuTeV Collaboration has extracted the electroweak parameter $\sin^2\theta_W$ from the measurement of the ratios of neutral current to charged current ν and $\overline{\nu}$ cross sections. Our value, $\sin^2\theta_W{}^{(\text{on-shell})} = 0.2277 \pm 0.0013(\text{stat}) \pm 0.0009(\text{syst})$, is 3 standard deviations above the standard model prediction. We also present a model independent analysis of the same data in terms of neutral-current quark couplings.

DOI: 10.1103/PhysRevLett.88.091802 PACS numbers: 12.15.Ji, 12.15.Mm, 13.15.+g

Neutrino-nucleon scattering is one of the most precise probes of the weak neutral current. The Lagrangian for weak neutral current ν-q scattering can be written as

$$\mathcal{L} = -\frac{G_F\rho_0}{\sqrt{2}}[\overline{\nu}\gamma^\mu(1-\gamma^5)\nu] \times [\epsilon_L^q\overline{q}\gamma_\mu(1-\gamma^5)q + \epsilon_R^q\overline{q}\gamma_\mu(1+\gamma^5)q], \quad (1)$$

where deviations from $\rho_0 = 1$ describe nonstandard sources of SU(2) breaking, and $\epsilon_{L,R}^q$ are the chiral quark couplings. For the weak charged current, $\epsilon_L^q = I_{\text{weak}}^{(3)}$ and $\epsilon_R^q = 0$, but for the neutral current ϵ_L^q and ϵ_R^q each contain an additional term, $-Q\sin^2\theta_W$, where Q is the quark's electric charge in units of e. By measuring ratios of the charged and neutral current processes on a hadronic target, one can thus extract $\sin^2\theta_W$ and ρ_0.

In the context of the standard model, this measurement of $\sin^2\theta_W$ is comparable in precision to direct measurements of M_W. Outside of the standard model, neutrino-nucleon scattering provides one of the most precise constraints on the weak couplings of light quarks, and tests the validity of electroweak theory in a range of momentum transfer far from M_Z. This process is also sensitive to nonstandard interactions, including possible contributions from leptoquark and Z' exchange [1].

The ratio of neutral current to charged current cross sections for either ν or $\overline{\nu}$ scattering from isoscalar targets of u and d quarks can be written as [2]

$$R^{\nu(\overline{\nu})} \equiv \frac{\sigma(\overline{\nu}N \to \overline{\nu}X)}{\sigma(\overline{\nu}N \to \ell^{-(+)}X)} = (g_L^2 + r^{(-1)}g_R^2), \quad (2)$$

where

$$r \equiv \frac{\sigma(\overline{\nu}N \to \ell^+X)}{\sigma(\nu N \to \ell^-X)} \sim \frac{1}{2}, \quad (3)$$

and $g_{L,R}^2 = (\epsilon_{L,R}^u)^2 + (\epsilon_{L,R}^d)^2$. Corrections to Eq. (2) result from the presence of heavy quarks in the sea, the production of heavy quarks in the target, higher order terms in the cross section, and any isovector component of the light quarks in the target. In particular, in the case where a final-state charm quark is produced from a d or s quark in the nucleon, there are large uncertainties resulting from the mass suppression of the charm quark. This uncertainty has limited the precision of previous measurements of electroweak parameters in neutrino-nucleon scattering [3–5].

To reduce the effect of uncertainties resulting from charm production, Paschos and Wolfenstein [6] suggested consideration of the observable:

$$R^- \equiv \frac{\sigma(\nu_\mu N \to \nu_\mu X) - \sigma(\overline{\nu}_\mu N \to \overline{\nu}_\mu X)}{\sigma(\nu_\mu N \to \mu^- X) - \sigma(\overline{\nu}_\mu N \to \mu^+ X)} = \frac{R^\nu - rR^{\overline{\nu}}}{1-r} = (g_L^2 - g_R^2). \quad (4)$$

R^- is more difficult to measure than R^ν, primarily because the neutral-current scatterings of ν and $\overline{\nu}$ yield identical observed final states which can be distinguished only through *a priori* knowledge of the initial state neutrino.

Method.—High-purity ν and $\overline{\nu}$ beams were provided by the Sign Selected Quadrupole Train (SSQT) beam line at the Fermilab Tevatron during the 1996–1997 fixed target run. Neutrinos were produced from the decay of pions and kaons resulting from interactions of 800 GeV protons in a BeO target. Dipole magnets immediately downstream of

the proton target bent pions and kaons of specified charge in the direction of the NuTeV detector, while oppositely charged and neutral mesons were stopped in beam dumps. The resulting beam was almost pure ν or $\overline{\nu}$, depending on the charge of the parent mesons. Antineutrino interactions comprised 0.03% of the neutrino beam events, and neutrino interactions 0.4% of the antineutrino beam events. In addition, the beams of almost pure muon neutrinos contained a small component of electron neutrinos (mostly from $K^{\pm}_{e3}$ decays) which created 1.7% of the observed interactions in the neutrino beam and 1.6% in the antineutrino beam.

Neutrino interactions were observed in the NuTeV detector [7], located 1450 m downstream of the proton target. The detector consisted of an 18 m long, 690 ton steel-scintillator target, followed by an iron-toroid spectrometer. The target calorimeter was composed of 168 (3 m $\times$ 3 m $\times$ 5.1 cm) steel plates interspersed with liquid scintillation counters (spaced every two plates) and drift chambers (spaced every four plates). The scintillation counters provided triggering information as well as a measurement of the longitudinal interaction vertex, event length, and energy deposition. The mean position of hits in the drift chambers established the transverse vertex for the event. The toroid spectrometer, used to determine muon charge and momentum, also provided a measurement of the muon neutrino flux in charged current events. In addition, the detector was calibrated continuously through exposure to beams of hadrons, electrons, and muons over a wide energy range [7].

For inclusion in this analysis, events are required to deposit at least 20 GeV of visible energy ($E_{\rm cal}$) in the calorimeter, which ensures full efficiency of the trigger, allows an accurate vertex determination, and reduces cosmic ray background. Events with $E_{\rm cal} > 180$ GeV are also removed. Fiducial criteria restrict the location of the neutrino interaction to the central region of the calorimeter. The chosen fiducial volume enhances interactions that are contained in the calorimeter, and minimizes the fraction of events from electron neutrinos or non-neutrino sources. After all selections, the resulting data sample consists of 1.62×10^6 ν and 0.35×10^6 $\overline{\nu}$ events with a mean visible energy ($E_{\rm cal}$) of 64 and 53 GeV, respectively.

In order to extract $\sin^2\theta_W$, the observed neutrino events must be separated into charged current (CC) and neutral current (NC) candidates. Both CC and NC neutrino interactions initiate a cascade of hadrons in the target that is registered in both the scintillation counters and drift chambers. Muon neutrino CC events are distinguished by the presence of a final state muon that typically penetrates beyond the hadronic shower and deposits energy in a large number of consecutive scintillation counters. NC events usually have no final state muon and deposit energy over a range of counters typical of a hadronic shower.

These differing event topologies enable the statistical separation of CC and NC neutrino interactions based solely on event length. For each event, this length is defined by the number of scintillation counters between the interaction vertex and the last counter consistent with at least single muon energy deposition. Events with a "long" length are identified as CC candidates, while "short" events are most likely NC induced. The separation between short and long events is made at 16 counters ($\sim$1.7 m of steel) for $E_{\rm cal} < 60$ GeV, at 17 counters for $60 \leq E_{\rm cal} < 100$ GeV, and otherwise at 18 counters. The ratios of short to long events measured in the ν and $\overline{\nu}$ beams are

$$R^{\nu}_{\rm exp} = 0.3916 \pm 0.0007 \quad \text{and} \quad R^{\overline{\nu}}_{\rm exp} = 0.4050 \pm 0.0016\,. \tag{5}$$

$\sin^2\theta_W$ can be extracted directly from these measured ratios by comparison with a detailed Monte Carlo simulation of the experiment. The Monte Carlo must include neutrino fluxes, the neutrino cross sections, and a detailed description of the detector response.

A detailed beam simulation is used to predict the ν and $\overline{\nu}$ fluxes. In particular, a precise determination of the electron neutrino contamination in the beam is essential. The ratios $R^{\nu}_{\rm exp}$ and $R^{\overline{\nu}}_{\rm exp}$ increase in the presence of electron neutrinos in the data sample because electron neutrino charged current interactions are almost always identified as neutral-current interactions.

The bulk of the observed electron neutrinos, 93% in the ν beam and 70% in the $\overline{\nu}$ beam, result from $K^{\pm}_{e3}$ decays. The beam simulation can be tuned with high accuracy to describe ν_e and $\overline{\nu}_e$ production from charged kaon decay because the $K^{\pm}$ contribution is constrained by the observed ν_μ and $\overline{\nu}_\mu$ fluxes. Because of the precise alignment of the beam line elements and the low acceptance for neutral particles, the largest uncertainty in the calculated electron neutrino flux is the 1.4% uncertainty in the $K^{\pm}_{e3}$ branching ratio [8]. Other sources of electron neutrinos include neutral kaons, charmed hadrons, and muon decays, all of which have larger fractional uncertainties (10%–20%). Finally, small uncertainties in the calibration of the calorimeter and the muon toroid affect the muon and electron neutrino flux measurements. Additional constraints from the data, including direct measurements of ν_e and $\overline{\nu}_e$ charged current events and measurements of ν_μ events in the $\overline{\nu}_\mu$ beam (which also result from charm and neutral kaon decay) [9] reduce the electron neutrino uncertainties. At the highest energies ($E_\nu > 350$ for ν_μ and $E_\nu > 180$ for ν_e), the beam Monte Carlo underpredicts the measured flux and is thus not used.

Neutrino-nucleon deep inelastic scattering processes are simulated using a leading order (LO) model for the cross section augmented with longitudinal scattering and higher twist terms. The cross-section parametrization incorporates LO parton distribution functions (PDFs) from charged current data measured, obtained with the same target and model as used in this experiment [10,11]. These PDFs include an external constraint on $\sigma^{\overline{\nu}}/\sigma^{\nu}$ [11], and make the standard assumptions that $\overline{u}_p(x) = \overline{d}_n(x)$, $\overline{d}_p(x) = \overline{u}_n(x)$, and $s(x) = \overline{s}(x)$. Small modifications adjust the parton densities to produce the inherent up-down

quark asymmetry consistent with muon scattering [12] and Drell-Yan [13] data. A LO analysis of $\overset{(-)}{\nu} N \to \mu^+\mu^- X$ events [14] provides the shape and magnitude of the strange sea. Mass suppression from charged current charm production is modeled using a LO slow rescaling formalism [15] whose parameters and uncertainties come from the same high-statistics $\mu^+\mu^-$ sample. A model for $c\bar{c}$ production is chosen to match EMC data [16]; it is assigned a 100% uncertainty. A global analysis [17] provides a parametrization of the longitudinal structure function, R_L, which is allowed to vary within its experimental and theoretical uncertainties. QED and electroweak radiative corrections to the scattering cross section are applied using code supplied by Bardin [18] and from V6.34 of ZFITTER [19], and uncertainties are estimated by varying the parameters in these corrections.

The Monte Carlo must also accurately simulate the response of the detector to the products of neutrino interactions in the target. The critical parameters that must be modeled are the calorimeter response to muons, the measurement of the position of the neutrino interactions, and the range of hadronic showers in the calorimeter. Precise determination of these effects is made through extensive use of both neutrino and calibration beam data. Measured detector parameters are then varied within their uncertainties to estimate systematic errors.

An important test of the simulation is its ability to predict the length distribution of events. Figure 1 shows event length distributions in the final data sample compared to the Monte Carlo prediction for our measured value of $\sin^2\theta_W$. Events reaching the toroid, which comprise about 80% of the CC sample, have been left out for clarity, but are included in the normalization of the data. Excellent agreement within uncertainties is observed in the overlap region of long NC and short CC events.

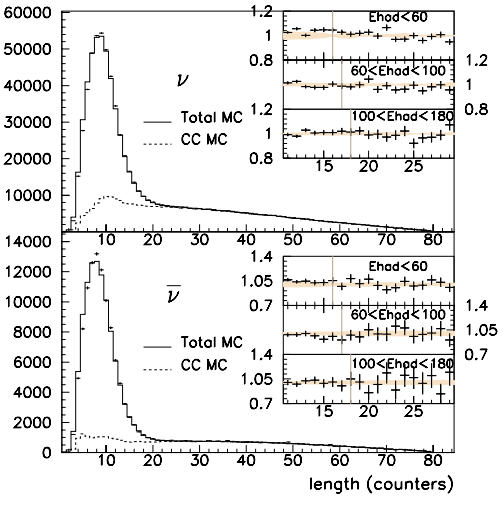

FIG. 1. Comparison of ν and $\overline{\nu}$ event length distributions in data and Monte Carlo (MC). The MC prediction for CC events is shown separately. Insets show data/MC ratio comparisons in the region of the length cut with bands to indicate the 1σ systematic uncertainty in this ratio.

Results.—Having precisely determined R^{ν}_{exp}, $R^{\overline{\nu}}_{\text{exp}}$, and their predicted values as a function of electroweak parameters $\sin^2\theta_W$ and ρ_0, we proceed to extract the best values of $\sin^2\theta_W$ and ρ_0. This is done by means of a fit that also includes the slow-rescaling mass for charm production (m_c) with its *a priori* constraint from $\mu^+\mu^-$ data [14]. $R^{\overline{\nu}}$ is much less sensitive to $\sin^2\theta_W$ than R^{ν}, but both are sensitive to m_c and ρ_0.

When fitting with the assumption $\rho_0 = 1$, $\sin^2\theta_W$ is simultaneously fit with the slow-rescaling parameter m_c. Like an explicit calculation of R^-, this procedure reduces uncertainties related to sea quark scattering as well as many experimental systematics common to both ν and $\overline{\nu}$ samples. Statistical and systematic uncertainties in the $\sin^2\theta_W$ fit and in the comparison of R^{ν} and $R^{\overline{\nu}}$ with the Monte Carlo prediction are shown in Table I.

The single parameter fit for $\sin^2\theta_W$ measures

$$\sin^2\theta_W{}^{(\text{on-shell})} = 0.2277 \pm 0.0013(\text{stat}) \pm 0.0009(\text{syst}) - 0.000\,22 \times \left(\frac{M^2_{\text{top}} - (175\ \text{GeV})^2}{(50\ \text{GeV})^2}\right) + 0.000\,32 \times \ln\left(\frac{M_{\text{Higgs}}}{150\ \text{GeV}}\right). \quad (6)$$

Leading terms in the one-loop electroweak radiative corrections [18] produce the small residual dependence of our result on M_{top} and M_{Higgs}. The prediction from the standard model with parameters determined by a fit to other electroweak measurements is 0.2227 ± 0.0004 [20,21], approximately 3σ from our result. In the on-shell scheme, where $\sin^2\theta_W \equiv 1 - M_W^2/M_Z^2$, and where M_W and M_Z are the physical gauge boson masses, our result implies $M_W = 80.14 \pm 0.08$ GeV. The world average of the direct measurements of M_W is 80.45 ± 0.04 GeV [20].

For the simultaneous fit to $\sin^2\theta_W$ and ρ_0, we obtain

$$\rho_0 = 0.9983 \pm 0.0040, \qquad \sin^2\theta_W = 0.2265 \pm 0.0031, \quad (7)$$

with a correlation coefficient of 0.85 between the two parameters. This suggests one but not both of $\sin^2\theta_W{}^{(\text{on-shell})}$ or ρ_0 may be consistent with expectations. We have also performed a two-parameter fit in terms of the isoscalar combinations [22] of effective [23] neutral-current quark couplings $(g^{\text{eff}}_{L,R})^2 = (u^{\text{eff}}_{L,R})^2 + (d^{\text{eff}}_{L,R})^2$ at $\langle q^2\rangle \approx -20\ \text{GeV}^2$, which yields

$$(g^{\text{eff}}_L)^2 = 0.3005 \pm 0.0014, \qquad (g^{\text{eff}}_R)^2 = 0.0310 \pm 0.0011, \quad (8)$$

with a negligibly small correlation coefficient. The predicted values from standard model parameters corresponding to the electroweak fit described earlier [20,21] are $(g^{\text{eff}}_L)^2 = 0.3042$ and $(g^{\text{eff}}_R)^2 = 0.0301$.

TABLE I. Uncertainties for both the single parameter $\sin^2\theta_W$ fit and for the comparison of R^ν and $R^{\overline{\nu}}$ with model predictions.

Source of uncertainty	$\delta \sin^2\theta_W$	δR^ν	$\delta R^{\overline{\nu}}$
Data statistics	0.001 35	0.000 69	0.001 59
Monte Carlo statistics	0.000 10	0.000 06	0.000 10
Total statistics	0.001 35	0.000 69	0.001 59
$\nu_e, \overline{\nu}_e$ flux	0.000 39	0.000 25	0.000 44
Energy measurement	0.000 18	0.000 15	0.000 24
Shower length model	0.000 27	0.000 21	0.000 20
Counter efficiency, noise, size	0.000 23	0.000 14	0.000 06
Interaction vertex	0.000 30	0.000 22	0.000 17
Total experimental	0.000 63	0.000 44	0.000 57
Charm production, strange sea	0.000 47	0.000 89	0.001 84
Charm sea	0.000 10	0.000 05	0.000 04
$\sigma^{\overline{\nu}}/\sigma^\nu$	0.000 22	0.000 07	0.000 26
Radiative corrections	0.000 11	0.000 05	0.000 06
Nonisoscalar target	0.000 05	0.000 04	0.000 04
Higher twist	0.000 14	0.000 12	0.000 13
R_L	0.000 32	0.000 45	0.001 01
Total model	0.000 64	0.001 01	0.002 12
Total uncertainty	0.001 62	0.001 30	0.002 72

In conclusion, NuTeV has made precise determinations of the electroweak parameters through separate measurements of R^ν and $R^{\overline{\nu}}$. We find a significant disagreement with the standard model expectation for $\sin^2\theta_W{}^{(\text{on-shell})}$. In a model-independent analysis, this result suggests a smaller left-handed neutral current coupling to the light quarks than expected.

We thank the staff of the Fermilab Beams, Computing and Particle Physics Divisions for design, construction, and operational assistance during the NuTeV experiment. This work was supported by the U.S. Department of Energy, the National Science Foundation, and the Alfred P. Sloan Foundation.

[1] P. Langacker *et al.,* Rev. Mod. Phys. **64**, 87 (1991).
[2] C. H. Llewellyn Smith, Nucl. Phys. **B228**, 205 (1983).
[3] K. S. McFarland *et al.,* Eur. Phys. J. C **1**, 509 (1998).
[4] A. Blondel *et al.,* Z. Phys. C **45**, 361 (1990).
[5] J. Allaby *et al.,* Z. Phys. C **36**, 611 (1985).
[6] E. A. Paschos and L. Wolfenstein, Phys. Rev. D **7**, 91 (1973).
[7] NuTeV Collaboration, D. A. Harris *et al.,* Nucl. Instrum. Methods Phys. Res., Sect. A **447**, 377 (2000).
[8] Particle Data Group Collaboration, D. E. Groom *et al.,* Eur. Phys. J. C **15**, 1 (2000).
[9] A. Alton *et al.,* Phys. Rev. D **64**, 012002 (2001).
[10] A. J. Buras and K. J. F. Gaemers, Nucl. Phys. **B132**, 249 (1978).
[11] U. K. Yang *et al.,* Phys. Rev. Lett. **86**, 2742 (2001).
[12] M. Arneodo *et al.,* Nucl. Phys. **B487**, 3 (1997).
[13] E. A. Hawker *et al.,* Phys. Rev. Lett. **80**, 3715 (1998).
[14] M. Goncharov *et al.,* Phys. Rev. D **64**, 112006 (2001).
[15] R. M. Barnett, Phys. Rev. Lett. **36**, 1163 (1976).
[16] J. J. Aubert *et al.,* Nucl. Phys. **B213**, 31 (1983).
[17] L. W. Whitlow, SLAC-REPORT-357, 1990, p. 109.
[18] D. Bardin and V. A. Dokuchaeva, Report No. JINR-E2-86-260, 1986.
[19] D. Bardin *et al.,* Comput. Phys. Commun. **133**, 229 (2001).
[20] Report No. CERN-EP/2001-98; hep-ex/0112021.
[21] M. Gruenewald (private communication) for the fit of Ref. [20] without neutrino-nucleon scattering data included.
[22] Because of the asymmetry between the strange and charm seas and the slight excess of neutrons in our target, this result is sensitive only to isovector combinations at about 3% of the sensitivity of isoscalar couplings.
[23] Effective couplings are those which describe observed experimental rates when the processes described by Eq. (1) are calculated without electroweak radiative corrections.

On the Effect of Asymmetric Strange Seas and Isospin-Violating Parton Distribution Functions on $\sin^2\theta_W$ Measured in the NuTeV Experiment

G. P. Zeller[5], K. S. McFarland[8,3], T. Adams[4], A. Alton[4], S. Avvakumov[8], L. de Barbaro[5], P. de Barbaro[8], R. H. Bernstein[3], A. Bodek[8], T. Bolton[4], J. Brau[6], D. Buchholz[5], H. Budd[8], L. Bugel[3], J. Conrad[2], R. B. Drucker[6], B. T. Fleming[2], R. Frey[6], J.A. Formaggio[2], J. Goldman[4], M. Goncharov[4], D. A. Harris[8], R. A. Johnson[1], J. H. Kim[2], S. Koutsoliotas[2], M. J. Lamm[3], W. Marsh[3], D. Mason[6], J. McDonald[7], C. McNulty[2], D. Naples[7], P. Nienaber[3], A. Romosan[2], W. K. Sakumoto[8], H. Schellman[5], M. H. Shaevitz[2], P. Spentzouris[2], E. G. Stern[2], N. Suwonjandee[1], M. Tzanov[7], M. Vakili[1], A. Vaitaitis[2], U. K. Yang[8], J. Yu[3], and E. D. Zimmerman[2]

[1]*University of Cincinnati, Cincinnati, OH 45221*
[2]*Columbia University, New York, NY 10027*
[3]*Fermi National Accelerator Laboratory, Batavia, IL 60510*
[4]*Kansas State University, Manhattan, KS 66506*
[5]*Northwestern University, Evanston, IL 60208*
[6]*University of Oregon, Eugene, OR 97403*
[7]*University of Pittsburgh, Pittsburgh, PA 15260*
[8]*University of Rochester, Rochester, NY 14627*

(Dated: June 3, 2002)

The NuTeV collaboration recently reported a value of $\sin^2\theta_W$ measured in neutrino-nucleon scattering that is 3 standard deviations above the standard model prediction. This result is derived assuming that (1) the strange sea is quark-antiquark symmetric, $s(x) = \overline{s}(x)$, and (2) up and down quark distributions are symmetric under the simultaneous interchange of $u \leftrightarrow d$ and $p \leftrightarrow n$. We report the impact of violations of these symmetries on $\sin^2\theta_W$ and discuss the theoretical and experimental constraints on such asymmetries.

PACS numbers: 11.30.Hv,12.15.Mm, 12.38.Qk, 13.15.+g

I. INTRODUCTION AND FORMALISM

Based on measurements of neutral current and charged current neutrino-nucleon scattering in both neutrino and antineutrino beams, the NuTeV collaboration recently reported a measurement of $\sin^2\theta_W^{(\mathrm{on-shell})}$. The result [1],

$$\begin{aligned}\sin^2\theta_W^{(\mathrm{on-shell})} &= 0.2277 \pm 0.0013(\mathrm{stat.}) \pm 0.0009(\mathrm{syst.}) \\ &- 0.00022 \times \left(\frac{M_{top}^2 - (175\,\mathrm{GeV})^2}{(50\,\mathrm{GeV})^2}\right) \\ &+ 0.00032 \times \ln\left(\frac{M_{Higgs}}{150\,\mathrm{GeV}}\right), \end{aligned} \quad (1)$$

is approximately 3 standard deviations above the expected value of 0.2227 ± 0.0004 [2, 3].

Ratios of neutral current to charged current cross sections on isoscalar targets of u and d quarks are experimental observables that can be related to fundamental electroweak parameters. Before NuTeV, high statistics neutrino experiments measured $\sin^2\theta_W$ using the Llewellyn Smith cross section ratios [4]:

$$R^{\nu(\overline{\nu})} \equiv \frac{\sigma(\overset{(-)}{\nu} N \to \overset{(-)}{\nu} X)}{\sigma(\overset{(-)}{\nu} N \to \ell^{-(+)} X)} = g_L^2 + r^{(-1)} g_R^2, \quad (2)$$

where

$$r \equiv \frac{\sigma(\overline{\nu}N \to \ell^+ X)}{\sigma(\nu N \to \ell^- X)} \sim \frac{1}{2}, \quad (3)$$

and

$$\begin{aligned} g_L^2 &= (\epsilon_L^u)^2 + (\epsilon_L^d)^2 \\ &= \frac{1}{2} - \sin^2\theta_W + \frac{5}{9}\sin^4\theta_W, \\ g_R^2 &= (\epsilon_R^u)^2 + (\epsilon_R^d)^2 \\ &= \frac{5}{9}\sin^4\theta_W. \end{aligned} \quad (4)$$

For the experimental values of r and $\sin^2\theta_W$, it follows that R^ν is much more sensitive to $\sin^2\theta_W$ than is $R^{\overline{\nu}}$.

Inspired by the Paschos-Wolfenstein relationship [5]:

$$\begin{aligned} R^- &\equiv \frac{\sigma(\nu_\mu N \to \nu_\mu X) - \sigma(\overline{\nu}_\mu N \to \overline{\nu}_\mu X)}{\sigma(\nu_\mu N \to \mu^- X) - \sigma(\overline{\nu}_\mu N \to \mu^+ X)} \\ &= \frac{R^\nu - rR^{\overline{\nu}}}{1-r} = g_L^2 - g_R^2, \end{aligned} \quad (5)$$

NuTeV uses high statistics separated neutrino and antineutrino beams to measure $\sin^2\theta_W$ and thereby reduces its sensitivity to uncertainties in cross sections resulting from scattering off q-$\overline{q}$ symmetric quark seas. Using the separate neutrino and antineutrino data sets, NuTeV also extracts effective neutral current quark couplings, $(g_L^{\mathrm{eff}})^2$ and $(g_R^{\mathrm{eff}})^2$ [1].

Let $\langle q(x)\rangle$ denote the momentum distribution of a particular flavor of quark averaged over the nucleons in the NuTeV target, and let $\langle Q\rangle \equiv \int \langle q(x)\rangle dx$, the total momentum carried by quark flavor q. Let nucleon-specific quark momentum distributions be denoted by $q_p(x)$ and $q_n(x)$, with corresponding integrals Q_p and Q_n, respectively. Both the Llewellyn Smith and Paschos-Wolfenstein relationships assume $\langle U\rangle = \langle D\rangle$

and $\langle\overline{U}\rangle = \langle\overline{D}\rangle$. The Llewellyn Smith interpretation of R^ν assumes additionally that $\langle S\rangle = \langle\overline{S}\rangle = \langle C\rangle = \langle\overline{C}\rangle$ (clearly $\langle S\rangle = \langle C\rangle$ is experimentally not a good assumption), while the Paschos-Wolfenstein R^- formula assumes only $\langle S\rangle = \langle\overline{S}\rangle$ and $\langle C\rangle = \langle\overline{C}\rangle$.

The NuTeV $\sin^2\theta_W$ analysis accounts for the violations of the assumption that $\langle u(x)\rangle = \langle d(x)\rangle$ and $\langle\overline{u}(x)\rangle = \langle\overline{d}(x)\rangle$ which result from the excess of neutrons over protons in the target. From a material inventory of the NuTeV target calorimeter, we measure a $5.67 \pm 0.05\%$ fractional excess of neutrons over protons [6]. However, the NuTeV result assumes exact isospin symmetry in neutron and proton quark distributions, $\overset{(-)}{u}_p(x) = \overset{(-)}{d}_n(x)$, $\overset{(-)}{d}_p(x) = \overset{(-)}{u}_n(x)$. The NuTeV analysis assumes furthermore that $\langle s(x)\rangle = \langle\overline{s}(x)\rangle$ and $\langle c(x)\rangle = \langle\overline{c}(x)\rangle$. It has been pointed out that such assumptions, if incorrect, produce sizable shifts in the NuTeV $\sin^2\theta_W$ [7–10].

Although the NuTeV experiment does not exactly measure R^-, in part because it is not possible experimentally to measure neutral current reactions down to zero recoil energy, it is nevertheless illustrative to calculate the effect of these violations on R^-. Denote the neutron excess of the NuTeV target as $\delta N \equiv A - 2Z/A$ and the total valence momentum carried by the proton as $V_p = U_p - \overline{U}_p + D_p - \overline{D}_p$. Let the following

$$\begin{aligned}
\delta D_v &\equiv D_p - \overline{D}_p - U_n + \overline{U}_n \\
\delta U_v &\equiv U_p - \overline{U}_p - D_n + \overline{D}_n \\
\delta\overline{D} &\equiv \overline{D}_p - \overline{U}_n \\
\delta\overline{U} &\equiv \overline{U}_p - \overline{D}_n \\
\delta S &\equiv \langle S\rangle - \langle\overline{S}\rangle
\end{aligned} \tag{6}$$

denote deviations from the above symmetry assumptions. To first order in δN, δQ_v, $\delta\overline{Q}$ and δS, we obtain

$$\begin{aligned}
R^- \approx\ & \Delta_u^2 + \Delta_d^2 \\
& + \delta N\left(\frac{U_p - D_p}{U_p + D_p}\right)(3\Delta_u^2 + \Delta_d^2) \\
& + \frac{\delta U_v - \delta D_v}{2V_p}(3\Delta_u^2 + \Delta_d^2) \\
& + \frac{\delta S}{V_p}(2\Delta_d^2 - 3(\Delta_d^2 + \Delta_u^2)\epsilon_c),
\end{aligned} \tag{7}$$

where $\Delta_{u,d}^2 = (\epsilon_L^{u,d})^2 - (\epsilon_R^{u,d})^2$ and where ϵ_c denotes the ratio of the scattering cross section from the strange sea including kinematic suppression of heavy charm production to that without kinematic suppression. In this calculation, we assume the massless quark-parton model which implies no longitudinal cross section, no target mass effects, and we also assume $\langle C\rangle = \langle\overline{C}\rangle = 0$.

As already noted, to extract $\sin^2\theta_W$, NuTeV does not measure directly R^-, but rather measures ratios of experimental candidates within kinematic criteria and compares this to a full Monte Carlo simulation which accounts for neutral current and charged current cross-talk, non-quark-parton model contributions to the cross section, radiative corrections, electron neutrino backgrounds, and detector resolution [1]. Therefore, the NuTeV $\sin^2\theta_W$ measurement does not depend on these symmetry violating terms in the way that Equations 5 and 7 would suggest.

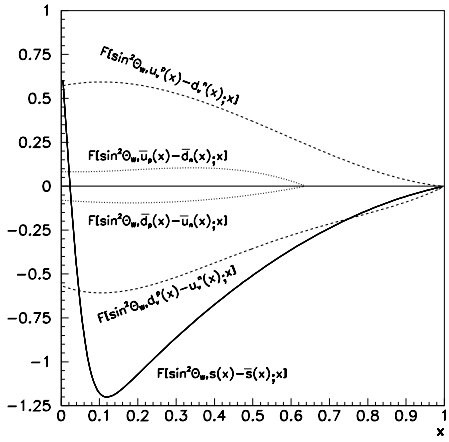

FIG. 1: The functionals describing the shift in the NuTeV $\sin^2\theta_W$ caused by not correcting the NuTeV analysis for isospin violating u and d valence and sea distributions or for $\langle s(x)\rangle \neq \langle\overline{s}(x)\rangle$. The shift in $\sin^2\theta_W$ is determined by convolving the asymmetric momentum distribution with the plotted functional.

To examine the exact effect of various symmetry violations on the NuTeV analysis, we first define a functional $F[\mathcal{E}, \delta; x]$ such that the shift in an experimental quantity, $\mathcal{E}$, due to a symmetry violating quark fractional momentum distribution, $\delta(x)$, is given by:

$$\Delta\mathcal{E} = \int_0^1 F[\mathcal{E}, \delta; x]\,\delta(x)\,dx. \tag{8}$$

All of the details of the NuTeV Monte Carlo simulation and measurement can be parameterized in terms of $F[\mathcal{E}, \delta; x]$, and therefore, this formalism provides a way to determine the shift in the NuTeV measurement for arbitrary symmetry violation in PDFs. Figures 1 and 2 show $F[\mathcal{E}, \delta; x]$ for an isospin symmetry violating u and d valence and sea and for $\langle s(x)\rangle \neq \langle\overline{s}(x)\rangle$. Figure 1 shows the functionals for the NuTeV measurement of $\sin^2\theta_W$, while Figure 2 shows the corresponding functionals for $(g_L^{\rm eff})^2$ and $(g_R^{\rm eff})^2$.

II. ASYMMETRIC STRANGE SEA

If the strange sea is generated by purely perturbative QCD processes, then neglecting electromagnetic effects, one expects $\langle s(x)\rangle = \langle\overline{s}(x)\rangle$. However, it has been noted that non-perturbative QCD effects can generate a significant momentum asymmetry between the strange and anti-strange seas

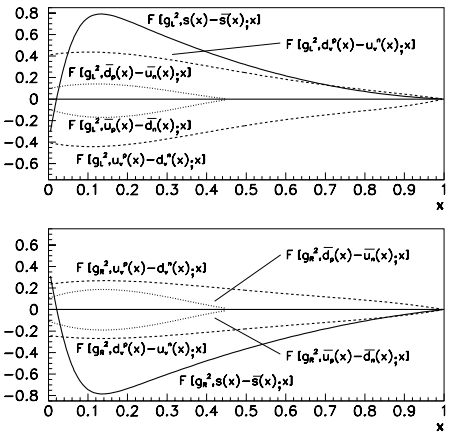

FIG. 2: The functionals describing the shifts in the NuTeV $(g_L^{\rm eff})^2$ and $(g_R^{\rm eff})^2$ caused by not correcting the NuTeV analysis for isospin violating u and d valence and sea distributions or for $\langle s(x)\rangle \neq \langle \overline{s}(x)\rangle$. The shifts in $(g_L^{\rm eff})^2$ and $(g_R^{\rm eff})^2$ are determined by convolving the asymmetric momentum distribution with the plotted functional.

[11–14]. Lending weight to this possibility, a joint fit to CDHS neutrino charged-current inclusive cross sections [16] (but not including CCFR [17] and NuTeV data or neutrino dimuon cross sections) and charged lepton structure function data reports some improvement in their fits if they allow for an asymmetry in the strange sea at high x [15]. The CCFR and CDHS charged current neutrino cross-sections differ significantly at high x where this joint fit finds a large strange sea asymmetry, $s \gg \overline{s}$.

By measuring the processes $\nu_N, \overline{\nu}_N \to \mu^+\mu^- X$ the CCFR and NuTeV experiments constrain the difference between the momentum distributions of the strange and anti-strange seas. For studying the effect on the NuTeV $\sin^2\theta_W$, it is important to study such effects within the same PDF formalism and corresponding cross sections as were used in the measurement itself [1]. In this enhanced leading order cross section model, the CCFR/NuTeV $\nu, \overline{\nu}$ dimuon data were fit [18] to the following form for the strange and anti-strange seas [23]:

$$\begin{aligned} \langle s(x)\rangle &= \kappa \frac{\langle \overline{u}(x)\rangle + \langle \overline{d}(x)\rangle}{2}(1-x)^{\alpha} \\ \langle \overline{s}(x)\rangle &= \overline{\kappa} \frac{\langle \overline{u}(x)\rangle + \langle \overline{d}(x)\rangle}{2}(1-x)^{\overline{\alpha}}, \end{aligned} \tag{9}$$

obtaining central values of

$$\begin{pmatrix} \kappa \\ \overline{\kappa} \\ \alpha \\ \overline{\alpha} \end{pmatrix} = \begin{pmatrix} .352 \\ .405 \\ -0.77 \\ -2.04 \end{pmatrix} \tag{10}$$

and a covariance matrix[24] incorporating both statistical and systematic uncertainties on these parameters:

$$\begin{pmatrix} 0.0034 & 0.0027 & -0.028 & -0.007 \\ 0.0027 & 0.0031 & -0.024 & -0.008 \\ -0.028 & -0.024 & 0.78 & 0.18 \\ -0.007 & -0.008 & 0.18 & 0.29 \end{pmatrix}. \tag{11}$$

Within this particular model, the measurement implies a *negative* asymmetry,

$$\langle S\rangle - \langle \overline{S}\rangle = -0.0027 \pm 0.0013, \tag{12}$$

and a resulting increase in the NuTeV value of $\sin^2\theta_W$,

$$\Delta\sin^2\theta_W = +0.0020 \pm 0.0009. \tag{13}$$

The initial NuTeV measurement, which assumes $\langle s(x)\rangle = \langle \overline{s}(x)\rangle$, becomes $\sin^2\theta_W = 0.2297 \pm 0.0019$. Hence, if we use the experimental measurement of the strange sea asymmetry, the discrepancy with the standard model is increased to 3.7σ significance.

A recent calculation [10] claims that a *positive* strange sea asymmetry of $\langle S\rangle - \langle \overline{S}\rangle = +0.0020$ could explain half of the NuTeV discrepancy ($\Delta\sin^2\theta_W = -0.0026$). It should be noted, however, that this is an overestimate, as Figure 1 makes clear, due to the fact that charged current charm suppression threshold effects have been neglected in their analysis, and because NuTeV does not exactly measure R^- [25].

Reference [15] reports favoring a significant positive strange sea asymmetry ($S - \overline{S} \sim +0.0020$) at high x. A fit to the form assumed in Equation 9 does not necessarily exclude such an asymmetry as it is dominated by data at low x. The asymmetry of Reference [15] would imply at least a 5% increase in the total ν dimuon cross section in the region $x > 0.5$. However, NuTeV has looked for such an excess at high x and excludes additional dimuon sources larger than 0.2% (0.6%) in the ν ($\overline{\nu}$) data at 90% confidence [18].

III. ISOSPIN VIOLATING PDFS

Several recent classes of non-perturbative models predict isospin violation in the nucleon [7–9]. We evaluate the shift in the NuTeV value of $\sin^2\theta_W$ under the assumption that the asymmetry occurs in nature and is not corrected for in the NuTeV analysis. The earliest estimation in the literature, a bag model calculation [7], predicts large valence asymmetries of opposite sign in $u_p - d_n$ and $d_p - u_n$ at all x, which would produce a shift in the NuTeV $\sin^2\theta_W$ of -0.0020. However, this estimate neglects a number of effects, and a complete calculation by Thomas *et al.* [8] concludes that asymmetries at very high x are larger, but the asymmetries at moderate x are smaller and of opposite sign at low x, thereby reducing the shift in $\sin^2\theta_W$ to a negligible -0.0001. Finally, the effect is also evaluated in the Meson Cloud model [9], and there the asymmetries are much smaller at all x, resulting in a modest shift in the NuTeV $\sin^2\theta_W$ of $+0.0002$.

The calculation of Thomas *et al.* [8] is particularly useful in evaluating uncertainties because it decomposes isospin

violating effects into different parts that are driven by experimental or theoretical inputs. The largest contributions to a shift in $\sin^2\theta_W$ in this calculation come from the single quark ($m_d - m_u \sim 4$ MeV) and nucleon ($m_n - m_p \approx 1.29$ MeV) mass differences. The former has a significant theoretical uncertainty, and we assign a fractional error of 25% to this source of isospin violation based on the uncertainty in $m_d - m_u$[19, 20]; such an uncertainty translates to a 0.0001 uncertainty in the NuTeV $\sin^2\theta_W$. Another contribution in this calculation with large theoretical uncertainties is the effect of diquark ($m_{dd} - m_{uu}$) mass differences. This causes isospin breaking predominantly at high x where both the PDFs are small *and* the effect on the NuTeV measurement is negligible. The uncertainty is therefore significantly smaller than that from the single quark mass shift.

In general, nuclear effects can also cause isospin-breaking, thereby producing $\langle U\rangle \neq \langle D\rangle$ in the NuTeV target, which is primarily iron. While less theoretically certain, one estimate of the effect exists [21] and would predict a modest increase in the NuTeV $\sin^2\theta_W$.

Although a particular nucleon or nuclear charge symmetry violation model could account for the NuTeV discrepancy with the standard model, such models, in their attempt to explain the NuTeV $\sin^2\theta_W$, must be evaluated in the context of a global fit to all experimental data derived from any such asymmetry assumptions because they may disagree with existing data [22].

IV. CONCLUSIONS

The fact that NuTeV does not measure directly R^- or exact ratios of neutral to charged current cross sections makes it difficult to predict the effect of parton level symmetry violations. Hence, we present a framework for evaluating the effects of both isospin violating u and d parton densities and asymmetric strange seas on the NuTeV measurements of $\sin^2\theta_W$, $(g_L^{\rm eff})^2$, and $(g_R^{\rm eff})^2$. While it is possible, in principle, to induce sizable shifts in the NuTeV $\sin^2\theta_W$ with variations in the former, the joint CCFR/NuTeV neutrino and anti-neutrino dimuon data limit possible charge asymmetry in the strange sea. In fact, relaxing the restriction that $\langle s(x)\rangle = \langle \overline{s}(x)\rangle$ in the LO fit to CCFR/NuTeV dimuon data increases the NuTeV discrepancy with the standard model.

Acknowledgments

This work was supported by the U.S. Department of Energy, the National Science Foundation, and the Alfred P. Sloan Foundation.

[1] G. P. Zeller *et al.*, Phys. Rev. Lett. **88**, 091802 (2002).
[2] "A Combination of Preliminary Electroweak Measurements and Constraints on the Standard Model", CERN-EP/2001-98, hep-ex/0112021.
[3] M. Gruenewald, private communication, for the fit of Ref. [2] without neutrino-nucleon scattering data included.
[4] C. H. Llewellyn Smith, Nucl. Phys. **B228**, 205 (1983).
[5] E. A. Paschos and L. Wolfenstein, Phys. Rev. **D7**, 91 (1973).
[6] Bruce King, Ph.D. thesis, Columbia University, 1993 (unpublished).
[7] E. Sather, Phys. Lett. **B274**, 433 (1992).
[8] E. N. Rodionov, A. W. Thomas, and J. T. Londergan, Mod. Phys. Lett. A **9**, 1799 (1994).
[9] F. Cao and A. I. Signal, Phys. Rev. **C62**, 015203 (2000).
[10] S. Davidson, S. Forte, P. Gambino, N. Rius, and A. Strumia, hep-ph/0112302.
[11] A.I. Signal and A.W. Thomas, Phys. Lett. **B191**, 205 (1987).
[12] M. Burkardt and B. J. Warr, Phys. Rev. **D45**, 958 (1992).
[13] S. Brodsky and B. Ma, Phys. Lett. **B381**, 317 (1996).
[14] W. Melnitchouk and M. Malheiro, Phys. Lett. **B451**, 224 (1999).
[15] V. Barone *et al.*, Eur. Phys. Jour. **C12**, 243 (2000).
[16] P. Berge *et al.*, Zeit. Phys. **C49**, 607 (1991).
[17] U. K. Yang *et al.*, Phys. Rev. Lett. **86**, 2742 (2001).
[18] M. Goncharov *et al.*, Phys. Rev. **D64**, 112006 (2001).
[19] J. Gasser and H. Leutwyler, Phys. Rep. **87**, 77 (1982).
[20] R. P. Bickerstaff and A. W. Thomas, Phys. Rev. **D25**, 1869 (1982).
[21] R. M. Davidson and M. Burkardt, Phys. Lett. **B403**, 134 (1997).
[22] A. Bodek *et al.*, Phys. Rev. Lett. **83**, 2892 (1999).
[23] At $Q^2 = 16$ GeV^2, the average Q^2 of the NuTeV data used in the $\sin^2\theta_W$ analysis, the NuTeV $(\langle\overline{u}(x)\rangle + \langle\overline{d}(x)\rangle)/2$ can be parameterized as $e^{-0.75-150x} + e^{-1.33-7.7x-8.1x^2}$ over the region $0 < x < 0.6$. NuTeV determines its leading order PDFs from fits to CCFR cross section data including external constraints [1, 17].
[24] This covariance matrix is from the fit of Ref. 18, although the matrix is not given in the original paper.
[25] The inclusion of an asymmetric strange sea induces a larger and opposite sign shift in $R^{\overline{\nu}}$ compared to the shift in R^{ν}. Because the NuTeV result is less sensitive to $R^{\overline{\nu}}$ than is R^-, the effect is reduced at all x. The large suppression of charged-current scattering from the low x strange sea explains the change of sign in the shift in $\sin^2\theta_W$ at very low x.

References

[1] S. Weinberg, Rev. Mod. Phys. **52**, 515 (1980),
A. Salam, Rev. Mod. Phys. **52**, 525 (1980),
S. L. Glashow, Rev. Mod. Phys. **52**, 539 (1980).

[2] F. J. Hasert *et al.*, Phys. Lett. **B46**, 121 (1973),
F. J. Hasert *et al.*, Phys. Lett. **B46**, 138 (1973).

[3] A. Benvenuti *et al.*, Phys. Rev. Lett. **32**, 800 (1974),
A. Benvenuti *et al.*, Phys. Rev. Lett. **37**, 1035 (1976).

[4] C. Y. Prescott *et al.*, Phys. Lett. **B77**, 347 (1978),
C. Y. Prescott *et al.*, Phys. Lett. **B84**, 524 (1979).

[5] L. M. Barkov and M. S. Zolotorev, Phys. Lett. **B85**, 308 (1979).

[6] M. Holder *et al.*, Phys. Lett. **B71**, 222 (1977),
H. Faissner *et al.*, Phys. Rev. Lett. **41**, 213 (1978).

[7] C. Quigg, Physics Today **50**, 20, (1997), hep-ph/9704332.

[8] R. P. Feynman and M. Gell–Mann, Phys. Rev. **109**, 193 (1958).

[9] E. Derman, Phys. Rev. **D7**, 2755 (1973).

[10] C. G. Callan and D. G. Gross, Phys. Rev. Lett. **22**, 156 (1969).

[11] T. van Ritbergen and R. G. Stuart, Phys. Rev. Lett. **82**, 488 (1999).

[12] D. E. Groom *et al.*, Eur. Phys. Jour. **C15**, 1 (2000).

[13] A. Sirlin, Phys. Rev. **D22**, 971 (1980).

[14] A. Sirlin, Rev. Mod. Phys. **50**, 573 (1978),
W. J. Marciano and A. Sirlin, Phys. Rev. **D22**, 2695 (1980).

[15] R. G. Stuart, Zeit. Phys. **C34**, 445 (1987),
G. Degrassi, S. Fanchiotti, A. Sirlin, Nucl. Phys. **B351**, 49 (1991),
S. Fanchiotti, B. Kniehl, and A. Sirlin, Phys. Rev. **D48**, 48 (1993).

[16] C . H. Llewellyn Smith, Nucl. Phys. **B228**, 205 (1983).

[17] K. S. McFarland *et al.*, Eur. Phys. Jour. **C31**, 509 (1998).

[18] Updated from K. S. McFarland, proceedings of the 28th International Conference on High Energy Physics (ICHEP 96), Warsaw, July 1996.

[19] E. A. Paschos and L. Wolfenstein, Phys. Rev. **D7**, 91 (1973).

[20] H. T. Edwards, Ann. Rev. Nucl. Part. Sci., **35**, 605 (1985).

[21] J. Thompson, Fermilab TM-1909 (1994).

[22] R. H. Bernstein *et al.*, FERMILAB-TM-1884 (1994),
J. Yu *et al.*, FERMILAB-TM-2040 (1998).

[23] D. A. Harris, J. Yu *et al.*, Nucl. Instr. Meth. **A447**, 373 (2000).

[24] W. Blum and L. Rolandi, Particle Detection with Drift Chambers, 1994.

[25] A. Vaitaitis, "Search for Neutral Heavy Leptons in a High Energy Neutrino Beam", Ph. D. thesis, Columbia University, New York, 2000.

[26] G. P. Zeller *et al.*, hep-ex/0010007, hep-ex/9906024,
K. S. McFarland *et al.*, hep-ex/9806013.

[27] T. A. Gabriel and D. E. Groom, Nucl. Instr. Meth. **A338**, 336 (1994).

[28] A. Romosan, "High Statistics Search for ν_μ ($\overline{\nu}_\mu$) $\rightarrow$ ν_e ($\overline{\nu}_e$) Oscillations in the Small Mixing Angle Regime", Ph. D. thesis, Columbia University, New York, 1996.

[29] M. Kobayashi and T. Maskawa, Prog. Theor. Phys. **49**, 652, (1973).

[30] D. Yu. Bardin and V. A. Dokuchaeva, Nucl. Phys. **B246**, 221 (1984), preprint JINR-E2-86-260 (1986).

[31] D. Bardin *et al.*, Comp. Phys. Commun. 133, 229 (2001), hep-ph/9908433v3 (March 1, 2000).

[32] S. Davidson *et al.*, J. High Energy Phys. **02**, 037 (2002), hep-ph/0112302.

[33] A. J. Buras and K. J. F. Gaemers, Nucl. Phys. **B132**, 249 (1978).

[34] U. K. Yang *et al.*, Phys. Rev. Lett. **86**, 2742 (2001).

[35] D. J. Gross and C. H. Llewellyn Smith, Nucl. Phys. **B14**, 337 (1969).

[36] W. G. Seligman *et al.*, Phys. Rev. Lett. **79**, 1213 (1997).

[37] M. Arneodo *et al.* (NMC collaboration), Nucl. Phys. **B487**, 3 (1997).

[38] E. A. Hawker *et al.*, Phys. Rev. Lett. **80**, 3715 (1998).

[39] A. Baldit *et al.*, Phys. Lett. **B332**, 244 (1994).

[40] R. S. Towell *et al.*, Phys. Rev. **D64**, 052002 (2001).

[41] U. K. Yang and A. Bodek, Phys. Rev. Lett. **82**, 2467 (1999).

[42] M. Goncharov *et al.*, Phys. Rev. **D64**, 112006 (2001).

[43] M. Goncharov, "Precise Measurement of Dimuon Production Cross–Sections in ν_μFe and $\overline{\nu}_\mu$Fe Deep Inelastic Scattering at the Tevatron", Ph. D. thesis, Kansas State University, Kansas, 2001.

[44] P. Collins and T. Spiller, J. Phys. **G11**, 1289 (1985).

[45] L. W. Whitlow, "Deep Inelastic Structure Functions from Electron Scattering on Hydrogen, Deuterium, and Iron at 0.6 GeV^2 $\leq$ Q^2 $\leq$ 30 GeV^2", Ph. D. thesis, Stanford University, California, 1990, SLAC–357 (1990).

[46] R. M. Barnett, Phys. Rev. **D14**, 70 (1976).

[47] H. Georgi and D. Politzer, Phys. Rev. **D14**, 1829 (1976).

[48] S. A. Rabinowitz *et al.*, Phys. Rev. Lett. **70**, 134 (1993).

[49] J. J. Aubert *et al.*, Nucl. Phys. **B213**, 31 (1983).

[50] J. Breitweg *et al.*, Eur. Phys. Jour. **C12**, 35 (2000).

[51] C. Adloff *et al.*, hep-ex/0108039, submitted to Phys. Lett. B, August 2001.

[52] A. Alton *et al.*, Phys. Rev. **D64**, 012002 (2001).

[53] S. V. Belikov *et al.*, IFVE-83-156, Zeit. Phys. **A320**, 625 (1985).

[54] G. P. Zeller, K. S. McFarland, "Neutral Current Analysis: Longexit Correction", memorandum, February 2001.

[55] R. G. Arnold *et al.*, Phys. Rev. Lett. **52**, 727 (1984), and J. Gomez *et al.*, Phys. Rev. **D49**, 4348 (1994).

[56] G. Amaudruz *et al.*, Nucl. Phys. **B441**, 3 (1995).

[57] M. R. Adams *et al.*, Zeit. Phys. **C67**, 403 (1995).

[58] W. G. Seligman, "A Next–to–Leading–Order QCD Analysis of Neutrino–Iron Structure Functions at the Tevatron", Ph. D. thesis, Columbia University, New York, 1997.

[59] SLAC-246, March 1982.

[60] C. H. Albright and C. Jarlskog, Nucl. Phys. **B84**, 467 (1975).

[61] C .G. Arroyo, "A Measurement of the Weak Mixing Angle in Neutrino-Nucleon Scattering", Ph. D. thesis, Columbia University, New York, 1996.

[62] M. Virchaux, A. Milsztajn, Phys. Lett. **B274**, 221 (1992).

[63] U. K. Yang, "A Measurement of Differential Cross Sections in Charged-Current Neutrino Interactions on Iron and a Global Structure Functions Analysis", Ph. D. thesis, University of Rochester, New York, 2000.

[64] S. E. Avvakumov, "Search for $\nu_\mu(\overline{\nu}_\mu) \to \nu_e(\overline{\nu}_e)$ Oscillations in the E815(NuTeV) Fixed Target Neutrino Experiment at Fermilab", Ph. D. thesis, University of Rochester, New York, 2001.

[65] L. deBarbaro, "Counter X-Ray and Alignment Memo", memorandum, March 1998.

[66] SLAC-246, March 1982.

[67] Atherton *et al.*, CERN-80-70.

[68] A. J. Malensek, "Empirical Formula for Thick Target Particle Production", FN-341, 1981.

[69] J. Ritchie Patterson, "Determination of $\mathrm{Re}(\epsilon'/\epsilon)$ by the Simultaneous Detection of the Four $K_{L,S} \to \pi\pi$ Decay Modes", Ph. D. thesis, University of Chicago, Illinois, 1990.

[70] R. Ammar *et al.*, Phys. Rev. Lett. **61**, 2185 (1988).

[71] K. Kodama *et al.*, Phys. Lett. **B263**, 573 (1991).

[72] M. Goncharov, private communication.

[73] "A Combination of Preliminary Electroweak Measurements and Constraints on the Standard Model", CERN-EP/2001-98, hep-ex/0112021.

[74] M. Gruenewald, private communication, for the fit of Ref. [73] without neutrino-nucleon scattering data included.

[75] M. S. Chanowitz, private communication.

[76] M. S. Chanowitz, Phys. Rev. Lett. **87**, 231802 (2001).

[77] S. C. Bennett and C. E. Wieman, Phys. Rev. Lett. **82**, 2484 (1999).

[78] A. Czarnecki and W. J. Marciano, Int. J. Mod. Phys. **A15**, 2365, (2000), hep-ph/0003049.

[79] D. Armstrong *et al.*, "The QWEAK Experiment: A Search for New Physics at the TeV Scale via a Measurement of the Proton's Weak Charge", proposal, December 3, 2001.

[80] J. Erler, private communication.

[81] E. Sather, Phys. Lett. **B274**, 433 (1992).

[82] E. N. Rodionov, A. W. Thomas, and J. T. Londergan, Mod. Phys. Lett. A **9**, 1799 (1994).

[83] F. Cao and A. I. Signal, Phys. Rev. **C62**, 015203 (2000).

[84] A. I. Signal and A. W. Thomas, Phys. Lett. **B191**, 205 (1987), M. Burkhardt and B. J. Warr, Phys. Rev. **D45**, 958 (1992), S. Brodsky and B. Ma, Phys. Lett. **B381**, 317 (1996), W. Melnitchouk and M. Malheiro, Phys. Lett. **B451**, 224 (1999).

[85] P. Langacker *et al.*, Rev. Mod. Phys. **64**, 87 (1992),
G. C. Cho *et al.*, Nucl. Phys. **B531**, 65 (1998),
D. Zeppenfeld and K. Cheung, hep-ph/9810277.

[86] J. Erler and P. Langacker, Phys. Rev. Lett. **84**, 212 (2000), hep-ph/9910315.

[87] F. Abe *et al.*, Phys. Rev. Lett. **22**, 2192 (1997),
V. M. Abazov *et al.*, Phys. Rev. Lett. **87**, 061802 (2001).

[88] G. P. Zeller *et al.*, Phys. Rev. Lett. **88**, 091802 (2002).

[89] G. P. Zeller *et al.*, Phys. Rev. **D65**, 111103 (2002), hep-ex/0203004.